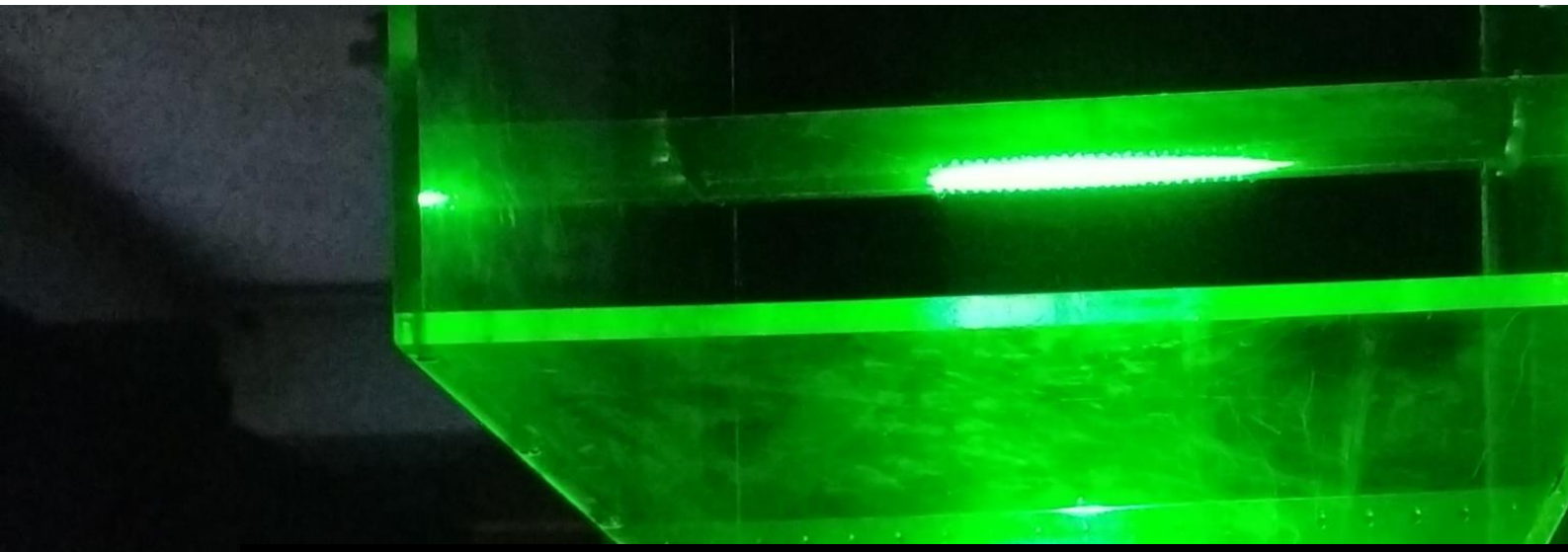

Film cooling aerodynamic performance: flow structures and aerodynamic losses in an airfoil with pressure side injection

MSc Thesis

Clara Paula Moreno Castán

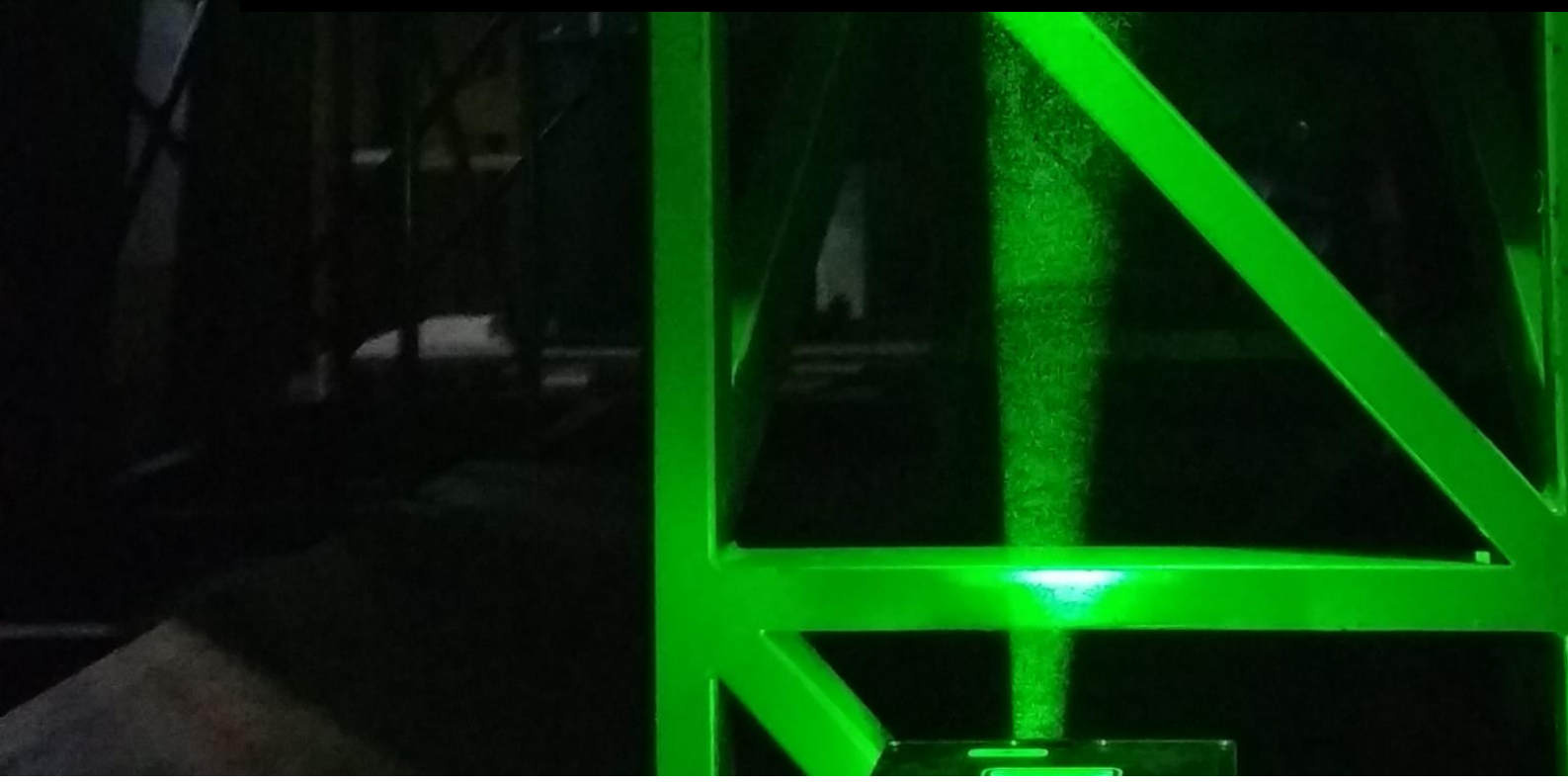

TU Delft Delft University of Technology

Challenge the future

Film cooling aerodynamic performance

Flow structures and aerodynamic losses in an airfoil with pressure side injection

By

Clara Paula Moreno Castán

in partial fulfilment of the requirements for the degree of
Master of Science in Aerospace Engineering

at the Delft University of Technology,

to be defended publicly on
Friday 8th June 2018 at 9:00

Student number:	4421760	
Project duration:	March 2017 - June 2018	
Thesis committee:	Dr. A. G. Rao,	TU Delft supervisor
	Dr. A. Sciacchitano,	TU Delft advisor
	Dr. G.A. Bohlin	TU Delft
	Dr. D. Ragni	TU Delft

This thesis is confidential and cannot be made public until 8th June 2018

TU Delft Delft University of Technology

Abstract

As a response to a socio-economic framework which demands lower fuel consumption and CO_2 emissions, gas turbine manufacturers strive to attain higher thermal efficiency and specific work output in their engines. The enhancement of these two performance parameters is linked to higher turbine inlet temperatures (TIT), which explains the increasing trend in TIT accompanying aero engines industrial development.

Turbine cooling technology is one of the disciplines strongly contributing to this aim, enabling operating hot gas temperatures to be higher than the melting temperature of the material. This study deals with film cooling: an external type of turbine cooling. Coolant air, bled from the compressor, is injected into the turbine blades and vanes and discharged through small holes into the airfoil´s external boundary layer, creating a thin insulating layer that reduces convective heat transfer from the hot gas to the surface. However, this gain in thermal capability brings along an aerodynamic penalty.

The purpose of this work is to understand the aerodynamic performance of a NACA 0012 airfoil with multi-row film cooling on the pressure side, as a follow-up experimental study of a previous one using the same model but with suction side injection. A configuration with angle of attack $\alpha = 0°$, freestream velocity $V_\infty = 15$ m/s ($Re_{\infty,c} = 1.18 \cdot 10^5$) and air as secondary flow is tested as a baseline to understand the effect of blowing ratio $BR \in (0,2)$ on flow field characteristics. Then, other configurations are tested to analyse the effect of angle of attack, freestream velocity, single row injection and density ratio by using CO_2 as secondary flow to simulate the temperature ratio existing in real gas turbine applications. With this experimental setup and operating conditions, the measured aerodynamic losses are limited to viscous effects in the airfoil boundary layer and wake shear layer including flow separation, and coolant-related losses due to mixing processes between primary and secondary flows.

Pointwise pressure measurements at a location downstream of the airfoil (x = 1.25·c) and planar and stereo PIV are used as flow measurement techniques. Wake velocity profile characteristics and aerodynamic losses are retrieved from pressure measurements. Results for the baseline configuration show how the wake velocity profile displaces towards the pressure side when blowing is introduced. For low blowing ratios, the low momentum of the coolant induces high mixing losses whereas for high blowing ratios, the energizing effect of the high momentum coolant outweighs the mixing losses resulting in an aerodynamic gain. Maximum losses are found for BR = 0.5 and they decrease for higher blowing ratios. For BR = 1.4, a shift from wake to jet local behaviour is observed. The high and low velocity regions in the 2D average velocity fields computed from planar PIV measurements show the same trend with blowing ratio in the wake region and provide further information about the mixing shear layer at a location close to the cooling holes. Finally, 3D average velocity fields computed from stereo PIV display the evolution of the mixing shear layer and jet in crossflow at different streamwise locations.

Table of Contents

Nomenclature

Latin symbol	Parameter
A	Area
C	Conversion factor in flowcontroller
c	Chord
c_p	Heat capacity at constant pressure
C_d	Discharge coefficient
d	Distance
D	Hole diameter
f	Focal length
$f_\#$	f-stop in PIV
h	Enthalpy
k	Coverage factor
L	Hole length
M	Mach number
N	Number of image pairs
$\dot{m}$	Mass flow
P	Pressure
q	Dynamic pressure
s	Entropy
R	Gas constant
T	Temperature
V	Velocity

Greek symbol	Parameter
Ω	Aerodynamic loss
γ	Ratio of specific heats
ξ	Aerodynamic loss
Y	Aerodynamic loss
α	Angle of attack
σ	Standard deviation
δ_z	Laser sheet thickness
β	Hole injection angle
ρ	Density

Subscript	Meaning
amb	Ambient
avg	Average
c	Coolant
cs	Cross-sectional
∞	Mainstream
is	Isentropic
i	Image
o	Object
s	Static magnitude
t	Total magnitude
1	Inlet
2	Exit

List of Abbreviations

Abbreviation	Meaning
AOA	Angle Of Attack
BR	Blowing Ratio
CCD	Charged Coupled Device
CFD	Computational Fluid Dynamics
CRVP	Counter Rotating Vortex Pair
DAS	Data Acquisition System
DLR	German Aerospace Center
DR	Density Ratio
FOV	Field of view
FREP	Fast Response Entropy Probe
FS	Full-scale
HSC	High-accuracy Silicon Ceramic
HWA	Hot Wire Anemometry
IAL	Integrated Aerodynamic Losses
IIM	Ideal Isentropic Mixing
IR	InfraRed
JICF	Jet In Cross Flow
KE	Kinetic Energy
LDV	Laser Doppler Velocimetry
LE	Leading Edge
MFR	Mass Flow Ratio
MRV	Magnetic Resonance Velocimetry
NGV	Nozzle Guide Vane
PIV	Particle Image Velocimetry
PS	Pressure Side
PSP	Pressure Sensitive Paint
PTU	Programmable Timing Unit
RD	Reading
SS	Suction Side
TBC	Thermal Barrier Coating
TIT	Turbine Inlet Temperature
TR	Temperature Ratio
VR	Velocity Ratio

List of Figures

List of Tables

1

Introduction

1.1. Framework and motivation

Contextualization

Gas turbine manufacturers strive to attain higher thermal efficiency and specific work output in their engines, as a response to a socio-economic framework which demands lower fuel consumption and CO_2 emissions. Brayton cycle thermodynamics in gas turbine theory ((Cohen, et al., 1996), (Farokhi, 2014)) show how the enhancement of these two performance parameters is linked to higher turbine inlet temperatures (TIT). Quantitatively, an increase of 55 K in TIT implies 1% efficiency gain in land-based gas turbines and 10% thrust gain in aero engines (Yao, et al., 2017)

This context and pushing set of demands explain the increasing trend in TIT accompanying gas turbine industrial development. More details about this rising trend can be found in the work of (Xu, et al., 2015) which presents the evolution of Rolls-Royce turbine inlet temperature from 1940 to 2010. In Boyce's Gas Turbine Engineering Handbook (Boyce, 2012), this steady increase in turbine temperatures is approximated as 10 K per year since 1950.

As a result of this persistent aim, current modern gas turbines reach an operating TIT beyond 1873 K according to (Hernández Rosette, et al., 2009), in line with the range of 1800K to 2000K stated by (Abdullah & Funakazi, 2013). This value is well above the melting temperature of the Nickel-based super alloys currently used in turbine blades, meaning that allowable hot gas temperatures are not constrained by thermal limits of available materials. This achievement is the result of combined research and development efforts on high temperature materials, manufacturing techniques, protective thermal barrier coatings (TBC) and turbine cooling methods. Figure 1.1. illustrates the coexistence and contribution of these disciplines to current gas turbines' thermal capability.

From all these disciplines, the focus of this study is placed on turbine cooling technology. Turbine cooling as a way to boost performance and durability is very old. As mentioned in Farokhi's book on Aircraft Propulsion: *'the first production turbojet engine, Jumo 004B, utilized internal cooling for the turbine blades. So, the concept is as old as the turbojet itself'* (Farokhi, 2014, p. 41). However, as (Khalatov, et al., 2017) report, in the last fifty years new and improved cooling methods have contributed to 80% of TIT growth in comparison to the 20% due to materials developments. In particular, this study deals with film cooling: an advanced external type of turbine cooling, which is acknowledged as *'the first and best line of defence for hot gas path surfaces against the onslaught of extreme heat fluxes'* (Bunker, 2005).

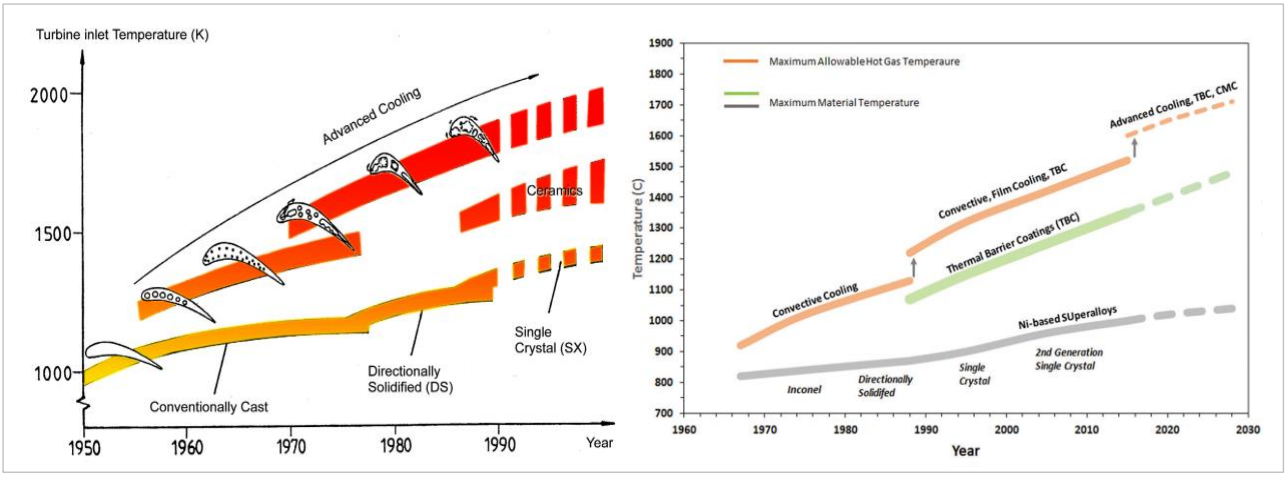

Figure 1.1. Evolution of gas turbine materials and cooling technology and contribution to hot gas temperatures. Left picture from (Vogel, 2002) and right picture from (Yao, et al., 2017)

Film cooling technology, challenges and motivation

Film cooling consists in the injection of a cold fluid, in the form of a thin insulating layer, along a surface exposed to a hot fluid. The function of this layer of coolant is to reduce convective heat transfer from the hot fluid to the surface, thus decreasing surface's temperature and thermal gradients and protecting it towards thermal damage and failure.

Applications of film cooling are not limited to gas turbine engines and turbine operating conditions. Film cooling is also used in rocket engines combustion chambers and exhaust systems. Moreover, its application extends to other hot gas path surfaces or components in gas turbine engines, such as combustion chamber and afterburner liners.

As we are focusing on turbine film cooling, the described hot fluid refers to the gases exiting the combustion chamber and the cold fluid is air before combustion, bled from the compressor stages. This coolant air is ducted into the inner channels of blades and vanes, where internal cooling methods are activated. Then it is discharged through small holes in discrete locations of blade and vane walls into the airfoil's external boundary layer. Due to the higher cooling needs of the airfoil's leading edge, the coolant holes in turbine vanes and blades are densely located in this area (i.e. showerhead film cooling) and more spaced in the rest of the airfoil's surface ((Bogard & Thole, 2005), (Han, et al., 2013)). In some cases, coolant air is also injected in the turbine blade tips and turbine endwalls. Each region exhibits different film cooling characteristics, as explained in (Thole & Knost, 2005).

Research on turbine film cooling started in the late 1950s, although film cooled turbine blades entered into service in military engines one decade later (Jindal, et al., 2016). Since then, a wealth of information concerning flow physics and thermal behaviour has been generated, leading to more optimized film cooling designs and more accurate computational models. According to Bunker's review (Bunker, 2005), literature on film cooling from 1970 to 2005 contains nearly 2700 publications. However, after six decades of studies and evolution on film cooling, there is still a lack of understanding of some of its multi-disciplinary aspects, which leaves room to their investigation.

Among them, the aero-thermal interaction between the hot (primary) and cold (secondary) fluid flows is extensively characterized as a complex phenomenon in literature. The mixing of the two flows induces a pair of counter rotating kidney-shaped vortices which cause the entrainment of the hot flow between the cold flow and the surface, decreasing film cooling effectiveness and surface coverage.

Hole geometry, coolant flow conditions and internal cooling schemes are just some of the multiple design parameters influencing the interaction. This complexity increases when considering the three dimensional and unsteady flow phenomena occurring in turbine stages.

The design challenge in film cooling is to maximize film cooling effectiveness while minimizing aerodynamic losses, which is directly related to limiting these vortical structures and increasing the ability of the coolant to stay attached to the surface downstream of the injection location. The aerodynamic penalty is relevant because it strongly impacts turbine efficiency and determines the amount of coolant flow to be bled from the compressor, affecting thermodynamic cycle performance and overall gas turbine performance. As stated by (Hassan Bashir, et al., 2017): *'it is pertinent to understand that the design objective (of film cooling) in practical application is to minimize coolant usage for the same or higher effectiveness'*.

In modern gas turbines, this amount of bled air for turbine cooling is 20-30% of compressor's air flow (Mazzei, et al., 2017) and numerous publications examine its detrimental effect on turbine performance ((Wilcock, et al., 2005), (Horlock & Torbidoni, 2008), (Romakhova, 2017)) and highlight the need of coolant savings.

In parallel, many studies emphasize the lack of understanding of film cooling flow physics and stress the need of conducting flow field measurements to gain deeper knowledge on the flows interaction and aerodynamic losses, helpful for design optimization and computational models validation. Citing some of these authors:

- *'a vast amount of film cooling effectiveness and heat transfer data exists, but a more detailed analysis of the flow field is required to gain more insight into the mechanisms governing these flow regimes in order to help design more accurate and robust computational film cooling codes. The advancement of film cooling technologies is severely hindered by the lack of understanding of the interactions between the coolant jet and mainstream flow'* (Voet, et al., 2017)*;*
- *'high fidelity (film cooling) measurements are necessary to validate existing, and future computational models for the purpose of producing the next generation of more efficient gas turbines'* (Natsui, et al., 2016)*;*
- *'since the thermodynamic cost of tapping air from the compressor is high, a thorough understanding of the flow-field and various parametric effects is of great value to the engine designer'* (Han & Rallabandi, 2010).

To this end, in the last two decades of film cooling research, newer and less intrusive optical flow measurement techniques such as Particle Image Velocimetry (PIV) or Pressure Sensitive Paint (PSP) have been progressively incorporated in experimental film cooling studies to investigate flow physics and evaluate aerodynamic losses.

1.2. Document structure

Once the relevance of film cooling aerodynamic performance has been introduced and the experimental approach justified, the document structure is presented.

Chapter 2 contains a literature review about experimental studies on aerodynamic losses and flow structures in turbine blades with film cooling. It covers three different topics: aerodynamic losses and flow structures, experimental conditions and flow scaling parameters and flow measurement techniques used for film cooling experiments. Each of the three topics is approached with an introductory theoretical background followed by a literature study. This literature review allows forming a broad picture of the research field and identifying the knowledge gaps that this project could contribute to.

Chapter 3 presents the research objectives, testing methodology and experimental setup for this MSc Project. First, the research goal is formulated in the form of research and sub-research questions. Second, the testing methodology presents the different film cooling configurations tested as well as the reference experimental matrix, which has the amount of coolant injection as the primary factor. Third, the experimental setup and approach used in the test campaigns is described, including information about the instrumentation and facilities used to conduct the tests. This encompasses specifications about the windtunnel, secondary flow system, airfoil model, pressure measurements system and PIV equipment, as well as a description of the setup arrangement and calibration process.

Chapter 4 introduces, analyses and discusses the pressure measurements results obtained for both air and CO_2. The effect of the primary factor (amount of coolant) on the aerodynamic performance of the model is analysed for a baseline configuration. Then, the effect of each of the nuisance factors (angle of attack, freestream velocity, partial injection, density ratio) on aerodynamic performance is subsequently introduced and understood. Finally, an uncertainty analysis is carried out.

Chapter 5 contains the PIV results, for both planar and stereoscopic PIV. First, global flowfield and local flowfield measurements are reported, investigating the effect of the variable factors in the flowfield and comparing the results with the pressure measurements obtained in Chapter 4. Then, stereo-PIV results present measurements at different streamwise locations. Finally, an uncertainty analysis is carried out.

Chapter 6 provides some concluding remarks from the project at hand and some recommendations for follow-up studies, both on possible research directions and experimental setup improvements.

At the end of the document, Appendices collate the literature study tables for each of the three topics of Chapter 2, technical information about the flow controller used for the secondary flow and some additional results not included in the main body of the report.

2

Literature review

The research aim of this Chapter is to review past and recent related publications, summarize their approach, methodology and conclusions, form a big picture of the field of research and gain theoretical insight in some areas. Its outcome will be the identification of the knowledge gap, a set of research goals and a testing methodology, presented in Chapter 3.

2.1. Research scope

This MSc Thesis Project will be a follow-up study of a previous one (Lanzillotta, et al., 2017), so the geometrical features of the model are already fixed and the windtunnel setup as well as available flow measurement techniques known. Consequently, due to the vast amount of open literature and the time constraints of the MSc Thesis Project, below are listed some interesting search results and influencing parameters which will ***not*** be thoroughly looked into.

Cooling holes

- Cooling holes size
- Cooling holes arrangement i.e. hole-to-hole spacing, inter-row distance, inline or staggered configuration, pitch-to-diameter ratio, coverage ratio
- Cooling hole geometry. This covers a big part of literature, involving factors like streamwise injection angle and lateral injection angle (i.e. compound angle); entry and exit shape (i.e. shaped holes) and entry and exit area ratio; expanded or converging cross-sectional area in axial or lateral directions (i.e. laidback or fan-shaped holes); hole length-to-diameter ratio, slot vs. discrete hole, round-to-slot combinations
- Novel hole designs, such as reverse-oriented or backward injection holes, sister holes, holes in transverse slots and trenches, upstream steps, ramps or ridge-shaped tabs, downstream vortex generators, louver scheme, double-jet, nekomimi, antivortex, arrowhead-shaped, wall-parallel inlet, tripod-shaped, cratered, threaded holes

Model

- Hole throat and surface roughness
- Manufacturing techniques, tolerances and defects
- Highly loaded or cambered airfoils
- Design methodology for cooled blades, i.e. thermal resistance models
- Leading edge shape
- Internal, showerhead or trailing edge cooling, and combined cooling configurations
- Effect of internal cooling design into external cooling
- Steam film cooling or transpiration cooling, i.e. through porous surface
- Flow control, i.e. boundary layer suction, plasma actuators, fluidic oscillators in film cooling

Test rig

- Design of test rigs for film cooling experiments
- Coolant pipe geometry and realistic hole inflow conditions
- Rotating setups and rotational effects
- Endwall cooling and secondary flows i.e. passage and corner vortices
- Blade tip cooling and gap leakage effects

Flow

- Turbine cascades or complete turbine stages
- Tracer particles in coolant flow
- Ludwieg tube windtunnel for film cooling experiments
- Transonic or supersonic flow regimes, with shockwave-boundary layer interaction and compressibility effects
- Freestream flow conditions resembling real engine operating conditions, such as non-uniformity, unsteadiness from unsteady wakes, high turbulence and temperature levels, flow acceleration or adverse pressure gradients
- Boundary layer displacement thickness and nature near hole entry
- Presence of crossflow at inlet or outlet

Field of research

- Heat transfer performance, evaluated by adiabatic film cooling effectiveness and heat transfer coefficient, boundary layer temperature distributions, Nusselt number
- Heat transfer measurement techniques, i.e. thermocouples, infrared thermography, temperature sensitive paint, liquid crystal thermometry, thin film gages, naphthalene sublimation
- Heat-mass transfer analogy assumptions and superposition principle for heat transfer and wall temperature measurements
- Computational studies, turbulence models and numerical analysis

Conversely, the following research areas will be more carefully reviewed to complement the mentioned study:

Flow structures and losses

- Cooled turbine blade flow structures and aerodynamic losses coefficients and variables
- Experimental characterization of the counter rotating vortex pair (CRVP) of the inclined jet in crossflow problem in film cooling
- Differences in aerodynamic behaviour between coolant ejection from airfoil's pressure side (or general concave surface) and suction side
- Differences in aerodynamic behaviour between pressure and suction side with same ejection location

Experimental conditions

- Models and windtunnel general setups
- Influence of simplified airfoil test model and 3D printed holes
- Effusion (multi-row) cooling, number of rows, injection patterns and partial film cooling
- Effect of incidence angle or velocity
- Operating conditions and scaling flowfield parameters
- Variable density ratio effect, foreign gas injection technique and secondary flow systems

Techniques

- Flow measurement and visualisation techniques for pressure and velocity fields in film cooling experiments
- PIV technique use and experimental setups

Based on these considerations, this Chapter is structured in three sections corresponding to the three relevant research areas (flow structures and losses, experimental conditions and measurement techniques). Section 2.1 introduces the flow structures appearing in film cooled turbine blades due to mainstream and coolant interaction and the methods to measure and calculate aerodynamic losses. Section 2.2 presents flowfield scaling parameters, with special focus on density ratio effect and foreign gas injection and summarizes the testing conditions in film cooling experiments. Section 2.3 describes the flow measurement and visualisation techniques used in film cooling aerodynamics, with special focus on the use of PIV technique. As mentioned, all three sections start with a theoretical

background before reporting the literature review. To present the literature review, the author has selected 69 experimental studies on turbine film cooling aerodynamic losses or flow structures. Then, basic information related to the section's topic is searched for in these studies and tabulated (tables for each topic can be found in Appendix I). The Chapter concludes with a summary table providing a general overview of the reviewed publications.

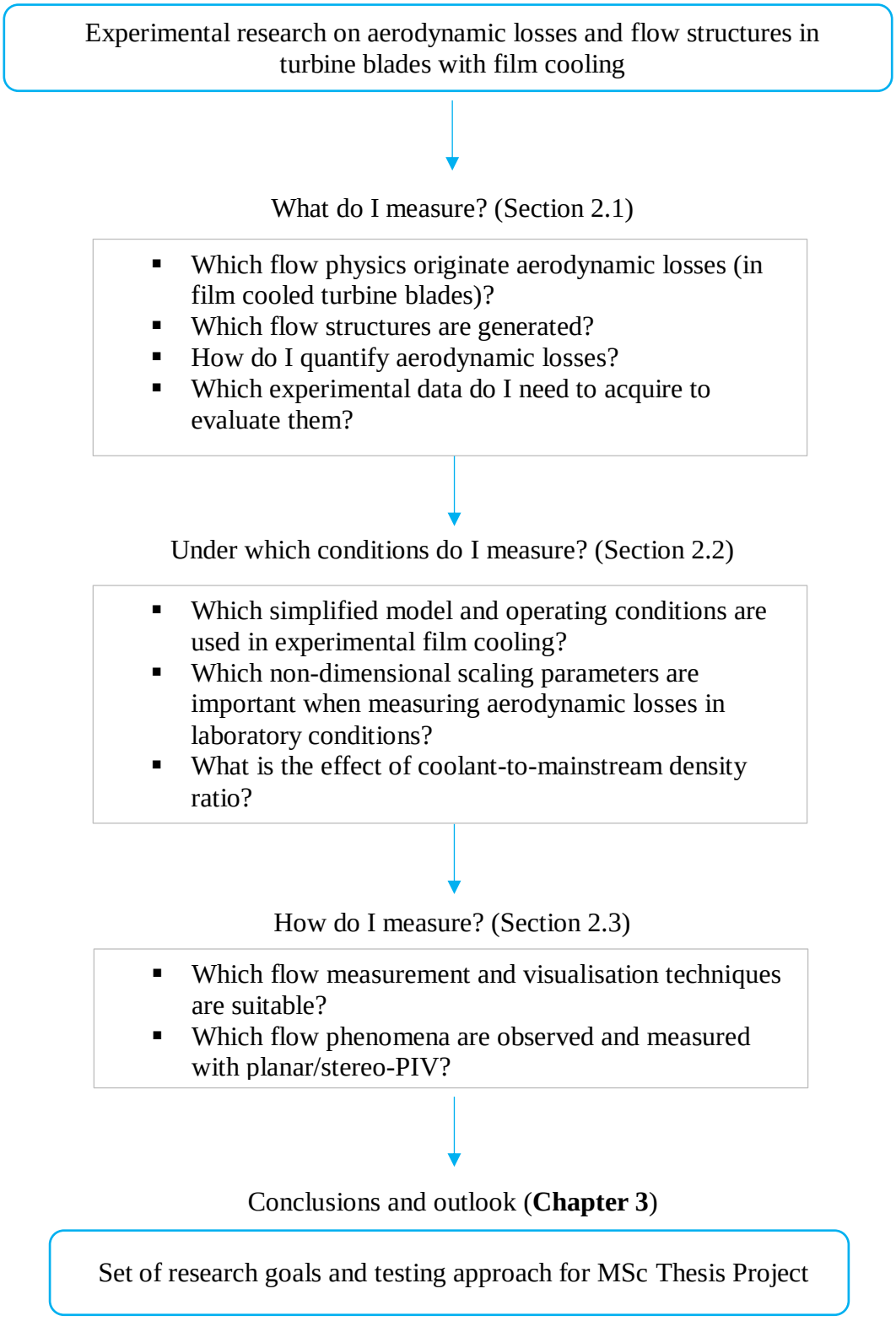

Figure 2.1. Overview of Chapter 2

2.2. Aerodynamic losses and flow structures

2.2.1. Theoretical background

Flow structures in jet and mainstream interaction

Some film cooling studies aim to understand the origins of aerodynamic losses by visualising the flow structures generated from the film cooling holes.

General subsonic or transonic aerodynamic phenomena (boundary layer transition, separation, laminar separation bubbles, shock waves) as well as uncooled turbomachinery flow features are also captured and analysed. The latter include endwall secondary flows (passage vortex, corner vortex and endwall crossflow) generated from the interaction between the incoming boundary layer and the cross-passage pressure gradient, together with the tip flows or blade wakes appearing in the highly turbulent and unsteady flow environment of turbine stages (see Figure 2.2.)

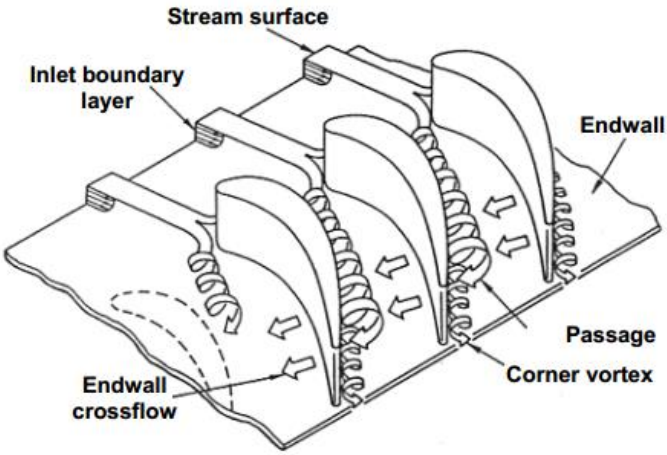

Figure 2.2. Passage flow in turbine cascade (source: (Langston, 1980))

However, most of the attention of these studies is placed on the complex flow structures generated from the jet and mainstream interaction, which modify the jet structure, generate aerodynamic mixing losses and are eventually detrimental for film cooling performance.

The physical problem of the interaction between a fluid exiting an orifice and a fluid flowing across the orifice is known as the jet in crossflow (JICF) problem. According to (Kim, et al., 2000), JICF is one of the most complex turbulent flow problems and the initial stages of its research date back to more than 50 years ago. A review of this work can be found in (Margason, 1993), (Holdeman, et al., 1997) or (Morton & Ibbetson, 1996). From all this work, we can highlight two publications: (Fric & Roshko, 1994) and (Kelso, et al., 1996), commonly taken as a reference to describe the flow structures appearing in JICF. These two studies visualized similar vortical structures formed in near field during the mixing process. They are depicted in Figure 2.3 and can be classified in four types:

- Jet shear layer vortices. They dominate the initial part of the jet, when the jet is still bending to align with the crossflow direction. They are intrinsically unsteady and are formed around the jet's perimeter, resulting from a Kelvin-Helmholtz instability in the shear layer at the hole's leading edge. Kelso, et al. (1996) refer to these vortices as 'ring vortices', 'loop-like vortices' or rolling-up of the shear layer. Other authors refer to them as 'windward' vortices.

- Horseshoe vortices. They are formed in the wall upstream of the jet. Similar to the vortices produced by a cylinder in a crossflow, they tend to evolve on the sides, wrapping around the base of the jet but far from the jet core region. Although they can have unsteady components, they have mean-flow definition. Kelso, et al. (1996) also refer to them as 'necklace vortices'.

- Wake vortices. They are formed downstream of the hole and their vorticity comes from crossflow's boundary layer separation at the wall. They follow the same direction as the original jet, extending from the wall to the jet. Like the jet shear vortices, they have an unsteady nature. Kelso, et al. (1996) subdivide the wake vortices into 'wall vortices' and 'upright vortices'.

- Counter-rotating vortices. Embedded in the jet, they appear in the jet's cross-section once it is bent in the crossflow direction. Like horseshoe vortices, they can be observed in time-averaged flow fields because its length scales are significantly bigger than those of the turbulent energy eddies. They are commonly referred to as 'kidney shaped' vortices or the counter-rotating vortex pair (CRVP). From all the vortical structures, special attention is placed in literature on the CRVP as a canonical and dominant feature of film cooling flows. Citing Peterson & Plesniak (Peterson & Plesniak, 2002, p. 889): *'the most physically significant and universal flow structure in JICF, and thus the most widely referenced, is the counter-rotating vortex pair (CRVP)'*. However, the formation mechanisms of CRVP are still unclear (Peterson & Plesniak, 2004).

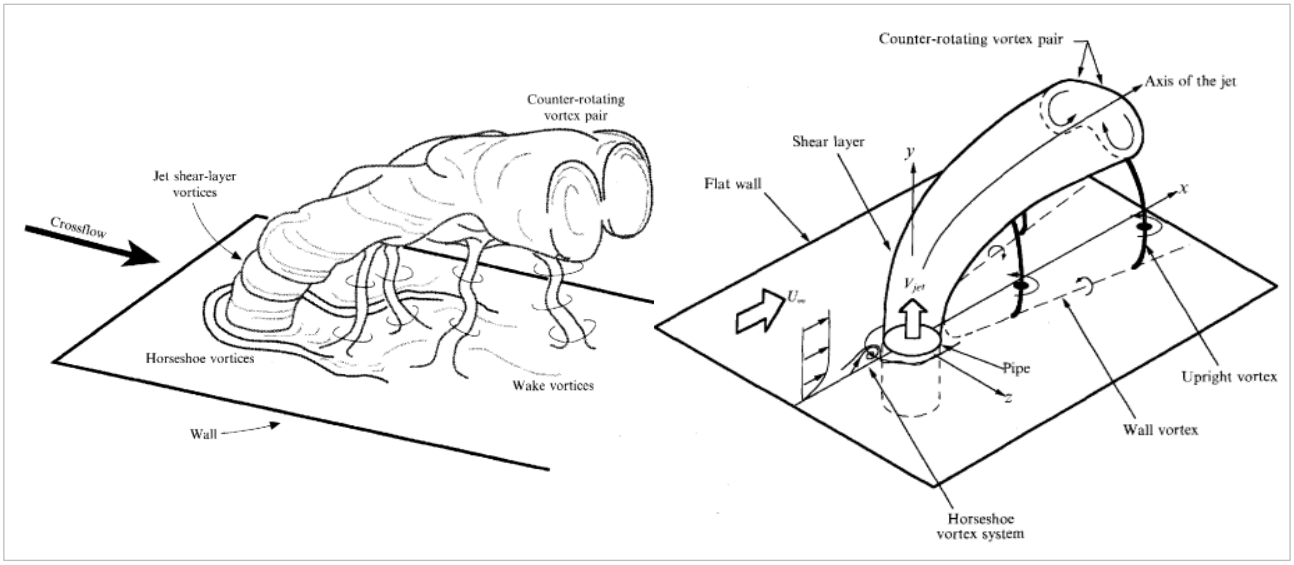

Figure 2.3. Four types of vortical structures in the near field of a jet in crossflow (JICF)

Some authors in literature propose that the formation of the CRVP depends on the in-hole vorticity and jet separation inside the hole. Other authors (Lemmon, et al., 1999) argue that the formation of the CRVP depends only on the shear layer between the mainstream and the coolant jet and not on the in-hole vorticity. Investigating in more depth the literature on CRVP formation mechanisms is beyond the scope of this document.

However, it is relevant to have a short look at how the CRVP affects the flowfield. The CRVP increases aerodynamic mixing, causing turbulence production, mixing losses and heat transfer increase. It dominates the turbulent structure in the shear layer, which affects the stability of the film and its protective effect. The counter rotative movement of the vortices and the turbulent diffusion provoke the entrainment of the mainstream into the jet, conveying hot crossflow below the coolant. Moreover, the CRVP modifies the jet trajectory, promoting coolant jet lift-off, delaying jet

reattachment and reducing the jet spreading in the spanwise direction. This is all detrimental for film cooling performance.

Even if the CRVP is originated in the near field of the hole, it propagates downstream in the jet's cross-section and extends in the far field. As a result, the CRVP governs the dominant features of the pressure, velocity and vorticity fields far away from the film cooling hole (Kamotani & Greber, 1979). This all shows the role of CRVP's strength, size and dynamics in defining the flowfield and heat transfer in film cooling and justifies the importance of analysing and controlling its characteristics and evolution. One example of how to influence the CRVP characteristics is the generation of 'anti-kidney vortex pairs' (Haven, et al., 1997), which rotate opposite to the CRVP thus creating destructive vortex interference and reducing CRVP's strength. These vortical structures can be created via hole design.

Aerodynamic losses quantification

Citing J.D. Denton (Denton, 1993, p. 622): '*a good physical understanding of the flow and particularly of the origins of loss is more important to the designer than is the availability of a good but oversimplified loss correlation'*. Following this advice, let us have a short look at the origins of loss in a film cooled turbine before presenting the parameters which are commonly used to quantify them.

(Denton, 1993) classifies the mechanisms for entropy creation in three groups:

- Viscous friction in boundary layers and free shear layers, where mixing processes are included
- Heat transfer with a finite temperature difference
- Non-equilibrium processes, such as shockwaves or very rapid expansions

When applying these mechanisms to turbines, Farokhi classifies turbine blade losses in six groups in his book on Aircraft Propulsion (Farokhi, 2014).

- **Profile losses**, including airfoil boundary layer viscous effects and trailing edge wake shear layers and dissipation losses; they can be established based on 2D cascade studies
- **Coolant-related losses**, including mixing losses and the induced separation losses
- Secondary flow losses, estimated using Hawthorne secondary flow theory
- Annulus losses, including tip clearance losses, leakage losses, corner vortex losses, casing boundary layer losses
- Shock waves and shock – boundary layer interaction losses in transonic turbine stages
- Unsteady flow losses, which include vortex shedding in the wake and shock oscillation

Section 7.7.2.4. of Lakshminarayana's book (Lakshminarayana, 1996) is recommended for a more in-depth insight on the modelling of aerodynamic losses due to film cooling. They are described as the sum of profile and jet-mainstream (i.e. 'coolant-related') mixing losses to enable the development of a calculation method. The modelling of the mixing process, with a constant pressure field or with a pressure gradient effect near the jet and a 'mixing layer' analysis is also introduced here.

When reviewing the literature, one finds multiple methods and parameters to quantify aerodynamic losses in cooled and uncooled turbine blades (Ligrani, 2012). The aim of this section is to briefly summarize and define the most commonly used ones, which we could classify in three groups: local aerodynamic performance parameters, aerodynamic losses between two locations and pressure losses through the cooling holes.

1) Flow parameters at one specific location, usually measured at the exit location. Sometimes they are normalized and used to calculate local-to-mainstream ratios (normalized local Mach number and normalized local kinetic energy), as presented in (Lanzillotta, et al., 2017) . They can also be measured at multiple locations around the airfoil's contour to reconstruct the flowfield around the turbine blade profile. These are:

   - Local Mach number, *M*.
   - Local flow angle,
   - Local static and total pressure, P_t or P_s
   - Local kinetic energy, *K.E.*

2) Differential losses between two locations (named as 1 and 2). In this group we can include:
   - Primary loss coefficient, ξ_p. It was defined by Horlock (Horlock, 1966), and in literature it is also referred to as energy or enthalpy loss coefficient (Denton, 1993) and kinetic loss coefficient (Sierverding, et al., 1994). The problem of the primary loss coefficient definition is that it neglects the kinetic energy of the coolant.

$$\xi_p = 1 - \frac{{V_2}^2}{{V_{2,is}}^2} = 1 - \frac{h_{t_2} - h_{s_2}}{h_{t_1} - h_{s_{2,is}}} = 1 - \frac{1 - \left(\frac{P_{s_2}}{P_{t_2}}\right)^{\frac{\gamma-1}{\gamma}}}{1 - \left(\frac{P_{s_2}}{P_{t_1}}\right)^{\frac{\gamma-1}{\gamma}}} \tag{2.1}$$

   - Thermodynamic loss coefficient, ξ_{th}. This is the definition of the jet-mainstream mixing losses component described in (Lakshminarayana, 1996) and is widely used in literature. Contrary to the enthalpy loss coefficient, it includes the ideal kinetic energy of the coolant. It is defined as the ratio of the kinetic energy of the gas at the mixed-out static conditions to the ideal kinetic energy that would be obtained at the mixed-out static conditions in an isentropic expansion from inlet total conditions.

$$\begin{aligned} \xi_{th} &= 1 - \frac{\left(1 + \frac{m_c}{m_\infty}\right) \cdot {V_2}^2}{{V_{2,is}}^2 + \frac{m_c}{m_\infty} \cdot {V_{2\,c,is}}^2} \\ &= 1 - \frac{h_{t_2} \cdot \left(1 + \frac{m_c}{m_\infty}\right)\left(1 - \left(\frac{P_{s_2}}{P_{t_2}}\right)^{\frac{\gamma_2-1}{\gamma_2}}\right)}{h_{t_1} \cdot \left(1 - \left(\frac{P_{s_2}}{P_{t_1}}\right)^{\frac{\gamma_1-1}{\gamma_1}}\right) + h_{t_c} \cdot \frac{m_c}{m_\infty} \cdot \left(1 - \left(\frac{P_{s_2}}{P_{t_c}}\right)^{\frac{\gamma_c-1}{\gamma_c}}\right)} \end{aligned} \tag{2.2}$$

   - Local total pressure loss coefficient C_p, used in various publications of Zhang & Ligrani.

$$C_p = \frac{P_{t_1} - P_{t_2}}{P_{t_1}} = 1 - \left(\frac{P_{t_2}}{P_{t_1}}\right) \tag{2.3}$$

- Loss coefficient in an airfoil cascade (Walters & Leylek, 2000)

$$\xi = \frac{P_{t_1} - P_{t_2}}{P_{t_1} - P_{s_2}} \cdot \left(\frac{V_2}{V_{2,avg}} \right) \tag{2.4}$$

- Entropy rise coefficient Y_S (Ligrani, 2012) or entropy loss coefficient ξ_s (Denton, 1993)

$$Y_S = \frac{T_2 \cdot (s_2 - s_1)}{\frac{{V_2}^2}{2}} \tag{2.5}$$

- Total pressure loss coefficient C_{pt} (Kubo, et al., 1998) or ω (Hartsel, 1970), stagnation pressure loss coefficient Y_P (Denton, 1993), omega aerodynamic loss coefficient Ω. (Ames & Plesniak, 1997). It is equivalent to the entropy rise coefficient for low speed incompressible flows and it is widely used in literature. In (Lin, et al., 2014) an ideal isentropic mixing (IIM) method is proposed to calculate the inlet total pressure P_{t_1}, as an alternative to the commonly used mass flow averaged (MFA) method.

$$\Omega = \frac{P_{t_1} - P_{t_2}}{P_{t_1} - P_{s_2}} \tag{2.6}$$

- Integrated aerodynamic losses, *IAL* (Zhang, et al., 2005). Dimensional magnitude resulting from the integration of total pressure in the transverse flow direction across the wake.

$$IAL = \int_{-p/2}^{p/2} \left(P_{t_1} - P_{t_2} \right) \cdot dy \tag{2.7}$$

- Area averaged loss coefficients, presented in (Zhang, et al., 2005), (Boyle, et al., 2002)
- Mass averaged loss coefficients, presented in (Ito, et al., 1980)
- Mixing loss coefficient, presented in (Köllen, 1986), (Stephan, et al., 2010). It represents the accumulated pressure losses in the mixing layer.

3) Losses through the cooling holes:

- Discharge coefficient, C_d. The discharge loss coefficient is a measure of the pressure losses inside the holes and is defined as the ratio between the measured coolant mass flow rate and the ideal mass flow rate through the hole.

$$C_d = \frac{\dot{m}_{c\,actual}}{\dot{m}_{c\,ideal}} \tag{2.8}$$

  Assuming an isentropic, one-dimensional expansion from the coolant channel total pressure to the discharge mainstream static pressure, $\dot{m}_{ideal}$ is expressed as in equation 2.9 in multiple publications ((Aghasi & Gutmark, 2017), (Singh, et al., 2017), (Drost, 1998), (Vogel, 2002), (Aga, 2009)). This expression results from applying thermodynamic

relations like the continuity equation, ideal gas law and isentropic relations (see (Brown & Helon, 1973)).

$$\dot{m}_{c_{ideal}} = A_{hole} \cdot P_{t_c} \cdot \left(\frac{P_{s_\infty}}{P_{t_c}}\right)^{\frac{\gamma+1}{2\gamma}} \cdot \sqrt{\frac{2\gamma}{(\gamma-1)\cdot R \cdot T_{t_c}}\left[\left(\frac{P_{t_c}}{P_{s_\infty}}\right)^{\frac{\gamma-1}{\gamma}} - 1\right]} \tag{2.9}$$

When compressibility effects can be ignored, Bernoulli equation can be directly applied as done in (Burd & Simon, 1999) and (Yao, et al., 2013).

$$\dot{m}_{c_{ideal}} = A_{hole} \cdot \sqrt{2\rho \cdot (P_{t_c} - P_{s_\infty})} \tag{2.10}$$

2.2.2. Literature study

As mentioned, the review of previous research is presented in the form of a table, extracting information from 69 experimental studies on relevant topics. This table can be found in Appendix I. For this section, it presents:

- Topic of the study
- Aerodynamic losses quantification, for those studies including aerodynamic performance
- Flow structures and flow field characteristics, for flowfield investigations

Note that there is one study (Nguyen, et al., 2012) in which there are no aerodynamic measurements performed, since only thermal parameters are measured. However, this study is included because it analyses the effect of injection patterns and necessary number of cooling holes rows in full-coverage film cooling. Also, it is important to clarify that 'streamwise' and 'spanwise' plane/measurement/location refer to the planes normal to the freestream or span direction, respectively (not aligned with them)

From the theory and literature review of this section on aerodynamic losses and flow structures, we can draw the following conclusions:

- The jet and mainstream interaction in film cooling generates complex flow structures, which modify the jet structure, generate aerodynamic mixing losses and reduce film cooling effectiveness.
- There are four main vortical structures generated in the jet in crossflow problem: jet shear layer or ring vortices, horseshoe vortices, wake vortices and counter-rotating vortices.
- From these four, the counter-rotating vortex pair is the most significant for film cooling performance. It increases aerodynamic mixing, turbulence and heat transfer, promotes jet lift-off, delays jet reattachment and affects the stability of the film, reducing its thermal protective function.
- It is important to understand the characteristics and evolution of the counter-rotating vortex pair because of its effect on velocity and vorticity fields far away from the cooling holes and effect on aerodynamic losses.
- Aerodynamic losses are synonym of entropy generation. From all the types of losses appearing in turbine blades, we will focus on profile and mixing losses, in which viscous friction is the entropy generation mechanism.

- There are multiple ways to quantify aerodynamic losses. In this document we classify them in three groups: local performance parameters, losses coefficients between two locations and losses through the cooling holes.
- From all the aerodynamic losses parameters between two locations, we can highlight the primary loss coefficient, thermodynamic loss coefficient, local total pressure loss coefficient, total pressure loss coefficient and integrated aerodynamic losses as the most common ones.
- The pressure losses through a cooling hole can be estimated with the discharge coefficient.

2.3. Experimental conditions and scaling parameters

2.3.1. Theoretical background

Coolant flow scaling parameters

In film cooling studies, the experimental flow conditions are commonly described using ratios between the primary and secondary flow conditions (i.e. velocity and density). These non-dimensional parameters are presented in this section.

- Mass flow ratio, *MFR*. It is rarely used in recent film cooling studies.

$$MFR = \frac{m_c}{m_\infty} \tag{2.11}$$

- Velocity ratio, *VR*. Coolant velocity is calculated using the area of the holes, A_{hole} in the continuity equation.

$$VR = \frac{V_c}{V_\infty} \tag{2.12}$$

- Density ratio, *DR*. It can be increased to test closer to realistic engine operating conditions, which typically have a density ratio between 1.5 and 2 (Eberly & Thole, 2014) due to the temperature ratio between the hot primary flow and cold secondary flow. There is no agreement in literature about the effect of density ratio on film cooling performance.

$$DR = \frac{\rho_c}{\rho_\infty} \tag{2.13}$$

- Blowing ratio, *BR*, also referred to as mass flux ratio. Blowing ratio is the most commonly used scaling flow parameter in film cooling experimental studies. It represents the mass addition to the boundary layer by the secondary flow (Voet, 2017) and it affects the instantaneous vortical structures characteristics ((Fawcett, et al., 2012), (Haydt, et al., 2017)), the shear stresses, jet strength and penetration into the mainflow and the in-hole flow physics (Peterson & Plesniak, 2004)

$$BR = \frac{(\rho \cdot V)_c}{(\rho \cdot V)_\infty} = DR \cdot VR \tag{2.14}$$

- Momentum flux ratio, *I*. It characterizes JICF separation behaviour and evaluates the ability of the mainstream flow to turn the coolant jet towards the wall (Anderson, et al., 2015). If the momentum of the jet is not large enough relative to the mainstream flow's, the viscous and pressure forces exerted by the mainstream flow and acting on the jet's boundary turn it, so then it can reattach to the wall. If the momentum of the jet is large enough, the jet separates and disperses without jet reattachment and allowing the mainstream flow underneath (jet lift-

off). According to (Bogard & Thole, 2005), if I < 0.4, the jet remains fully attached and if I > 0.8 the jet remains fully detached. For 0.4 < I < 0.8, the jet is initially detached but then it is turned and reattached to the surface.

$$I = \frac{(\rho \cdot V^2)_c}{(\rho \cdot V^2)_\infty} = DR \cdot VR^2 = BR \cdot VR \tag{2.15}$$

As mentioned above, from all these parameters, blowing ratio is commonly used as the independent variable to characterize film cooling performance. For a fixed BR, when setting the DR from the experimental setup, VR and I are fixed too.

Variable density ratio: effect and techniques

To test the mixing process of the flows closer to real engine operating conditions, some research groups state that it is important to create a temperature ratio between the mainstream and jet flows. This can be done with diverse techniques, such as heating the mainstream flow, cooling the secondary flow with a cryogenic N_2 heat exchanger or injecting a foreign gas at the same temperature as the mainstream flow but with a higher density (Voet, et al., 2017). Other research groups argue that the effect of density ratio on film cooling performance is negligible, or that creating it could be undesirable when using the foreign gas injection technique, which modifies other fluid properties. All in all, despite the big amount of publications the research community has not reached an agreement on the effect of density ratio on film cooling hydrodynamics.

For a fixed BR, when increasing DR, VR and I decrease (continuity equation). As a result, considering the link between momentum flux ratio and jet separation exposed above, there is a lower possibility that the jet lifts off. Increasing DR would then have the same effect as decreasing I, so it would be beneficial for film cooling performance and the laboratory measurements would be conservative with respect to enginelike conditions. When considering the effect of DR in film cooling heat transfer, the computational study of Chang et al. (Chang, et al., 2012) concludes that a higher density ratio is beneficial for film cooling performance only when the jets have separated from the wall; then, a higher density ratio constrains or delays jet lift-off. But when the jet is not separated then film cooling effectiveness is dominated by BR and the effect of DR is negligible.

There are also some studies examining which is the most adequate scaling parameter (BR, VR or I) to characterize the jet and mainstream interaction and eventually film cooling performance in the cases with variable density ratio or a density ratio higher than unity. Among them, we can highlight the work of Anderson et al. (Anderson, et al., 2015), one of the very few experimental studies fully devoted to analysing which is the proper flow scaling parameter to match for variable density ratio studies, or the work of Johnson et al. (Johnson, et al., 2014) which also discusses the adequacy of each scaling parameter for thermal performance. The research aim of these studies is to understand which scaling parameter should be fixed so that the produced results are less dependent on the chosen density ratio, or as commonly said in literature leads to a better 'collapse of the data' for varying density ratios. Together with these two studies, there are more publications dealing with scaling parameters in variable density ratio studies. The conclusions of all of them are summarized below.

A group of publications argues that momentum flux ratio is the correct scaling parameter at any mass flow rate condition for studying aerodynamic losses in variable density ratio cases. In this group we include the works of (Mee, 1992), (Osnaghi, et al., 1997), (Oldfield, et al., 1999) and (Day, et al., 2000).

(Sinha, et al., 1991) concluded that when analysing film cooling thermal performance (not aerodynamic losses) BR should be used as scaling parameter for attached jets and I should be used for detached-reattached jets.

(Ethridge , et al., 2001) conducted an experimental study about scaling parameters on the suction side of a highly loaded airfoil. Their results indicate that BR is appropriate for scaling at low blowing conditions and I outperforms at high blowing conditions, although at very low blowing rates neither BR or I are successful to match high and low DR.

(Johnson, et al., 2014) concluded from their analysis with different scaling quantities that the scaling parameters which describe the dynamic processes by including DR in their definition (i.e. BR and I) are more suitable for low coolant flow rates and the purely kinematic scaling parameter (i.e. VR) is more suitable for high coolant flow rates when evaluating film cooling thermal performance.

(Anderson, et al., 2015) studied the effect of coolant-to-mainstream scaling parameters on both cylindrical and shaped holes with thermal performance. The conclusions of this work are that for cylindrical holes VR and I are more adequate than BR at any coolant flow rate and VR is the proper scaling parameter at high coolant flow rates. For shaped holes, VR is the most suitable scaling parameter at any coolant flow rate. This work highlights the importance of VR in describing the shear layer between the coolant and the mainstream and the turbulence production, while recognizes the importance of BR in providing a measure of the amount of coolant available at low coolant rates and of I in providing information about jet separation at high coolant rates.

(Voet, 2017) carried out hydrodynamic measurements of density ratio effects by independently holding BR, I or VR constant. The conclusion of this work is that jet velocity magnitudes and trajectory are better correlated with BR, followed by I. VR is the least recommended scaling parameter when analysing jet structure.

(Zeng, et al., 2017) performed a numerical investigation of coolant-to-mainstream scaling parameters on the pressure and suction side of a turbine blade, independently varying BR, DR and I for four different density ratios and evaluating film cooling thermal performance. They conclude that with film cooling effectiveness as criterion parameter, no parameter is independent of density ratio in the full range of simulation conditions for both pressure and suction side. In the pressure side, BR is linearly correlated with DR. The outcome of their work is a new evaluation parameter which has two different definitions depending on the value of VR.

(Sakai & Takahashi, 2017) also conducted a numerical study on density ratio effects stating that the momentum flux ratio should be used as scaling parameter. In their study they analysed the effect of density ratio on flow structures and concluded that at low density ratios a hairpin vortex is formed instead of a jet shear layer vortex downstream of the hole exit.

Finally, section IV in (Bogard & Thole, 2005) presents a small review about other researchers' conclusions on the effect of scaling parameters based on thermal performance. (Ornano & Povey, 2017) also present a brief review of publications claiming that momentum flux ratio should be used as scaling parameter, especially at high flow rates.

2.3.2. Literature study

For this section, the literature table in Appendix I presents:

- Model used
- Operating conditions (Reynolds and Mach number)
- Range of coolant flow scaling parameters
- Technique for high or variable density ratio

Some notes can be useful when looking at the literature study table. Regarding the model used, a common trend has been observed in flat plate studies which is to test various hole geometries by interchanging an insert with several types of holes from test to test. Since investigating the various shapes of coolant holes is beyond the scope of this document, the information about the model collected in the table is mainly related to its shape, number of rows and location of the holes.

As far as the Reynolds and Mach number are concerned, they are included in the table to have their usual values as a frame of reference, although as stated in (Fraas, et al., 2017) for cylindrical holes in subsonic flow neither Reynolds or Mach number influence film cooling effectiveness. Reynolds number is calculated with different characteristic velocities (freestream at inlet or outlet) and characteristic lengths (coolant hole diameter, model chord, boundary layer momentum thickness - theta - or x-distance from upstream location). In the table, unless it is specified differently, the characteristic velocity is the inlet freestream speed and the characteristic length the model's chord. Mach number is calculated at inlet or exit locations. In the table, unless specified differently, the values correspond to the exit location.

Finally, the studies with variable density ratio or a density ratio higher than unity have been marked in blue. Next to them, the used experimental technique for density ratio creation is specified. However, in these studies, information about which scaling parameter (BR, I, VR) has been matched is not collected; only the range of values of the scaling parameters, when specified in the papers. Note also that there are many more papers studying the effect of density ratio on heat transfer performance than the ones included in the table, but those were not selected because they do not study aerodynamic phenomena. For the interested reader, it is recommended to visit the review on coolant density effect on film cooling by Ekkad and Han (Ekkad & Han, 2015).

From the theory and literature review of Section 2.3 on experimental conditions and scaling parameters, we can draw the following conclusions:

- There are five coolant-to-mainstream scaling parameters used in film cooling experiments: mass flow ratio, velocity ratio, density ratio, blowing ratio and momentum flux ratio.
- When fixing the density ratio from the experimental setup, one of the other scaling parameters can be chosen as independent variable. Once it is fixed, the other scaling parameters are fixed too.
- When the density ratio is unity, meaning that main and secondary flow are the same fluid at the same temperature, the most used scaling parameter is blowing ratio which is equal to velocity ratio in this case.
- The most usual range of values for blowing ratio is between 0 and 2, in increments of 0.5.
- To test with experimental conditions closer to real engine operating conditions, density ratio is increased to reproduce the temperature ratio existing between coolant and hot gas in gas turbine engines.
- From the literature study table, half of the papers (34/69) have a density ratio higher than DR=1. Some of them compare the effect of different density ratios on film cooling

performance and some of them test at only one density ratio higher than 1 to simulate enginelike conditions.

- The most usual range of values for density ratio is between 1 and 2.
- To generate the density ratio, three techniques have been found in these studies: cooling of the secondary flow with a cryogenic N_2 heat exchanger, heating of the mainstream flow and foreign gas injection with CO_2, Freon-12 or a Ar/SF_6 mixture.
- Some studies argue that for variable density ratio, momentum flux ratio is a more appropriate scaling parameter than blowing ratio to evaluate aerodynamic losses. To evaluate film cooling thermal performance for variable density ratio, the conclusions on which scaling parameter to use vary for different blowing rates and are less homogeneous among researchers.

2.4. Flow measurement techniques and use of PIV

2.4.1. Theoretical background

Flow measurement techniques

In this section, the flow measurements techniques found to be applied for hydrodynamic measurements in film cooling studies are shortly introduced. Thermal flow measurement techniques are not included.

- Single point pressure measurements
- Particle image velocimetry (PIV)
- Laser doppler velocimetry (LDV)
- Hot wire anemometry (HWA)
- Pressure sensitive paint (PSP)
- Magnetic resonance velocimetry (MRV)
- Laser-two-focus velocimetry (L2F)
- Fringe imaging skin friction oil-film interferometry
- Fast response entropy probe (FREP)
- Thermographic PIV

For more theoretical information about flow measurement techniques, it is recommended to read related chapters in books like the Springer Handbook on Experimental Fluid Mechanics (Tropea, et al., 2007), Ratharishnan's book on instrumentation and measurements in experiments with fluids (Ratharishnan, 2007) or Chapter 6 from Han, Dutta and Ekkad 's book on gas turbine cooling technology (Han, et al., 2013), which summarizes the experimental methods used in turbine cooling studies. It is also particularly interesting Chapter 14 from the Springer Handbook on Experimental Fluid Mechanics, which provides the reader with an extensive classification of non-optical and optical flow measurement techniques applied in turbomachinery studies, including a literature survey for each measurement technique.

Qualitative flow visualization techniques

Qualitative flow visualisation techniques are useful as a complement to aerodynamic ad thermal measurements. They usually use photography and special light illumination to freeze instantaneous flow structures and their evolution. Below are listed some flow visualisation techniques found to be used in film cooling studies.

- Schlieren photography
- CO_2 vapour jets photography
- Oil flow visualisation
- Shear stress sensitive liquid crystals
- Holography
- Seeding and illumination of jet flow
- Laser induced fluorescence
- High speed photography
- Particle scattering

Use and working principle of PIV

PIV is an optical non-intrusive flow measurement technique which does not modify the flow properties at the scale of interest. Contrary to single point measurement techniques, PIV provides whole-field quantitative velocity measurements together with a qualitative visualization of the flow. The working principle consists of capturing images of a seeded flow contained in a laser sheet. The image is captured using charged couple device (CCD) digital cameras taking double exposure images. The flow is seeded using small tracer particles and illuminated with a pulsed laser whose light is optically spread into a sheet. The time between the laser pulses is determined based on the flow velocity and the particle image displacement is calculated from the autocorrelation of the image intensity distribution in the two image frames.

Depending on the experimental setup and number of CCD cameras used, PIV systems can generate different sets of data. They can be classified in three types: planar (1 camera), stereoscopic (2 cameras) or tomographic PIV (3 cameras). Tomographic PIV has been used in some turbomachinery flowfield studies; however, the author has found no study in which tomographic PIV is used to examine the film cooling flowfield. Usually, planar or stereo-PIV are used.

Planar PIV allows 2D investigations which reveal information about flow separation and recirculation regions in the velocity field, vorticity contours and evolution of the jet structure as a function of design parameters. It is normally employed to characterize the streamwise evolution of the jet and its turbulence. Stereo-PIV allows more complete 3D studies revealing information on the formation and evolution of vortical structures and the three components of the velocity and vorticity fields. In film cooling, it is employed to observe the vortical structures of the jet-in-crossflow problem.

Extensive information about the theory and practical applications of PIV can be found in (Raffel, et al., 2007) or (Cavazzini, 2012).

2.4.2. Literature study

For this section, the literature table in Appendix I presents:

- Flow measurement techniques used.
- PIV setup configuration, distinguishing between planar and stereoscopic PIV.
- Qualitative flow visualization techniques used.

More interesting papers using PIV to study film cooling flows have been found, but they are not included in the literature study table. Among them we can highlight PIV application to study trailing edge coolant ejection ((Raffel & Kost, 1998), (Uzol & Camci, 2001), (Yang & Hu, 2012), (Guanghua Wang, et al., 2015)) or compressibility effects (Zhou, et al., 2015).

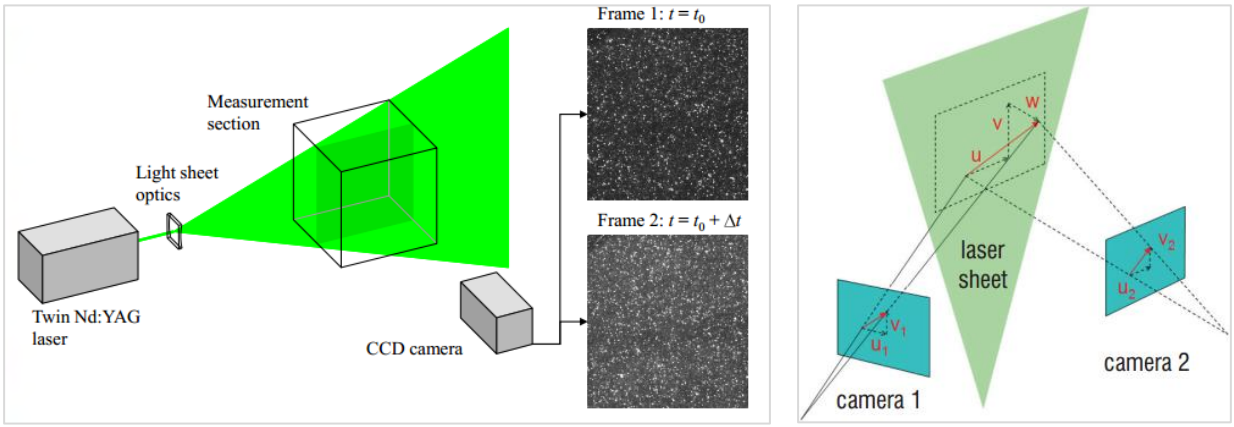

Figure 2.4 Schematic representations of planar (left) and stereoscopic PIV (right)

From the theory and literature review of Section 2.4 on flow measurement techniques and use of PIV, we can draw the following conclusions:

- The author found the first application of PIV from 1996, and most of the investigations with PIV have been carried out in the last 15 years.
- More than half of the film cooling studies (39/69) use PIV as flow measurement technique.
- From these studies, around half of them (16/39) use stereoscopic PIV to measure the 3D velocity and vorticity fields.
- None of these studies uses PIV to evaluate aerodynamic losses.
- None of these studies uses PIV with a field of view large enough to capture the whole test model and analyse the overall aerodynamic performance.
- The usual application of PIV found in these publications is to assist in the visualization of flow structures such as CRVP near the coolant holes, reconstruct jet evolution at different streamwise locations and calculate time-resolved/time-averaged 2D/3D velocity and vorticity distributions for different flow scaling or geometrical parameters.
- Qualitative flow visualization techniques are normally used to complement single point measurement techniques or planar PIV studies by collecting information about the vortical structures resulting from coolant-mainstream interaction. There is no study using qualitative flow visualization techniques with stereoscopic PIV, because it already provides three-dimensional information about flow structures.

2.5. Chapter remarks

This Chapter concludes with a summary table, which compiles the most essential information from the three sections above and their tables in Appendix I. From Section 2.2, the summary table includes: which papers evaluate aerodynamic losses and which papers analyse the flow structures and characteristics in film cooling experiments. From Section 2.3, being blowing ratio the most widely used flow scaling parameter, the summary table provides information on the range of values that it has in each study. It also presents the papers which study the effect of variable density ratio or have a density ratio higher than unity to simulate enginelike operating conditions. From Section 2.4, the summary table shows which papers use PIV, specifying which type of PIV setup, and which papers use flow visualisation.

In the opinion of the author, the publications analysing variable or high-density ratio effects and using PIV as measurement technique are specially interesting. These ones are marked in blue.

Table 2.1. Literature survey summary table

Reference (authors, date)	Aerodynamic losses	Flow characteristics	BR (min-max)	DR >1	PIV	Flow visualization
(Brown & Helon, 1973)	×		0-1			
(Stabe & Kline, 1975)	×		-			
(Prust, 1975)	×		-			
(Ito, et al., 1980)	×		-	1, 1.52		
(Haller & Camus, 1984)	×	×	0-1.5	1-2		×
(Pietrzyk, et al., 1990)		×	0.5	2		
(Schwarz, et al., 1990)		×	0.3-2.7	0.95, 2		×
(Day, et al., 1996)		×	0.35-0.79		planar	
(Thole, et al., 1996)		×	1			
(Osnaghi, et al., 1997)	×		0.56- 1.28	1, 1.52		
(Haven, et al., 1997)		×	1		planar	×
(Drost, 1998)	×	×	0.3-1.5	1,1.6		×
(Urban, et al., 1998)	×		0.63-2.6	1.47, 1.65		
(Burd & Simon, 1999)	×		-			
(Drost & Bölcs, 1999)	×		0-4.5	1.05, 1.38, 1.39, 1.52, 1.65		
(Jackson, et al., 2000)	×	×	0-0.605	0.839-1.23		×
(Day, et al., 2000)	×	×	-	1.77		×
(Kim, et al., 2000)		×	3.3		planar	×
(Barthet & Bario, 2001)	×		1		planar	
(Keogh, 2001)	×		0-1.4			
(Kost & Nicklas, 2001)	×	×	1.4 (SS) -3.7 (PS)			×
(Peterson & Plesniak, 2002)		×	1		planar	
(Peterson & Plesniak, 2004)		×	0.5, 1		planar	
(Bernsdorf, et al., 2006)		×	0.994-2.692	1-1.53	stereo	
(Jovanovic, 2006)		×	0.25 - 1.50		planar	×

Reference (authors, date)	Aerodynamic losses	Flow characteristics	BR (min-max)	DR>1	PIV	Flow visualization
(Jessen, et al., 2007)		×	0.28- 0.73	1, 1.53	planar and stereo	
(Peterson & Plesniak, 2007)		×	0.5 - 1		planar	
(Aga, et al., 2008)		×	1-3	1, 1.55	stereo	
(Bernsdorf, et al., 2008)		×	0.99-2.69	1.01-1.73	stereo	
(Narzary, 2009)	×		1-2	1.1, 1.8, 2.1		
(Aga, 2009)	×	×	1-2	1,1.5	stereo	
(Chappell, et al., 2010)	×		0.6 - 1.2	1.77-1.99		
(Stephan, et al., 2010)	×		-			
(Aga & Abhari, 2011)		×	1-2	1-1.5	stereo	
(auf dem Kampe, et al., 2011)		×	0.5-2	1.1, 1.4	stereo	
(Wright, et al., 2011)		×	0.5-1.5		planar	
(Fawcett, et al., 2012)	×	×	0.5-2		planar	
(Issakhanian, et al., 2012)		×	0.25 - 1			
(Jessen, et al., 2012)		×	0.28 - 0.48	1,1.53	planar and stereo	
(Nguyen, et al., 2012)			4			
(Schulz, et al., 2012)		×	1-2		planar	
(Zhang, et al., 2012)		×	0.5-1.5		planar	
(Abdullah & Funazaki, 2013)		×	1-2			
(Hassan, 2013)		×	0.5-2		stereo	
(Wright, et al., 2013)		×	0.5 - 1.5		stereo	
(Johnson, et al., 2014)		×	0-2	0.97, 1, 1.53	planar	
(Eberly & Thole, 2014)		×	0.25-2	1.2, 1.6	planar	

Reference (authors, date)	Aerodynamic losses	Flow characteristics	BR (min-max)	DR>1	PIV	Flow visualization
(Lin, et al., 2014)	×		0.5-2			
(Pu, et al., 2014)		×	0 - 1.5		planar	
(Zheng & Hassan, 2014)		×	0.5-2		stereo	
(Anderson, et al., 2015)			0.3 - 1	1.2, 1.4, 1.6		
(Mamaev, et al., 2015)	×		-			
(Wang, et al., 2015)		×	0- 2.5		planar	×
(Zhou & Hui, 2015)		×	0.4- 1.25	1.53	planar	
(Nikparto & Schobeiri, 2016)		×	1			
(Rouina, et al., 2016)	×	×	0.5-1.5		planar	×
(Natsui, et al., 2016)		×	0.45-1.05	1.52	planar	×
(Watson, et al., 2016)		×	0.5 - 1.5	1,2,3,4	stereo	
(Schroeder & Thole, 2016)		×	1.5 - 3	1.5	planar and stereo	
(Berkache & Dizene, 2017)		×	2		planar	
(Haydt, et al., 2017)		×	1- 6	1.2	stereo	
(Wernet, et al., 2017)		×	1 - 2		dual-plane PIV	
(Prenter, et al., 2017)	×	×	0.25 - 1		planar	×
(Strausswald, et al., 2017)		×	3.6	1.6		
(Vinton & Wright , 2017)		×	0.5-1.5	1, 3	stereo	
(Voet, et al., 2017)		×	0.31-0.54	1, 1.5	planar	
(Voet, 2017)		×	0.32-1.45	1, 1.5	planar	
(Yao, et al., 2017)		×	0.5 - 2			

3

Testing methodology and experimental setup

3.1. Research objective

In this section, the research goal and research questions of this work are outlined. Based on what has been done in the research field, the contribution of my MSc Thesis Project is to add to the body of knowledge of experimental film cooling studies which use PIV as a whole-field measurement technique that can complement or substitute single point pressure or velocity measurements.

The research goal is to understand the effect of some operating and scaling parameters on aerodynamic losses and flow structures characteristics and to validate PIV as a suitable tool for film cooling losses quantification.

As a follow-up of the previous work of (Lanzillotta, et al., 2017), the knowledge gap is to evaluate the aerodynamic performance of the airfoil model film cooling holes in the pressure side, in order to complement the results from suction side cooling; to measure the 3D velocity and vorticity distributions in various streamwise locations retrieving information about the vortical structures, in order to complement the measured 2D flowfield in the midspan and to analyse the effect of a higher density ratio in film cooling performance, in order to complement the measurements with density ratio close to unity.

From all the papers listed above which study the influence of density ratio by means of PIV, all of them have been carried out with a flat plate as a model, so the effect of airfoil's curvature has not been investigated. If we look now at all the papers using PIV, also without density ratio effects, none of them uses PIV to calculate aerodynamic losses of a film cooled airfoil. PIV is mostly used to visualize the flowfield, the CRVP and sample the jet in a small field of view.

The novelty of this study is to study both aerodynamic losses and flowfield structures using PIV and high-density ratio in a multi-row airfoil with pressure side film cooling.

The research and sub-research questions can now be formulated as follows. It is important to note that the biggest part of this research work will focus on answering research question 1.

1) ***What is the effect of blowing ratio on the aerodynamic losses of a NACA 0012 model with four rows of film cooling holes in the pressure side?***

   1.1. Are the measurements repeatable when compared to (Lanzillotta, et al., 2017) at zero angle of attack?
   1.2. How is the wake velocity profile affected by changes in blowing ratio?
   1.3. How is the 2D velocity field affected by changes in blowing ratio?
   1.4. Are the wake profile results retrieved from pressure measurements and from PIV comparable?
   1.5. How are aerodynamic losses affected by changes in blowing ratio?
   1.6. How does the relationship between blowing ratio and aerodynamic losses change when varying other parameters? These parameters include:
      - Angle of attack.
      - Mainstream velocity.
      - Number of open rows and their chordwise location.
   1.7. What are the differences with suction side film cooling aerodynamic performance?

Research question 1 is the main research question of the present work. In addition, two secondary research questions are posed:

2) *What are the characteristics of the jet-mainstream flow interaction at different streamwise locations?*

   2.1. Can I observe flow structures derived from jet-mainstream interaction at each streamwise location?
   2.2. How does the jet evolve in the streamwise direction, from the near hole region to a downstream location far away from the ejection hole?
   2.3. What is the effect of blowing ratio on jet-mainstream flow interaction?
   2.4. Can I observe jet-to-jet interaction or row-to-row interaction?

3) *What is the effect of density ratio on wake profile characteristics and aerodynamic losses?*

3.2. Testing methodology and experimental matrix

Three test campaigns are carried out, each one answering each of the three research questions.

1) To give an answer to the first and main research question and sub-research questions, midspan wake pressure measurements and planar PIV are used. For planar PIV, two fields of view (FOV) are used: a large one to observe the global flowfield around the airfoil and smaller one to study coolant-mainstream interaction and flowfield in a specific location.

2) To give an answer to the second research question and sub-research questions, similar film cooling configurations as in the first campaign will be used with a stereoscopic PIV setup. Stereoscopic PIV measurements will be carried out at various streamwise locations and care will be taken to position the measurement planes in locations where the jet structure can be visualized.

3) To give an answer to the third research question and sub-research questions, CO_2 gas will be used as secondary flow. Blowing ratio will be matched with the case with air as secondary flow, so some conversions will need to be done in the secondary flow system to correct for the density difference. Care will be taken to acquire subsequent measurements for air and CO_2, to assure that the testing conditions are the same and only the density ratio plays a role in the results.

In the next page, the experimental matrix for the first test campaign is presented (Table 3.1). This experimental matrix will experience changes with the lessons learnt in the previous test campaign. The reasons for the chosen set of values for the variable parameters are the following.

- Blowing ratio: 0/0.3/0.5/0.7/0.9/1/1.5/2. The reason is that in most of the papers, the maximum tested blowing ratio is BR=2 in increments of 0.5 (BR=0/0.5/1/1.5/2). Therefore, it is important to test at these blowing ratios to be able to compare the results with previous publications. The reason for testing at BR=0.3 is that being the goal of film cooling to use as little coolant as possible, it is interesting to analyse what happens for low blowing ratios. The reason for not testing at BR>2 is the mentioned limitation of the flow controller (260 l/min), since for BR=2 the volumetric air flow rate is already 256 l/min. Finally, the reason for including BR=0.9 is that at this value of blowing ratio the momentum flux ratio becomes I=0.8 and as mentioned in Chapter 3, for $I \geq 0.8$ the jet separates and does not reattach, so the jet lift-off phenomena should be captured for $BR \geq 0.9$.

- Angle of attack: 0/5/10 (°). These values are chosen to be able to compare with (Lanzillotta, et al., 2017). The angle of attack of 2° tested in that work will not be tested here because there was a small difference observed with respect to 5°.

- Freestream velocity: 15/25 (m/s). The velocity of 15 m/s is chosen as the baseline configuration to compare the results with (Lanzillotta, et al., 2017). The velocity V=10 m/s tested in that work will not be tested here because there was a small difference observed with respect to V=15 m/s, so only V=25 m/s will be tested to analyse the effect of freestream velocity. Note that for this speed, the maximum BR achievable with the available flow controller is BR=1.2.

- Partial film cooling: opening each of the rows of holes separately and sealing the other three rows, as in (Lanzillotta, et al., 2017).

With this set of values, a total of 72 runs are needed to complete the measurements with each measurement technique. Therefore 72 runs will be done with pressure measurements and 72 runs will be done for the large field of view in PIV measurements. For the planar PIV zoomed-in case, stereoscopic PIV tests and experiments with CO_2 only some runs are repeated.

Table 3.1 Reference experimental matrix

Variation in angle of attack																		
#Run	AoA (º)	Vinf (m/s)	rhoinf (kg/m3)	rhoc (kg/m3)	DR	Ah (m2)	#holes				Ac (m2)	BR	Vc (m/s)=Vinf x BR/DR	VR=Vc/Vinf	I=DR x VR^2	mc (kg/s)= rhoc x Vc x Ac	mc (m3/h) = Vc x Ac x 3600	mc (l/min)	mc (l/min) rounded	m_inf (kg/s)	MFR (%)
							PS1	PS2	PS3	PS4											
1	0	15	1.1947	1.2008	1.0051	0.00000143	0	0	0	0	0.00014314	0.00	0.00	0.00	0.00	0.0000000	0.0000000	0.00	0	2.87	0.00
2												0.00	0.00	0.00	0.00	0.0000000	0.0000000	0.00	0		0.00
3												0.30	4.48	0.30	0.09	0.0007695	2.3070692	38.45	38		0.03
4												0.50	7.46	0.50	0.25	0.0012826	3.8451153	64.09	64		0.04
5							25	25	25	25		0.70	10.45	0.70	0.49	0.0017956	5.3831614	89.72	90		0.06
6												0.90	13.43	0.90	0.81	0.0023086	6.9212075	115.35	115		0.08
7												1.00	14.92	0.99	0.99	0.0025651	7.6902306	128.17	128		0.09
8												1.50	22.39	1.49	2.24	0.0038477	11.5353459	192.26	192		0.13
9												2.00	29.85	1.99	3.98	0.0051302	15.3804612	256.34	256		0.18
10	-5	15	1.1947	1.2008	1.0051	0.00000143	0	0	0	0	0.00014314	0.00	0.00	0.00	0.00	0.0000000	0.0000000	0.00	0	2.87	0.00
11												0.00	0.00	0.00	0.00	0.0000000	0.0000000	0.00	0		0.00
12												0.30	4.48	0.30	0.09	0.0007695	2.3070692	38.45	38		0.03
13												0.50	7.46	0.50	0.25	0.0012826	3.8451153	64.09	64		0.04
14							25	25	25	25		0.70	10.45	0.70	0.49	0.0017956	5.3831614	89.72	90		0.06
15												0.90	13.43	0.90	0.81	0.0023086	6.9212075	115.35	115		0.08
16												1.00	14.92	0.99	0.99	0.0025651	7.6902306	128.17	128		0.09
17												1.50	22.39	1.49	2.24	0.0038477	11.5353459	192.26	192		0.13
18												2.00	29.85	1.99	3.98	0.0051302	15.3804612	256.34	256		0.18
19	-10	15	1.1947	1.2008	1.0051	0.00000143	0	0	0	0	0.00014314	0.00	0.00	0.00	0.00	0.0000000	0.0000000	0.00	0	2.87	0.00
20												0.00	0.00	0.00	0.00	0.0000000	0.0000000	0.00	0		0.00
21												0.90	13.43	0.90	0.81	0.0023086	6.9212075	115.35	115		0.08
22							25	25	25	25		1.00	14.92	0.99	0.99	0.0025651	7.6902306	128.17	128		0.09
23												1.25	18.65	1.24	1.55	0.0032064	9.6127882	160.21	160		0.11
24												1.50	22.39	1.49	2.24	0.0038477	11.5353459	192.26	192		0.13
25												1.75	26.12	1.74	3.05	0.0044890	13.4579035	224.30	224		0.16
26												2.00	29.85	1.99	3.98	0.0051302	15.3804612	256.34	256		0.18
Variation in freestream velocity																					
#Run	AoA (º)	Vinf (m/s)	rhoinf (kg/m3)	rhoc (kg/m3)	DR	Ah (m2)	#holes				Ac (m2)	BR	Vc=Vinf x BR/DR (m/s)	VR=Vc/Vinf	I=DR x VR^2	mc (kg/s)= rhoc x Vc x Ac	mc (m3/h) = Vc x Ac x 3600	mc (l/min)	mc (l/min) rounded	m_inf (kg/s)	MR (%)
28	0	25	1.1900	1.2080	1.0151	0.00000143	0	0	0	0	0.00014314	0.00	0.00	0.00	0.00	0.0000000	0.0000000	0.00	0	4.76	0.00
29												0.00	0.00	0.00	0.00	0.0000000	0.0000000	0.00	0		0.00
30												0.30	7.39	0.30	0.09	0.0012775	3.8071607	63.45	63		0.03
31												0.50	12.31	0.49	0.25	0.0021292	6.3452678	105.75	106		0.04
32							25	25	25	25		0.70	17.24	0.69	0.48	0.0029809	8.8833750	148.06	148		0.06
33												0.90	22.16	0.89	0.80	0.0038325	11.4214821	190.36	190		0.08
34												1.00	24.63	0.99	0.99	0.0042584	12.6905357	211.51	212		0.09
35												1.10	27.09	1.08	1.19	0.0046842	13.9595893	232.66	233		0.10
36												1.20	29.55	1.18	1.42	0.0051101	15.2286428	253.81	254		0.11
Variation in ejection location																					
#Run	AoA (º)	Vinf (m/s)	rhoinf (kg/m3)	rhoc (kg/m3)	DR	Ah (m2)	#holes				Ac (m2)	BR	Vc=Vinf x BR/DR (m/s)	VR=Vc/Vinf	I=DR x VR^2	mc (kg/s)= rhoc x Vc x Ac	mc (m3/h) = Vc x Ac x 3600	mc (l/min)	mc (l/min) rounded	m_inf (kg/s)	MR (%)
37	0	15	1.1947	1.2008	1.0051	0.00000143	0	0	0	0	0.00003578	0.00	0.00	0.00	0.00	0.0000000	0.0000000	0.00	0	2.87	0.00
38												0.00	0.00	0.00	0.00	0.0000000	0.0000000	0.00	0		0.00
39												0.30	4.48	0.30	0.09	0.0001924	0.5767673	9.61	10		0.01
40												0.50	7.46	0.50	0.25	0.0003206	0.9612788	16.02	16		0.01
41							25	0	0	0		0.70	10.45	0.70	0.49	0.0004489	1.3457904	22.43	22		0.02
42												0.90	13.43	0.90	0.81	0.0005772	1.7303019	28.84	29		0.02
43												1.00	14.92	0.99	0.99	0.0006413	1.9225576	32.04	32		0.02
44												1.50	22.39	1.49	2.24	0.0009619	2.8838365	48.06	48		0.03
45												2.00	29.85	1.99	3.98	0.0012826	3.8451153	64.09	64		0.04
46	0	15	1.1947	1.2008	1.0051	0.00000143	0	0	0	0	0.00003578	0.00	0.00	0.00	0.00	0.0000000	0.0000000	0.00	0	2.87	0.00
47												0.00	0.00	0.00	0.00	0.0000000	0.0000000	0.00	0		0.00
48												0.30	4.48	0.30	0.09	0.0001924	0.5767673	9.61	10		0.01
49												0.50	7.46	0.50	0.25	0.0003206	0.9612788	16.02	16		0.01
50							0	25	0	0		0.70	10.45	0.70	0.49	0.0004489	1.3457904	22.43	22		0.02
51												0.90	13.43	0.90	0.81	0.0005772	1.7303019	28.84	29		0.02
52												1.00	14.92	0.99	0.99	0.0006413	1.9225576	32.04	32		0.02
53												1.50	22.39	1.49	2.24	0.0009619	2.8838365	48.06	48		0.03
54												2.00	29.85	1.99	3.98	0.0012826	3.8451153	64.09	64		0.04
55	0	15	1.1947	1.2008	1.0051	0.00000143	0	0	0	0	0.00003578	0.00	0.00	0.00	0.00	0.0000000	0.0000000	0.00	0	2.87	0.00
56												0.00	0.00	0.00	0.00	0.0000000	0.0000000	0.00	0		0.00
57												0.30	4.48	0.30	0.09	0.0001924	0.5767673	9.61	10		0.01
58												0.50	7.46	0.50	0.25	0.0003206	0.9612788	16.02	16		0.01
59							0	0	25	0		0.70	10.45	0.70	0.49	0.0004489	1.3457904	22.43	22		0.02
60												0.90	13.43	0.90	0.81	0.0005772	1.7303019	28.84	29		0.02
61												1.00	14.92	0.99	0.99	0.0006413	1.9225576	32.04	32		0.02
62												1.50	22.39	1.49	2.24	0.0009619	2.8838365	48.06	48		0.03
63												2.00	29.85	1.99	3.98	0.0012826	3.8451153	64.09	64		0.04
64	0	15	1.1947	1.2008	1.0051	0.00000143	0	0	0	0	0.00003578	0.00	0.00	0.00	0.00	0.0000000	0.0000000	0.00	0	2.87	0.00
65												0.00	0.00	0.00	0.00	0.0000000	0.0000000	0.00	0		0.00
66												0.30	4.48	0.30	0.09	0.0001924	0.5767673	9.61	10		0.01
67												0.50	7.46	0.50	0.25	0.0003206	0.9612788	16.02	16		0.01
68							0	0	0	25		0.70	10.45	0.70	0.49	0.0004489	1.3457904	22.43	22		0.02
69												0.90	13.43	0.90	0.81	0.0005772	1.7303019	28.84	29		0.02
70												1.00	14.92	0.99	0.99	0.0006413	1.9225576	32.04	32		0.02
71												1.50	22.39	1.49	2.24	0.0009619	2.8838365	48.06	48		0.03
72												2.00	29.85	1.99	3.98	0.0012826	3.8451153	64.09	64		0.04

3.3. Equipment specifications and experimental approach

3.3.1. Windtunnel

The experiments for the MSc Thesis Project are carried out at the M-tunnel in the Low Speed Laboratory of TU Delft. In this windtunnel, the (theoretical) maximum speed is limited to 30 m/s, although in practice the maximum velocity reached during the test campaigns was $V_\infty = 26\ m/s$. For this work, the windtunnel operates in open jet configuration.

The windtunnel test section is square and with dimensions $0.4m\ x\ 0.4m$. To fix the model, a $0.4m\ x\ 0.4m\ x\ 0.6m$ plexiglass test section is screwed to the windtunnel test section. The reason to use plexiglass (transparent material) for the test section is to allow optical access for PIV experiments. In both sides of this test section holes are drilled to fix the model with the cooling holes on the pressure side at five different angles of attack ($\alpha = 0°, 5°, -5°, 10°, -10°$)

To monitor the operating conditions of the tunnel, the following sensors are in place:

- A thermocouple placed in the settling chamber, which measures freestream temperature, T_∞.
- An analog barometer placed on the control table, which measures ambient static pressure, P_∞.
- A pitot-static tube placed in the settling chamber, which measures freestream dynamic pressure as the difference between total and static pressure, $q_\infty = (P_{t_\infty} - P_\infty)$. The reading from this pitot tube is connected to a Mensor DPG 2400 digital pressure gauge.

With the measurements from this set of sensors, a LabVIEW script in the windtunnel computer enables monitoring of all these variables and computation of ρ_∞ and V_∞. Then, the freestream velocity can be modified by increasing or decreasing the counts of a potentiometer which changes the windtunnel engine rotational speed.

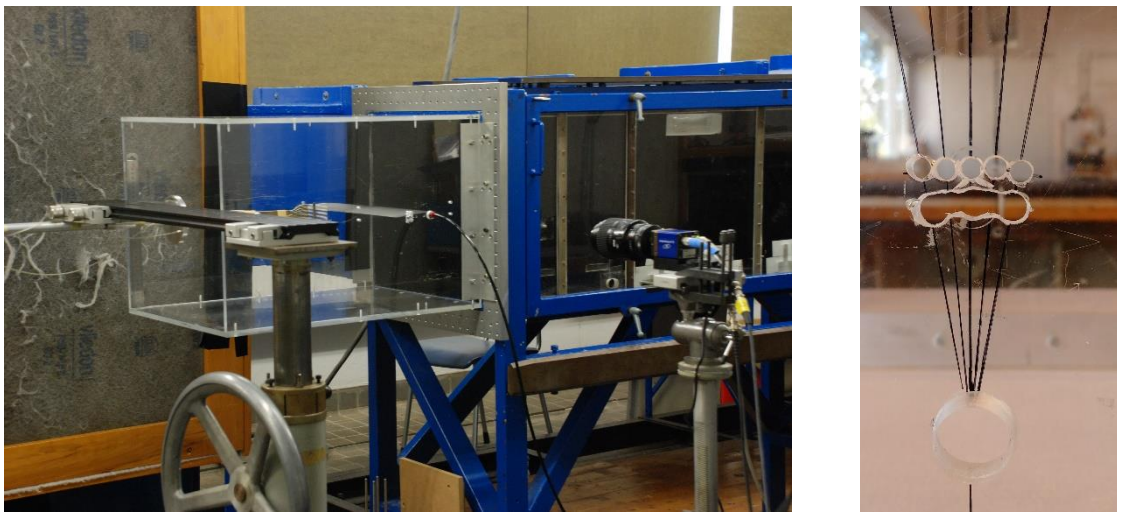

Figure 3.1 M-tunnel test section with the plexiglass test section attached to it and the airfoil model inside (left). Detail of the holes in the plexiglass test section to fix the airfoil at five different angles of attack (right)

Figure 3.2. M-tunnel various parts, sensors and freestream velocity control and display (top). Details of analog barometer to measure static ambient pressure (bottom left) and the Mensor DPG 2400 digital pressure gauge to measure freestream dynamic pressure (bottom right)

3.3.2. Secondary flow system

The secondary flow is controlled using a Bronkhorst flowcontroller. Initial tests were conducted using a VP Instruments flowmeter (VPFlowmate in-line model, 1 inch diameter) and manual control through a manual flow regulation valve. However, the instantaneous flow fluctuations were too high. They were found to be periodic, with an amplitude of the volumetric flow fluctuation $\Delta\dot{m}{\sim}50\ l/min$ in an acquisition time $\Delta t{\sim}5\ min$. The reason for the fluctuations is the limitation in capacity of the storage vessel from the air supply and the periodic behaviour is due to the pumping of the compressor to deliver the required mass flow rate.

This air supply system for the M-tunnel facility is a Grassair storage vessel with a maximum volumetric flow $\dot{m} = 420\ l/min$ and a Grassair compressor with a maximum feeding pressure $P = 10\ bar$. Mitigation of the amplitude and frequency of flow fluctuations was attempted by ensuring enough length for fully developed flow at the inlet and outlet of the flowmeter, by increasing the feeding pressure, by lowering the lower pressure limit in the compressor and by using a pressure regulating valve before the flow meter inlet. But fluctuations were still too high, taking into account the required PIV acquisition times (see Figure 3.3).

For this reason, a flowcontroller is used for the experiments. It is a Bronkhorst flowcontroller, model F-202AV-M20-DGD-55-V. This flow controller is calibrated for air and without changing the internal control valves (designated by 'M20' in the model specification), the maximum attainable air

flow rate is $\dot{m} = 260\ l/min$. Note that if higher injection rates want to be tested in future experiments, the internal valves could be replaced and changed for bigger ones, e.g. M30.

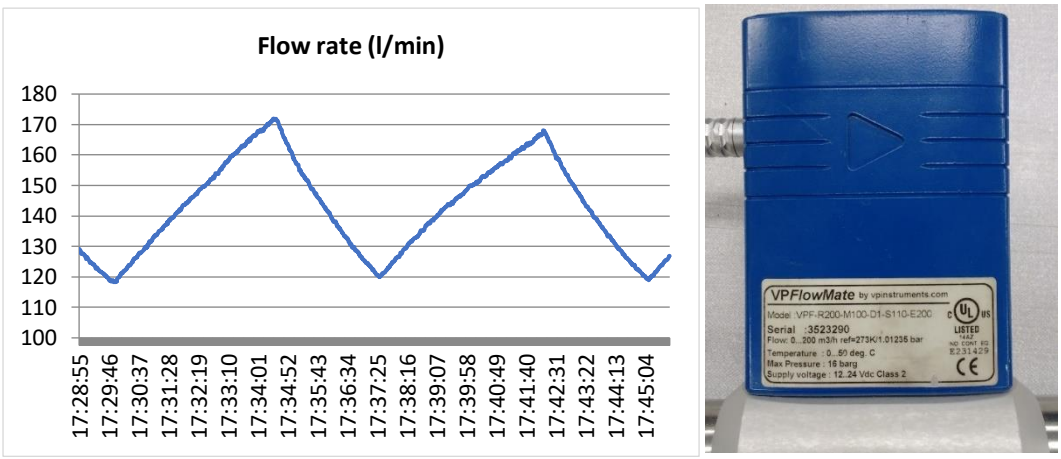

Figure 3.3. Flow rate fluctuations in secondary air supply when using a flow meter in the M-tunnel experimental facility (left) and specifications of the VPFlowmate flowmeter (right). Due to this elevated level of fluctuations when using a flowmeter, a flowcontroller is needed for film cooling experiments.

The working principle of Bronkhorst flowcontroller is based in fluid's heat conductivity to determine the mass flow, which is directly proportional to a constant temperature difference generated inside the flowcontroller (constant temperature anemometry (CTA) mass flow sensor). Two software tools, FlowPlot and FlowView, with free download from Bronkhorst webpage were used to control and visualize the flowcontroller setpoint, expressed as a percentage of the maximum attainable flow rate. By using the flowcontroller, flow fluctuations are seldomly observed. When flow fluctuations were observed, these were easily mitigated by closing the air supply for some time and waiting for the Grass air compressor to increase the available feeding pressure to provide the required mass flow. The calibration certificate of the Bronkhorst F-202AV flowcontroller used is included in Appendix II, and it specifies the calibration conditions and the measurement accuracy level.

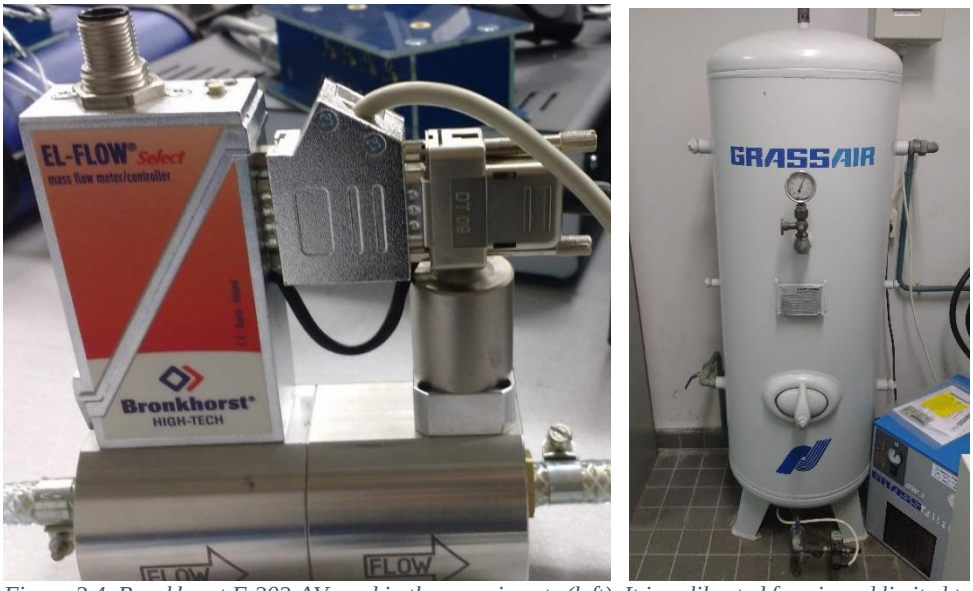

Figure 3.4. Bronkhorst F-202-AV used in the experiments (left). It is calibrated for air and limited to a maximum volumetric flow rate $\dot{m} = 260\ l/min$. Grassair compressor that provides the air supply at a pressure $P \sim 10$ bar (right).

When using CO_2 as secondary flow, the gas is supplied from CO_2 Gloor 5100 tanks, which deliver a maximum flow rate of $500\ l/min$. The tanks include a regulator valve adapted to a working pressure $P = 10\ bar$. Bronkhorst flowcontroller has eight memories to include the calibration curves of eight different gases, which could be of use for future experiments. However, for the current experimental setup the flowcontroller was only calibrated for air. Therefore, a correction needs to be made so that the output signal matches the actual flow rate. This correction is made by applying a conversion factor C as suggested in Bronkhorst instruction manual, which accounts for the density and heat capacity of CO_2 with respect to air. For CO_2, $C = 0.74$. Further details on the conversion factor are provided in Appendix II.

Finally, to measure the coolant pressure and temperature:

- A PT100 thermistor (temperature sensor) is used to measure the secondary flow temperature, T_c.
- A total pressure gauge probe is included in the airfoil model to measure the coolant total pressure at the airfoil plenum, P_{t_c}. This probe is connected to a Mensor 2101 digital pressure gauge, in which ambient pressure is set as a reference pressure.

3.3.3. Airfoil model

The airfoil model used in these experiments is the same one as the one in (Lanzillotta, et al., 2017). It is a 3D printed NACA 0012 airfoil with the following characteristics:

- The airfoil is hollow and has a single plenum chamber for all the holes.
- It is manufactured using the laser sintering technique and polyamide as material.
- Airfoil chord length, $c = 12\ cm$.
- Span length equal to the test section width, $b = 40\ cm$.
- Multi-row configuration, with four rows of holes. They are located at a distance $x = 0.05c\ (PS1), x = 0.1c\ (PS2), x = 0.15c\ (PS3)$ and $x = 0.5c\ (PS4)$ from the airfoil´s leading edge.
- Each row has 61 holes, out of which only 25 holes are used (the rest are sealed). Therefore, the total number of holes used is 100.
- The holes follow an in-line arrangement.
- The holes injection angle is $\beta = -45°$ with respect to local surface tangent.
- Hole length-to-diameter ratio, $L/D \sim 1.9$.
- Cross-sectional diameter of the hole was measured to be $D_{CS} \sim 1.35\ mm$.

More detailed information and sketches of the model can be found in (Lanzillotta, et al., 2017).

Figure 3.5. Sketch of the model adapted from (Lanzillotta, et al., 2017). PS1 refers to the cooling holes row in the pressure side located at a 5% of chord length distance from airfoil´s leading edge; PS2 at 10%, PS3 at 15% and PS4 at 50%.

3.3.4. Pressure measurements system

Equipment description

The pressure measurements system used during the experiments consists of a pressure wake rake and an automatic pressure scanning system.

The pressure rake is composed of a total of 18 channels, equally spaced along a total length of 3.75 cm, i.e. with a 2.2 mm separation between each other. The two channels at the top and bottom sides of the rake are static pressure probes and the rest are total pressure probes. This means that static pressure was not measured at the exact location where total pressure was measured, so an average from the top and bottom local static pressure measurements was used as reference value for exit static pressure. The reason for this simplified approach is that the magnitude of static pressure is not significantly changing along the wake. Total pressure is measured as gauge total pressure, i.e. differential pressure with respect to absolute ambient pressure.

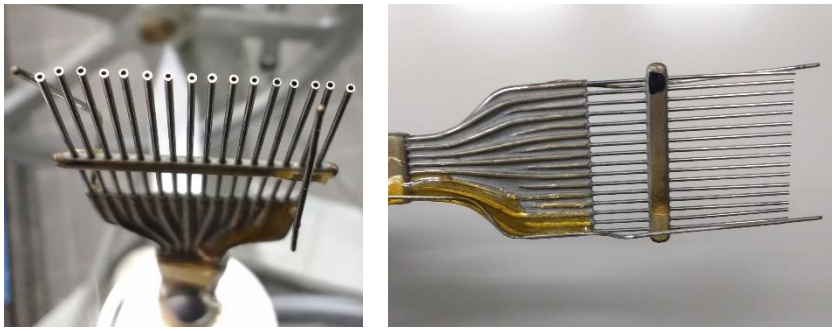

Figure 3.6 Front and side view of the wake pressure rake

The automatic pressure scanning system is a system developed by a PhD student at TU Delft and now offered by *Nub Systems* company. This system is composed by the data acquisition system (DAS) and several measurement units or modules containing pressure sensors and electronics. The pressure sensors are High Accuracy Silicon Ceramic (HSC) lines of differential pressure sensors from Honeywell.

There are three types of available modules to measure in the ranges $\pm 160\ Pa$, $\pm 600\ Pa$ and $\pm 2500\ Pa$. In this work, the $160\ Pa$ module was sufficient for the wake measurements at $V_\infty = 15\ m/s$ and the $600\ Pa$ module was needed for the measurements at $V_\infty = 25\ m/s$. Each module contains 16 pressure sensors (8 in side A and 8 in side B) and is connected to one port of the DAS. During the tests, it was found that the $600\ Pa$ module had one broken channel, so only 15 pressure sensors were active. Then the acquired pressure data are sent to a user computer via Ethernet and a LabVIEW interface displays the instantaneous measurement data. The software provides both instantaneous and average output files during a fixed acquisition time. For each run, 20 seconds acquisition time was set. This system allows considerable time saving when compared to manually reading the data from each channel with a digital pressure gauge like a Mensor 2101, since it enables simultaneous reading and storage of all channels pressure measurements.

General setup: position of the pressure rake

The pressure rake was located at the midspan of the model (i.e. 20 cm from the lateral walls of the test section) and at 3 cm from the airfoil's trailing edge in the streamwise direction (i.e. 1.25·c from leading edge). For the baseline configuration, the rake was centered with the model's trailing edge in the vertical direction. When changing the airfoil's angle of attack, the pressure rake was vertically displaced to capture the flow physics in the wake and then kept at the same location for all the runs in that test configuration. For simplicity of the setup, no traverse system was used, so the vertical displacement was done by means of a tripod to which the pressure rake was fixed.

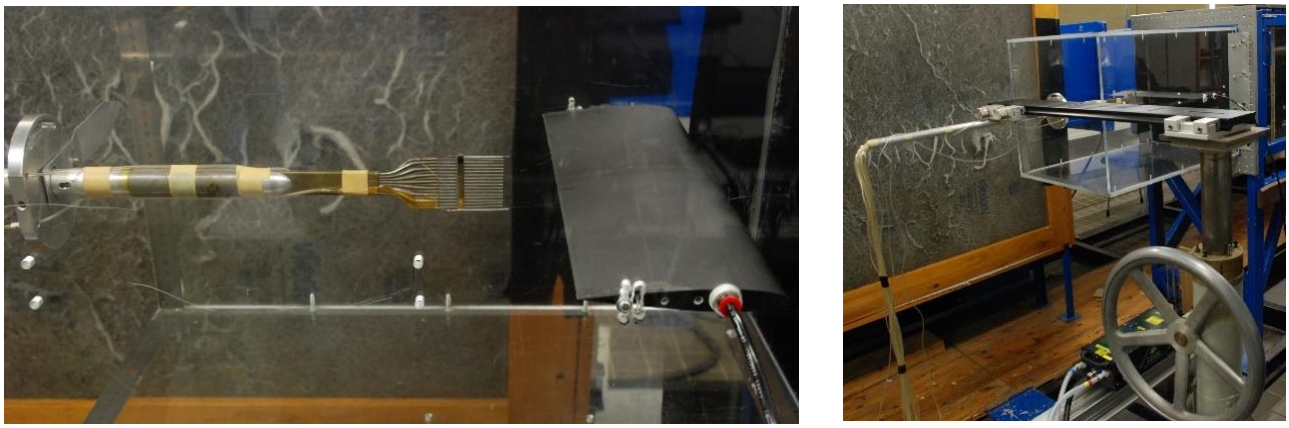

Figure 3.7 Location of the pressure rake with respect to the model (left). Tripod and general setup to displace the pressure rake in the vertical direction (right).

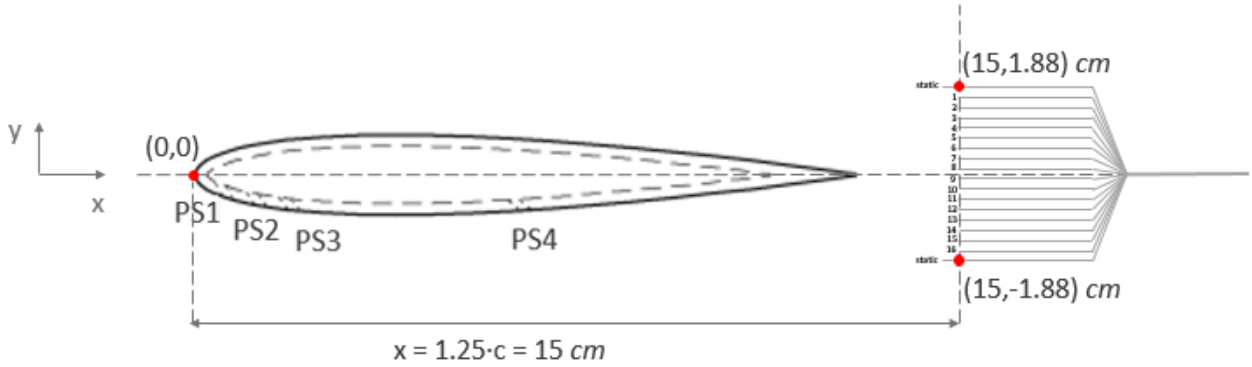

Figure 3.8 Schematic showing the reference system and the location of the pressure rake with respect to the model. Note that the distances are not drawn to scale.

Prior to data acquisition, a functional test was performed to check the correct functioning of each of the probes in the pressure rake and the result was that none of them was blocked. This was done by creating a small pressure difference in each channel, using a regulator valve to blow air from the windtunnel's secondary air supply. This test also served to associate each pressure probe with its corresponding plastic tube and to number them (see Figure 3.9).

Then, the plastic tubes were connected to the pressure scanning system electronic modules. For the test cases at V_∞=15 m/s, the 160 Pa modules were sufficient. The 16 total pressure tubes were connected to a 160 Pa module (channels 1-8 in side A and channels 9-16 in side B) and the 2 static pressure tubes to a different 160 Pa module. For the test cases at V_∞=25 m/s, total pressure measurements required the 600 Pa module. While performing the functional test of the 600 Pa module, the pressure sensor associated to one of the channels was found defect, so it was interchanged with channel 1, exposed to freestream conditions (due to its higher relevance for the wake profile

results). Therefore, in the higher freestream velocity configuration only 15 total pressure channels were active in the pressure scanning system. For static pressure measurements, the 160 Pa module was sufficient.

Calibration of the pressure rake

Calibration of the pressure measurements system was performed by acquiring freestream data (no model present in the test section) with the pressure rake located at the aforementioned position and then comparing this data with the windtunnel display readings. For both 160 Pa and 600 Pa modules, calibration curves were obtained for each pressure channel.

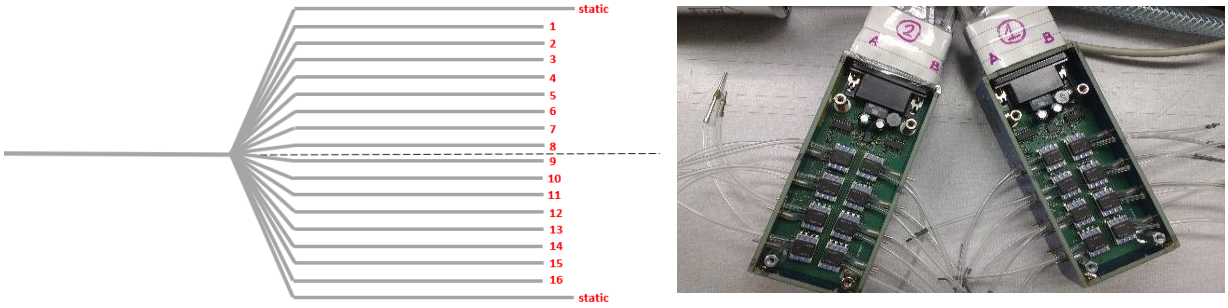

Figure 3.9 Pressure rake channels numbering (left) and electronic modules from the pressure scanning system (right)

Below are presented these calibration curves showing the error in dynamic pressure, q with respect to windtunnel sensors measurements. To test the repeatability of the calibration process, the 160 Pa module calibration curves were acquired in both pressure measurements test campaigns (with air and with CO_2 as secondary flows). Figure 3.10, Figure 3.11 and Figure 3.12 depict the calibration curves for the three cases: 160 Pa module in test campaign with air, 160 Pa module in test campaign with CO_2 and 600 Pa module.

Some general observations can be derived from these calibration curves:

- For all channels, the error follows a similar trend with respect to freestream velocity.
- There are some channels with a higher deviation from the average than the rest.
- For most of the range of the freestream velocity V_∞, the speed measured by the windtunnel sensor is higher than the one measured by the pressure rake.

When looking closer at Figures 3.10 and Figure 3.11, with the 160 Pa module, we observe that:

- Channels 2, 12, and 16 present a higher offset from the average than the rest of the channels. This occurs in both calibration sets.
- For V_∞=15 m/s, our case of interest, the maximum difference in dynamic pressure q between the pressure rake and the windtunnel display represents a 5% of the 160 Pa maximum P_t allowed in this module of the pressure scanning system.

When analysing Figure 3.12, with the 600 Pa module, we observe that:

- In this case, channel 11 presents a higher offset from the average than the rest of the channels.
- For V_∞=25 m/s, our case of interest, the maximum difference in dynamic pressure q between the pressure rake and the windtunnel display represents a 3.3% of the 600 Pa maximum P_t allowed in this module of the pressure scanning system

To correct for these discrepancies, the average velocity from all the channels has been calculated and the offset of each channel with respect to the average has been corrected for in the pressure rake data.

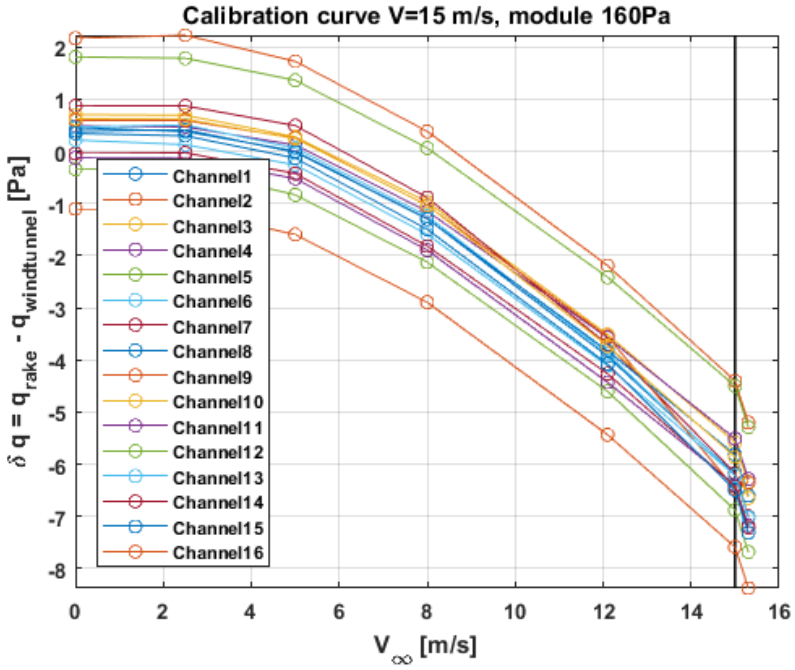

Figure 3.10 Calibration curves for V=15 m/s and 160 Pa module, performed during the test campaign in which only air as secondary flow was used. Error in dynamic pressure, δq.

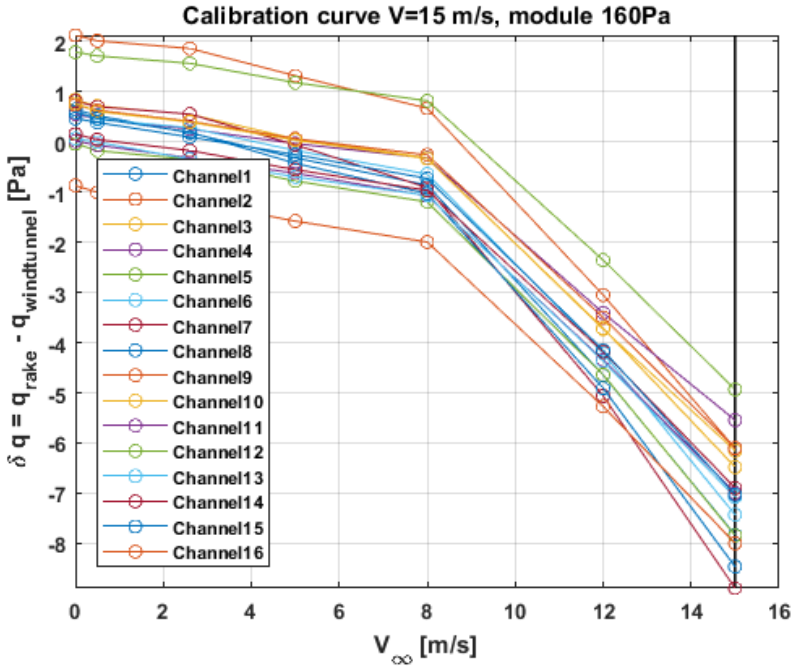

Figure 3.11 Calibration curves for V=15 m/s and 160 Pa module, performed during the test campaign in which both air and CO_2 were used as secondary flow. Error in dynamic pressure, δq.

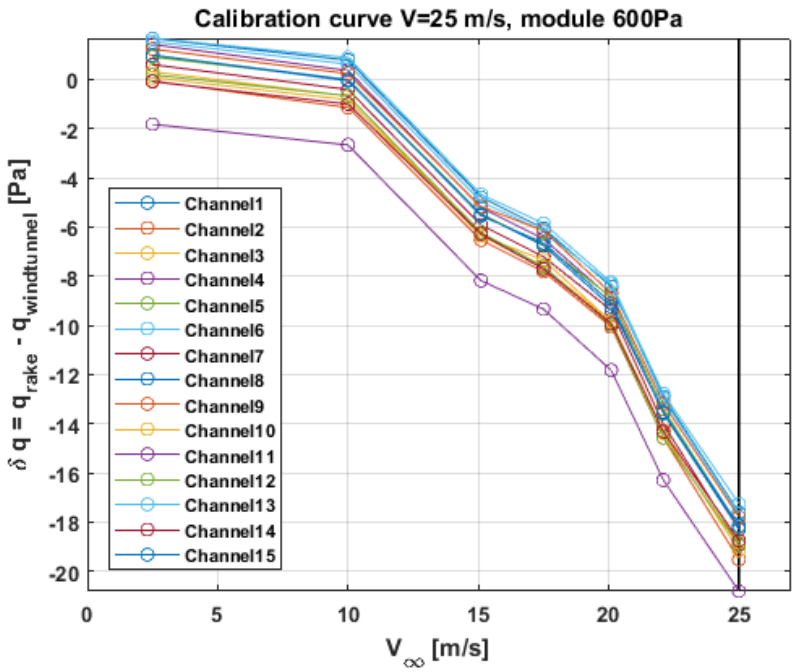

Figure 3.12 Calibration curves for V=25 m/s and 600 Pa module. Error in dynamic pressure, δq.

Modification of original experimental matrix

While performing the tests, we realized that the test cases of low blowing ratios (i.e. BR<1) did not reveal a meaningful change in aerodynamic performance. Conversely, an inversion in the trend of wake's momentum deficit was observed for blowing ratios between 1 and 1.5, as also identified in the work of (Lanzillotta, et al., 2017) for BR=1.28. To gain resolution in this range, more test cases were added for BR ∈ (1, 1.5) in some configurations. In some cases, a run with BR=1.75 was added too, to complete the evolution from BR=1.5 and BR=2.

For the second pressure measurements test campaign using CO_2 as secondary flow, no effect of higher freestream velocity or partial injection was studied. Instead, the effect of angle of attack was investigated for both pressure and suction side injection, to complete the work of (Lanzillotta, et al., 2017) in which no tests with CO_2 were carried out with suction side coolant injection. Note that for this set of tests with foreign gas injection, every test run was subsequently performed with air, to isolate the effect of CO_2 injection from any other change in the experimental setup and maximize comparability of the air and CO_2 results.

3.3.5. PIV setup

Equipment description

To finish with the experimental equipment description, the instrumentation used in the PIV tests is presented. All parts of equipment used in both planar and stereo-PIV setups are the same, except for the camera and camera lenses. First, the common parts of equipment are described. Second, the cameras specifications are collected for both cases.

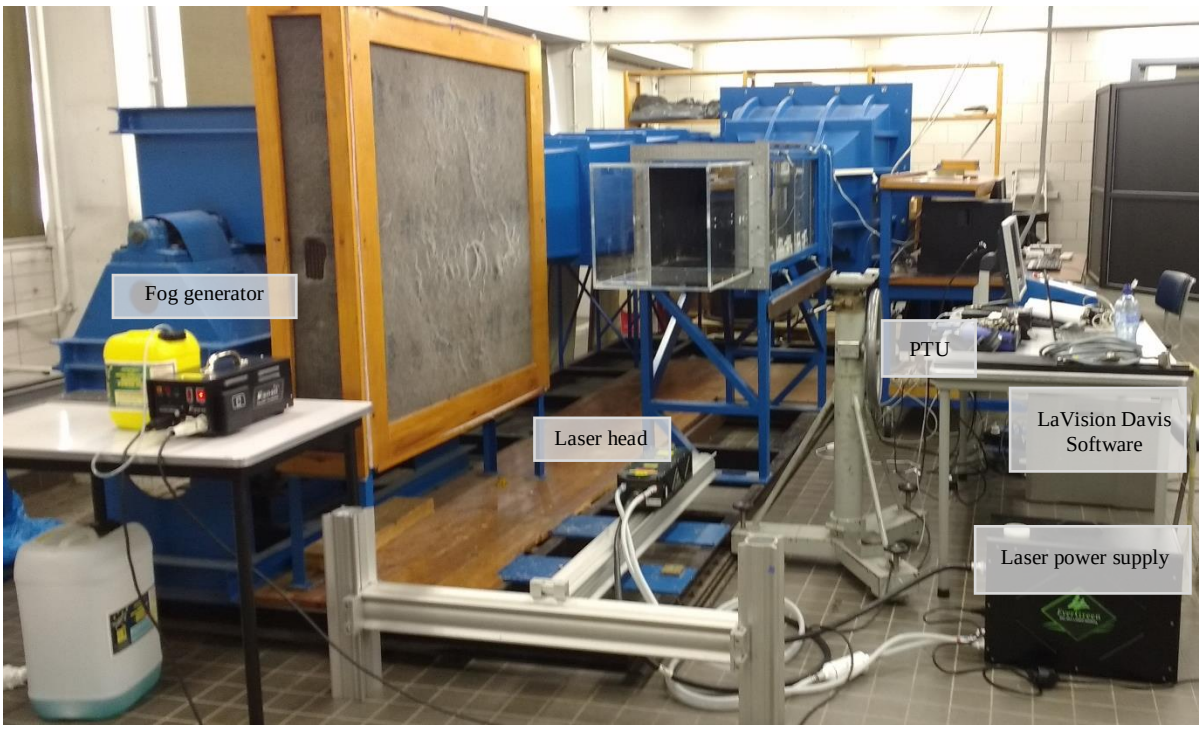

Figure 3.13. Location of equipment for PIV setup common to planar and stereo-PIV setups

Table 3.2 Specifications of the PIV equipment common to planar and stereo-PIV setups

PIV Equipment	Type	Function	Specifications
Smoke generator	SAFEX F2010	Generate tracer particles by creating a dense fog by evaporation and condensation of a water-based mixture	▪ Water-based mixture: 'inside nebelfluid, normal power mix' ▪ Mean droplet size, d_p~1μm
Laser system	Quantel Evergreen 200	Illuminate the smoke particles	▪ Double-pulsed Nd:YAG laser ▪ Wavelength: 532 nm ▪ Pulse energy: 200 mJ ▪ Pulse duration < 10 ns
Laser optics	▪ Convex (f>0) / concave (f<0) ▪ Cylindrical/spherical	Convert the laser beam into a thin laser sheet which will be the measurement plane	Depends on setup, but normally: ▪ 2 concave spherical (3 if higher laser power required and 1 if lower) ▪ 1 convex cylindrical
PTU	LaVision	Control the recording and illumination frequencies	Integrated device trigger generation in DaVis

Table 3.3 Specifications of the PIV cameras equipment for both planar and stereo-PIV setups

PIV CCD Cameras	Planar PIV	Stereo-PIV
Type	Imperx Bobcat	LaVision Imager Intense ('Sensicam')
Resolution (px)	1628 x 1236	1376 x 1040
Pixel size/pitch (μm)	4.40	6.45
Sensor size (mm)	7.16 x 5.44	8.88 x 6.71
Lenses, $f\,(mm)$	▪ Nikkor f=35 for global flowfield ▪ Nikkor f=105 for local flowfield	Nikkor f=180

Planar PIV setup

The planar PIV setup is shown in Figure 3.14. Global flowfield measurements are carried out in the first place, by defining a field of view large enough to study the flow around the whole airfoil and in the wake downstream of the airfoil. Then the local flowfield at a location between the three upstream rows of holes (PS1, PS2 and PS3) and the furthest downstream one (PS4) is analysed by positioning the PIV CCD camera closer to the model and increasing the focal length of the camera lenses (from $f = 35\ mm$ to $f = 105\ mm$) so that the field of view (FOV) is reduced to around one fifth of the original one.

In both situations, the laser is located below the test section, which means that the suction side is in shadow. The laser beam is expanded by means of concave spherical lenses. For the global field of view study, since a larger field of view needs to be illuminated, three concave spherical lenses ($f = -150, -200, -50\ mm$) are located immediately after the laser head. In the local flowfield measurements, a smaller FOV needs to be illuminated. This allows having a less expanded laser beam and thus removing two out of the three spherical laser lenses. As a result, there is higher laser power concentrated in a smaller illuminated area. Then, to optimize the experimental setup the laser power set for the global flowfield configuration is reduced to avoid reflections in the test section, the seeding is increased and $f_\#$ is increased too (from $f_\# = 4$ to $f_\# = 11$). This is because with the higher focal length of the camera lenses in the zoomed-in configuration, the depth of field is smaller and by increasing $f_\#$ we can make sure that the particles are in focus.

To create a thin laser sheet at the midspan of the model, the laser beam is tilted 90° by means of a mirror and a convex cylindrical lens contracts the expanded laser beam to a thinner laser sheet ($\delta_z \sim 2\ mm$) which creates the measurement plane with an appropriate depth of field to illuminate the tracer particles.

Another adjusted parameter during the experiments is the time between laser pulses, Δt. Based on PIV optimization rules, the maximum in-plane particle image displacement should be lower than one fourth of the interrogation window size. As a first approximation, the maximum in-plane image displacement can be limited to 10 pixels. For the baseline configuration ($V_\infty = 15\ m/s$) in the global flowfield setup, this translates into $\Delta t = 100\ \mu s$.

$$\Delta t = \frac{\Delta x}{M \cdot V_\infty} = \frac{10\ px \cdot 4.4\ \frac{\mu m}{px}}{0.03 \cdot 15\ m/s} \sim 100\ \mu s$$

When increasing freestream velocity from $V_\infty = 15\ m/s$ to $V_\infty = 25\ m/s$, to maintain the same pixel displacement, the time between pulses needs to be reduced to $\Delta t = 60\ \mu s$.

When changing the setup for the local flowfield study, the magnification factor is five times higher, so the time between pulses is reduced to $\Delta t = 20\ \mu s$ for $V_\infty = 15\ m/s$. Table 3.4 summarizes the relevant PIV setup parameters for both global and local flowfield configurations.

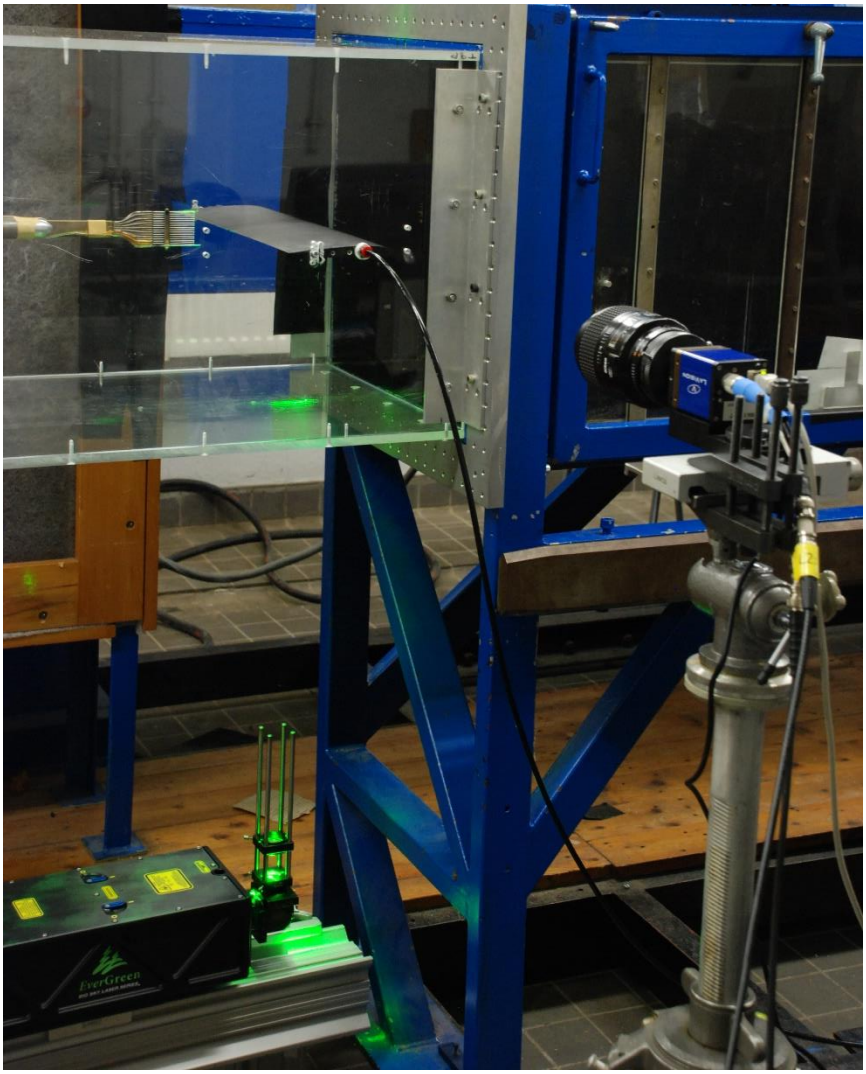

Figure 3.14 Experimental setup for planar PIV measurements. The laser is located below the test section and the laser sheet is created at the midspan of the model. The CCD camera is located at the side of the test section, to record the flow evolution in the streamwise direction.

Table 3.4 PIV setup parameters for both global and local flowfield configurations

PIV setup parameter	Global flowfield	Local flowfield
Object distance, d_o (m)	1.20	0.85
Camera lens focal length, f (mm)	35	105
$f_{\#}$	4	11
Magnification factor, M	0.03	0.14
FOV (cm x cm)	23.84 x 18.10	5.08 x 3.86
Time between laser pulses, Δt (μs)	▪ $\Delta t = 100\ \mu s$ ($V_\infty = 15\ m/s$) ▪ $\Delta t = 60\ \mu s$ ($V_\infty = 25\ m/s$)	$\Delta t = 20\ \mu s$ ($V_\infty = 15\ m/s$)
Focal depth, ΔZ_o (mm)	48.83	2.72

Stereoscopic PIV setup

The stereoscopic PIV setup is shown in Figure 3.15. Like in the planar PIV setup, the laser head is located below the test section and three spherical lenses and a concave lens were used to create the laser sheet. But in this case the laser sheet is aligned with the model's spanwise direction. This is achieved by adjusting the concave laser lens. The laser sheet thickness is thicker than for planar PIV (δ_z~3 cm). This is to ensure that the illuminated region is big enough to capture the particle

displacement, since the cameras are inclined with respect to the measurement plane. For $V_\infty = 15\ m/s$, the time between laser pulses was set to $\Delta t = 45\ \mu s$. Note that this is lower than for the planar PIV setup, again due to the cameras perspective.

The cameras are located downstream of the test section at 2.10 m from the model and they form an angle of 30º with each other. They are fixed to the metallic beams structure by means of camera mounts which allow rotation along the three axes. In this way, the cameras height is set by means of the tripod and the inclination angle by means of the camera mounts. This allows adjusting the cameras position for different streamwise measurement locations, so that only the desired row of holes (and not the upstream ones) is included in the field of view.

In each camera, a Nikkor f=180 mm lens is mounted, which allows capturing 15 holes in the field of view. Due to the inclination of the optical axis with respect to the measurement plane, a scheimpflug is used to help matching the measurement plane with the focus plane. $f_\#$ was set to $f_\# = 8$.

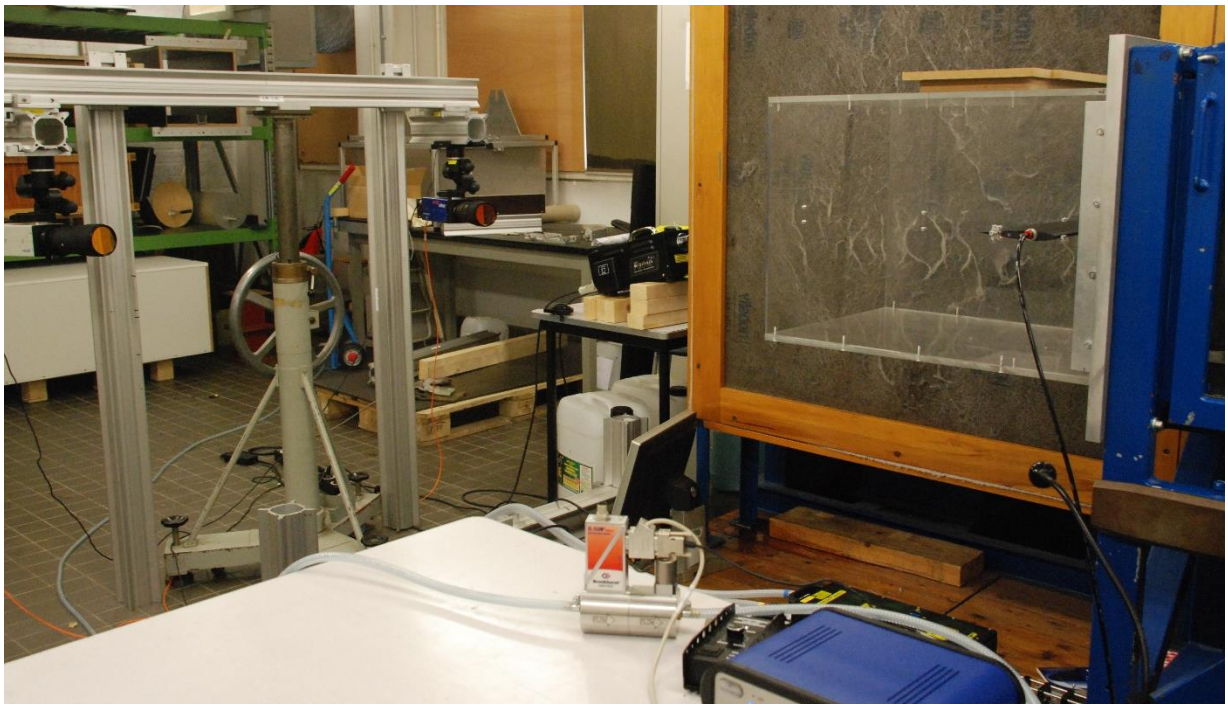

Figure 3.15. Experimental setup for stereoscopic PIV measurements.

Measurements were acquired at six different streamwise locations:

- z = 0.3c, to study the effect of PS1, PS2 and PS3 injection.
- z = 0.45c, upstream of PS4.
- z = 0.55c, downstream of PS4.
- z = 0.75c, to study the evolution of flow mixing downstream of PS4.
- z = 1.1c, to study the flowfield at the trailing edge.
- z = 1.3c, to study the flowfield at the wake.

Note that initially some measurements were planned downstream of PS1, PS2 and PS3, to study the effect of each individual row injection. However, with the current setup and spatial resolution of the cameras this was not possible. Note also that for the stereo-PIV setup the reference system is changed with respect to the planar PIV setup, so the streamwise direction corresponds to the z-axis and not to the x-axis.

Calibration

The calibration of the planar PIV system is carried out using a millimeter paper aligned with the measurement plane, which corresponds to the first illuminated plane seen by the PIV camera. The camera is focused on the lines of the millimeter paper and images for calibration are obtained using a high exposure time. A scaling process is carried out to correlate the number of pixels in the recorded images with the distance in millimetres from the millimeter paper.

Once the scaling process is finished, the cameras are focused on the tracer particles with a low freestream velocity set in the windtunnel. To achieve statistical convergence, 400 image pairs are acquired for each test configuration. Images are acquired with the commercial software DaVis 8.1.2 from LaVision and processed with DaVis 8.4.0 version.

The calibration process for the stereo PIV system consists of two parts: a geometrical calibration and a self-calibration process.

The geometrical calibration allows correlating the dimensions in the image with the physical space. It is carried out using a Type 10 calibration plate (i.e. 10 x 10 cm). The laser sheet is aligned with the front face of the calibration plate, which becomes the measurement plane, and both cameras are focused on the dots of the calibration plate. To ensure that the FOV of both cameras is capturing the same region, two areas of interest are defined in the central part of the calibration plate and are made to coincide. A set of 10 images is acquired with high exposure time and geometrical calibration is applied in DaVis.

The self-calibration process corrects the geometrical calibration process by forcing a particle to be the same in both cameras. A set of 100 images (removing the calibration plate and with illuminated particles) is acquired and masked to eliminate reflections from the laser. Then the self-calibration iterative process is applied and refined until a very small deviation between the two camera images is reached.

Since the PIV cameras and the laser head were not mechanically linked, the calibration process was repeated every time that they were displaced to measure at different streamwise locations.

Processing

The used processing settings are summarized in Table 3.5. First, unwanted laser reflections are eliminated by applying a time filter that subtracts the temporal minimum.

Second, a geometric mask is applied over the airfoil, where no flowfield velocity needs to be calculated. The cross-correlation function to calculate particle displacement is done using a multi-pass algorithm with decreasing size of the interrogation window, from 64 x 64 pixel to 32 x 32 pixel. The small size interrogation window allows visualizing the smaller scale flow structures. A less computationally consuming top-hat weighting function is used for the higher size interrogation window, which is then refined by a rounded Gaussian weighting function (more accurate but more time consuming) in the lower size interrogation window. High accuracy mode is set for final passes and the window shift is set constant for the initial passes and symmetric for the deformed interrogation windows. Finally, vector postprocessing is carried out using a universal outlier detection median filter.

Third, vector statistics are computed, being the outcome the mean velocity components and standard deviation of the velocity vector field. These processing and postprocessing settings are the same for all configurations. The only differences between planar and stereo-PIV processing are that for stereo-PIV, stereo-cross correlation function is applied and geometrical masking is enabled for both cameras.

Table 3.5 PIV processing parameters

PIV processing parameters		
Single pass or multi-pass algorithm		Multi-pass decreasing
Initial settings	Interrogation window size	64 x 64 pixels
	Overlap	50%
	Weighting function	Top-hat
	Number of passes	2
Final settings	Interrogation window size	32 x 32 pixels
	Overlap	75%
	Gaussian weighting function	Rounded
	Number of passes	3

As a final note, for the global flowfield measurements the original experimental matrix is used. Instead, for the local flowfield measurements, the modified experimental matrix introduced in Chapter 4 with higher number of measurements between $BR \in (1, 1.5)$ is used. The most representative results are show below, and the rest of them can be found in Appendix IV.

3.3.6. Equipment uncertainties

The equipment uncertainties specified in the manufacturers manuals are specified in Table 3.6, where % FSS stands for uncertainty as a percentage of full scale span (difference between the maximum and minimum measurable pressure) and % RD for uncertainty as a percentage of the reading.

Table 3.6 Equipment uncertainties

Instrument	Relative uncertainty (%)	Range or reading	Absolute uncertainty
Mensor DPG2400	$\pm$ 0.03% RD	135 Pa ($V_\infty = 15\,m/s$)	+/- 0.04 Pa
Mensor 2101	-	-	+/- 0.1 Pa
HSC pressure sensors	$\pm$ 1% FSS	160 Pa	+/- 1.6 Pa
Analog barometer	-	-	+/- 1 hPa
PT100	-	21 ºC	+/- 0.41 ºC Class B sensor: +/- (0.3 + 0.005T)
Bronkhorst flowcontroller	$\pm$ 0.8% RD	260 l/min	+/- 2.08 l/min

3.4. Chapter remarks

From this chapter describing the research objectives, testing methodology and experimental setup, we can draw the following conclusions:

- The research goal of this project is to understand the effect of some operating and scaling parameters on the aerodynamic losses and flow structures appearing in a symmetrical airfoil with pressure side film cooling.

- Focus is placed on the effect of blowing ratio as scaling parameter, up to a maximum blowing ratio $BR = 2$. The main research question to answer is: *what is the effect of blowing ratio on the aerodynamic losses of a NACA 0012 model with film cooling holes in the pressure side?* This research question is answered by means of midspan wake pressure measurements and planar PIV as flow measurement techniques.

- Additionally, the JICF flow structures and effect of density ratio are analysed by means of stereoscopic PIV and injection of CO_2 gas as secondary flow respectively.

- Different film cooling configurations are studied by varying angle of attack, freestream velocity and injecting secondary flow from individual rows.

- The experiments are carried out at the low speed M-tunnel at TU Delft. The 3D printed model is fixed to a plexiglass test section for optical access. Secondary flow is controlled by means of a Bronkhorst flowcontroller. Pressure measurements are carried out using a pressure rake connected to an automatic scanning system. For PIV experiments, a Quantel Evergreen double-pulsed Nd:YAG laser is used and two different types of $\sim 2MPx$ resolution cameras are used for planar and stereoscopic PIV.

4

Pressure measurements results

4.1. Air as secondary flow

In this section, the results of the pressure measurements with air as secondary flow are presented. Firstly, the effect of blowing ratio on the wake profile and aerodynamic losses coefficients is analysed for the baseline configuration. Once this is understood, we will investigate the influence of angle of attack, freestream velocity and partial injection on the wake profile and aerodynamic losses and on the relationship between aerodynamic performance and blowing ratio.

4.1.1. Baseline configuration, V_∞=15 m/s and AoA=10º: effect of BR

Wake velocity profile

The wake profile can be characterized by the local exit velocity V_2 or by the exit total pressure P_{t_2}. As shown in Figure 4.1, due to the small variation of the exit static pressure P_{s_2} along the wake, equivalent information about local flow momentum is retrieved from both magnitudes. For the sake of conciseness, only V_2 is presented in this section. Appendix III contains the results for P_{t_2}.

For our case of study with an incompressible flow and steady-state analysis, the wake velocity V_2 can be derived from Bernoulli equation using the gauge total and static pressure data from the rake and a constant coolant density ρ_c. The secondary fluid is air at similar temperature and pressure conditions

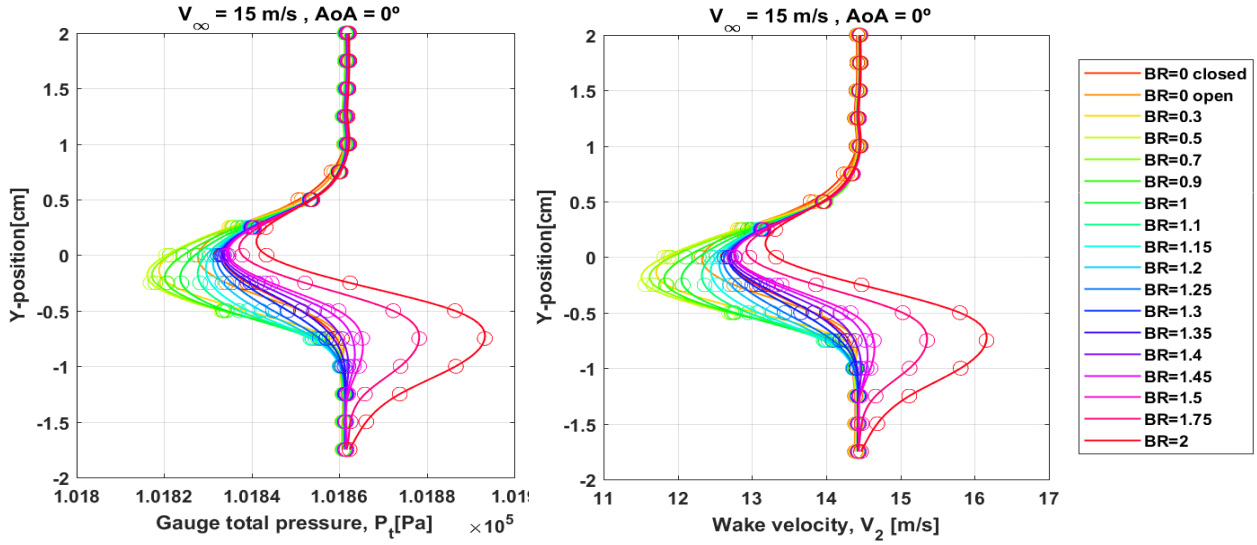

Figure 4.1 Similarity between wake velocity (left) and gauge total pressure (right) profiles for the baseline configuration, V_∞=15 m/s and AoA=10º

to those of the primary flow, $\rho_c \sim \rho_\infty$ and DR~1. In particular, $\rho_c = 1.206$ kg/m^3 and $\rho_\infty = 1.194$ kg/m^3, resulting in a density ratio DR=1.01.

The purpose of the wake survey is to gain insight on the following aspects:

- Wake ($V_2 < V_\infty$) or jet ($V_2 > V_\infty$) local behaviour, through comparison of V_2 with local freestream velocity V_∞.
  - For wake behaviour, maximum momentum deficit or total pressure loss ($V_{2,min}$).
  - For jet behaviour, maximum momentum or total pressure gain, ($V_{2,max}$).
- Symmetry or asymmetry of the wake profile with respect to the airfoil's symmetry plane.
  - For asymmetric wake profiles, magnitude and direction of the wake displacement or wake shift (y-position of $V_{2,min}$).
- Width or spreading of the wake/jet area, represented by the distance between two measurements with local exit velocity equal to freestream conditions ($V_2 = V_\infty$).

Figure 4.2 provides a schematic representation of these parameters used to characterize the wake profile for both wake and jet local behaviour.

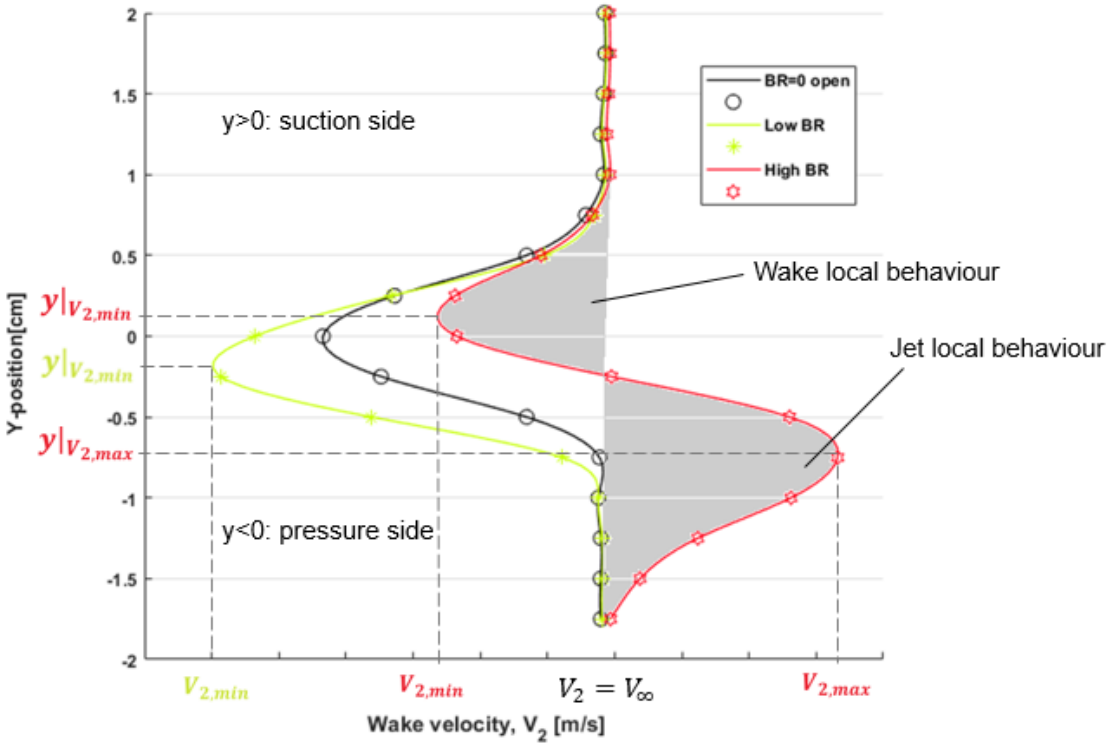

Figure 4.2 Schematic representation of the wake profile for a low BR and high BR, showing the maximum momentum deficit ($V_{2,min}$) for wake behaviour and maximum momentum gain ($V_{2,max}$) for jet behaviour.

Table 4.1 presents a summary of the trends in these wake parameters for different blowing ratios. Note that the values are the result of interpolating the original measurements, which only have a resolution of Δy = 0.25 cm between channels. From this analysis, we can draw some general and descriptive observations.

Table 4.1 Summary of wake structure and local behaviour, including numerical values for maximum momentum deficit or gain, displacement and width.

BR [−]	wake local behaviour			jet local behaviour		
	$V_{2,min}$ $[m/s]$	$y\|_{V_{2min}}$ $[cm]$	width $[cm]$	$V_{2,max}$ $[m/s]$	$y\|_{V_{2max}}$ $[cm]$	width $[cm]$
0 closed	12.67	0	1.85	No jet local behaviour		
0 open	12.33	0	1.75			
0.30	11.71	-0.12	1.88			
0.50	11.51	-0.16	2.18			
0.70	11.62	-0.16	2.11			
0.90	11.81	-0.20	2.11			
1	12.05	-0.20	2.11			
1.1	12.32	-0.16	2.11			
1.15	12.45	-0.12	2.11			
1.2	12.56	-0.08	2.11			
1.25	12.62	-0.04	2.11			
1.3	12.68	-0.01	2.11			
1.35	12.69	-0.01	2			
1.4	12.72	-0.01	1.77	14.47	-0.99	0.45
1.45	12.76	-0.01	1.61	14.56	-0.88	0.65
1.5	12.77	0.03	1.53	14.65	-0.84	0.73
1.75	12.92	0.07	1.36	15.36	-0.77	1.20
2	13.18	0.11	1.26	16.16	-0.73	1.49

- Wake or jet local behaviour. At $BR = 1.4$, we observe a shift in the trend, from wake to jet behaviour in the pressure side. From all the tested configurations, the maximum momentum deficit from the wake occurs at $BR = 0.5$, after which it continuously decreases. For $BR > 1.4$, the momentum gain from the jet continuously increases until the maximum is reached at $BR = 2$. It is also noticeable that for $BR = 0$, the momentum deficit with open holes is higher than with closed holes.

- Symmetric or asymmetric profile and vertical displacement. The wake profile is symmetrical only for $BR = 0$. When low momentum coolant is blown from the pressure side, the wake region is displaced towards it. The maximum shift towards the pressure side occurs at $BR = 1$, after which the displacement is reduced. At $BR = 1.4$, the wake total pressure deficit is almost centered with the airfoil´s symmetry plane and at $BR = 1.5$, the wake region is shifted towards the suction side as the jet gets energized. For higher BR, the wake region continues to displace along the suction side, while the maximum momentum gain from the jet moves closer to the symmetry plane.

- Width of the wake or jet region. The wake is the broadest at $BR = 0.5$. Between $BR = 0.5$ and $BR = 1.4$, the wake maintains a similar width. For $BR > 1.4$, the wake starts shrinking as the jet starts spreading.

A more visual picture of the local flowfield and the effect of blowing ratio on the wake velocity profile as well as a physical interpretation of these results is offered below. Figure 4.3 shows the wake velocity profile for the set of blowing ratios chosen in the original experimental matrix. Figure 4.4 presents the set of measurements performed to detect more accurately the change from wake to jet behaviour (see explanation in Section 3.3.4.). For clarity, the test cases in which the jet is observed $\{BR \in (1.4, 2)\}$ are depicted with a thicker line in Figure 4.4.

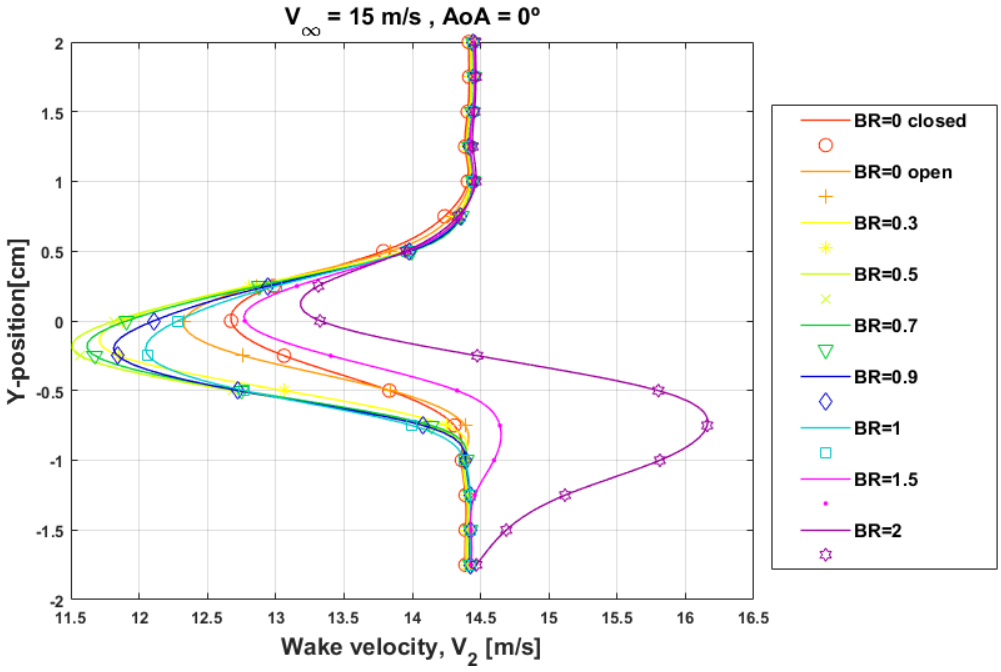

Figure 4.3 Wake velocity profile for the baseline configuration, $V_\infty = 15\ m/s$ and AoA=0°. Set of blowing ratios chosen in the original experimental matrix, $BR \in (0, 2)$. Measurement location x=1.25·c. i.e. 3 cm downstream of the model.

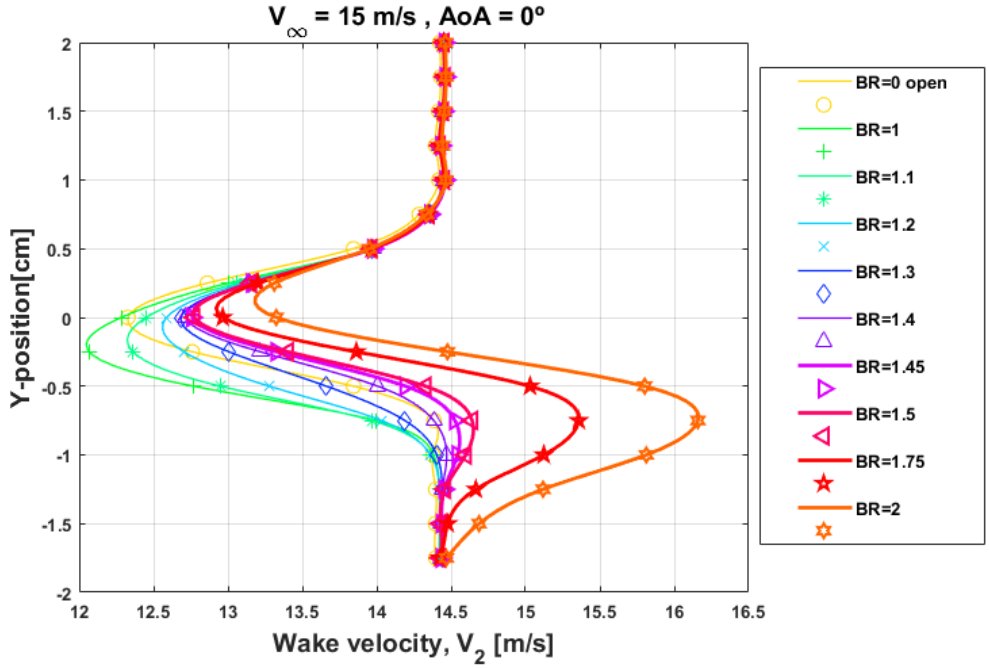

Figure 4.4 Wake velocity profile for the baseline configuration, $V_\infty = 15\ m/s$ and AoA=0°. Set of blowing ratios to detect the appearance of the jet, with increased test cases in $BR \in (1, 1.5)$. Measurement location x=1.25·c. i.e. 3 cm downstream of the model.

The physical explanation for this wake profiles' distribution for different blowing ratios lies in the opposing effects that blowing secondary air has on local flow characteristics. Some local effects of secondary flow injection into the airfoil´s boundary layer are:

- Energization of the flow. The flow gains momentum and accelerates. This facilitates boundary layer transition to turbulent, increases its resistance to adverse pressure gradients and reduces the wake total pressure deficit and its width.

- Increase in boundary layer thickness. A higher viscous region makes the flow more sensitive to adverse pressure gradients, increases the wake total pressure deficit and widens the wake.

- Since the density ratio is constant and close to unity ($DR = 1.01$), an increase in blowing ratio is equivalent to an increase in velocity ratio *VR* and momentum flux ratio *I* (see Table 4.2). This difference in momentum between the coolant and the mainstream flows translates into shear augmentation, with higher velocity gradients in the shear layer leading to mixing losses and higher sensitivity to adverse pressure gradients. For $I > 0.8$ (i.e. $BR > 0.9$), jet lift-off can be expected, causing a higher intrusion of the jet into the mainstream flow.

- Mixing processes increase turbulence production mechanisms, originating a higher diffusion and momentum transport from the wake to the local surrounding freestream flow and causing mixing losses and spreading of the wake region.

As a result, for $\boldsymbol{BR = 0}$ the wake profile is symmetric with respect to the airfoil´s chord, as expected from a symmetrical airfoil at zero angle of attack. The wake velocity profile for the open and closed holes configurations can be seen in Figure 4.5. The closed holes configuration was achieved by sealing all the holes in the model and it shows NACA 0012 airfoil's wake profile in the absence of cooling holes for the selected testing conditions. As mentioned, the momentum deficit in the wake is higher for the open holes configuration than for the one with sealed holes ($V_{2,min_{\text{open}}} = 12.33\ m/s$ vs $V_{2,min_{\text{closed}}} = 12.67\ m/s$, see Table 4.1). The reason for this is the higher surface roughness which appears in the presence of holes, inducing turbulence in the boundary layer and friction losses.

When blowing some low momentum air (low *BR*, *VR* and *I*) from the pressure side, the pressure and suction side boundary layers grow and develop differently. The wake profile becomes asymmetric and displaces towards the pressure side- where the blowing takes place. Since the blown air has low momentum, it is not able to energize the local flow. However, it increases the thickness of the pressure side boundary layer and the peak of the velocity deficit with respect to the no blowing condition. Since the difference in velocity between the coolant and the freestream is high, shear augmentation and turbulent momentum transport occur, leading to mixing losses and spreading of the wake. The test at $\boldsymbol{BR = 0.5}$ with the maximum momentum deficit is the most representative of this low *BR* injection condition.

For $BR > 0.5$, the energizing effect of a higher momentum coolant becomes slightly more important. The local flow accelerates and recuperates part of the momentum loss caused by viscous and turbulent mixing effects, but a big pressure side wake is still visible. At $\boldsymbol{BR = 1}$ ($VR \sim 1, I \sim 1$), there is no difference in momentum between the two flows and since $I > 0.8$, jet lift-off could occur. As a result, for $BR > 1$ the wake ceases to deviate in the pressure side and starts displacing back towards the symmetry plane. The total momentum loss due to viscous effects still outweighs the momentum gain due to the energization of the flow, although the momentum deficit continues to decrease.

When the momentum of the blown air is high enough to compensate for the mixing effects, at $\boldsymbol{BR = 1.4}$, the wake starts acting as a jet in the pressure surface - where the high energy coolant is injected. The exit Mach number increases and becomes higher than the local freestream conditions. The outlet flow angle also changes: the wake region gets shrunk and shifted towards the suction side as the jet keeps spreading for higher blowing ratios. The test at $\boldsymbol{BR = 2}$ with the maximum momentum gain is the most representative of this high *BR* injection condition. Figure 4.6 summarizes these relevant test cases, illustrating how the wake flowfield pattern differs for low and high blowing ratio.

Table 4.2 Coolant flow scaling parameters

BR	*VR*	*I*
0	0	0
0.30	0.30	0.09
0.50	0.50	0.25
0.70	0.69	0.49
0.90	0.89	0.80
1	0.99	0.99
1.1	1.09	1.20
1.15	1.14	1.31
1.2	1.19	1.43
1.25	1.24	1.55
1.3	1.29	1.67
1.35	1.34	1.80
1.4	1.39	1.94
1.45	1.44	2.08
1.5	1.49	2.23
1.75	1.73	3.03
2	1.98	3.96

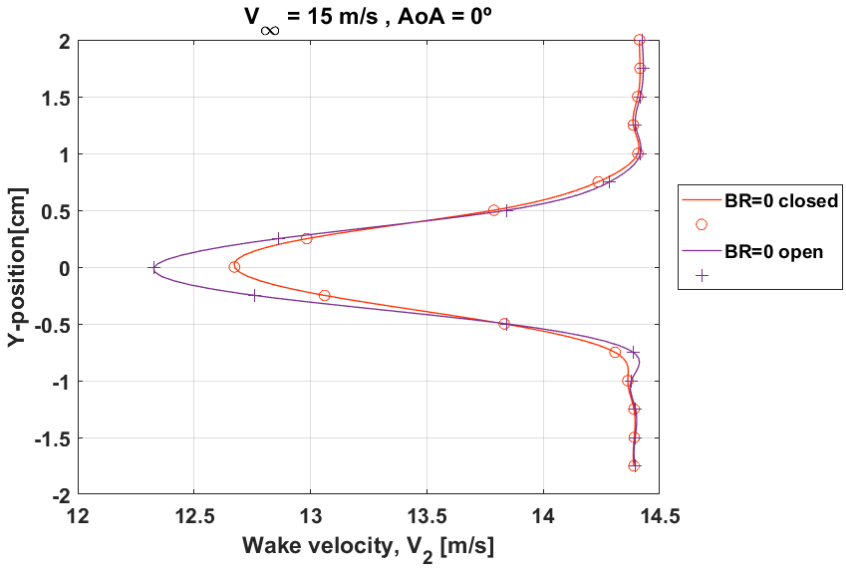

Figure 4.5. Wake velocity profile for no blowing case with open and closed holes in baseline configuration. It illustrates how the presence of the holes originates a total pressure loss

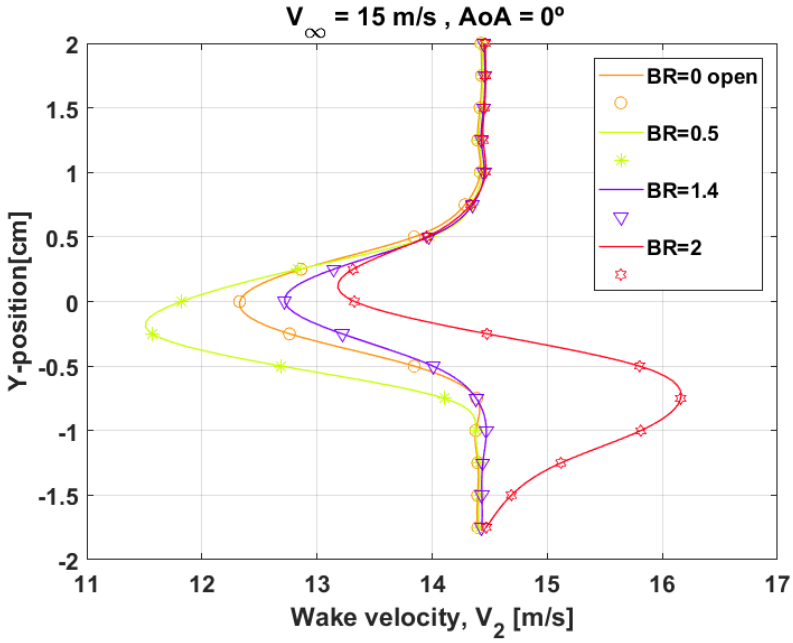

Figure 4.6 Most representative test cases to visualize the relationship between blowing ratio and wake aerodynamic performance in baseline configuration. The case with BR=0.5 presents the wake structure for a low momentum flow injection, showing the maximum total pressure deficit in the wake. The case with BR=2 presents the wake structure for a high momentum flow injection, showing the maximum total pressure gain. The case with BR=1.4, with a wake profile similar to no blowing (open holes) case, represents the point at which the wake aerodynamic behaviour changes.

To complete the wake profile analysis, the obtained results are compared with the ones from (Lanzillotta, et al., 2017).

First, we tested the repeatability of these measurements with our current experimental setup. Since the model is the same for both studies but the set of tested blowing ratios is different, a set of runs was performed using the same blowing ratios as in (Lanzillotta, et al., 2017) with blowing from the suction side. As shown in Figure 4.7, the repeatability of the results looks acceptable: the width of the wake is $\sim 2\ cm$ for both cases, it starts displacing towards the suction side and turns into a local jet for the same value of blowing ratio ($BR = 1.28$), the magnitude of the displacement is similar ($y|_{V_{2_{min}}} < 0.5\ cm$ and $y|_{V_{2_{max}}} < 1\ cm$) and the velocity deficit with respect to freestream conditions is the same at $BR = 0$ ($\Delta V_2 = V_\infty - V_{2_{min}} \sim 2\ m/s$). The freestream conditions are lower in this study ($V_\infty = 14.4\ m/s$), which shows a lack of repeatability of the windtunnel conditions. However, this offset is maintained for the whole velocity profile, i.e. the wake velocity profile is only translated along the x-axis, but the velocity gains and losses with respect to freestream are similar in both cases. Another difference is the extension of the measurement area ($9\ cm$ vs. $3.75\ cm$), but our smaller measurement region is enough to capture the wake flow physics. Also, some of the blockage effect mentioned in the study of (Lanzillotta, et al., 2017) is observed in the pressure side region of the present study, where the freestream flow is accelerated because of the airfoil acting as an obstacle to the flow in the test section. However, the number of freestream data points is not big enough to observe blockage effect as clear as in (Lanzillotta, et al., 2017).

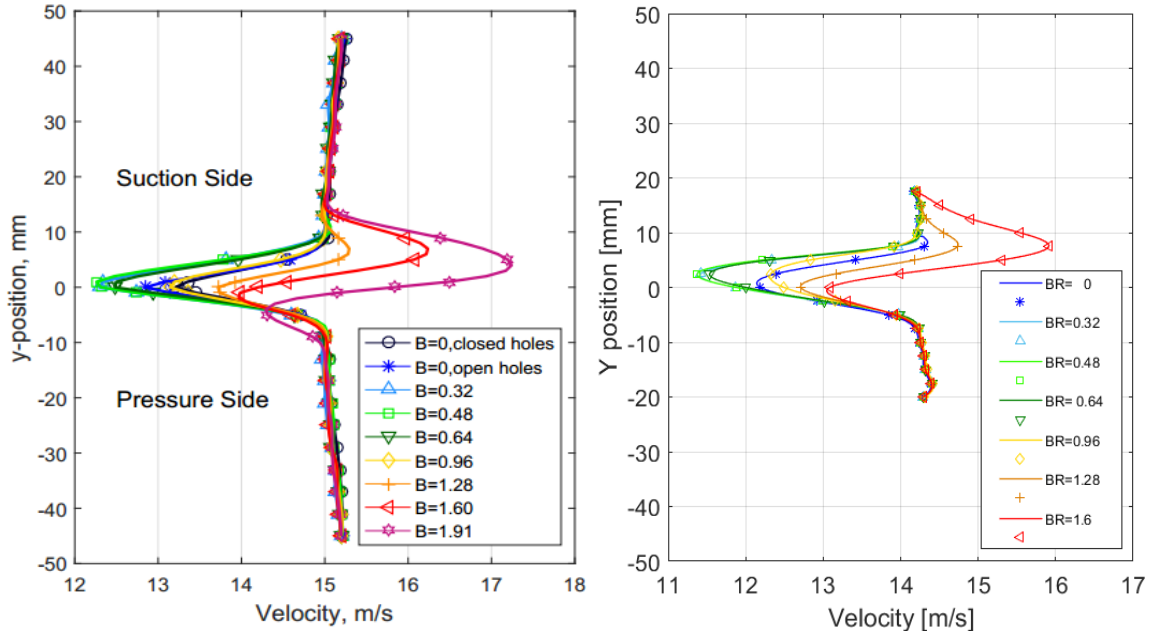

Figure 4.7. On the left, wake velocity profile in the study of (Lanzillotta, et al., 2017) for the baseline configuration, $V_\infty = 15\ m/s$ and AoA=0° [source: (Lanzillotta, et al., 2017)]. On the right, wake velocity profile obtained with the experimental setup of the present study using the same set of blowing ratios and blowing the secondary flow from the suction side.

With repeatability of the measurements analysed, the differences in the wake profile behaviour between suction side and pressure side injection are evaluated for the baseline configuration. From Figure 4.12, we observe that the wake profiles are mirrored. The evolution of wake velocity with blowing ratio follows the same trend: equal velocity distribution for $BR = 0$, increase in momentum deficit and wake spreading, change from wake to jet local behaviour and increase in momentum gain and jet spreading. But since the asymmetry in the wake profile is created by blowing air from the suction or from the pressure side, the wake and jet areas are in the suction or in the pressure side respectively.

When quantifying the relationship with BR, the shift from wake to jet is already visible at $BR = 1.28$ in (Lanzillotta, et al., 2017) while in this study it is not detected until $BR = 1.4$. Note that although the specific case $BR = 1.28$ has not been tested, measurements were performed for $BR \in (1.25, 1.4)$. Since the airfoil is symmetric, the aerodynamic performance should be the same for α=0º. Therefore, this lower sensitivity of the pressure side to blowing ratio changes could be due to measurement uncertainties, air leakages or minor changes in the setup.

Also, the magnitude of maximum velocity gain is higher for suction side injection case ($\Delta V_2 = V_{2_{max}} - V_\infty > 2\ m/s$ already at $BR = 1.91$ vs. $\Delta V_2 < 2\ m/s$ at $BR = 2$). As for the maximum momentum deficit, the differences between pressure and suction side are not visible: the velocity deficit peak has similar magnitude and is visible at $BR = 0.48$ in (Lanzillotta, et al., 2017), in comparison to $BR = 0.5$ in the current study.

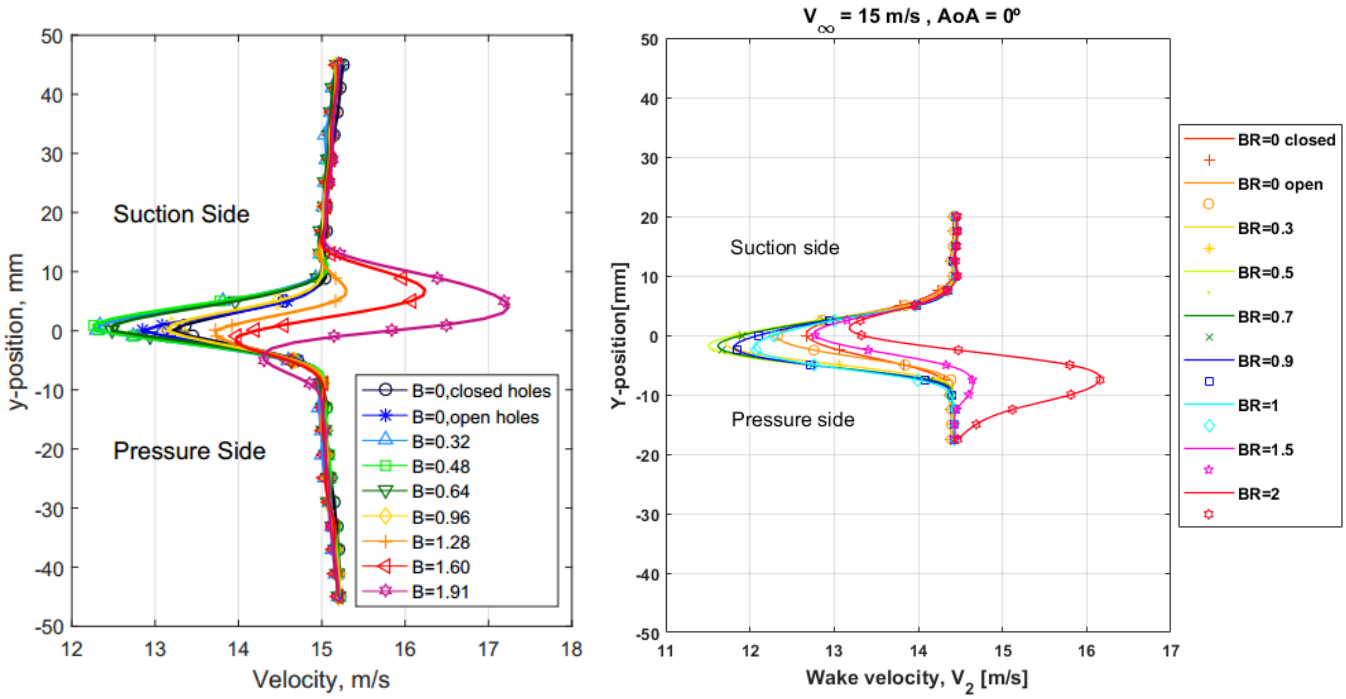

Figure 4.8. On the left, wake velocity profile in the study of (Lanzillotta, et al., 2017) for the baseline configuration, $V_\infty = 15\ m/s$ and AoA=0º [source: (Lanzillotta, et al., 2017)]. On the right, wake velocity profile in the present study with pressure side injection for the baseline configuration.

Finally, when comparing the wake velocity results with open literature, the author found that most of the studies calculate directly the wake aerodynamic losses coefficients, as explained in Chapter 2. Only few studies characterize the wake local flow using local flow parameters such as local outlet angle or local exit Mach number. However, the author did not find in the results of these studies the shift from wake to jet local behaviour for high BR, so no comparison can be established.

Aerodynamic losses

Aerodynamic losses between an inlet location upstream of the airfoil and an exit location at the wake can be characterized by several loss coefficients, as introduced in Chapter 2. In this section, five of them are calculated to evaluate losses. These are:

- Primary loss coefficient
- Local total pressure loss coefficient
- Total pressure loss coefficient
- Integrated aerodynamic losses
- Area-averaged loss coefficient

Additionally, the area-averaged loss coefficient is calculated subtracting the test case at BR=0 with closed holes to assess the losses exclusively caused by film cooling injection, as done in (Lanzillotta, et al., 2017). Table 4.3 presents a summary of the mathematical definition, order of magnitude, maximum and minimum values and changes with blowing ratio for each of the coefficients.

Loss coefficient	Symbol	Definition	Order of magnitude	Results for relevant BR		
				$BR = 0$	$BR = 0.5$	$BR = 2$
Primary	ξ_p [-]	$1 - \frac{1 - \left(\frac{P_{s_2}}{\boldsymbol{P_{t_2}}}\right)^{\frac{\gamma-1}{\gamma}}}{1 - \left(\frac{P_{s_2}}{P_{t_1}}\right)^{\frac{\gamma-1}{\gamma}}}$	$\cdot 10^{-1}$	2.7	$\xi_{p_{max}} = 3.6$	$\xi_{p_{min}} = -2.6$
Local total pressure	C_p [-]	$\frac{P_{t_1} - \boldsymbol{P_{t_2}}}{P_{t_1}}$	$\cdot 10^{-4}$	3.3	$C_{p_{max}} = 4.4$	$C_{p_{min}} = -3.2$
Total pressure	C_{pt} [-]	$\frac{P_{t_1} - \boldsymbol{P_{t_2}}}{P_{t_1} - P_{s_2}}$	$\cdot 10^{-1}$	2.7	$C_{pt_{max}} = 3.6$	$C_{pt_{min}} = -2.6$
Integrated aerodynamic losses	IAL [N/cm]	$\int \left(P_{t_1} - \boldsymbol{P_{t_2}}\right) \cdot dy$	$\cdot 10^{-3}$	2.6	$IAL_{max} = 3.7$	$IAL_{min} = -1.7$
Area-averaged	λ [-]	$\frac{P_{t_1} - \boldsymbol{P_{t_{2,avg}}}}{P_{t_1} - P_{s_{2,avg}}}$	$\cdot 10^{-2}$	5.6	$\lambda_{max} = 8$	$\lambda_{min} = -3.7$

Table 4.3. Summary of the calculated aerodynamic loss coefficients: mathematical formulation, typical order of magnitude and results for the three BR which were found relevant in the wake survey. These results show minimum (<0) and maximum (>0) values of the loss coefficients, occurring for $BR = 0.5$ (minimum) and $BR = 2$ (maximum).

A more visual picture of the local flowfield and the effect of blowing ratio on the wake aerodynamic losses coefficients as well as a physical interpretation of these results is offered below. Figure 4.9, shows the primary, local total pressure and total pressure loss coefficients. The same pattern as in the wake velocity profile is recognised, with a shift in the trend also for $BR = 1.4$.

In this case, the distinction is made between positive or negative loss coefficients, i.e. detrimental or beneficial effect of cooling on aerodynamic performance. For $BR \geq 1.4$, the loss coefficient becomes negative for the same test cases in which a jet local behaviour was detected in the wake velocity survey. We observe how the low momentum regions translate into high positive aerodynamic losses (viscous, momentum diffusion, shear augmentation and mixing effects) and the maximum aerodynamic loss coefficient is reached at $BR = 0.5$, like for the maximum velocity deficit. Similarly, the regions in the wake with a local total pressure gain (beneficial energizing effect) translate into negative loss coefficients and the minimum loss coefficient takes place at $BR = 2$, like for the maximum wake velocity gain. The asymmetrical displacement of the wake towards the pressure side has the same evolution as in the wake velocity profile. The wake losses profile is only symmetrical for $BR = 0$ and the peak of the aerodynamic losses is higher for the open holes configuration than for the closed holes one, as expected.

In fact, when looking at the mathematical definition of all the losses coefficients in Table 4.3, since the inlet total pressure P_{t_1} is kept constant and the exit static pressure P_{s_2} stays nearly constant along the wake (the two static pressure measurements at the top and bottom of the pressure rake have consistently similar values and the same conclusion was reached in (Lanzillotta, et al., 2017) with 25 static pressure measurements along the wake), the evaluated losses turn out to be inversely proportional to the exit total pressure, P_{t_2}. This explains the complete similarity between the wake velocity profile and the losses coefficients distribution.

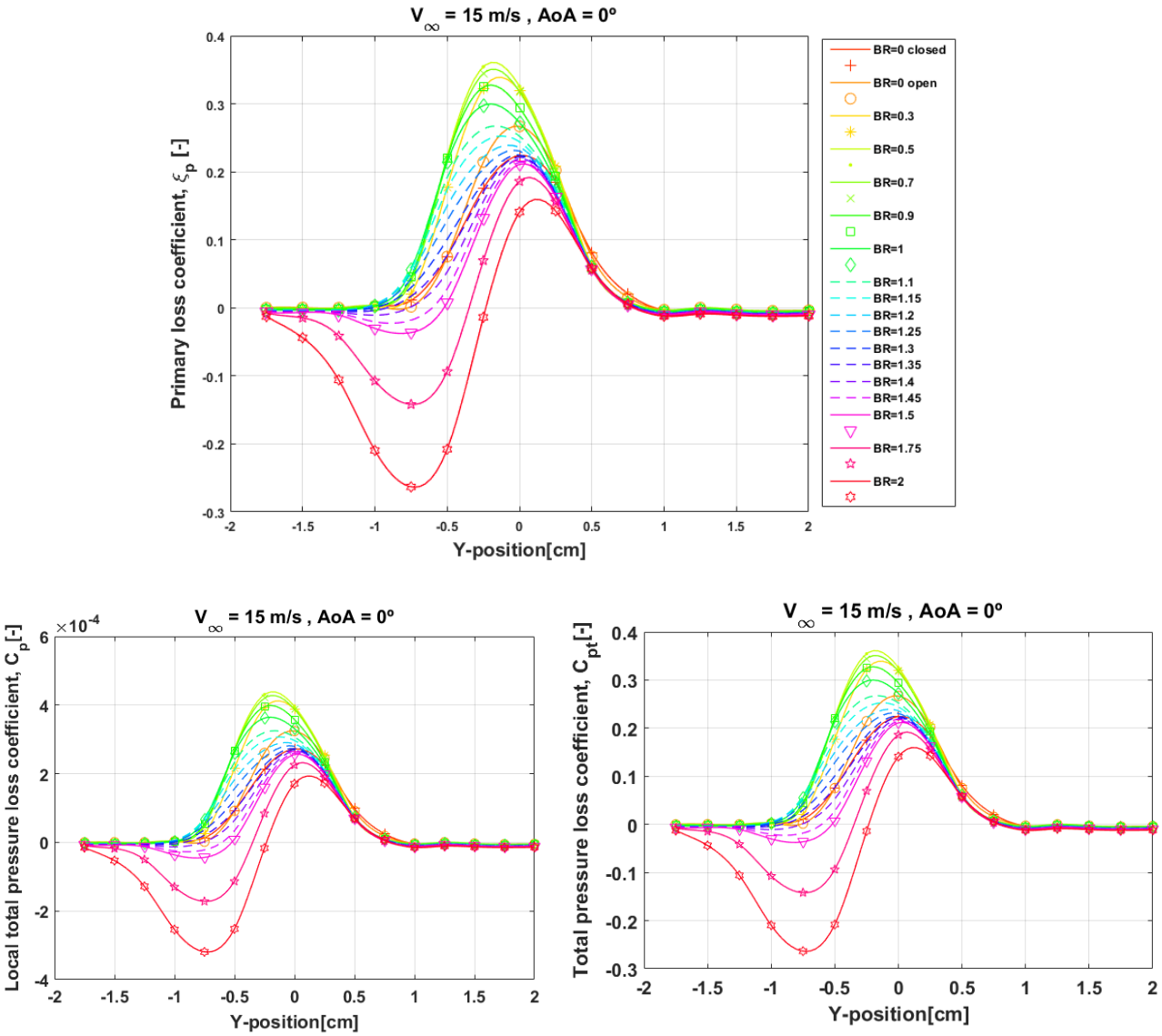

Figure 4.9. Primary loss coefficient, ξ_p (top), local total pressure loss coefficient, C_p (bottom left) and total pressure loss coefficient, C_{pt} (bottom right) for the baseline configuration, $V_\infty = 15\ m/s$ and AoA=0°. Note the similarity between the results for the total pressure loss coefficient C_{pt} and the primary loss coefficient ξ_p.

When comparing these results with the work of (Lanzillotta, et al., 2017), results agree in order of magnitude and values. In literature, a negative value for the total pressure loss coefficient C_{pt} is also obtained in (Kubo, et al., 1998) and the provided explanation is that: *´the negative value of the loss coefficient (in the experimental results) may be caused by the momentum of the injection flow with negligible mixing loss* (Kubo, et al., 1998, p. 5). In (Lin, et al., 2014), it is found that at high BR the total pressure loss coefficient C_{pt} decreases: *´in a sense, it can be stated that the film cooling with high blowing ratios will decrease the loss of the wake region, by raising the local total pressure'* (Lin

et al., 2014, p.5). Other works in literature only conclude an increase in losses for higher BR, although sometimes the maximum BR tested is not as high as $BR = 1.28$ or $BR = 1.4$ and this might be the reason to not detect the wake-to-jet shift (Chappell, et al., 2010).

Figure 4.10 show the integrated aerodynamic losses and area-averaged loss coefficients with and without the losses induced by the airfoil with closed holes. These coefficients offer a more graphic view of the cumulative wake losses for each blowing ratio.

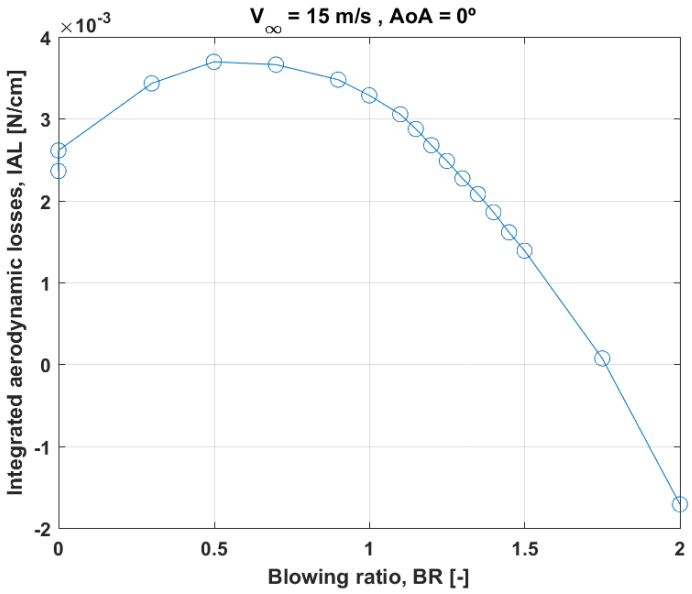

Figure 4.10. Integrated aerodynamic losses, IAL (top), area-averaged loss coefficient, λ (bottom left) and area-averaged loss coefficient subtracting the test case BR=0 with closed holes, $\Delta\lambda$ (bottom right) for the baseline configuration, $V_\infty = 15\ m/s$ and AoA=0°. Note that for $BR = 0$, the higher value corresponds to the open holes configuration and the lower one to the closed holes configuration. The increase in overall losses is appreciated for $BR < 0.5$, where the peak is reached. For $BR > 0.5$, the losses start decreasing.

The results of the integrated aerodynamic losses and area-averaged loss coefficients calculations show the increase in losses for $BR < 0.5$, the peak at $BR = 0.5$ and the decrease in losses for $BR > 0.5$. They also suggest that when including the losses of the airfoil without cooling in the overall wake

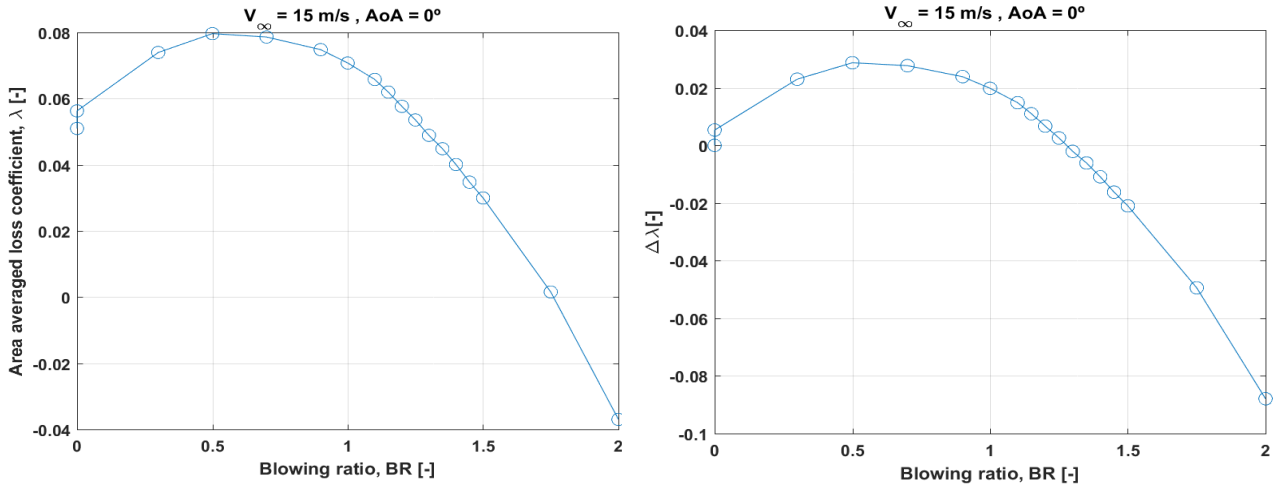

losses calculations, the benefits of high momentum added to the flow only turn into an overall gain (i.e. $IAL < 0$) for $BR = 2$. For $BR \in (1.4, 2)$ the local energizing effect in the jet region does not compensate for the losses induced by the airfoil and momentum deficit region, leading to net overall losses in the wake. When subtracting the losses of the airfoil profile with closed holes, the difference

in area-averaged loss coefficient $\Delta\lambda$ represents the net effect of cooling on the wake losses, showing the beneficial effect of flow energization for $BR \in (1.4, 2)$.

When comparing the results of IAL with the work of (Lanzillotta, et al., 2017), the trends and order of magnitude is the same: maximum losses at $BR \sim 0.5$ followed by decreasing losses for higher BR (see Figure 4.11). However, the maximum loss and gain are slightly higher in magnitude for suction side cooling. The slope in the losses curve, $\Delta IAL/\Delta BR$, is higher for the suction side measurements, which confirms what was already anticipated about the lower sensitivity of the pressure side injection to changes in blowing ratio. Integrated aerodynamic losses for $BR > 0.65$ are slightly higher for pressure side injection, meaning that the aerodynamic penalty of pressure side coolant injection is higher for the wide range of blowing ratios $BR \in (0.65, 2)$.

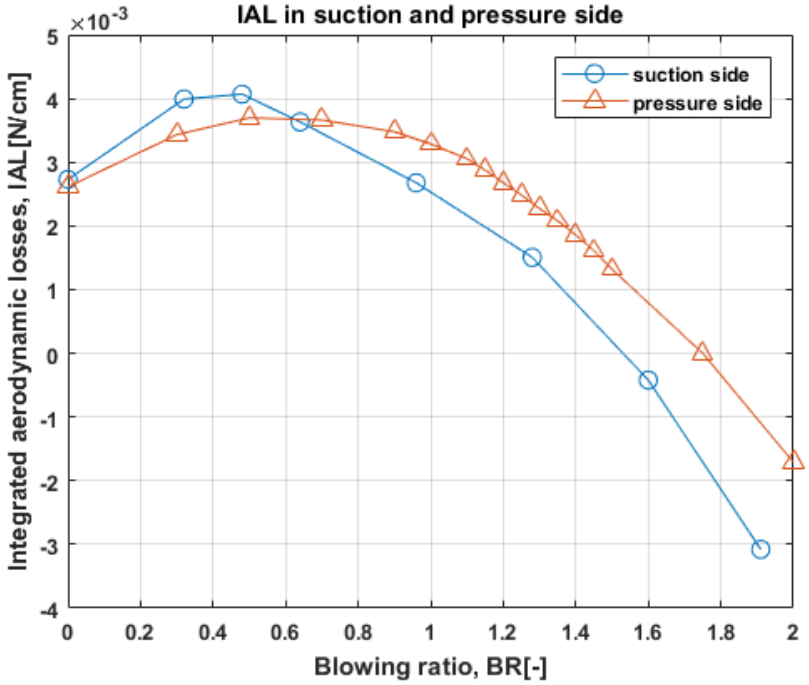

Figure 4.11 Comparison of integrated aerodynamic losses, IAL in pressure and suction sides. Source for the results corresponding to suction side film cooling: (Lanzillotta, et al., 2017)

Finally, when comparing the results with open literature, the calculation of integrated aerodynamic losses is only found in two of the papers listed in Chapter 2: (Jackson, et al., 2000) and (Chappell, et al., 2010). In the results of both publications, IAL shows an increasing trend as a function of BR. For high blowing ratios, the rate of increase of IAL is lower, but no decreasing trend of IAL with BR or negative values of IAL are reported. The explanation for this can be that the highest blowing ratios tested in these two studies are $BR = 0.8$ and $BR = 1.2$ respectively, which are lower than the blowing ratio for which $IAL < 0$ found in the present study.

By the end of this section, the wake velocity profiles and aerodynamic losses coefficients have been introduced for the baseline configuration. In the three following sections, the effect of changing angle of attack, freestream velocity and injection location will be looked into.

4.1.2. Effect of angle of attack

In this section, the effect of angle of attack on aerodynamic performance and its relationship with blowing ratio is analysed for the same freestream velocity, coolant mass flow and blowing ratios as in the baseline configuration. In general terms, when increasing the angle of attack of an airfoil without cooling the maximum momentum deficit and profile losses increase. This is the result of a higher adverse pressure gradient, acceleration and thicker boundary layer in the suction side with respect to a higher favourable pressure gradient, deceleration and thinner boundary layer in the pressure side, leading to shear augmentation in the wake and separation in the suction side boundary layer, with flow recirculation or eventual airfoil stall. Moreover, due to the change in outlet angle and downwash of the airfoil, the streamlines in the wake incline themselves to align with the exit flow direction. Therefore, the wake profile is no longer symmetrical for $BR = 0$.

When including pressure side blowing, these changes in the flowfield will be reflected in the wake profile. Sensitivity to blowing ratio increases with respect to the baseline case, meaning that the flow energization effect and the shift from wake to jet behaviour (or from positive to negative losses) occurs for a lower BR at higher angles of attack.

Since the information retrieved from the primary pressure loss, local total pressure loss and total pressure loss coefficients is equivalent, only the primary loss coefficient is presented together with the wake velocity profile (Figures 4.12 and 4.13). The rest of plots derived from the pressure measurements experiments are included in Appendix III. Note that the maximum velocity deficit for $BR = 0$ has been centered with $y = 0$, so the downwards y-displacement due to the change in angle of attack is not visible in the figures. For a quantitative picture of the losses increase, Table 4.4 summarizes the profile losses (i.e. $BR = 0$ and closed holes), the maximum losses with blowing for the tested angles of attack and the BR at which the jet-to wake shift takes place.

		$\alpha = 0°$ (baseline)	$\alpha = 5°$	$\alpha = 10°$
Profile losses (BR=0, closed holes)	$V_{2,min}\ [m/s]$	12.67	11.48	8.50
	$\xi_{p_{max}}[-]$	0.22	↑ 0.37	↑ 0.65
Maximum wake momentum deficit & losses	$BR\ [-]$	0.5	0.5	0 (open)
	$V_{2,max}\ [m/s]$	11.51	10.95	8.46
	$\xi_{p_{min}}[-]$	-0.36	↑ -0.43	↑ 0.66

Table 4.4. Summary of the profile losses and maximum losses for each angle of attack configuration. The profile losses correspond to the tests with sealed holes and $BR = 0$ measured for each angle of attack. The maximum losses are expressed using the wake velocity deficit and primary loss coefficient. For $\alpha = 5°$, the maximum losses occur at $BR = 0.5$ like for the baseline configuration. For $\alpha = 10°$, the maximum losses occur for $BR = 0$ and open holes.

Angle of attack AoA= 5°

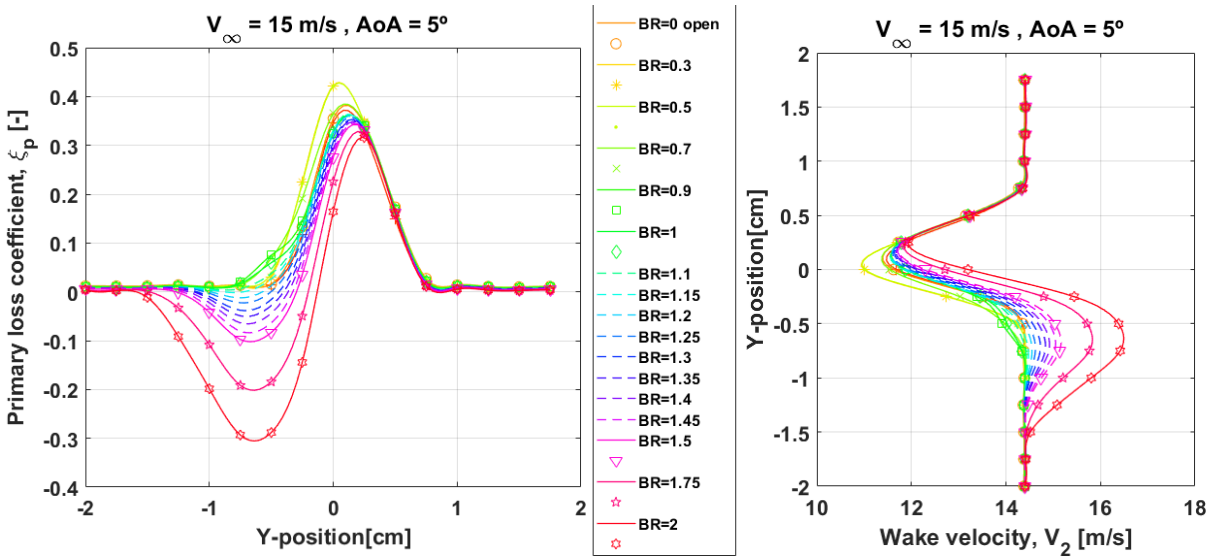

Figure 4.12. Primary loss coefficient, ξ_p (left) and wake velocity, V_2 (right) profiles for the testing configuration $V_\infty = 15\ m/s$ and AoA=5°.

For this configuration, in comparison with the baseline configuration:

- for $BR = 0$, the losses from the open holes are higher than with closed holes, like for the baseline configuration.
- the peak of momentum deficit occurs at $BR = 0.5$, like for the baseline configuration.
- the maximum primary loss coefficient increases by 68%.
- the wake is narrower ($\sim$1.5 cm vs 1.85 cm for baseline configuration at $BR = 0$), due to the earlier boundary layer transition to turbulent for higher angles of attack.
- the wake-to-jet shift occurs at $\boldsymbol{BR = 1.2}$, lower than $BR = 1.4$. The explanation for this is the higher sensitivity to pressure side blowing with higher angle of attack, as explained above.
- the maximum aerodynamic gain occurs also at $BR = 2$ and increases with respect to the baseline configuration by 16%.

When comparing these results with (Lanzillotta, et al., 2017), a difference can be noted in the sensitivity to BR changes. When increasing the angle of attack, the wake-to-jet shift in (Lanzillotta, et al., 2017) is visible for $BR = 1.60$, a higher blowing ratio than the critical blowing ratio for the baseline configuration ($BR = 1.28$). This is opposite to what occurs for pressure side injection, where the wake-to-jet shift occurs at $BR = 1.2$, a lower blowing ratio than the critical blowing ratio for the baseline configuration ($BR = 1.4$).

Angle of attack AoA= 10°

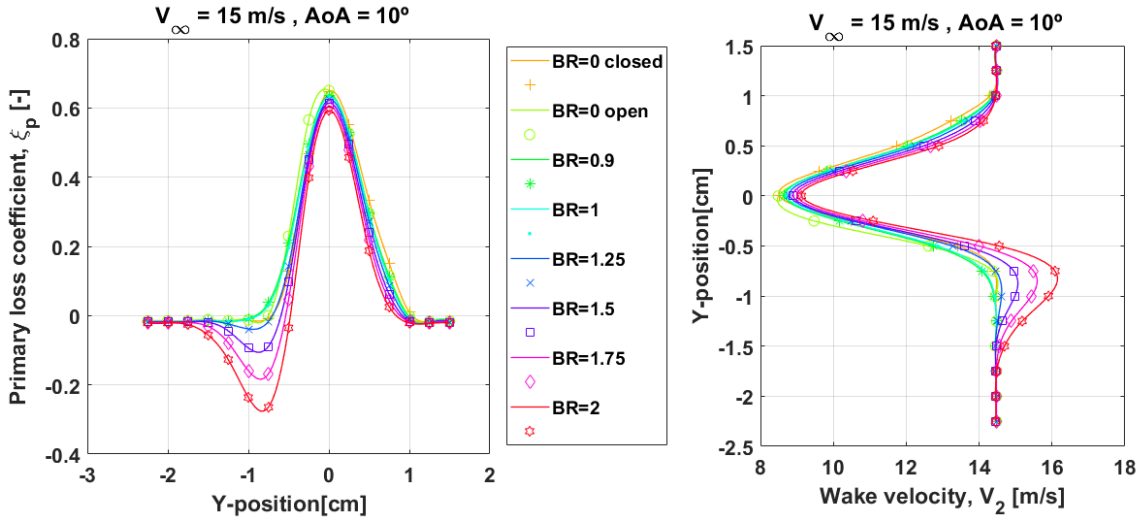

Figure 4.13. Primary loss coefficient, ξ_p (left) and wake velocity, V_2 (right) profiles for the testing configuration $V_\infty = 15\ m/s$ and AoA=10°.

For this configuration, in comparison with the baseline configuration:

- for $BR = 0$, the losses from the open holes are higher than with closed holes, like for the baseline configuration.
- the peak of momentum deficit occurs at $\boldsymbol{BR = 0}$, instead of at $BR = 0.5$ as occurs for the baseline configuration and for AoA=5°.
- the maximum primary loss coefficient is almost 3 times higher than for the baseline case.
- the wake is narrower ($\sim 1.75\ cm$ vs $1.85\ cm$ for baseline configuration at $BR = 0$), due to the earlier boundary layer transition to turbulent for higher angles of attack.
- the wake-to-jet shift occurs for $BR \in (1, 1.25)$ – no further tests were performed in this range for this configuration. This value is in any case lower than $BR = 1.4$ and the explanation for this is again the higher sensitivity to pressure side blowing with higher angle of attack, as explained above.
- the maximum aerodynamic gain occurs also at $BR = 2$ and increases with respect to the baseline configuration by only 5%.

During the tests at AoA=10°, contrary to the results of (Lanzillotta, et al., 2017) no stall is detected at $BR = 0$. To conclude the analysis of the angle of attack effect, Figure 4.14 introduces a comparison of the integrated and area-averaged aerodynamic losses for different angles of attack.

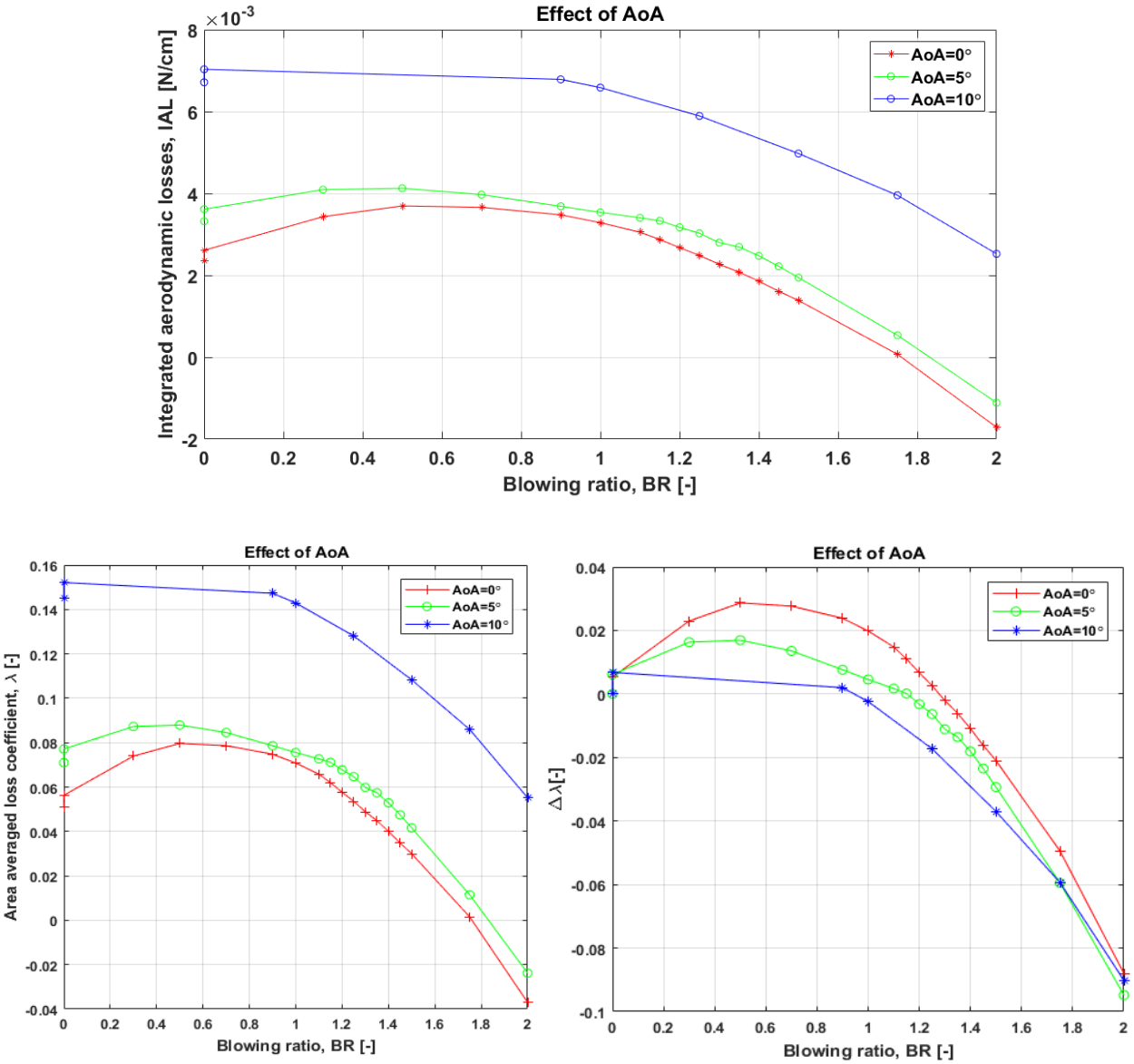

Figure 4.14. Effect of different angles of attack ($AoA = 0°, 5°, 10°$) on integrated aerodynamic losses, IAL (top) and area-averaged loss coefficients, λ (bottom left) and area-averaged loss coefficients subtracting the losses induced by the airfoil with closed holes, $\Delta\lambda$ (bottom right), $V_\infty = 15\ m/s$

The comparison of the integrated aerodynamic losses, IAL and area-averaged loss coefficient, λ summarizes what already concluded above: the maximum losses occur at $BR = 0.5$ for $AoA = 5°$ and at $BR = 0$ with open holes for $AoA = 10°$. For $AoA = 5°$ as for the baseline configuration, $IAL < 0$ for $BR > 1.75$, i.e. high BR allows an aerodynamic gain even including the losses induced by the airfoil without cooling. For $AoA = 10°$, overall integrated or averaged losses are not negative at any of the measured blowing ratios. This is because of the significant difference in the losses of the airfoil without cooling occurring at $AoA = 10°$: these losses are so high due to the high angle of attack that the injection of coolant cannot compensate even at high BR.

When looking at the net losses due solely to coolant injection, the trend shifts: the net area-averaged loss coefficient is higher for the baseline configuration and decreases with increasing angle of attack. This suggests that for higher angles of attack, although the losses without cooling are higher due to a different pressure distribution around the airfoil, pressure side coolant injection entails less losses and produces an aerodynamic gain for lower BR than the baseline.

4.1.3. Effect of freestream velocity

In this section, the effect of freestream velocity on aerodynamic performance and its relationship with blowing ratio is analysed. Tests were conducted at $V_\infty = 25\,m/s$. This higher freestream velocity means an increase in Reynolds number (based on airfoil chord and mainstream velocity) from $Re_{\infty,_c} = 1.18 \cdot 10^5$ at $V_\infty = 15\,m/s$ to $Re_{\infty,_c} = 1.95 \cdot 10^5$ - still in the same order of magnitude. The increase in freestream velocity is limited by the maximum speed attainable in the windtunnel.

The implications of a higher Reynolds number in the boundary layer characteristics of an uncooled airfoil (further upstream location of boundary layer transition to turbulent and reduction in boundary layer thickness) are reflected in a narrower wake flowfield for $BR = 0$ with respect to the baseline configuration. Regarding the profile losses, despite of the lower thickness of the boundary layer, losses are found higher than for the baseline configuration. This can be due to the higher turbulent dissipation in the turbulent boundary layer.

This explanation is given by (Drost & Bölcs, 1999): after measuring profile losses downstream of a solid blade with no cooling for 5 different exit Reynolds numbers, they conclude that profile losses decrease until a certain value of Re due to the reduction of boundary layer thickness, and increase for higher values of Re possibly due to laminar-to-turbulent transition in the pressure side and extension of the turbulent boundary layer in the suction side.

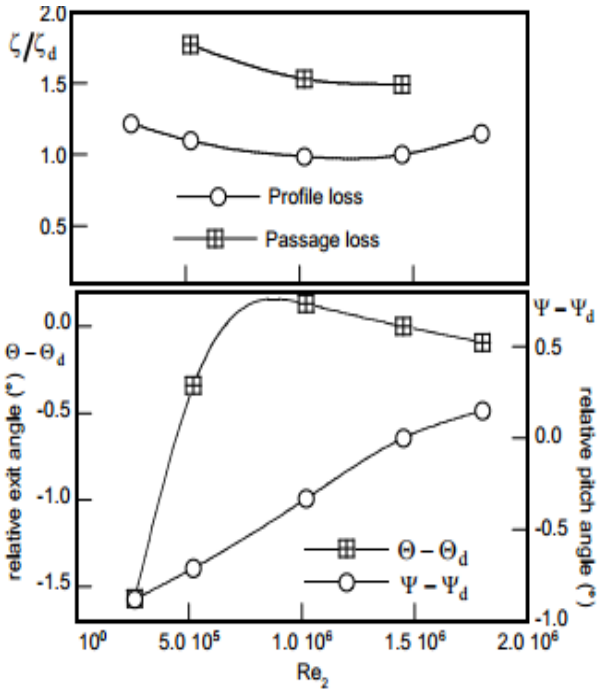

Figure 4.15. Evolution of uncooled blade profile losses with Reynolds number, for five different Reynolds number and profile losses measured downstream of a solid uncooled blade (Drost & Bölcs, 1999). (source: (Drost & Bölcs, 1999))

When including cooling, to obtain the same set of blowing ratios as in the baseline configuration with a higher freestream velocity, the velocity of the coolant V_c and therefore the coolant volumetric flow rate set in the flow controller must be higher too. Since the Bronkhorst F-202AV-M20 flow controller has been calibrated for a maximum air flow of $\dot{m}_{c_{max}} = 260\,\mathrm{l/min}$, the maximum blowing ratio attainable for $V_\infty = 25\,m/s$ with the current experimental setup is $BR = 1.2$. As a result, the effect of coolant injection at high BR cannot be analysed for this configuration and the wake-to-jet shift is not detected. However, when looking at the tests results (Figure 4.16), we can imply a similar behaviour of the wake flowfield with changes in BR for low BR.

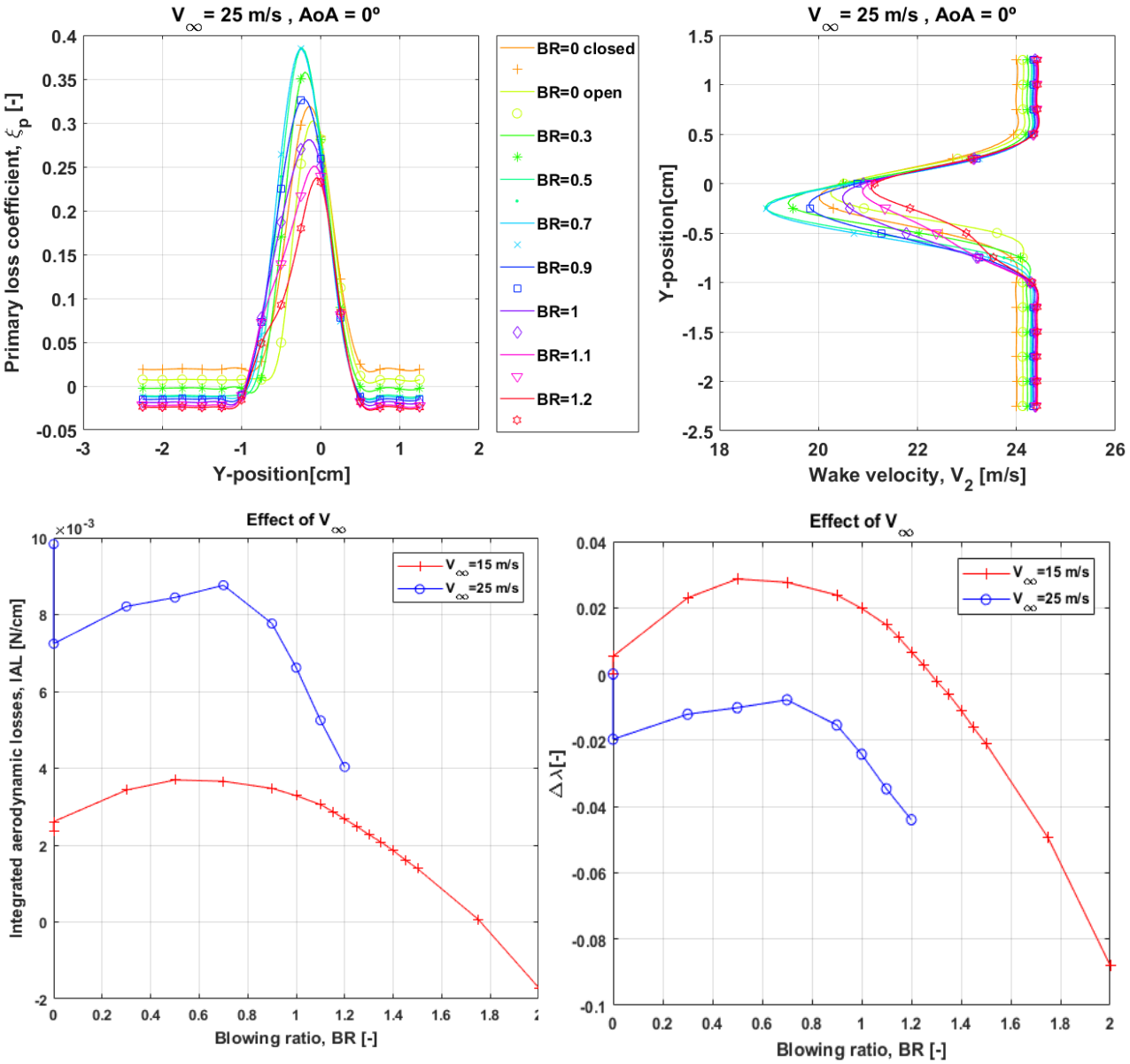

Figure 4.16. Effect of higher freestream velocity ($V_\infty = 25\ m/s$) on primary loss coefficient, ξ_p (top left), wake velocity profile (top right), integrated aerodynamic losses, IAL (bottom left) and area-averaged loss coefficient subtracting profile losses, $\Delta\lambda$ (bottom right), $AoA = 0°$.

Some comments can be derived from Figure 4.16:

- average freestream velocity at the wake is equal to $V_\infty = 24.4$ m/s.
- the wake is narrower ($\sim 1.5\ cm$ vs. 1.85 cm for baseline configuration at $BR = 0$), due to the earlier laminar-to-turbulent transition and decrease in boundary layer thickness at higher Re.
- with $BR = 1.2$ as the maximum attainable BR, the wake-to-jet shift is not visible.
- maximum losses occur at $BR = 0.7$ instead of $BR = 0.5$.
- the losses for $BR = 0$ with closed holes (i.e. profile losses) are higher than for the open holes configuration. This behaviour has no plausible physical explanation and the reason for it has to be a faulty test data acquisition. Probably, the measurement for sealed holes was taken in a different moment of time than the whole data set with open holes, so the windtunnel flow conditions or something else in the experimental setup were not fully replicated and a lower total pressure value was measured by the wake rake.

- aerodynamic losses are higher for $V_\infty = 25\ m/s$ than for $V_\infty = 15\ m/s$ at every BR test case. The explanation for this could be the higher turbulent dissipation in the boundary layer as explained above.
- the net cooling effect subtracting profile losses is more beneficial for $V_\infty = 25\ m/s$ than for $V_\infty = 15\ m/s$. However, since the data for profile losses at $V_\infty = 25\ m/s$ is not correct, the net cooling effect losses should be higher in absolute value and not negative for low BR.

All in all, the losses increase and the wake narrows for higher freestream velocity, but the behaviour with BR is similar: losses increase until $BR = 0.7$ and start decreasing for higher BR.

4.1.4. Effect of partial injection

In this section, the effect of single-row injection on aerodynamic performance and its relationship with blowing ratio is analysed. These experiments were conducted by opening one of the four rows of cooling holes and sealing the other three. The intention of these tests is to understand the effect of the injection location along the pressure side on the wake flowfield and losses, and how this location influences flowfield's sensitivity to BR changes. Note that only one row is opened at a time, so no row-to-row interactions (i.e. influence of upstream jets on downstream flow) are measured.

Since the freestream velocity and angle of attack are the same as in the baseline configuration, losses of the airfoil without film cooling are extracted from the baseline configuration test run. To obtain the same set of blowing ratios as with full coverage film cooling, since freestream velocity is kept the same, the coolant velocity is kept the same as well. Therefore, since the cooling area when only one row is open is one fourth of the original one, applying continuity equation the coolant mass flow is reduced by a factor of four in each test case. Figure 4.17 contains the resulting integrated aerodynamic losses and area-averaged losses for each of the rows. The addition of all the row´s partial film cooling losses is also plotted together with the full coverage film cooling losses for the baseline configuration. The individual wake flowfield and losses profiles are not included here (collated in Appendix III).

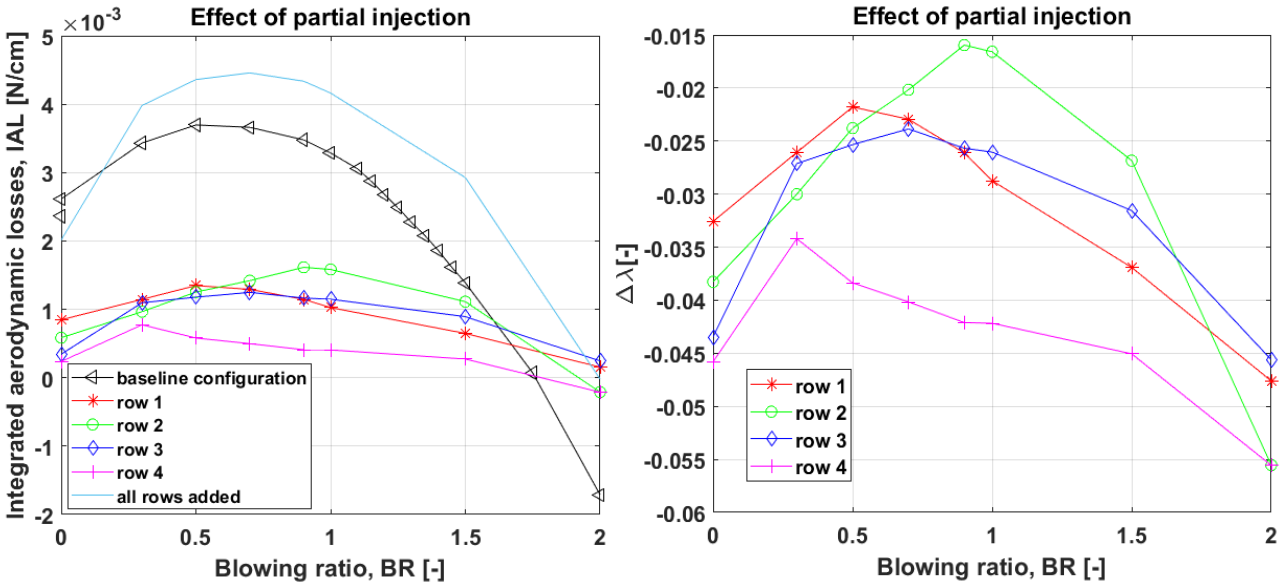

Figure 4.17. Effect of injection row location on integrated aerodynamic losses, IAL (left) and on area-averaged loss coefficient subtracting profile losses, Δλ (right). In the IAL plot, integrated aerodynamic losses for the baseline configuration with all rows open and the result of adding each row´s individual losses are represented for comparison.

		All rows open	PS1	PS2	PS3	PS4
Maximum losses	Distance from LE	-	$0.05c$	$0.10c$	$0.15c$	$0.50c$
	BR $[-]$	0.5	0.5	0.9	0.7	0.3
	$IAL_{max} \cdot 10^3$ $[N/cm]$	3.7	1.35	1.61	1.25	0.77

Table 4.5. Summary of the maximum integrated aerodynamic losses and the BR at which this maximum occurs for each injection location case. Maximum loss for the baseline configuration with all holes open is also included for reference and the chordwise location of each row is included as a reminder. From partial injection, the highest losses are obtained in PS2 and lowest losses in PS4 injection.

Some observations can be extracted from these results:

- when comparing partial injection from individual rows to total injection, partial injection has a lower sensitivity to BR (lower $\Delta IAL/\Delta BR$).
- losses from partial injection are lower than profile losses from the baseline configuration. This offset might be due again to the data acquisition process taking place in separate moments, reducing repeatability of the measurements.
- when adding up the individual losses of each row from partial film cooling results, the trend with BR is similar to that of the baseline configuration with all rows of holes open, although the absolute values differ. Thus, superposition principle cannot be applied.
- when comparing the behaviour of each of the individual rows, the maximum losses induced by injection at the last row (PS4) are the lowest. The reason for this can be that this location is closer to the trailing edge and separation point, thus contributing greatly to the energization of the flow and less to the mixing losses. Also, the position of PS4 is the only one in which injection takes place after the point of maximum thickness of the NACA0012 airfoil. As a result, local surface curvature changes increasing the flow energizing effect. This behaviour of PS4 injection was also found in the work of (Lanzillotta, et al., 2017).
- the maximum losses induced by injection at the second row (PS2) are the highest and they occur for the highest BR compared to the rest of the rows. Also, the rate of change of the losses when increasing BR is the highest. A similar behaviour of PS2 injection can be observed in the work of (Lanzillotta, et al., 2017). However, the author cannot explain why this location presents this behaviour when compared to PS1 or PS3.

In literature, some publications study the effect of single row injection, including losses variation for different injection locations, comparison of summary effect of all rows vs. effects of separate injection rows or effect of upstream rows on downstream rows boundary layer and cooling output. Among them, we can highlight: (Prust, 1975), (Urban, et al., 1998), (Day, et al., 2000), (Lin, et al., 2014), (Mamaev, et al., 2015) and (Nikparto & Schobeiri, 2016).

Summarizing the diverse conclusions of these studies is above the scope of this section. However, it is worth mentioning the some of them agree in the importance of measuring the difference between coolant exit pressure from the holes (including the pressure loss of the coolant from the plenum to the hole exit) and surface static pressure or mainstream total pressure. Also, some studies show the variation of local BR with P_{t_c}/P_{t_∞} or fix a certain P_{t_c}/P_{t_∞} as design condition, adjusting the mass flow for it. Complexity to partial injection analysis is added when considering the differences in injection angle for each location due to the variation of surface curvature, which affects the jet lift-off behaviour and therefore turbulence intensity, kinetic energy and eddy dissipation. On top of this, the presence of a separation bubble, its laminar or turbulent nature and the relative position of the

injection location to it also plays a role in determining the effect of a particular injection location on the wake characteristics.

4.2. CO_2 as secondary flow

In this section, the results of the pressure measurements with CO_2 as secondary flow are presented. Firstly, the effect of blowing ratio on the wake profile and aerodynamic losses coefficients is analysed for the baseline configuration. Once this is understood, we will investigate the influence of angle of attack and coolant flow scaling parameter on the wake profile and aerodynamic losses and on the relationship between aerodynamic performance and blowing ratio.

Some general comments on the experiments

The aim of these experiments is to analyse the effect of density ratio on aerodynamic performance, in an attempt to simulate the temperature ratio between the coolant and the mainstream flows existing in real gas turbine cooling applications. The coolant is at a lower temperature, $T_c < T_\infty$ so to simulate this ratio we need $\rho_c > \rho_\infty$. At the tested conditions the density of CO_2 is higher than that of air, leading to a density ratio $DR = 1.52$ (see Table 4.6, $\rho_\infty = 1.195\ kg/m^3$).

	Air	CO_2
$\Delta P_c\ [Pa]$	80	30
$T_c\ [°C]$	21	22
$R_c\ [J/kgK]$	287	189
$\rho_c [kg/m^3]$	1.20	1.82
DR [-]	1.005	1.52

Table 4.6 Density difference between air and CO_2 at testing conditions

As mentioned in Chapter 3, no freestream or partial injection are studied, so the test cases only include the baseline configuration and changes in angle of attack. As for the changes in angle of attack, AoA=5º is not tested, since previous section shows that similar qualitative trends can be obtained from tests at AoA=10º. However, this series of experiments includes tests at AoA= -10º. Due to the symmetry of the airfoil, this is equivalent to suction side blowing at AoA=10º. The reason for this test configuration is to study the effect of density ratio on suction side injection performance, since in the work of (Lanzillotta, et al., 2017) no density ratio effects were studied, so this set of data could complete the whole picture. Also, no profile losses measurements (i.e. BR=0 with closed holes) were obtained in this test campaign, due to the limited amount of time for experiments.

For the sake of comparability of the results (i.e. be as sure as possible that the differences in the results between CO_2 and air are due to the difference in fluid density and not due to minor changes in the experimental setup) every test was subsequently performed for both air and CO_2. In this way, we are able to draw conclusions about density ratio effects with density of secondary flow was the only variable in the system.

Blowing ratio was chosen as matching scaling parameter. Table 4.7 provides a quantitative picture of what this implies for the rest of flow scaling parameters when using air and CO_2. Since freestream conditions and total area of cooling holes are kept constant, the only way to match blowing ratios is by keeping the factor $(\rho \cdot V)$ constant as well. Therefore, the ejecting velocity for CO_2 is lower than for air. Consequently, for a certain blowing ratio, momentum flux ratio is lower for CO_2. Recalling

the theory from Chapter 2 (i.e. jet lift-off present for $I > 0.8$), jet lift-off is expected to be postponed for CO_2.

BR	DR [-]		$V_c = \frac{BR}{DR} V_\infty$ $[m/s]$		VR [-]		$I = DR \cdot VR^2$ [-]		$\dot{m}_c \cdot 10^3$ $[kg/s]$
Both	Air	↑ CO_2	Air	↓ CO_2	Air	↓ CO_2	Air	↓ CO_2	Both
0	1.005	1.52	0	0	0	0	0	0	0
0.5			7.46	4.93	0.5	0.33	0.25	0.16	1.28
1			14.92	9.86	0.99	0.66	0.99	0.66	2.57
1.1			16.42	10.84	1.09	0.72	1.20	0.80	2.82
1.2			17.91	11.83	1.19	0.79	1.43	0.95	3.08
1.3			19.40	12.81	1.29	0.85	1.68	1.11	3.33
1.4			20.89	13.80	1.39	0.92	1.95	1.29	3.59
1.5			22.39	14.79	1.49	0.99	2.24	1.48	3.85
2			29.85	19.71	1.99	1.31	3.98	2.63	5.13

Table 4.7. Summary of the coolant flow scaling parameters (BR, DR, VR, I) for air and CO2 with matching BR. To match BR with constant freestream conditions and total area of coolant holes, due to continuity equation the mass flow is kept the same for both gases. For CO2, DR increases, VR decreases and this results in lower I. Therefore, a lower tendency for jet lift-off is expected for CO2 than for air, i.e. let lift off is expected to occur at a higher BR for CO2 than for air.

Finally, since the flowcontroller used in the present experimental setup is only calibrated for air, the signal (% of maximum flow) provided by the instrument without correction would not be equal to the actual CO_2 volumetric flow desired to match BR. The conversion factor $C = 0.74$, dependent on CO_2 gas properties (i.e. c_p and ρ, see Chapter 3 and Appendix II), is applied. Resulting numbers from this conversion are shown in Table 4.8 for all BR test cases.

$\dot{m}_c$ $[kg/s]$	$\dot{m}_{c\ actual}[l/min]$		$\dot{m}_{c\ signal}[l/min]$	
Both	Air	↓ CO_2	Air	↓ CO_2
0	0	0	0	0
$1.28 \cdot 10^{-3}$	64	42	64	57
$2.57 \cdot 10^{-3}$	128	85	128	114
$2.82 \cdot 10^{-3}$	141	93	141	126
$3.08 \cdot 10^{-3}$	154	102	154	137
$3.33 \cdot 10^{-3}$	167	110	167	149
$3.59 \cdot 10^{-3}$	179	119	179	160
$3.85 \cdot 10^{-3}$	192	127	192	172
$5.13 \cdot 10^{-3}$	256	169	256	229

Table 4.8. Summary of mass flow and volumetric flow for air and CO_2. Since density is higher, volumetric flow is lower for CO_2. Because the flowcontroller used in the setup is calibrated only for air, the CO_2 volumetric flow set as an input and read form the flowcontroller signal is corrected using the conversion factor specified in Bronkhorst instruction manual ($\dot{m}_{c\ signal}$).

4.2.1. Baseline configuration, V_∞=15 m/s and AoA=10°: effect of BR

Wake velocity profile and aerodynamic losses

In this section, the obtained results for the wake velocity profile and aerodynamic losses are presented for the baseline configuration. The analysis of wake behaviour will be less detailed than in Section 4.2, since basic wake flow patterns and the physical explanation of them are better understood at this point. Since wake velocity and losses analysis provide similar information, both will be done

simultaneously. The analysis will be focused in maximum momentum deficit (or maximum losses), wake-to-jet shift (or positive to negative shift in loss coefficient) and maximum momentum gain (minimum losses) and the BR at which these take place. Figure 4.18, Figure 4.19, Figure 4.20 and Table 4.9 present some results for the baseline configuration. More results can be found in Appendix III.

Wake velocity profile:

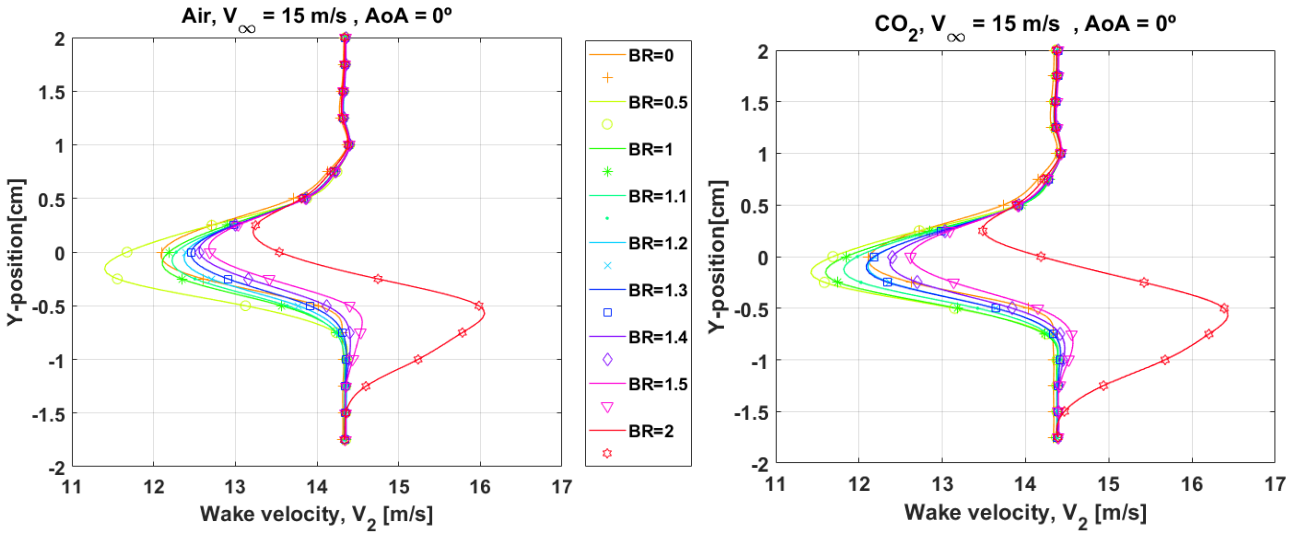

Figure 4.18. Wake velocity profile for air (left) and CO_2 (right) for the baseline configuration, $V_\infty = 15\ m/s$ and AoA=0º.

Primary loss coefficient:

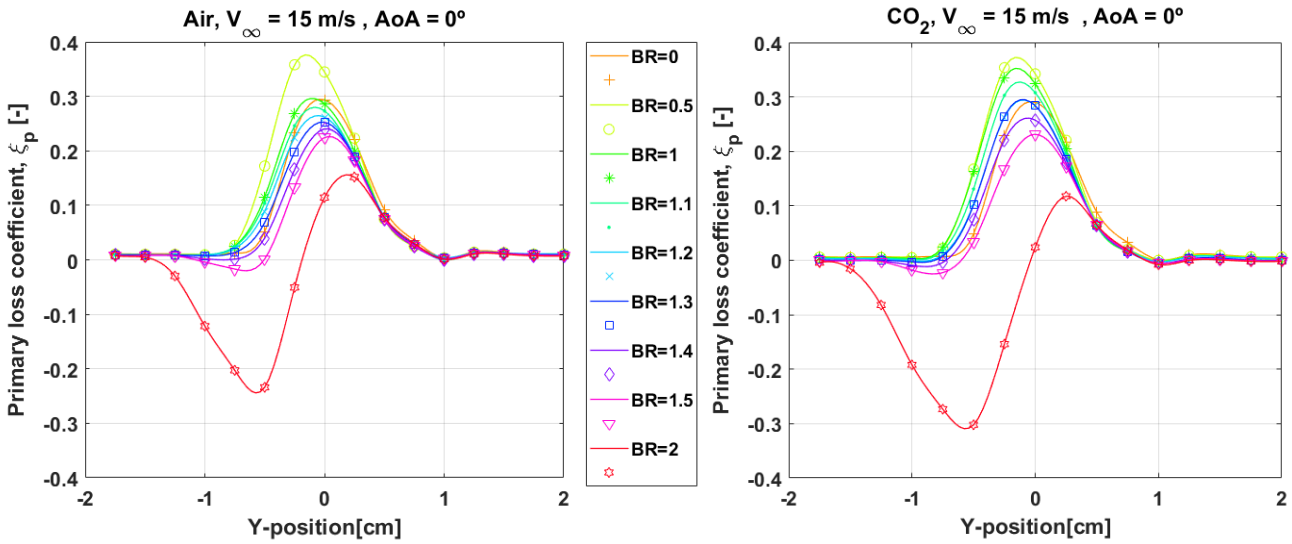

Figure 4.19. Wake primary loss coefficient for air (left) and CO_2 (right) for the baseline configuration, $V_\infty = 15\ m/s$ and AoA=0º.

We observe that a very similar wake flow pattern is obtained for both air and CO_2 as secondary flows, only minor changes are appreciated. These could even be due to the accuracy of the conversion factor to correct CO_2 volumetric flow through the flow controller or small fluctuations in the experimental setup and experimental conditions, although the test-to-test uncertainty and replicability between air

and CO_2 was minimized as much as possible as previously mentioned. This lack of information to draw relevant conclusions suggests that whole flowfield measurement techniques such as PIV should be used to observe further and clearer differences in the flow characteristics.

However, even if these changes are small, CO_2 injection shows lower energization of the flow. As presented in Table 4.9, the momentum deficit reached is similar and reached at $BR = 0.5$ in both cases. But for CO_2 the decrease in deficit and losses with increasing BR due to energization of the flow is less sensitive to raising BR and also the wake-to-jet shift occurs for higher BR ($BR_{air} = 1.4$ vs. $BR_{CO_2} = 1.5$). This could be explained by the lower coolant velocity and momentum of CO_2. Despite this lower energization for CO_2, the behaviour changes at $BR = 2$, for which the maximum momentum and aerodynamic gain is higher for CO_2. The width and displacement of the wake is similar for both coolants as well as the orders of magnitude of all the losses coefficients.

Baseline configuration		Air	CO_2
Maximum momentum deficit & losses	BR [−]	0.5	
	$V_{2,min}$ [m/s]	11.40	11.42
	$\xi_{p_{max}}$ [−]	0.38	0.37
Wake-to-jet shift	BR [−]	1.4	1.5
Maximum momentum gain and minimum losses	BR [−]	2	
	$V_{2,max}$ [m/s]	16.05	16.43
	$\xi_{p_{min}}$ [−]	-0.24	-0.31

Table 4.9 Summary of the maximum and minimum losses for the baseline configuration, including the BR at which they take place. Maximum and minimum losses are expressed using the wake velocity deficit and primary loss coefficient. For CO_2 injection, the wake-to-jet shift occurs for a slightly higher BR and the maximum aerodynamic gain is higher.

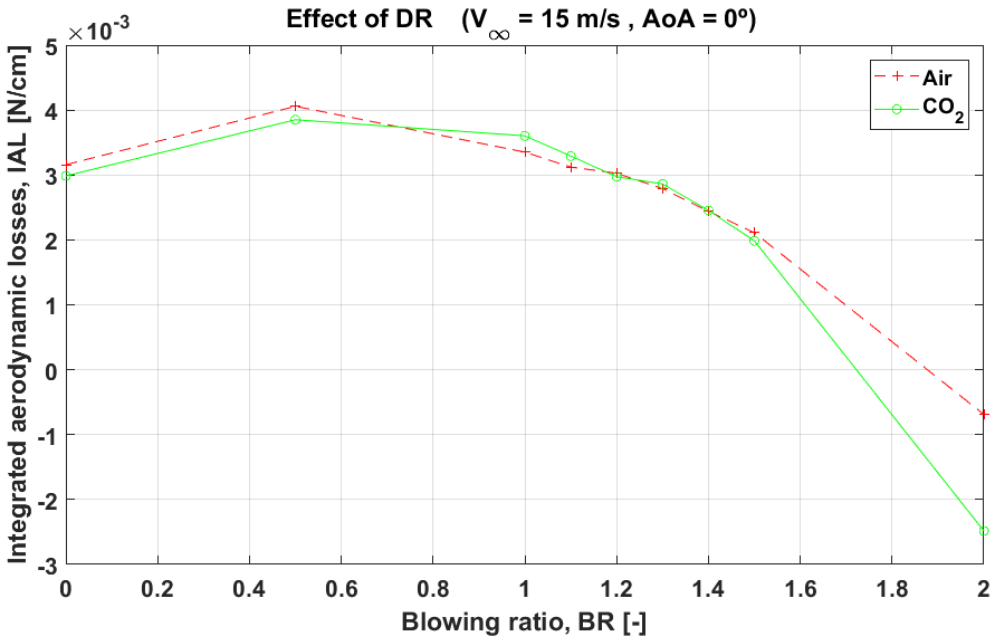

Figure 4.20 Effect of density ratio on integrated aerodynamic losses, IAL and on its sensitivity to BR for both air and CO_2, baseline configuration. The trend is similar and only differs for $BR = 2$.

Figure 4.20 shows the impact of density ratio on integrated aerodynamic losses, IAL. The trend of the area-averaged loss coefficient is the same as for IAL, as can be seen in Appendix III. This graph summarizes the behaviour: very similar behaviour for both fluids, with a slightly lower sensitivity to BR for CO_2 for low BR and higher only for $BR = 2$.

4.2.2. Effect of angle of attack

In this section, the effect of angle of attack on aerodynamic performance and its relationship with blowing ratio is analysed for the same freestream velocity, coolant mass flow and blowing ratios as in the baseline configuration.

To start with, Table 4.10 introduces an overview of the maximum and minimum momentum deficit and the BR at which these take place for each test configuration, comparing them between air and CO_2. Note that the behaviour at AoA= -10º corresponds to airfoil stall and this will be explained below. At AoA=10º, the general wake behaviour is as anticipated in Section 4.2: lower wake velocity values and higher sensitivity of pressure side injection to BR changes due to the local changes in geometry seen by the flow. The slight differences in wake flow between air and CO_2 are maintained, and also the lower sensitivity to BR at low BR but higher at $BR = 2$ for CO_2, providing a higher maximum flow energization and aerodynamic gain.

Effect of angle of attack		$\alpha = 0°$ (baseline)		$\alpha = +10°$		$\alpha = -10°$	
		Air	CO_2	Air	CO_2	Air	CO_2
Maximum momentum deficit & losses	$BR\ [-]$	0.5		0	0.5	0.5	1
	$V_{2,min}\ [m/s]$	11.4	11.42	8.51	8.38	6.94	6.95
	$\xi_{p_{max}}[-]$	0.38	0.37	0.66	0.67	0.7	0.77
Wake-to-jet shift	$BR\ [-]$	1.4	1.5	1.2	1.3	No shift	
Maximum momentum gain and minimum losses	$BR\ [-]$	2		2		-	
	$V_{2,max}\ [m/s]$	16.05	16.43	15.81	15.97	V_∞	
	$\xi_{p_{min}}[-]$	-0.24	-0.31	-0.20	-0.22	0	

Table 4.10 Summary of the maximum and minimum losses for each angle of attack configuration. The maximum and minimum losses are expressed using the wake velocity deficit and primary loss coefficient. General trends in wake flow due to higher angles of attack are the same as in Section 4.2. (lower wake velocities and higher sensitivity of pressure side injection to BR changes). As for the differences between air and CO_2 injection for $\alpha = 10°$, these are small but a similar trend to the baseline configuration is observed for CO_2: wake-to-jet shift at higher BR, lower sensitivity to BR at low BR and higher sensitivity at $BR = 2$.For $\alpha = -10°$, airfoil stall is detected.

Angle of attack AoA= 10°

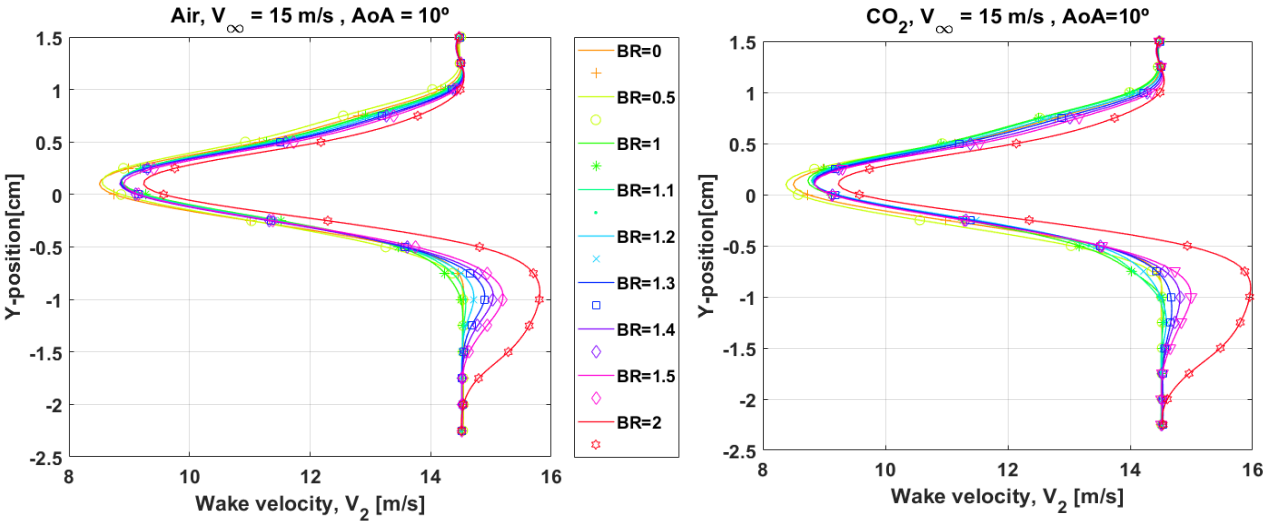

Figure 4.21. Wake velocity profile for air (left) and CO_2 (right) for AoA=10º, $V_\infty = 15\ m/s$

From the detailed wake velocity profile, we can also conclude that the wake width and vertical displacement is similar for both air and CO_2 When comparing the wake velocity profile with the baseline configuration, the lower wake velocity magnitudes and higher sensitivity to BR changes due to the change in angle of attack are noted, with the wake-to-jet shift occurring at lower BR. The wake-to-jet shift occurs for a lower BR for air, as a result of a lower flow energization of CO_2 as a coolant when matching BR between air and CO_2.This lower energization of the flow is reflected in the higher losses for CO_2 at low BR: this is observed for the primary loss coefficient and integrated aerodynamic losses below (Figure 4.22 and Figure 4.23). The of integrated aerodynamic losses with BR depicts a more visual representation of the higher losses of CO_2 injection, except for high blowing ratio ($BR = 2$). This difference in losses is more noticeable than for the baseline configuration.

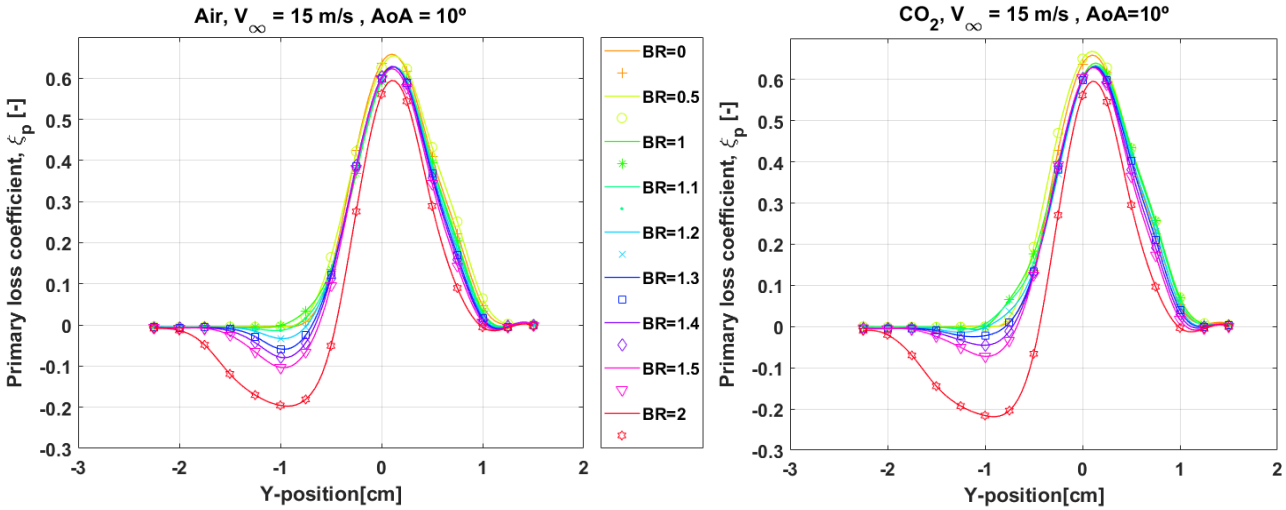

Figure 4.22 Wake primary loss coefficient for air (left) and CO_2 (right) for AoA=10°, $V_\infty = 15\ m/s$

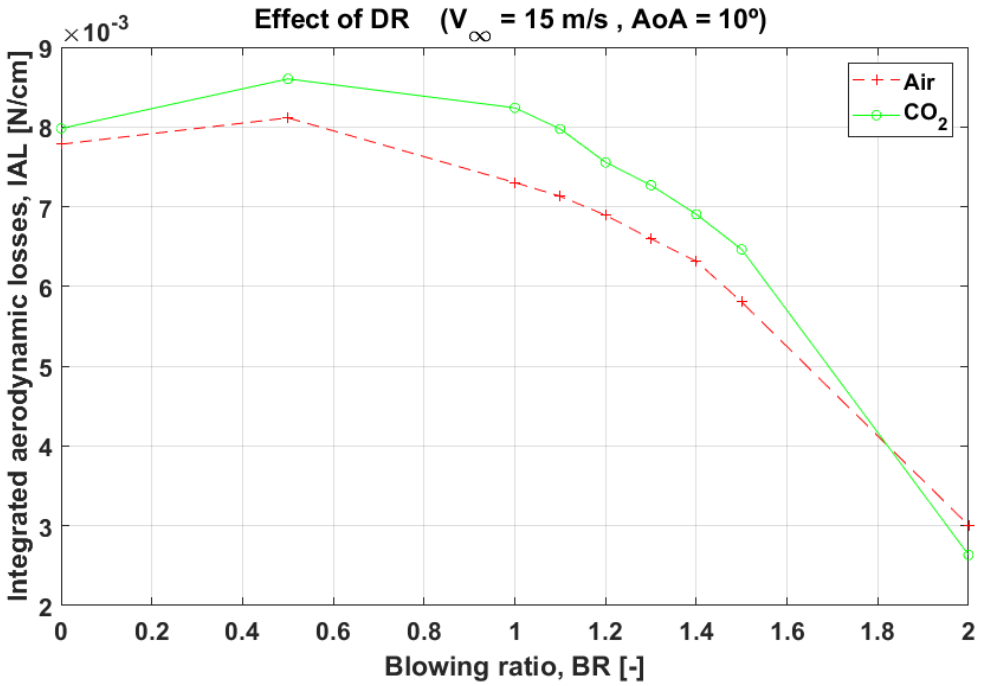

Figure 4.23. Effect of density ratio on integrated aerodynamic losses, IAL and on its sensitivity to BR for both air and CO_2, AoA=10°. The trend is similar and only differs for $BR = 2$.

Angle of attack AoA= −10°

As mentioned, this configuration is tested to simulate the impact of density ratio on suction side film cooling performance at high angle of attack. Due to the symmetry of the airfoil, suction side cooling performance at AoA=10º is equivalent to pressure side cooling performance at AoA= -10º. Since the holes in the test section to fix the model were conditioned to test pressure side cooling, maintaining this setup instead with a negative angle of attack is simpler than relocating the airfoil. As can be seen in Figure 4.24 and Figure 4.25, airfoil stall due to flow separation at high angles of attack occurs.

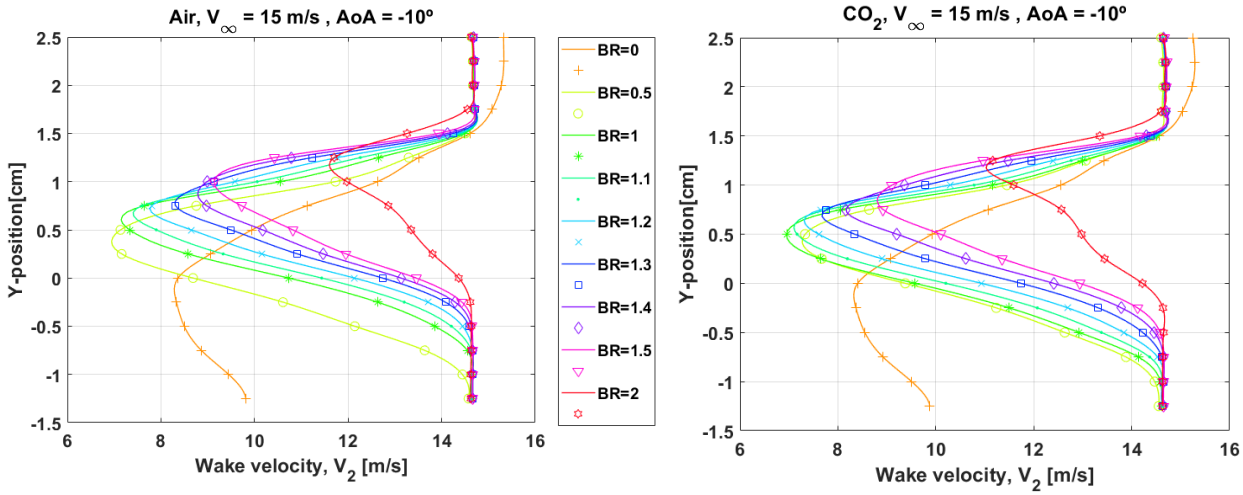

Figure 4.24 Wake velocity profile for air (left) and CO_2 (right) for AoA= -10º, $V_\infty = 15\ m/s$

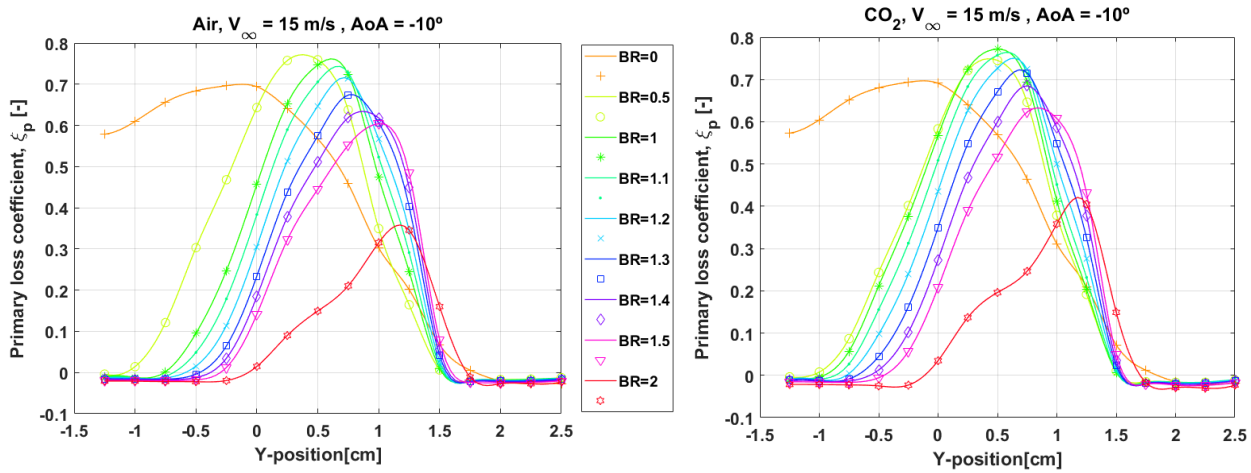

Figure 4.25 Wake primary loss coefficient for air (left) and CO_2 (right) for AoA= -10º, $V_\infty = 15\ m/s$

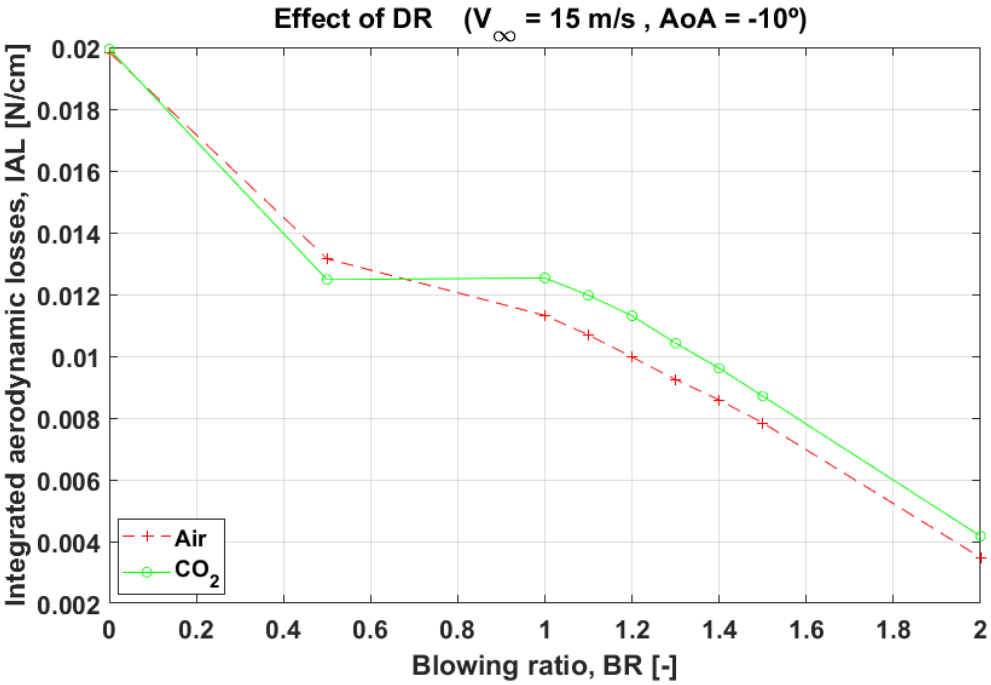

Figure 4.26. Effect of density ratio on IAL and on its sensitivity to BR for both air and CO_2, AoA=-10º.

Some observations can be extracted from the figures above:

- Stall is visible in the wake velocity and primary loss coefficient profiles in the form of a very wide wake at $BR = 0$, due to flow separation at high angles of attack with a very upstream separation point.
- This airfoil stall was also observed in the work of (Lanzillotta, et al., 2017) for AoA=10º with the cooling holes located in the suction side. A wide wake was observed in the suction side for $BR = 0$.
- This same behaviour should have been observed in the suction side in all the test cases at AoA=10º discussed above, even with the cooling holes in the pressure side since stall occurs for no injection (i.e. $BR = 0$). An explanation for this is that the pressure losses and flow separation caused by the surface roughness solely induced by the presence of the holes (without injection) triggers stall. This could explain why for the smoother surface without cooling holes stall does not take place. Another possible explanation could be that the opposite angles of attack (i.e. AoA=10º and AoA=-10º) are not exactly symmetrical, so the local flow seen by the airfoil slightly changes, thus inducing a measuring error.
- For the test case with AoA= -10º at $BR = 0.5$, during the instantaneous data acquisition process the differences between air and CO_2 became more apparent: for CO_2, the stalled region reattached earlier in time than for air. The explanation for this can be the lower momentum of CO_2, which reduces the blowing-induced flow separation at low BR. This suggests that unsteady measurements would be useful to understand better the differences between air and CO_2 behaviour.

4.2.3. Effect of scaling parameter: momentum flux ratio

In this section, the variation of losses with BR and I scaling parameters is analysed for both air and CO_2 injection. Table 4.11 presents an overview summary of maximum and minimum losses and loss-to-gain shift. Figure 4.27 shows the comparison for integrated aerodynamic losses, and the same behaviour is observed for the area-averaged loss coefficient (included in Appendix III).

Effect of scaling parameter (baseline configuration)		BR as scaling parameter		I as scaling parameter	
		Air	CO_2	Air	CO_2
Maximum losses	Value of scaling parameter [-]	0.5		0.25	0.16
	$IAL_{max} \cdot 10^3$ $[N/cm]$	4.1	3.9	4.1	3.9
	λ_{max} [-]	0.09	0.08	0.09	0.08
Loss-to-gain shift		> 1.8	< 1.8	3.5	2
Maximum gain	Value of scaling parameter [-]	2		4	2.6
	$IAL_{min} \cdot 10^3$ $[N/cm]$	-0.7	↑ -2.5	-0.7	↑ -2.5
	λ_{min} [-]	-0.01	↑ -0.05	-0.01	↑ -0.05

Table 4.11 Summary of the maximum and minimum losses for the baseline configuration as a function of BR or I, including the value of the scaling parameter at which they take place. Maximum and minimum losses are expressed using integrated aerodynamic losses, IAL and area-averaged loss coefficient, λ. Results show higher aerodynamic gain for CO_2 injection and a higher variation of aerodynamic losses with CO_2, with the loss-to-gain shift taking place at lower momentum flux ratio.

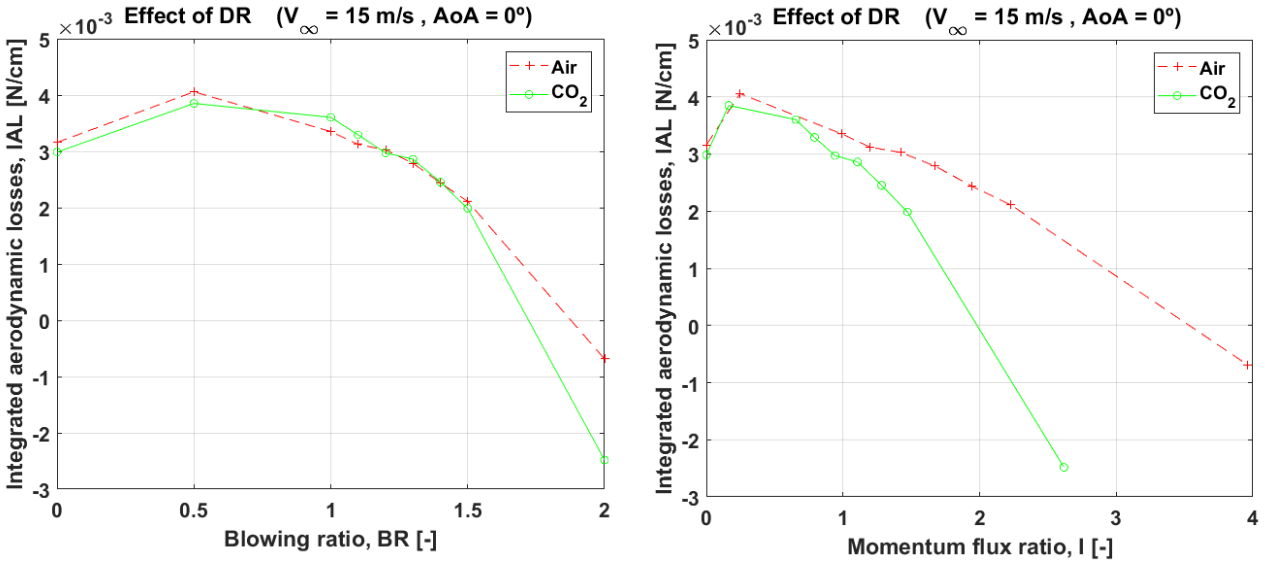

Figure 4.27 Comparison of the variation of integrated aerodynamic losses, IAL with BR (left) or I (right) as coolant flow scaling parameters for the baseline configuration.

When studying the variation of losses with momentum flux ratio I, the results show the lower momentum flux ratio for CO_2 than for air when matching blowing ratio in the experiments (see Table 4.7 at the beginning of this section). Since for the same blowing ratio, the momentum flux ratio of CO_2 is lower than that of air, the similar level of losses of air and CO_2 obtained before now diverges and the variation of losses with momentum flux ratio is greater for CO_2 than for air. Therefore, the aerodynamic gain (i.e. $IAL < 0$) occurs significantly earlier for CO_2 than for air. This higher variation of IAL with momentum flux ratio is also observed for the tests at AoA=10º and AoA=-10º (included in Appendix III).

A general conclusion can be drawn here, although more and different tests would be needed to understand flow structures: due to the lower momentum of CO_2, jet lift-off occurs at a higher BR for CO_2 and this postpones the coolant intrusion into the mainstream flow and mixing processes, reducing aerodynamic losses and leading to a higher aerodynamic gain when using CO_2. This means that when studying only aerodynamic performance without heat transfer between the mainstream and the coolant, flow injection with $DR > 1$ (i.e. closer to gas turbine application, with a temperature ratio $TR < 1$) has lower aerodynamic losses than air. This could mean that testing with $DR = 1$ is conservative to analyse aerodynamic performance with respect to the real gas turbine cooling application.

Obviously, the thermal performance needs to be assessed to understand how accurately foreign gas injection replicates the difference in temperature between the coolant and the mainstream flows and to check if the same aerodynamic performance is obtained when inducing a temperature ratio by heating the mainstream or cooling the secondary flow. Additionally, it would be interesting to repeat the tests with CO_2 matching a different scaling parameter such as I or VR and see the differences in aerodynamic losses. Finally, as mentioned before, visualization of formed flow structures and jet trajectory recorded with whole field flow measurement techniques rather than only pointwise measurements at the specific wake location would be of major help to understand the effect of DR on aerodynamic performance. As stated in Chapter 2, the effect of DR on aerodynamic performance of film cooling is an open discussion in the research community with limited agreement, so more exhaustive tests should be devoted to draw solid conclusions.

4.3. Uncertainty analysis

During the pressure measurements tests, there are sources of error affecting the experimental results to be quantified. Some of them, the systematic error sources, produce the same error in each measurement. In the pressure measurements setup, some of them could be: the angle of attack of the airfoil when fixed to the test section, a consistent misalignment of the pressure rake channels with respect to mainstream flow direction or a consistent inclination of the windtunnel total-static pitot probe with respect to mainstream flow direction. The other type of error sources are the random ones, which vary within the measurement period. They can be due to changes in ambient conditions, windtunnel vibrations, errors in the sealing of the cooling holes and other random fluctuations affecting the pressure measurement results. Random errors can be split in two types: maximum errors, associated to equipment accuracy or sensitivity level and statistical errors, associated to fluctuations of the results even when measured with the same instrument.

The uncertainty analysis provides an interval in which the error is included with a certain confidence level. Table 4.12 presents the uncertainty analysis for the results of interest in Chapter 4. Since these quantities are not directly measured but derived from directly measured quantities, an uncertainty propagation mechanism is used to derive the uncertainty, u_F associated to a function, F of multiple independent variables, x_i (equation 4.1). This expression of uncertainty only accounts for the random measurement errors and is valid when assuming normal distribution of all the independent variables and the result.

$$u_F = \left[\sum_i \left(\frac{\partial F}{\partial x_i}\right)^2 \cdot {u_{x_i}}^2\right]^{1/2} \tag{4.1}$$

Table 4.12. Uncertainty analysis of the pressure measurements results

Parameter	Typical value	Absolute uncertainty	Relative uncertainty
Blowing ratio, BR	1	$2.71 \cdot 10^{-3}$	0.27 %
Wake velocity, V_2	10	$1.48 \cdot 10^{-2}$	0.15 %
Primary loss coefficient, ξ_p	10^{-1}	$4.04 \cdot 10^{-4}$	0.4 %
Local total pressure loss coefficient, C_p	10^{-4}	$7.1 \cdot 10^{-8}$	0.071 %
Total pressure loss coefficient, C_{p_t}	10^{-1}	$1.15 \cdot 10^{-3}$	1.15 %
Area averaged loss coefficient, λ	10^{-2}	$3 \cdot 10^{-4}$	0.03 %

4.4. Chapter remarks

From the test results and discussion in Chapter 4, we can draw the following general conclusions:

- Pointwise pressure measurements were conducted by means of a pressure rake at a downstream location of the airfoil to understand wake flow characteristics when injecting different rates of secondary flow.

- Aerodynamic losses have been evaluated by computing: primary loss coefficient, local total pressure loss coefficient, total pressure loss coefficient, integrated aerodynamic losses and area-averaged loss coefficient with and without pressure losses.

- The wake flowfield pattern and aerodynamic performance is directly related to the momentum of the injected secondary flow with respect to the momentum of the mainstream flow. For low momentum injected air, mixing losses predominate and the injection of secondary flow produces aerodynamic losses. After a certain blowing ratio in which the injected flow has already a higher momentum than the mainstream flow, the energizing effect is higher than the mixing losses and jet spreading with aerodynamic gain is produced in the region close to secondary flow injection. In this study, the airfoil´s pressure side.

- When no injection takes place at AoA=0º, the wake is symmetrical, and the roughness induced by the presence of the holes adds up to the airfoil's profile losses.

- For the baseline configuration with air injection (i.e. $DR \sim 1$), maximum wake momentum deficit and losses occur for $BR = 0.5$, wake-to-jet shift for $BR = 1.4$ and aerodynamic gain with jet spreading in the pressure side increases and becomes maximum at $BR = 2$, the highest tested blowing ratio. Vertical wake displacement occurs as a result of the change in exit flow angle. The maximum displacement of the wake towards the pressure side occurs at $BR = 1$.

- When increasing the angle of attack, the wake profile is no longer symmetrical for $BR = 0$, profile losses and maximum momentum deficit increase and the wake width decreases. Sensitivity to BR increases for pressure side injection, leading to an earlier wake-to-jet shift.

- When increasing the freestream velocity, profile losses increase, the wake width decreases, and the average wake velocity and losses coefficients values increase. The wake flow pattern and effect of low BR injection is similar to the baseline configuration case. The effect of high BR injection cannot be studied due to experimental limitations in the maximum flow rate of the flowcontroller used. Therefore, the wake-to-jet shift is not detected.

- When studying the effect of individual rows or partial injection, the sensitivity to BR changes is lower than for total injection and superposition principle does not apply. Lower losses and higher energization are obtained for injection from the fourth row of holes PS4, the only injection location which is downstream of the maximum thickness point of the airfoil and closer to the separation point and downstream measurement location. Maximum losses are obtained for PS2 location. A higher measurement resolution for P_c/P_∞ at the exit of the holes could enable a better understanding and conclusions about each individual row behaviour.

- When studying the effect of density ratio (i.e. $DR > 1$) on aerodynamic performance using CO_2 gas injection, blowing ratio was matched, meaning that the velocity ratio and momentum flux ratio are lower for CO_2, so jet lift-off is postponed for CO_2. Slight differences are visible in the wake flow characteristics, although the lower momentum of CO_2 injection could be visible at low BR. Because of the lower momentum flux ratio of CO_2, the sensitivity of losses to I variation is higher for CO_2 than for air. For AoA=-10º, airfoil stall is detected. This topic begs a deeper analysis: whole flowfield measurements and flow visualization as well as matching different scaling parameters or inducing coolant-to-mainstream density ratio with a heating system could provide a more solid approach and further insight.

5

PIV results

5.1. Planar PIV: Global flowfield

In this section, the results for the global flowfield setup are introduced. Note that to eliminate the areas with too low or too high illumination, the images have been cropped, so the presented fields of view are lower than the original ones from the raw images presented in Table 5.1.

Baseline configuration: effect of blowing ratio

Figure 5.1 compares the axial component of the average velocity, V_x normalized by the freestream velocity for the cases with $BR = 0$ and $BR = 2$. Note that the dark blue area close to the trailing edge (encircled) is due to the reflections of the holes drilled in the test section to fix the airfoil at different angles of attack. The white areas correspond to the regions where the mask is applied, and the velocity field is not computed.

By comparing the axial velocity contour plots in the pressure side region, we observe the energization of the flow due to pressure side injection ($\sim 10\%$ higher velocity magnitude). In the wake region, what predicted in Chapter 4 is confirmed: at high blowing ratios, the wake shrinks and is shifted towards the suction side due to a local jet behaviour that energizes the flow and avoids flow separation.

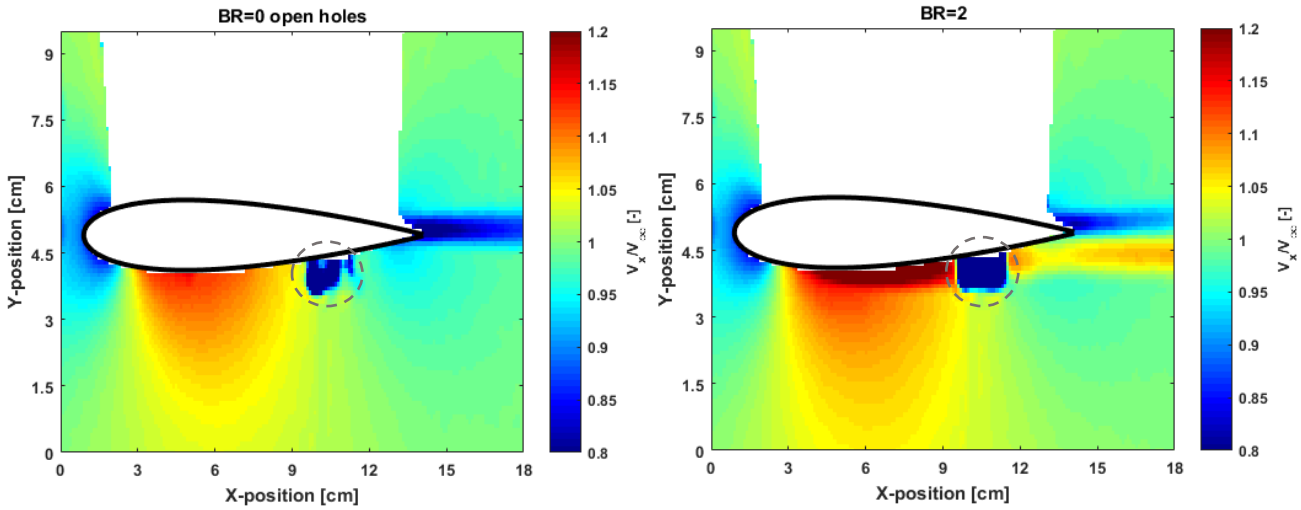

Figure 5.1 Effect of secondary flow injection on the average axial velocity component for the baseline configuration between BR=0 with open holes and BR=2.Note that the (encircled) dark blue area close to the trailing edge is due to the reflections of the holes drilled in the test section to fix the airfoil at different angles of attack and does not represent a physically lower velocity region.

Effect of angle of attack, freestream velocity and partial injection

Figure 5.2 shows the global flowfield at a higher angle of attack (AoA=5º and AoA=10º) for the maximum blowing ratio, $BR = 2$. We observe an asymmetric flowfield. At the leading edge, a high velocity region appears in the suction side and a low velocity region in the pressure side. This effect is higher for a higher angle of attack. The streamlines at the wake are bent and the velocity deficit at the wake is lower than for the baseline configuration. In this global flowfield configuration, the energization of the flow due to coolant injection at high BR is only observed downstream of PS1, PS2 and PS3, i.e. $x/c > 0.15$.

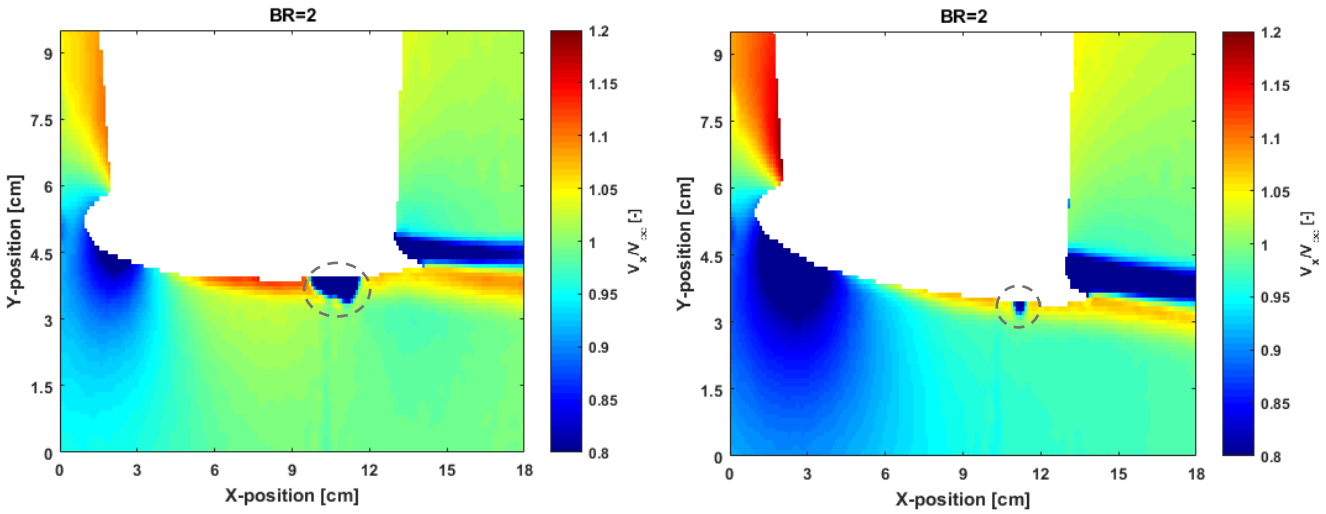

Figure 5.2 Effect of secondary flow injection on the average axial velocity component for $BR = 2$ with higher angles of attack (AoA=5º and AoA=10º). Note that the (encircled) dark blue area close to the trailing edge is due to the reflections of the holes drilled in the test section to fix the airfoil at different angles of attack and does not represent a physically lower velocity region.

As for the cases with a higher freestream velocity or partial injection, no big differences are observed in the flowfield patterns to draw relevant conclusions. The results can be found in Appendix IV.

5.2. Planar PIV: local flowfield

In this section, the results for the local flowfield setup at a location between PS3 and PS4 are presented. Note that to eliminate the areas with too low or too high illumination, the images have been cropped, so the presented fields of view are lower than the original ones from the raw images presented in Table 5.1.

Baseline configuration: effect of blowing ratio

Figure 5.3 presents the changes on the local flowfield with blowing ratio, which provides some information about the mixing shear layer.

For low blowing ratios, the mixing shear layer presents lower velocity than the freestream and increases in thickness as blowing ratio increases. The low momentum coolant is attached to the surface and the velocity increases for locations further away from the surface. At $BR = 0.9$, which corresponds to $I > 0.8$ (i.e. jet lift-off expected) there is a change in the behaviour as we can see a higher entrainment of the secondary flow into the mainstream. The minimum velocity is now found in the central region of the shear layer and the velocity increases next to the airfoil surface. For $BR =$

1.1 and $BR = 1.2$, local jet behaviour starts to be detected and for $BR > 1.3$ the local flowfield has a higher velocity than the mainstream flow at every point of the mixing layer. As the blowing ratio increases, the energization of the flow becomes more intense, affecting a larger region of the flowfield (both in x and y directions), increasing the magnitude of axial velocity. Since the jet is detached already and is more curved towards the mainstream, the velocity reaches its maximum value in the central part of the jet and the energization effect is lower close to the model´s surface.

Note that for BR=2 there is a low velocity (dark blue) region which does not have any physical explanation, but is an artefact of the measurement system. Since no seeding is applied to the coolant flow, this faulty region is due to the lack of signal caused by the absence of particles in the coolant flow. To avoid this, introducing seeding in the secondary flow could be considered for future experiments.

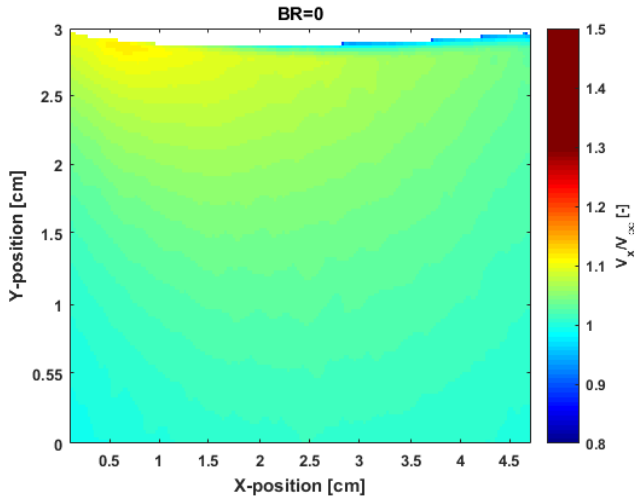

BR=0

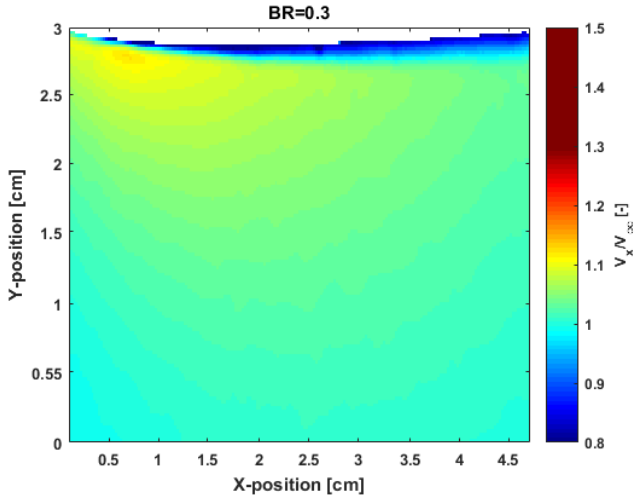

BR=0.3

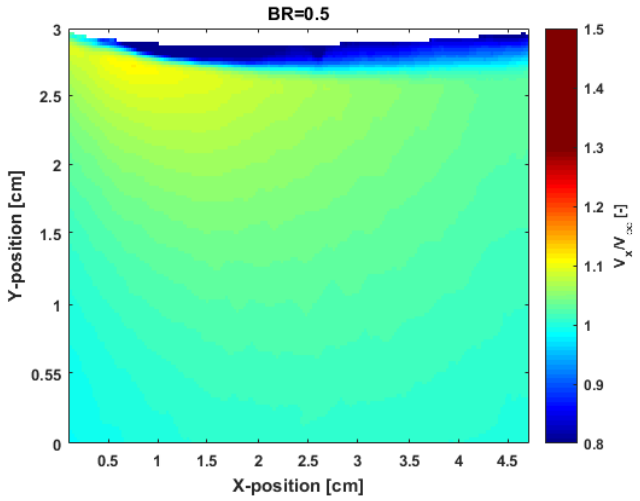

BR=0.5

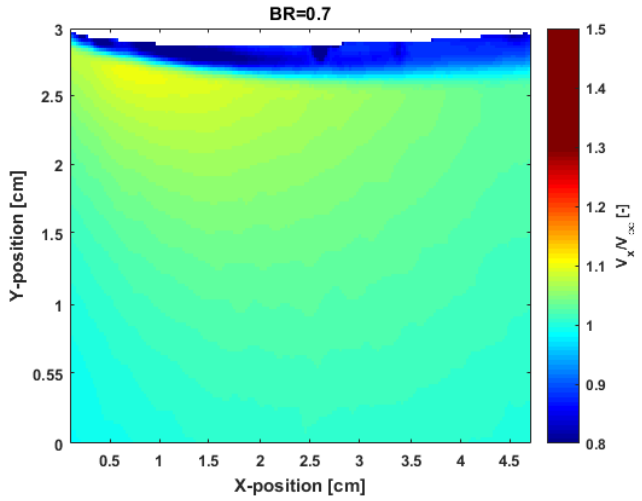

BR=0.7

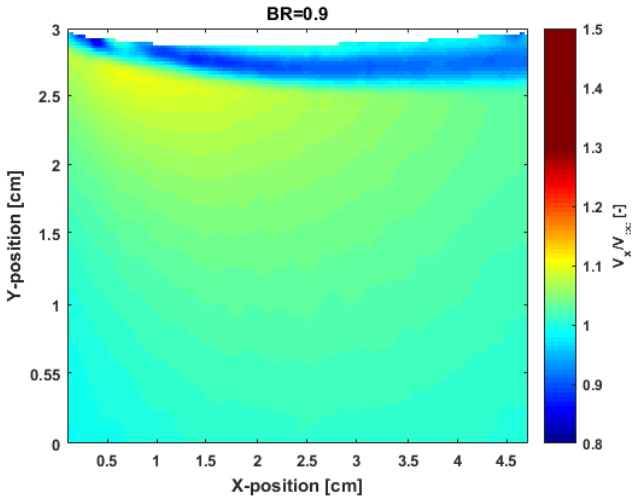

BR=0.9

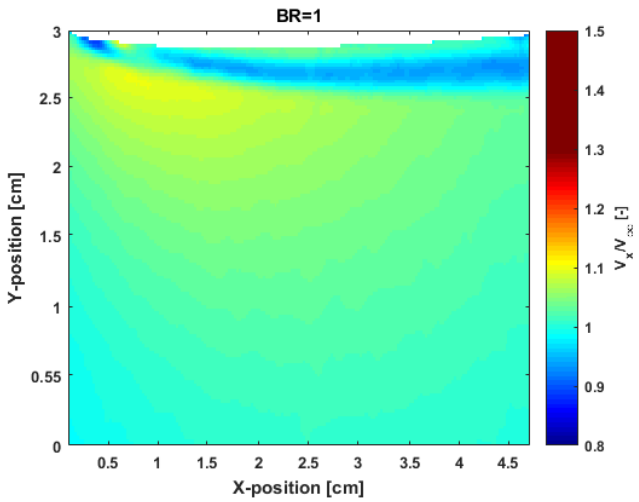

BR=1

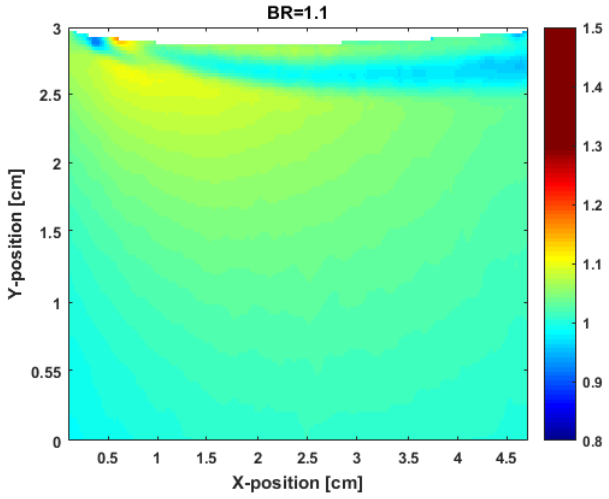

BR=1.1

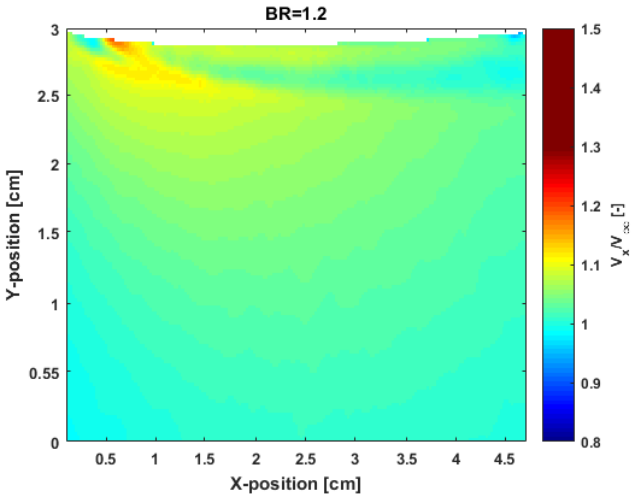

BR=1.2

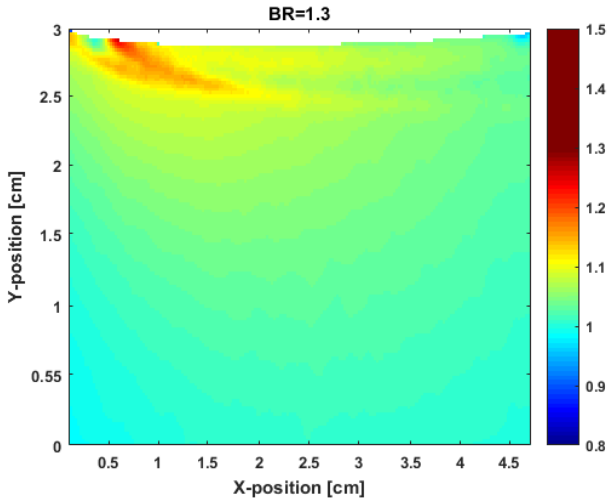

BR=1.3

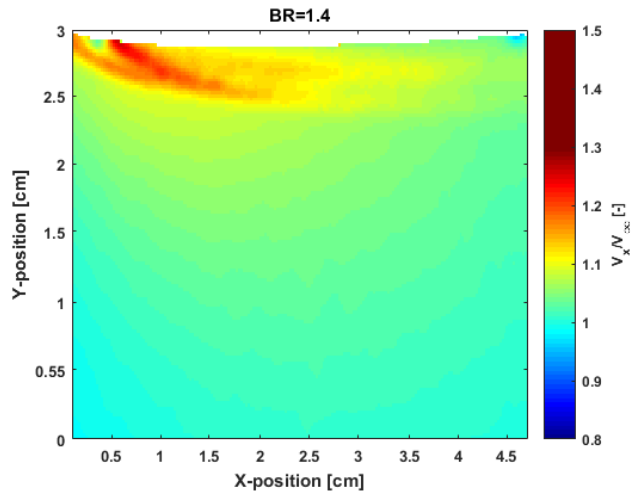

BR=1.4

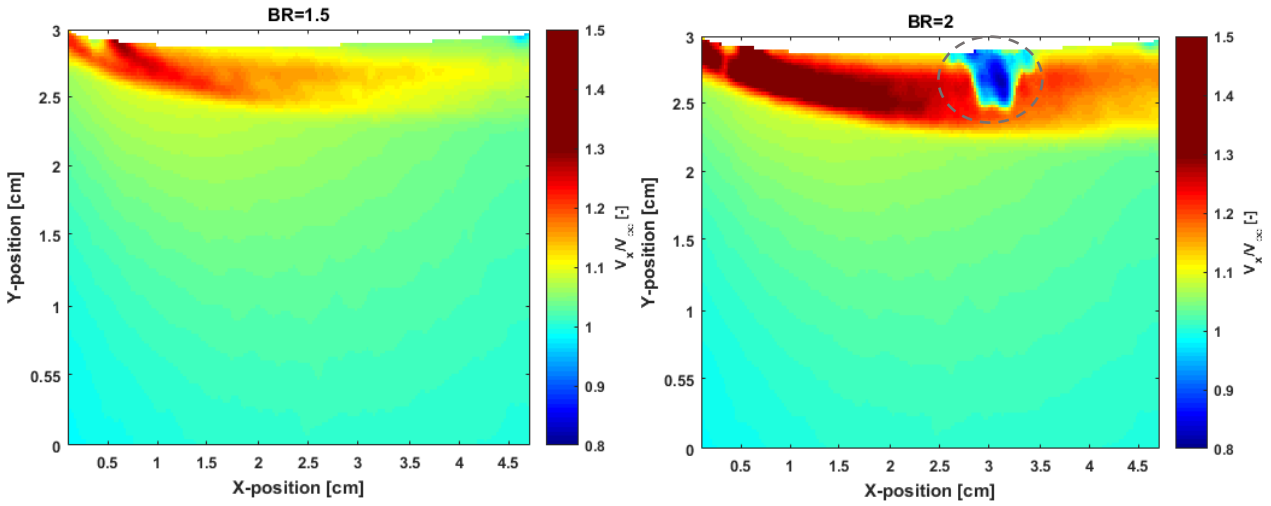

Figure 5.3 Effect of blowing ratio on the local flowfield. Note that for BR=2, the (encircled) blue region encountered in the mixing shear layer does not represent a lower physical velocity, but is due to the lack of signal caused by the absence of seeding particles in the coolant flow.

5.3. Comparison with pressure measurements results

To compare the PIV results with the pressure measurement results, the velocity at the location of the pressure rake is extracted from the global flowfield PIV results. We can observe the similarities when compared to Figure 4.3. The minimum momentum deficit occurs for BR=0.5 and the jet behaviour is observed for BR > 1.5. The wake is also displaced towards the pressure side, except for BR=2 for which it is shifted towards the suction side due to the jet spreading. The peak of the momentum deficit for BR=0.5 has a similar value than for the pressure measurements results, but the maximum momentum gain is lower in the PIV reconstructed data.

Blockage effect due to the windtunnel walls is observed in the freestream velocity. The reason why this effect is so visible in the PIV reconstructed data and not in the pressure measurements results is that the measurement region exposed to freestream flow is double the size (note $y \in (-4.4)cm$ for PIV and $y \in (-2,2)\ cm$ for pressure measurements). Therefore, there are not enough freestream velocity data points from pressure measurements to detect blockage effect.

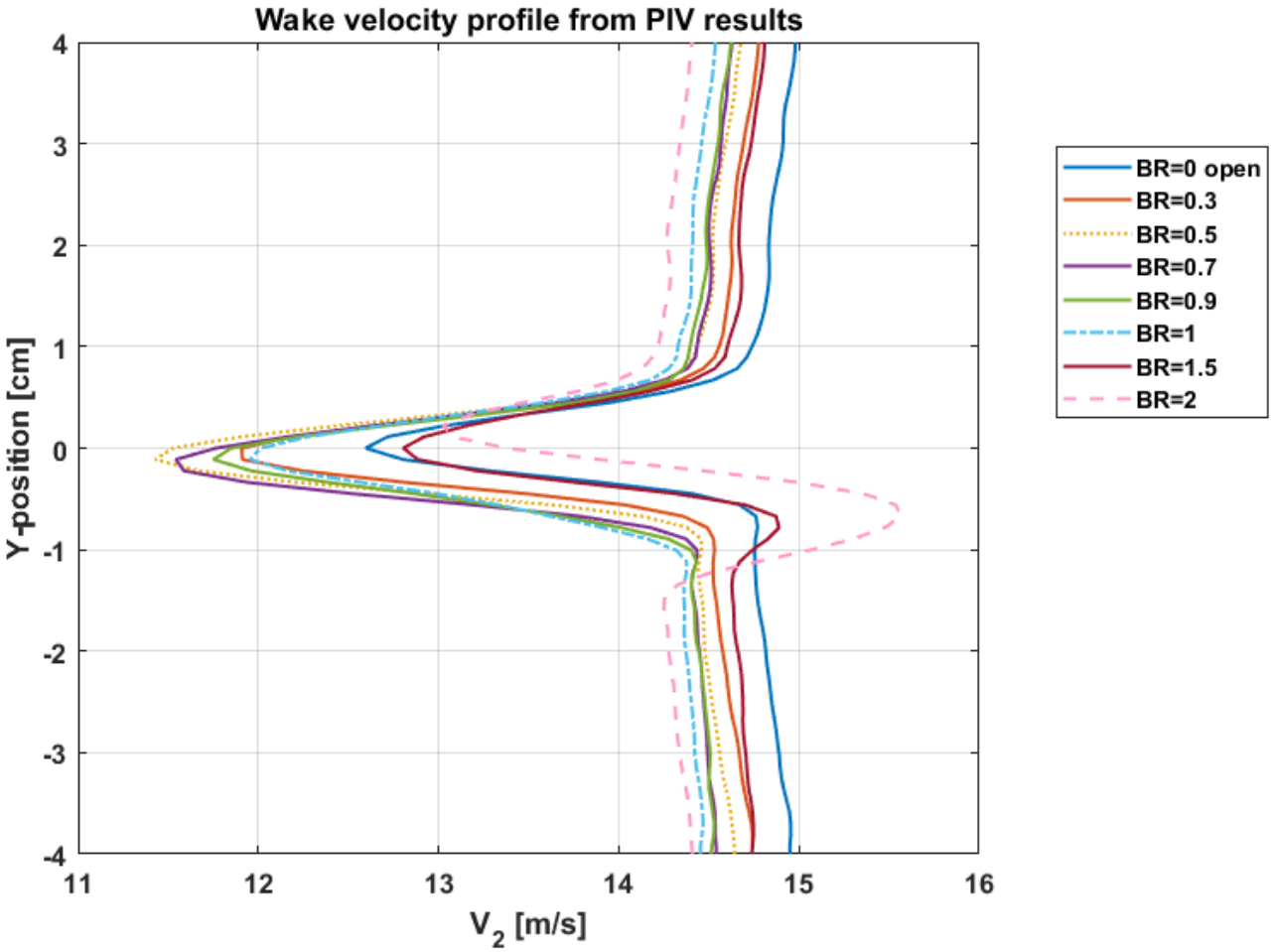

Figure 5.4 Wake velocity profiles for different blowing ratios extracted from the PIV data at the location of the pressure rake, x=1.25·c

5.4. Stereo-PIV

From all the stereo-PIV results, Figure 5.5 presents the streamwise velocity, V_z for BR=2 at the six streamwise measurement locations. This depicts how the jet in crossflow due to the interaction between mainstream and secondary flows evolves closer and further away from the injection locations. Note that the original images are cropped, so only 10 film cooling holes are captured in the field of view.

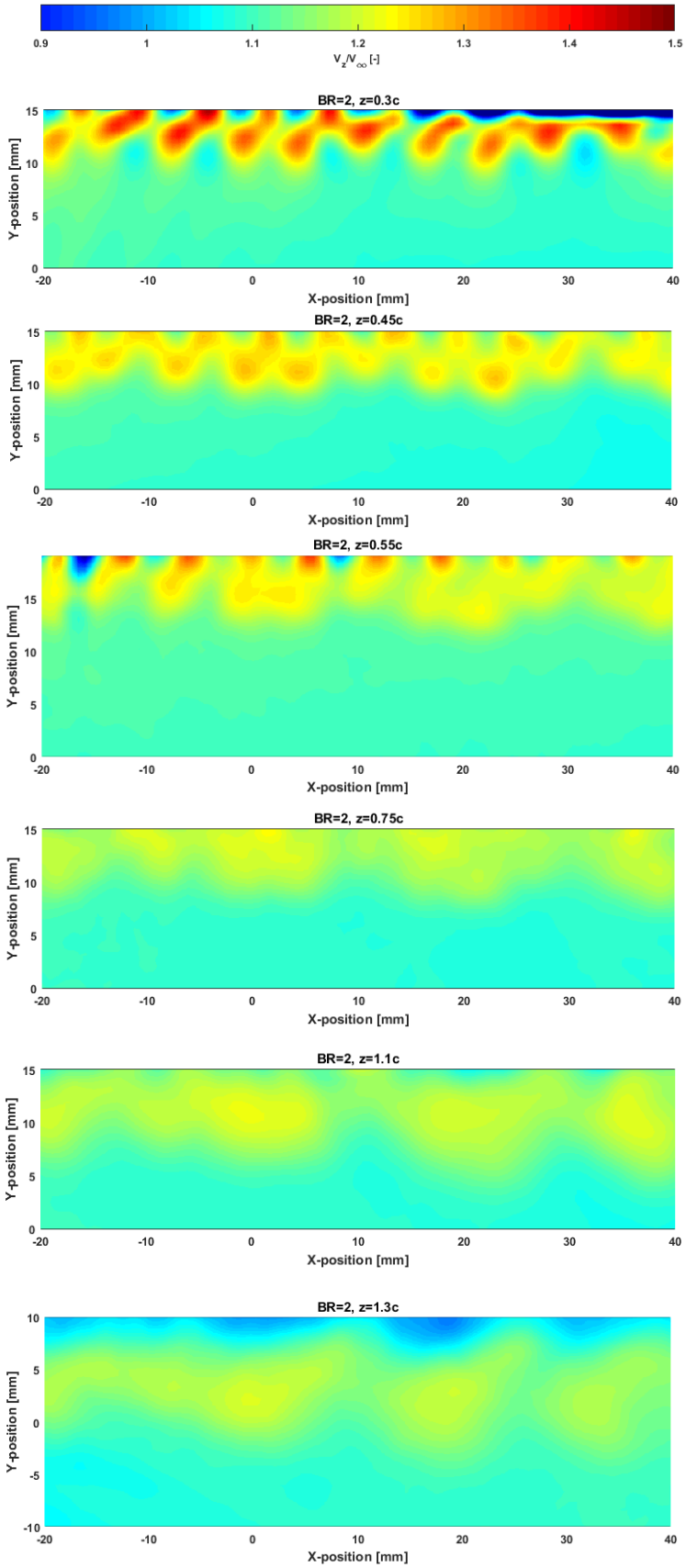

Figure 5.5 Evolution of the jet in crossflow for BR=2 at the measured streamwise locations

At the further upstream locations (i.e. z = 0.3c, z = 0.45c and z = 0.55c) the region affected by the mixing of the mainstream and secondary flows is smaller and the jet in crossflow structure is more defined. At z = 0.3c, the magnitude of velocity is higher because this location is affected by the injection from PS1, PS2 and PS3 rows of holes. The jet diffuses and its velocity is reduced, as observed for z = 0.45c upstream of PS4 and increases again at z = 0.55c, after injection from PS4.

At the further downstream locations (i.e. z = 0.75c, z = 1.1c and z = 1.3c) the region affected by the mixing of the mainstream and secondary flows is significantly bigger, the flowfield structures are less defined and the velocity magnitude is lower. The detachment of the jet is visible, since the mixing region is displaced further away from the surface and a low velocity region is observed immediately next to the airfoil´s surface for z = 1.1c and z = 1.3c.

Figure 5.6 and 5.7 show the effect of blowing ratio and angle of attack at one specific location, z =1.3c. When increasing the angle of attack, the mixing shear layer is displaced downwards due to the airfoil´s downwash. When increasing blowing ratio, the velocity magnitude increases and the mixing shear layer increases in size.

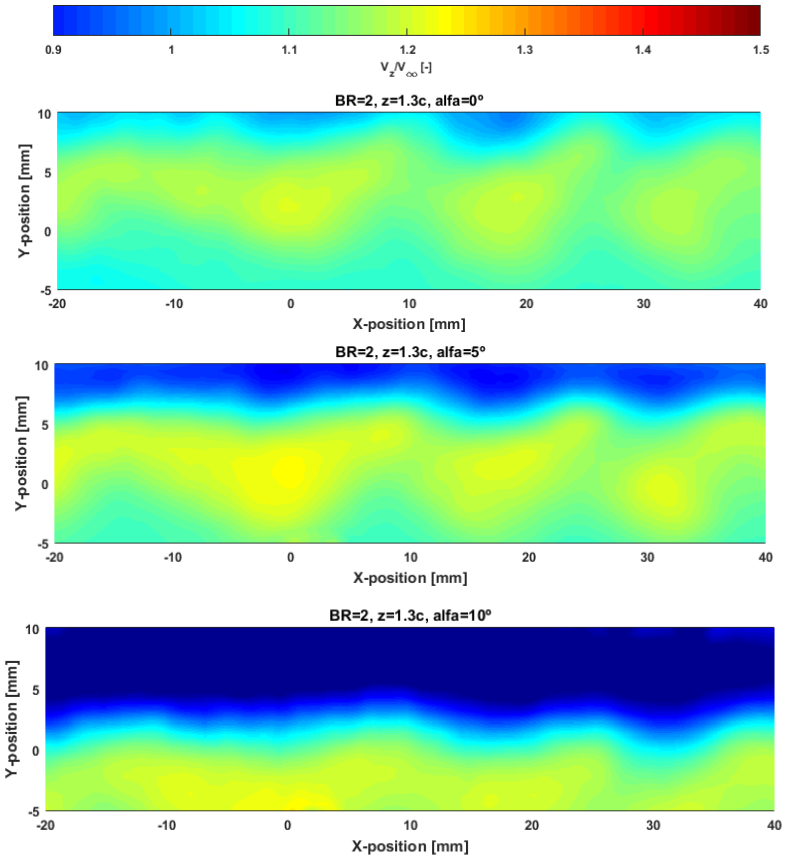

Figure 5.6 Effect of angle of attack on the streamwise flowfield at z=1.3c and BR=2

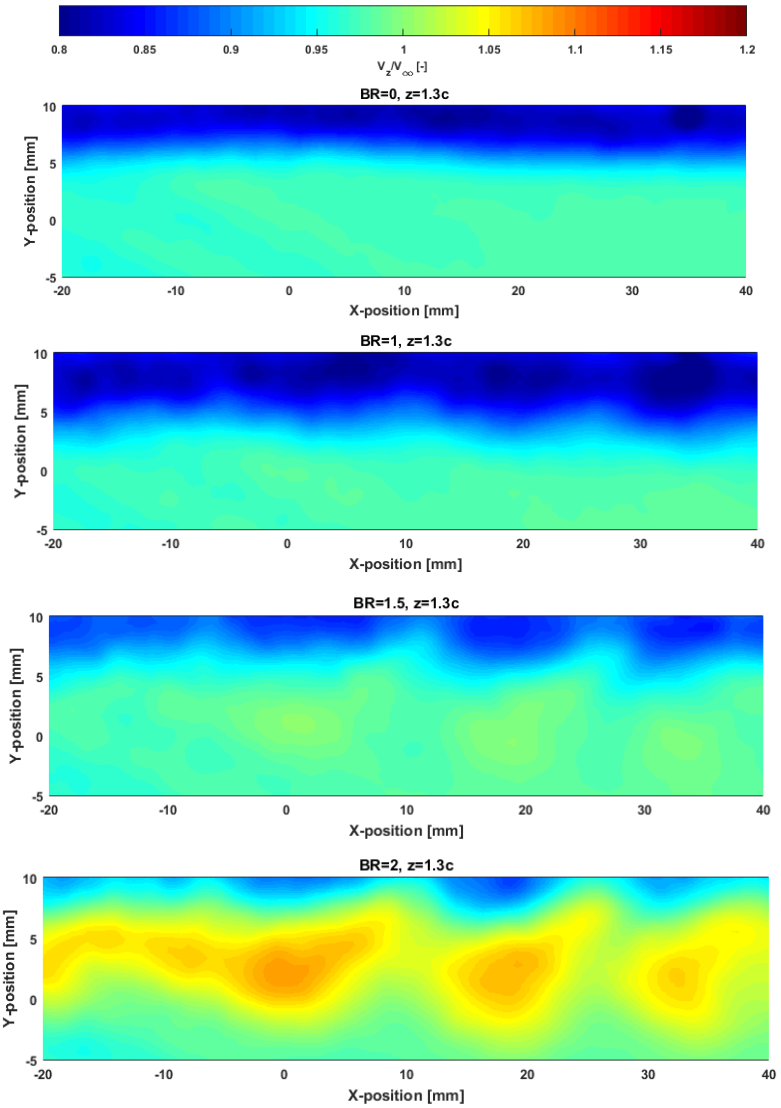

Figure 5.7 Effect of blowing ratio on the streamwise flowfield, z=1.3c, alfa=0º

5.5. Uncertainty analysis

During the PIV experiments, the sources of error affecting the resulting velocity field can be associated with changes in seeding particles density, laser misalignment, scratches and holes in the test section, reflections from the light sources, vibrations of the windtunnel transmitted to the laser or cameras and changes in the testing conditions, among others.

In this section, the focus is placed on the random statistical errors which describe the intrinsic fluctuations in the measured velocity, providing information about flow turbulence. With the standard deviation calculated during PIV processing and using a coverage factor $k = 2$ (95% confidence level), the error associated to PIV measurements, δ_{PIV} can be expressed as in equation 5.1, where N represents the number of image pairs acquired for each configuration ($N = 400$)

$$u_{PIV} = \frac{2 \cdot \sigma}{\sqrt{N}} \tag{5.1}$$

Figure 5.8 presents the standard deviation of the axial velocity for the global flowfield configuration and Figure 5.9 for the local flowfield configuration for different blowing ratios.

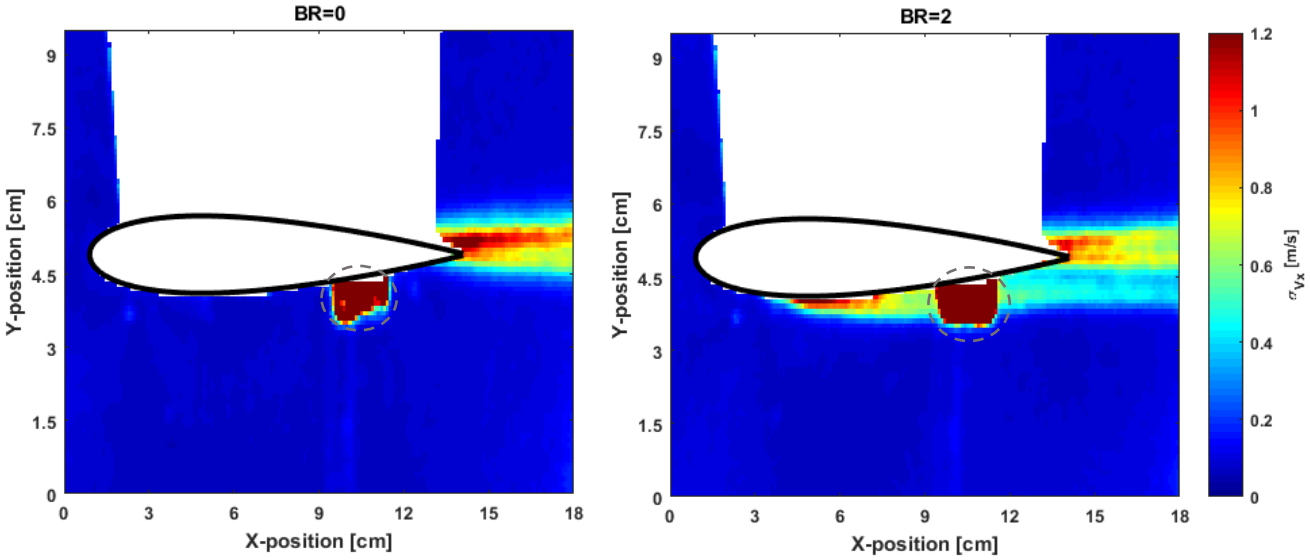

Figure 5.8 Standard deviation of the axial velocity, σ_{V_x} at BR=0 (left) and BR=2 (right) for the global flowfield configuration. Note that the (encircled) dark red area close to the trailing edge is due to the reflections of the holes drilled in the test section to fix the airfoil at different angles of attack.

The magnitude of the fluctuations is lower in the freestream flow and higher in the wake and in the shear layer between the freestream and the wake. This is due to the higher shear stresses and turbulence present in these regions, which lead to higher fluctuations. For the freestream flow region, $\sigma_\infty = 0.08\ m/s$, leading to an uncertainty $u_{PIV_\infty} = 0.008\ m/s$. For the central part of the wake, $\sigma_2 = 1.2\ m/s$, leading to an uncertainty $u_{PIV_2} = 0.12\ m/s$. For the case with BR=2, a higher standard deviation is present in the area close to the holes (downstream of PS1, PS2 and PS3), again due to the higher shear stresses and local mixing which increase turbulence production and flow velocity fluctuations.

The effect of local flow mixing near the holes when increasing blowing ratio is more clearly observable in Figure 5.9. Results show that magnitude of the fluctuations is the highest for BR=0.5 and for BR=2, the two cases in which the difference in velocity between the mainstream and the secondary flows is the highest. The fact that the fluctuations are higher for BR=0.5 than for BR=1 shows that they are associated to the difference in velocity between the two flows rather than to the amount of injected coolant.

For BR=0.5, the maximum fluctuation close to the cooling holes is $\sigma_{BR=0.5} = 3.8\ m/s$, which translates into an uncertainty $u_{PIV_{BR=0.5}} = 0.38\ m/s$. For BR=2, the maximum fluctuation close to the cooling holes is $\sigma_{BR=2} = 4.4\ m/s$, which translates into an uncertainty $u_{PIV_{BR=2}} = 0.44\ m/s$. For the freestream flow region, $\sigma_\infty = 0.06\ m/s$, leading to an uncertainty $u_{PIV_\infty} = 0.006\ m/s$.

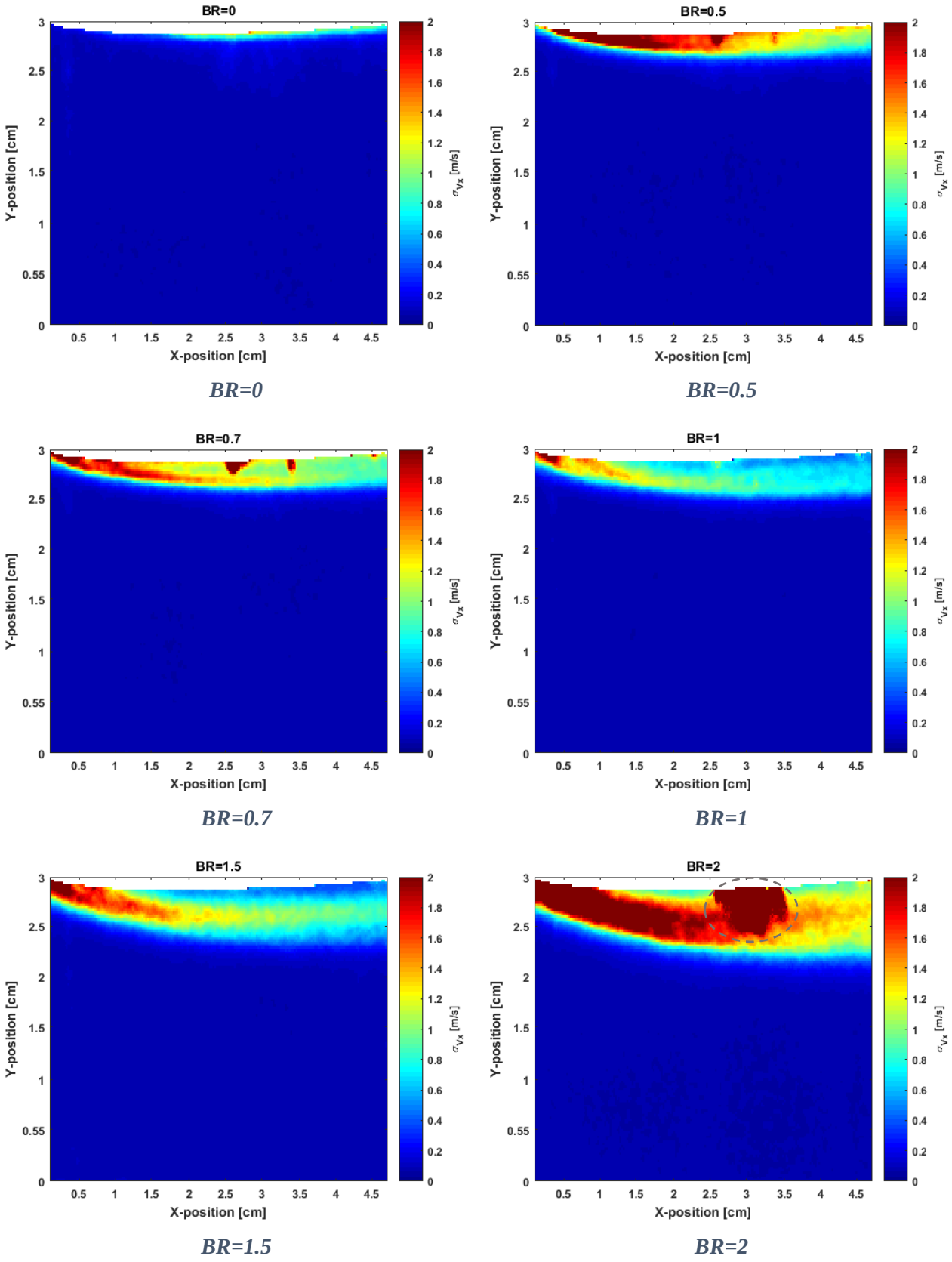

Figure 5.9. Standard deviation of the axial velocity, σ_{V_x} at different blowing ratios for the local flowfield configuration. Note that for BR=2, the (encircled) red region encountered in the mixing shear layer does not represent a lower physical velocity, but is due to the lack of signal caused by the absence of seeding particles in the coolant flow.

Figure 5.10 shows the standard deviation of the axial velocity σ_{V_x} at the wake pressure rake location. Fluctuations are higher in the shear layers (especially in the suction side) than in the central part of the wake, due to the higher turbulence in these regions.

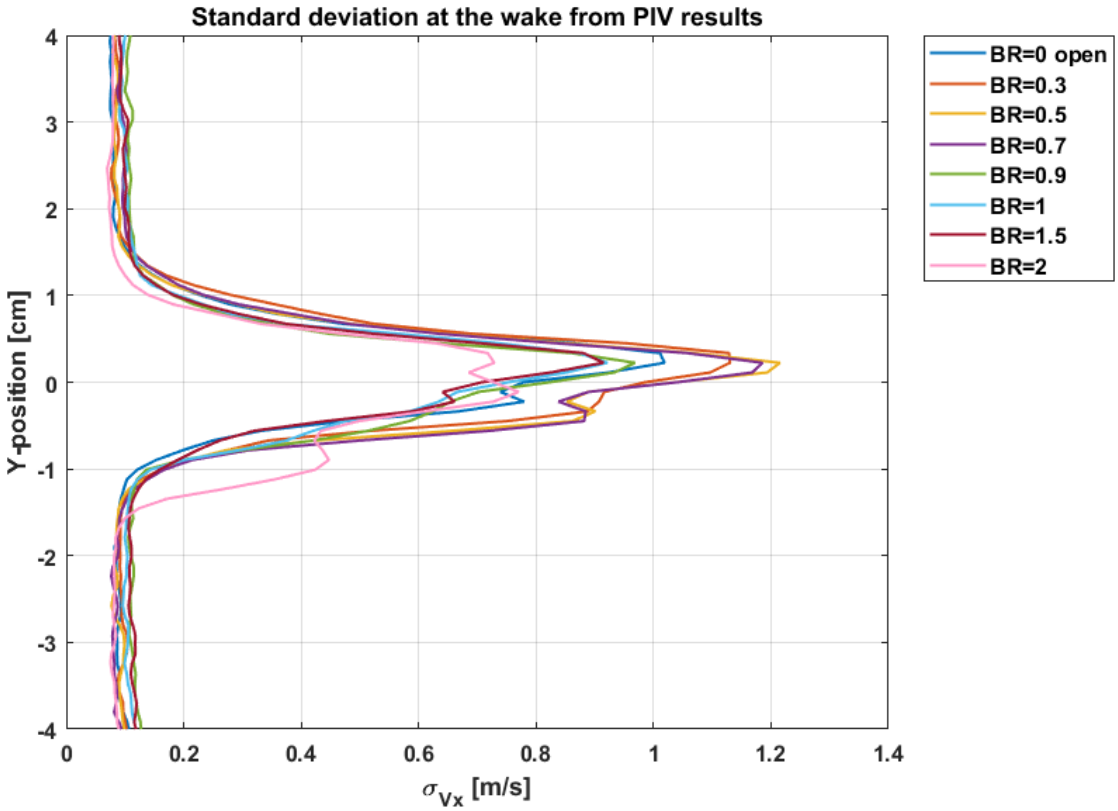

Figure 5.10. Standard deviation of the axial velocity, σ_{V_x} at the wake pressure rake location, x=1.25c

5.6. Chapter remarks

In this Chapter, the results from the PIV experiments have been presented and discussed. From them we can draw the following general conclusions:

- A planar PIV setup has been used to study the flowfield around the airfoil. At high blowing ratios, the wake shrinks and is shifted towards the suction side due to a local jet behaviour that energizes the flow and avoids flow separation. At high angles of attack, the flowfield is asymmetric and the velocity deficit at the wake is lower than for the baseline configuration.

- The global flowfield configuration allows retrieving information from the wake pressure rake location. The wake velocity profiles follow a similar trend to the one obtained with pointwise pressure measurements, with local jet behaviour for BR>1.5. The maximum momentum deficit is like the one with pressure measurements, but the maximum momentum gain obtained with PIV is lower.

- The local flowfield configuration provides information about the mixing shear layer. For low BR, a low momentum secondary flow attached to the surface is observed. When increasing BR, the secondary flow gains momentum and detaches from the surface due to jet lift-off.

- Statistical analysis of the global flowfield configuration PIV data shows that the standard deviation of the axial velocity is higher in the wake than in the freestream region. Fluctuations with respect to the mean velocity are higher in the shear layer than in the central part of the wake. When secondary flow is injected, fluctuations are also higher close to the injection holes location. Statistical analysis of the local flowfield close to the injection holes shows that standard deviation is higher for the BR cases presenting a higher difference in velocity deficit or gain between the mainstream and secondary flows.

- The stereo-PIV results show the evolution of the flowfield at different streamwise locations. For the upstream locations closer to the injection holes, the region affected by the mixing of the mainstream and secondary flows is smaller, the flow structures are more defined and the magnitude of the axial velocity is higher. For the further downstream locations, diffusion and detachment of the jet is observed in a larger mixing region with less defined flow structures.

6

Conclusions and outlook

6.1. Concluding remarks

In this work, the aerodynamic performance of a multi-row film cooled NACA 0012 airfoil has been experimentally studied in the M-tunnel, a low speed windtunnel at TU Delft. Pressure measurements at a midspan location downstream of the airfoil and PIV have been employed as flow measurement techniques. This project aims to complement the study of (Lanzillotta, et al., 2017), so the same model with four rows of cooling holes (at 5%, 10%, 15% and 50% of the chord from leading edge) has been used. But in this case pressure side injection is analysed.

Various film cooling configurations have been tested, to analyse the effect of angle of attack, freestream velocity, partial injection and gas used as secondary flow. The baseline configuration is defined as $V_\infty = 15\ m/s$, $\alpha = 0°$, injection from all rows of holes and air as secondary flow.

Aerodynamic performance has been evaluated as a function of blowing ratio, tested in a range $BR \in (0, 2)$. For the baseline configuration, wake profile characteristics and aerodynamic losses coefficients show that the maximum momentum deficit associated to the maximum losses occurs for BR=0.5. This is due to the low momentum of the blown air, which increases the thickness of the pressure side boundary layer and induces mixing losses due to high shear stresses and turbulence production mechanisms. At BR=1.4, the momentum of the blown air is high enough to energize the flow and compensate for the mixing losses, leading to a shift in the wake flowfield pattern with the presence of a local jet behaviour. The maximum momentum gain occurs for BR=2, the highest blowing ratio tested. The energization of the flow for high BR is also observed in the planar PIV results. When comparing with suction side injection for the baseline configuration, the results show repeatability although a lower sensitivity of pressure side injection to changes in BR is observed.

The effect of increasing the angle of attack is an asymmetric flowfield, a decrease in the maximum momentum deficit due to flow injection and a wake-to-jet shift for a lower BR. The effect of increasing the freestream velocity is an increase in profile losses and in average velocity field values, and the wake-to-jet shift cannot be observed due to limitations in the experimental setup. When studying partial injection, lower losses and higher energization are obtained for the injection from the furthest downstream row of holes. To study the effect of density ratio on aerodynamic performance, CO_2 has been injected as secondary flow, BR matched as scaling parameter and pressure measurements conducted in the wake. Slight differences are visible in the wake flowfield. Although for CO_2 injection, a lower energization is visible at low BR as well as a higher sensitivity of losses with respect to momentum flux ratio. Carrying out PIV measurements using CO_2 would be of help to draw further conclusions.

The planar PIV measurements at a location close to the injection holes allowed visualizing the evolution of the mixing shear layer for increasing BR. Stereoscopic PIV measurements allowed visualizing the evolution of mainstream and secondary flows mixing at different streamwise locations, closer and further away from the injection locations. Further spatial resolution from the measurement system would be needed to extract conclusions on CRVP and jet structure.

Finally, the research questions posed in Chapter 3 are revisited and answered below.

1) ***What is the effect of blowing ratio on the aerodynamic losses of a NACA 0012 model with four rows of film cooling holes in the pressure side?***

   Injection of a secondary flow in the pressure side of a symmetric airfoil induces changes in the local flowfield close to the injection location. These include energization of the flow, increase in boundary layer thickness, shear augmentation due to the difference in momentum between the coolant and the mainstream flow and mixing processes, which increase turbulence production mechanisms and diffusion and momentum transport. This translates into viscous and mixing losses. The effects of injection not only affect the local flowfield, but also the downstream locations and the wake characteristics. The wake profile becomes asymmetric, displaced towards the pressure side, and a shift in the wake profile pattern occurs for a certain blowing ratio or amount of coolant introduced.

   1.1. Are the measurements repeatable when compared to (Lanzillotta, et al., 2017) at zero angle of attack?

   Yes, the repeatability of the setup is acceptable. To test this, experiments with suction side cooling were conducted at the same blowing ratios as in (Lanzillotta, et al., 2017). The results show that the width of the wake is $\sim 2\ cm$ for both cases, it is displaced towards the suction side a similar distance, a shift in the wake profile pattern is observed at $BR = 1.28$ for both cases and the velocity deficit with respect to freestream conditions is the same at $BR = 0$. Some differences are a lower freestream velocity in the present study, showing the lack of repeatability of the windtunnel conditions, and a lower extension of the measurement area which impedes visualizing blockage effect as clear as in (Lanzillotta, et al., 2017).

   1.2. How is the wake velocity profile affected by changes in blowing ratio?

   Blowing coolant from the pressure surface induces asymmetry in the wake profile of a symmetric airfoil, since it causes differences in the growth and development of the pressure side boundary layer with respect to suction side. When injecting low momentum air, it is not able to energize the local flow. But due to the difference in momentum with respect to the mainstream flow, mixing losses occur and the wake momentum deficit decreases with respect to the case without blowing. During the experiments, it was found that the tests at $BR = 0.5$ lead to the maximum momentum deficit. When increasing blowing ratio, the energizing effect becomes more important, reducing the momentum deficit and displacing the wake back towards the symmetry plane. At a certain blowing ratio, when the momentum of the blown air is high enough to compensate for the mixing losses, the wake starts acting as a jet in the pressure surface. In this study, this critical blowing ratio was found to be $BR = 1.4$. The wake region gets shrunk and shifted towards the suction side as the jet keeps spreading when increasing blowing ratio, leading to a momentum gain which becomes maximum at $BR = 2$.

1.3. How is the 2D velocity field affected by changes in blowing ratio?

The 2D velocity field retrieved from planar PIV result shows the energization of the flow close to the pressure side and in further downstream locations for high BR. Examining the local flowfield reveals information about the mixing shear layer. For low blowing ratios, the coolant is attached to the surface. The mixing shear layer presents lower velocity than the freestream and its thickness increases as blowing ratio increases. At $BR = 0.9$, which corresponds to $I > 0.8$ (jet lift-off expected), there is a higher entrainment of the secondary flow into the mainstream, with the minimum velocity region found now in the central part of the shear layer. As blowing ratio increases, flow energization becomes visible and since the jet is already detached from the surface, the axial velocity is higher in the central part of the mixing shear layer and lower close to the model´s surface.

1.4. Are the wake profile results retrieved from pressure measurements and from PIV comparable?

Yes, they are. When extracting the wake velocity profiles at the location x=1.25c, where the pressure rake was positioned, there is high similarity in the results. The maximum momentum deficit occurs for $BR = 0.5$ and a local jet behaviour is observed for $BR > 1.5$. The wake is also displaced towards the pressure side, except for $BR = 2$ for which the wake is shifted towards the suction side due to the spreading of the jet. The peak of the momentum deficit for $BR = 0.5$ has a similar value to that of the pressure measurements results, but the maximum momentum gain is lower in the PIV reconstructed data.

1.5. How are aerodynamic losses affected by changes in blowing ratio?

Aerodynamic losses have been evaluated at the wake by means of five coefficients: primary loss coefficient, local total pressure loss coefficient, total pressure loss coefficient, integrated aerodynamic losses and area-averaged loss coefficient. Losses increase when the momentum deficit increases, i.e. when the exit total pressure decreases, as shown in the mathematical definition of all of them when taking inlet total pressure and exit static pressure as nearly constant. The evolution of the three first coefficients with blowing ratio is identical to what was described for the wake velocity profile. For the regions showing a wake local behaviour, aerodynamic losses are positive whereas for the regions with a jet local behaviour, the coefficients become negative meaning that there is an aerodynamic gain due to the energization of the mainstream with the secondary flow. Regarding the integrated aerodynamic losses and area-averaged loss coefficient, they increase with low blowing ratios, reach their peak at $BR = 0.5$ and then decrease for higher blowing ratios. They only become negative for $BR = 2$.

1.6. How does the relationship between blowing ratio and aerodynamic losses change when varying other parameters? These parameters include:

- *Angle of attack.* When increasing the angle of attack, the wake profile is no longer symmetrical for $BR = 0$. Profile losses and maximum momentum deficit increase and the wake width decreases. Sensitivity to BR increases for pressure side injection, leading to an earlier wake-to-jet shift.

- *Mainstream velocity*. When increasing freestream velocity, profile losses increase, the wake width decreases and the average wake velocity and losses coefficients values increase. The wake flow pattern and effect of low BR injection is similar to the baseline configuration case. The effect of high BR injection cannot be studied due to experimental limitations in the maximum flow rate of the flowcontroller used, so the wake-to-jet shift is not detected.

- *Number of open rows and their chordwise location.* When studying the effect of individual rows or partial injection, the sensitivity to BR changes is lower than for total injection and superposition principle does not apply. Lower losses and higher energization are obtained for injection from PS4 (at 50% of the chord), the only injection location which is downstream of the maximum thickness point of the airfoil and closer to the separation point and downstream measurement location. Maximum losses are obtained for PS2 injection.

1.7. What are the differences with suction side film cooling aerodynamic performance?

The evolution with blowing ratio of the wake velocity profiles follows the same trend when injecting flow in the suction or in the pressure side of the airfoil: equal velocity distribution for $BR = 0$, increase in momentum deficit and wake spreading, change from wake to jet local behaviour and increase in momentum gain and jet spreading. But since the asymmetry in the flow is created by blowing air from different locations, the displacement of the wake and the location of the wake and jet areas are mirrored with respect to the symmetry plane of the airfoil. For the baseline configuration, when observing the blowing ratio at which the wake-to-jet shift takes place it is found to be $BR = 1.28$ for the suction side and $BR = 1.4$ for the pressure side. When increasing the angle of attack, the sensitivity of the pressure side flow to blowing ratio changes increases too.

2) What are the characteristics of the jet-mainstream flow interaction at different streamwise locations?

The interaction between the mainstream and secondary flow (jet in crossflow problem) at different streamwise locations shows a mixing region that increases in size at further downstream locations, where the jet is more diffused and less defined in the mixing shear layer.

2.1. *Can I observe flow structures derived from jet-mainstream interaction at each streamwise location?*

With the used stereoscopic PIV setup, the flow structures described in Section 2.2. (jet shear layer vortices, horseshoe vortices, wake vortices and the counter-rotating vortex pair) are not observed. Higher spatial resolution of the experimental setup closer to the film cooling holes would be needed.

2.2. *How does the jet evolve in the streamwise direction, from the near hole region to a downstream location far away from the ejection hole?*

At the further upstream locations studied (i.e. z = 0.3c, z = 0.45c and z = 0.55c) the region affected by the mixing of the mainstream and secondary flows is smaller and the jet in

crossflow is more defined. At z = 0.3c, the magnitude of the velocity is higher because this location is affected by the injection from PS1, PS2 and PS3 rows of holes. The jet diffuses and its velocity is reduced, as observed for z = 0.45c upstream of PS4 and increases again at z = 0.55c, after injection from PS4. At the further downstream locations (i.e. z = 0.75c, z = 1.1c and z = 1.3c) the region affected by the mixing of the mainstream and secondary flows is significantly bigger, the flowfield structures are less defined and the velocity magnitude is lower. The detachment of the jet is visible, since the mixing region is displaced further away from the surface.

2.3. *What is the effect of blowing ratio on jet-mainstream flow interaction?*

When increasing blowing ratio at a specific streamwise location, the streamwise component of the velocity increases and the mixing shear layer increases in size.

2.4. *Can I observe jet-to-jet interaction or row-to-row interaction?*

No jet-to-jet interaction or row-to-row interaction is clearly observed in the obtained stereo- PIV results.

3) What is the effect of density ratio on wake profile characteristics and aerodynamic losses?

When studying the effect of density ratio on aerodynamic performance using CO_2 gas injection, blowing ratio was matched, meaning that the velocity ratio and momentum flux ratio are lower for CO_2, so jet lift-off is postponed for CO_2. Slight differences are visible in the wake flow characteristics, although the lower momentum of CO_2 injection could be visible at low BR. Because of the lower momentum flux ratio of CO_2, the sensitivity of losses to I variation is higher for CO_2 than for air. This topic begs a deeper analysis: whole flowfield measurements and flow visualization as well as matching different flow scaling parameters or inducing coolant-to-mainstream density ratio with a heating system could provide a more solid approach and further insight.

6.2. Recommendations for future work

This section presents some recommendations for follow-up studies. First, some possible changes in the experimental setup. Second, some possible research topics or directions.

Experimental setup

Some possible changes to the current experimental setup or added features for a new setup for film cooling experiments are listed below:

First, some possible changes to the general setup:

- Rotating test facility.
- Possibility to test a cascade of blades or a complete turbine stage, to study vanes and blades interaction and endwall secondary flow structures.
- Include a turbulence grid to study the influence of freestream turbulence intensity.
- Do boundary layer measurements.
- For the stereo-PIV setup: increase the spatial resolution of the PIV cameras to observe row-to-row interactions, jet development and the structural features of the jet-crossflow interactions. Also, mitigate cameras' vibrations located downstream of the test section to be able to capture images closer to the film cooling holes and enable higher tilting angles to the PIV cameras to visualize the most upstream rows of holes.
- Use seeding in the coolant to gain further insight into coolant flow physics.
- Test section with a Germanium window to allow infrared transmission for heat transfer measurements.
- Use another flow measurement technique like PSP or repeat oil flow visualization experiments.
- Include a heating system to generate the temperature ratio, instead of with foreign gas injection.

Second, some suggested changes to the secondary flow system:

- For the experiments using CO_2, incorporate a valve that allows switching easily from CO2 to air as coolant flows without needing to remove the tubing from the connectors every time that the gas changes.
- Use another gas different from CO_2, such as Nitrogen or Freon 12.
- Calibrate the flowcontroller to have the CO_2 calibration curve stored in a second memory (contact person: Jethro Molenaar, from Bronkhorst Nederland B.V.).
- Improve the connectors from the flowcontroller to the tubing (½" OD compression Swagelok fittings were suggested).
- Consider the possibility of changing the internals (M20) of the flowcontroller to allow higher flow rates with the same flowcontroller model.
- Improve the measurement system for the coolant temperature, so that continuous monitoring is possible.
- Improve the measurement system for the coolant pressure. It could be beneficial to have pressure probes to measure the coolant exit static pressure at each injection location and assess better the difference with surface static pressure.

Third, some possible modifications to the model:

- Manufacture the model from a different material and/or manufacturing technique, to compare 3D printing to more accurate manufacturing techniques.

- Change the geometrical aspects of the model (twist, camber) for a less simplified blade design.
- Combine film cooling with internal cooling.
- Design a model suitable for heat transfer measurements: understand the emissivity of the model's surface and reduce the thermal conductivity of the model.
- Change the hole geometry: change the streamwise jet injection angle, include compound angle, anti-kidney vortices generators or other novel holes designs.
- Change the in-line configuration of the rows of holes to staggered and study the row-to-row interaction.
- Consider not having only a single airfoil plenum, together with a way to measure and monitor the coolant pressure at the exit of the coolant holes, so that the pressure ratio with respect to ambient can be measured for each row of holes.

Research directions

Additionally, some other topics for future research could be:

- Numerical studies and CFD analysis of flow structures.
- Carry out a heat transfer analysis: analyse the impact of film cooling flow structures on heat transfer to understand the interaction between fluid dynamics and heat transfer phenomena and the flow physics that govern film cooling effectiveness.
- Couple and integrate this experimental study with gas turbine cooling performance models, so that the impact of blowing ratio on engine thermodynamic cycle efficiency is assessed.
- Conduct unsteady measurements.
- Do jet trajectory tracking as a method to reconstruct the jet trajectories.
- Do more investigations related to the effect of density ratio, such as investigating the effect when matching momentum flux ratio or velocity ratio instead of blowing ratio and using time-resolved PIV for whole flowfield measurements.
- Analyse the correlation between 3D printing manufacturing tolerances, pressure ratio across the holes and aerodynamic losses.
- Revisit the list of the topics presented in Chapter 2 as not part of the scope of this literature search but relevant in film cooling open literature.

Bibliography

Abdullah, K. & Funazaki, K.-i., 2013. *Experimental investigations on aero-thermal interaction of film cooling air ejected from multiple shallow angle cooling holes: effect of freestream turbulence.* Texas, s.n.

Aga, V., 2009. *Experimental investigation of the influence of flow structure on compund angled film cooling performance, PhD Thesis,* s.l.: s.n.

Aga, V. & Abhari, R. S., 2011. Influence of flow structure on compound angled film cooling effectiveness and heat transfer. *Journal of Turbomachinery,* Issue 133.

Aga, V., Rose, M. & Abhari, R. S., 2008. Experimenta flow structure investigation of compound angled film cooling. *Journal of Turbomachinery,* Issue 130.

Anderson, J. B., Boyd, E. J. & Bogard, D. G., 2015. *Experimental investigation of coolant-to-mainstream scaling parameters with cylindrical and shaped film cooling holes.* Montréal, s.n.

auf dem Kampe, T. et al., 2011. *Experimental and numerical investigation of flow field and downstream surface temperatures of cylindrical and diffuser shaped film cooling holes.* Vancouver, s.n.

Barthet, S. & Bario, F., 2001. *Experimental investigation of film cooling flow induced by shaped holes on a turbine blade,* s.l.: s.n.

Berkache, A. & Dizene, R., 2017. Numerical and experimental investigation of turbine blade film cooling. *Heat Mass Transfer.*

Bernsdorf, S., Rose, M. G. & Abhari, R. S., 2006. Modeling of film cooling - Part I: Experimental study of flow structure. *Journal of Turbomachinery,* Issue 128, pp. 141-149.

Bernsdorf, S., Rose, M. G. & Abhari, R. S., 2008. Experimental validation of quasisteady assumption in modeling of unsteady film-cooling. *Journal of Turbomachinery,* Issue 130.

Bogard, D. & Thole, K., 2005. Gas turbine film cooling. *Journal of Propulsion and Power.*

Boyce, M. P., 2012. *Gas Turbine Engineering Handbook.* 4th ed. s.l.:s.n.

Brown, D. B. & Helon, R. M., 1973. *Cold-air aerodynamic study in a two-dimensional cascade of a turbine stator blade with suction-surface film cooling. NASA Technical Report,* s.l.: s.n.

Bunker, R. S., 2005. A review of shaped hole turbine film-cooling technology. *Journal of Heat Transfer,* Volume 127, pp. 441-453.

Burd, S. & Simon, T., 1999. Measurements of discharge coefficients in film cooling. *Journal of Turbomachinery,* Volume 121, pp. 243-248.

Cavazzini, G., 2012. *The particle image velocimetry: characteristics, limits and possible applications.* s.l.:InTech.

Chang, H., Jing, R. & Hong-de, J., 2012. Multi-parameter influence on combined-hole film cooling system. *International Journal of Heat and Mass Transfer,* Volume 55, pp. 4232-4240.

Chappell, J. et al., 2010. Aerodynamic performance of suction-side gill region film cooling. *Journal of Turbomachinery,* Issue 132.

Cohen, H., Rogers, G. & Saravanamuttoo, H., 1996. *Gas Turbine Theory.* 4th ed. s.l.:s.n.

Day, C., Oldfield, L. & Lock, G., 2000. Aerodynamic performance of an annular cascade of film cooled nozzle guide vanes under engine representative conditions. *Experiments in Fluids,* Volume 29, pp. 117-129.

Day, K. M., Lawless, P. & Fleeter, S., 1996. *Particle image velocimetry measurements in a low speed two stage research turbine.* Buena vista, s.n.

Denton, J., 1993. Loss mechanisms in turbomachines.

Dickhoff, J., Kazari, M. & Tanaka, R., 2017. *Improving cooling effectiveness of gas turbines through design exploration,* s.l.: s.n.

Drost, U., 1998. *An experimental investigation of gas turbine airfoil aero-thermal film cooling performance, PhD Thesis,* s.l.: s.n.

Drost, U. & Bölcs, A., 1999. Performance of a turbine airfoil with multiple film cooling stations. Part II: Aerodynamic losses.

Eberly, M. K. & Thole, K. A., 2014. Time-resolved film-cooling flows at high and low density ratios. *Journal of Turbomachinery,* Issue 136.

Ekkad, S. & Han, J.-C., 2015. A review of hole geometry and coolant density effect on film cooling. *Frontiers in Heat and Mass Transfer ,* 6(8), pp. 1-14.

Ethridge , M. I., Cutbirth, J. M. & Bogard, D. G., 2001. Scaling of performance fot varying density raito coolants of an airfoil with strong curvature and pressure gradient effects. *Journal of Turbomachinery,* Volume 123, pp. 231-237.

Farokhi, S., 2014. *Aircraft Propulsion.* 2 ed. s.l.:s.n.
Fawcett, R. J., Wheeler, A. P., He, L. & Taylor, R., 2012. Experimental investigation into unsteady effects on film cooling. *Journal of Turbomachinery,* Issue 134.

Foster, N., 1976. *Film cooling of gas turbines, PhD Thesis,* s.l.: s.n.

Fraas, M., Glasenapp, T., Schulz, A. & Bauer, H.-J., 2017. *Introducing a new test rig for film cooling measurements with realistic hole inflow conditions.* Charlotte, s.n.

Fric, T. & Roshko, A., 1994. Vortical structure in the wake of a transverse jet. *Journal of Fluid Mechanics,* Volume 279, pp. 1-47.

Guanghua Wang, J., Bailey, J., Kopriva, J. & Laskowski, G., 2015. *Experimental and numerical investigations of the heat transfer and flow field in a trailing edge cooling geometry. Part 1: Experimental study with IR Thermography and PIV.* Montreal, s.n.

Haller, B. & Camus, J.-J., 1984. Aerodynamic loss penalty produced by film cooling transonic turbine blades. *Journal of Engineering for Gas Turbines and Power,* Volume 106, pp. 198-205.

Han, J.-C., Dutta, S. & Ekkad, S., 2013. *Gas Turbine Heat Transfer and Cooling Technology.* 2 ed. s.l.:s.n.

Han, J.-C. & Rallabandi, A. P., 2010. Turbine blade film cooling using PSP technique.

Hassan Bashir, M., Shiau, C.-C. & Han, J.-C., 2017. Film cooling effectiveness for three-row compound angle hole design on flat plate using PSP technique. *International Journal of Heat and Mass Transfer,* pp. 918-929.

Hassan, O., 2013. *Thermal and flow field investigations of a micro-tangential-jet film cooling scheme on gas turbine components, PhD Thesis,* s.l.: s.n.

Haven, B. et al., 1997. *Anti-kidney pair of vortices in shaped-holes and their influence on film cooling effectiveness.* Florida, s.n.

Haydt, S., Lynch, S. & Lewis, S., 2017. *The effect of area ratio change via increased hole length for shaped film cooling holes with constant expansion angles.* Charlotte NC, s.n.

Hernández Rosette, A., Mazur, Z., Demeulenaere, A. & López Hernández, R., 2009. *The effect of start-up cycle in ceramic coating used as thermal barrier for a gas turbine bucket.* s.l.:s.n.

Holdeman, J., Liscinsky, D. S. & Bain, D. B., 1997. *Mixing of Multiple Jets with a Confined Subsonic Crossflow. NASA Technical Memorandum,* s.l.: s.n.

Horlock, J. & Torbidoni, L., 2008. Calculations of Cooled Turbine Efficiency. *Journal of Engineering for Gas Turbines and Power.*

Issakhanian, E., Elkins, C. & Eaton, J., 2012. In-hole and mainflow velocity measurements of low-momentum jets in crossflow emanating from short holes. *Experiments in Fluids,* Issue 53, pp. 1765-1778.

Ito, S., Eckert, E. & Goldstein, R., 1980. Aerodynamic loss in a gas turbine stage with film cooling. *Journal of Engineering for Power,* Volume 102, pp. 964-970.

Jackson, D., Lee, K., Ligrani, P. & Johnson, P., 2000. Transonic aerodynamic losses due to turbine airfoil, suction surface film coolin. *Journal of Turbomachinery,* Issue 122, pp. 317-326.

Jessen, W., Konopka, M. & Schroeder, W., 2012. Particle-image velocimetry measurements of film cooling in an adverse pressure gradient flow. *Journal of Turbomachinery,* Issue 134.

Jessen, W., Schröder, W. & Klaas, M., 2007. Evolution of jets effusing from inclined holes into crossflow. *International Journal of Heat and Fluid Flow,* Issue 28, pp. 1312-1326.

Jindal, P., Agarwal, S. & Sharma, R., 2016. A brief review on experimental film cooling. *Carbon-Science and Technology*.

Johnson, B., Tian, W., Zhang, K. & Hu, H., 2014. An experimental study of density ratio effects on the film cooling injection from discrete holes by using PIV and PSP techniques. *International Journal of Heat and Mass Transfer,* Issue 76, pp. 337-349.

Jovanovic, M., 2006. *Film cooling through imperfect holes, PhD Thesis,* s.l.: s.n.

Kamotani, Y. & Greber, I., 1979. Experiments on a turbulent jet in a cross flow. *AIAA J.*, Volume 32, pp. 1451-1460.

Kelso, R., Lim, T. & Perry, A., 1996. An experimental study of round jets in cross-flow. *Journal of Fluid mechanics,* Volume 306, pp. 111-144.

Keogh, R., 2001. *Aerodynamic performance measurements of a film-cooled turbine stage, PhD Thesis,* s.l.: s.n.

Khalatov, A., Panchenko, N., Borisov, I. & Severina, V., 2017. Numerical simulation of film cooling with a coolant supplied through holes in a trench. *Journal of Engineering Physics and Thermophysics,* pp. 637-643.

Kiger, K., n.d. *Introduction of Particle Image Velocimetry,* University of Maryland: s.n.

Kim, K., Kim, S. & Yoon, S., 2000. PIV measurements of the flow and turbulent characteristics of a round jet in crossflow. *Journal of Visualization,* 3(2), pp. 157-164.

Kost, F. & Nicklas, M., 2001. Film-cooled turbine endwall in transonic flow field: Part I-Aerodynamic Measurements. *Journal of Turbomachinery,* Issue 123, pp. 709-719.

Kubo, R., Otomo, F., Fukuyama, Y. & Nakata, Y., 1998. *Aerodynamic loss increase due to individual film cooling injections from gas turbine nozzle surface.* Stockholm, s.n.

Lakshminarayana, B., 1996. *Fluid Dynamics and Heat Transfer of Turbomachinery.* s.l.:John Wiley & Sons, Inc..

Langston, L., 1980. Crossflows in a Turbine Cascade Passage. *ASME Journal Engineering for Power,* Volume 102, pp. 866-874.

Lanzillotta, F., Sciacchitano, A. & Gangoli Rao, A., 2017. Effect of film cooling on the aerodynamic performance of an airfoil. *International Journal of Heat and Fluid Flow.*

Lemmon, C., Kohli, A. & Thole, K., 1999. *Formation of counter-rotating vortices in film cooling flow.* Indianapolis, s.n.

Ligrani, P., 2012. Aerodynamic losses in turbines with and without film cooling, as influenced by mainstream turbulence, surface roughness, airfoil shape and mach number. *International Journal of Rotating Machinery.*

Lin, X.-C., Liu, J.-J., Li, C. & Fu, J.-L., 2014. *Impacts of film cooling parameters on aerodynamic loss of a cooled turbine vane.* Zurich, s.n.

Mamaev, B., Saha, R. & Fridh, J., 2015. Aerodynamic investigation of turbine cooled vane block. *Thermal Engineering,* 62(2), pp. 97-102.

Margason, R. J., 1993. *Fifty years of jet in cross-flow research.* s.l., s.n.

Mazzei, L., Winchler, L. & Andreini, A., 2017. Development of a numerical correlation for the discharge coefficient of round inclined holes with low crossflow. *Computer and Fluids.*

Mee, D., 1992. *Techniques for aerodynamic loss measurement of transonic turbine cascades with trailing edge region coolant ejection.* Cologne, s.n.

Morton, B. & Ibbetson, A., 1996. Jets deflected in a crossflow. *Experimental Thermal and Fluid Science,* Volume 12, pp. 112-113.

Naik, S., 2017. *INTECH Report, Chapter 6: Basic Aspects of Gas Turbine Heat Transfer,* s.l.: s.n.

Narzary, D., 2009. *Experimental study of gas turbine blade film cooling and heat transfer, PhD Thesis,* s.l.: s.n.

Natsui, G. et al., 2016. Adiabatic film cooling effectiveness measurements throughout multi-row film cooling arrays.

Natsui, G. et al., 2016. *Hydrodynamic measurements throughout a flat plate multi-row film cooling array with inclined holes.* Seoul, s.n.

Nguyen, M.-N., Fénot, M., Lalizel, G. & Dorignac, E., 2012. Experimental study of full coverage film cooling optimization. *Journal of Physics: Conference Series 395.*

Nikparto, A. & Schobeiri, M. T., 2016. *Experimental investigation of film cooling effectiveness of a highly loaded turbine blade under steady and periodic unsteady flow conditions.* Seoul, s.n.

Oldfield, M., Lock, G. & Day, C., 1999. The influence of film cooling on the efficiency of an annular nozzle guide vane cascade. *Journal of Turbomachinery,* 121(1), pp. 145-151.

Ornano, F. & Povey, T., 2017. *Experimental and computational study of the effect of momentum-flux ratio on high pressure NGV endwall cooling systems.* Charlotte, s.n.

Osnaghi, C. et al., 1997. *The influence of film-cooling on the aerodynamic performance of a turbine nozzle guide vane.* Orlando, s.n.

Peterson, S. D. & Plesniak, M. W., 2007. Flow structure and skin friction in the vicinity of a streamwise-angled injection hole fed by a short pipe. *Experiments in Fluids,* Issue 43, pp. 627-638.

Peterson, S. & Plesniak, M., 2002. Short-hole jet-in-crossflow velocity field and its relationship to film-cooling performance. *Experiments in Fluids,* Issue 33, pp. 889-898.

Peterson, S. & Plesniak, M., 2004. Evolution of jets emanating from short holes into crossflow. *Journal of Fluid Mechanics,* Issue 503, pp. 57-91.

Pietrzyk, J., Bogard, D. & Crawford, M., 1990. Effects of density ratio on the hydrodynamics of film cooling. *Journal of Turbomachinery,* Volume 112, pp. 437-443.

Prenter, R. et al., 2017. *Experimental characterization of reverse-oriented film cooling.* Charlotte, s.n.

Prust, H. W., 1975. *Two-dimensional cold-air cascade study of a film-cooled turbine stator blade. NASA Technical Memorandum,* s.l.: s.n.

Pu, J. et al., 2014. An experimental investigation of secondary flow characteristics in a lineal turbine cascade with upstream converging slot-holes using TR-PIV. *Experimental Thermal and Fluid Science,* Issue 59, pp. 56-71.

Raffel, M. & Kost, F., 1998. Investigation of aerodynamic effects of coolant ejection at the triling edge of a turbine model by PIV and pressure measurements. *Experiments in Fluids,* Volume 24, pp. 447-461.

Raffel, M., Willert, C. E., Wereley, S. T. & Kompenhans, J., 2007. *Particle Image Velocimetry: a practical guide.* Second ed. s.l.:Springer.

Ratharishnan, E., 2007. *Instrumentation, Measurements and Experiments in Fluids.* s.l.:CRC Press Taylor & Francis Group.

Romakhova, G., 2017. Effect of coolant flow rate on the performance of gas-turbine units. *Power technology and Engineering.*

Rouina, S., Miranda, M. & Barigozzi, G., 2016. *Experimental investigation of the unsteady flow behavior on a film cooling flat plate.* Turin, s.n., pp. 726-733.

Sakai, E. & Takahashi, T., 2017. *Numerical study on effects of density ratio on film cooling flow structure and film cooling effectiveness.* Charlotte, s.n.

Schroeder, R. P. & Thole, K. A., 2016. Effect of high freestream turbulence on flowfields of shaped film cooling holes. *Journal of Turbomachinery,* Volume 138.

Schulz, S., Maier, S. & Bons, J. P., 2012. *An experimental investigation of an anti-vortex film cooling geometry under low and high turbulence conditions.* Copenhagen, s.n.

Schwarz, S., Goldstein, R. & Eckert, E., 1990. *The influence of curvature on film cooling performance.* Brussels, s.n.

Sinha, A., Bogard, D. & Crawford, M., 1991. Film-cooling effectiveness downstream of a single row of holes with variable density ratio. *Journal of Turbomachinery,* Volume 113, pp. 442-449.

Stabe, R. G. & Kline, J. F., 1975. *Aerodynamic performance of a fully film cooled core turbine vane tested with cold air in a two-dimensional cascade. NASA Technical Report,* s.l.: s.n.

Stephan, B., Krückels, J. & Gritsch, M., 2010. *Investigation of aerodynamic losses and film cooling effectiveness for a NGV profile.* Glasgow, s.n.

Strausswald, M., Schmid, K., Müller, H. & Pfitzner, M., 2017. *Experimental and numerical investigation of turbulent mixing in film cooling applications.* Charlotte, s.n.

Thole, K., Gritsch, M. & Wittig, S., 1996. *Flowfield measurements for film-cooling holes with expanded exits.* Birmingham, s.n.

Thole, K. & Knost, D., 2005. Heat transfer and film-cooling for the endwall of a first stage turbine vane.

Thole, K., n.d. 4.2.3 Airfoil Endwall Heat Transfer.

Tropea, C., Yarin, A. L. & Foss, J. F., 2007. *Handbook of Experimental Fluid Mechanics.* s.l.:Springer.

Urban, M. F., Hermeler, J. & Hosenfeld, H.-G., 1998. *Experimental and numerical investigations of film-cooling effects on the aerodynamic performance of transonic turbine blades.* Stockholm, s.n.

Uzol, O. & Camci, C., 2001. Aerodynamic loss characteristics of a turbine blade with trailing edge coolant ejection: part 2 - external aerodynamics, total pressure losses and predictions. *Journal of Turbomachinery,* Volume 123, pp. 1-9.

Vinton, K. R. & Wright , L. M., 2017. *Effect of flow acceleration on mainstream-to-coolant flow interaction for round and shaped cooling holes.* Charlotte, s.n.

Voet, M., 2017. *Hydrodynamic measurements of the flow structure emanating from a multi-row film cooling configuration, MSc Thesis,* s.l.: s.n.

Voet, M. T. et al., 2017. *Effect of density ratio on multi-row film cooling performance.* Charlotte, s.n.

Vogel, G., 2002. Experimental study on a heavy film cooled nozzle guide vane with contoured platforms.

Wang, J., Sundén, B., Zeng, M. & Wang, Q., 2015. Film cooling effects on the tip flow characteristics of a gas turbine blade. *Propulsion and Power Research,* 4(1), pp. 9-22.

Watson, T. B. et al., 2016. *Application of s-PIV for investigation of roud and shaped film cooling holes at high density ratios.* Seoul, s.n.

Wernet, M. P., Wroblewski, A. C. & Locke, R. J., 2017. *A dual-plane PIV study of turbulent heat transfer flows. NASA Report,* s.l.: s.n.

Wilcock, R., Young, J. & Horlock, J., 2005. The effect of turbine blade cooling on the cycle efficiency of gas turbine power cycles. *Journal of Engineering for Gas Turbines and Power,* pp. 109-120.

Wright, L. M., McClain, S. T., Brown, C. P. & Harmon, W. V., 2013. *Assessment of a double hole film cooling geometry using s-PIV and PSP.* Texas, s.n.

Wright, L. M., McClain, S. T. & Clemenson, M. D., 2011. Effect of freestream turbulence intensity on film cooling jet structure and surface effectiveness using PIV and PSP. *Journal of Turbomachinery,* Issue 133.

Xu, L., Bo, S., Hongde, Y. & Wang, L., 2015. *Evolution of Rolls Royce air-cooled turbine blades and feature analysis,* s.l.: s.n.

Yang, Z. & Hu, H., 2012. An experimental investigation on the trailing edge cooling of turbine blades. *Propulsion and Power Research,* 1(1), pp. 36-47.

Yao, J. et al., 2017. Effect of density ratio on film-cooling effectiveness distribution and its uniformity for several hole geometries on a flat plate.

Yao, J. et al., 2017. *Interaction of flow and film-cooling effectiveness between double-jet film-cooling holes with various spanwise distances.* Charlotte, s.n.

Zeng, L., Li, X., Ren, J. & Jiang, H., 2017. *Numerical investigation of coolant-to-mainstream scaling parameters with film cooling on pressure and suction side of a gas turbine blade.* Charlotte, s.n.

Zhang, L., Dong, H. & Wen, G., 2012. Experimental study on film cooling flow characteristics of turbine stator blade at different setting angles. *Advanced materials research,* Volume 614-615, pp. 592-595.

Zheng, Y. & Hassan, I., 2014. Experimental flow field investigations of a film cooling hole featuring an orifice. *Applied Thermal Engineering,* Issue 62, pp. 766-776.

Zhou, W. & Hui, H., 2015. *An experimental study on film cooling performance behind barchan dune-shaped ramps using PSP and PIV techniques.* Montréal, s.n.

Zhou, W., Johnson, B. & Hu, H., 2015. *An experimental study of compressibility effects on the film cooling effectiveness using PSP and PIV Techniques.* Florida, s.n.

Appendices

Appendix I: Literature study tables

This Appendix collates the literature survey tables from Chapter 2, corresponding to Sections 2.2, 2.3 and 2.4. These tables contain relevant information to the section´s topic extracted from each of the publications about experimental film cooling studies that were selected by the author.

Section 2.2. Flow structures and aerodynamic losses

Table I.1 Literature study table for Section 2.2.

Reference (authors, date)	Topic	Aerodynamic losses	Flow characteristics
(Brown & Helon, 1973)	Aerodynamic performance of single and multi-row film cooling from suction side (SS)	▪ Primary efficiency ▪ Discharge coefficient	-
(Stabe & Kline, 1975)	Full coverage film cooling of core turbine vane	▪ Primary loss coefficient ▪ Thermodynamic loss coefficient ▪ After-mix flow angle and weight flow	-
(Prust, 1975)	Aerodynamic performance of single and multi-row film cooling from pressure side (PS) and suction side	▪ Primary-air efficiency ▪ Discharge coefficient	-
(Ito, et al., 1980)	Aerodynamic performance of single row film cooling from PS and SS	Local total pressure loss coefficient	-
(Haller & Camus, 1984)	Aerodynamic performance of single row film cooling from SS in transonic rotor blade	Thermodynamic efficiency	Shock waves
(Pietrzyk, et al., 1990)	Single row film cooling, density ratio effect on hydrodynamics	-	Mean and turbulent velocity and shear stress in streamwise direction (1D upstream to 30D downstream of hole)
(Schwarz, et al., 1990)	Influence of curvature in film cooling thermal performance	-	Jet lift-off in curved surfaces
(Day, et al., 1996)	Flowfield in turbine vane row with showerhead film cooling and application of PIV in turbomachinery	-	Spanwise measurements of flowfield at 5 locations (10%, 25%, 50%, 75% and 90%)
(Thole, et al., 1996)	Flowfield from three different hole geometries	-	Mean and turbulent vertical velocity profiles at 14 streamwise locations and 7 spanwise positions on one side of the hole

(Osnaghi, et al., 1997)	Aerodynamic performance of full-coverage and partial film cooling in high pressure nozzle guide vane (NGV)	▪ Primary loss coefficient ▪ Thermodynamic loss coefficient	-
(Haven, et al., 1997)	Vortex dynamics in single-row film cooling from shaped holes	-	2D-velocity and vorticity fields; presence of CRVP and anti-kidney vortices, jet lift-off, lateral separation of the jet, jet leading edge vorticity
(Drost, 1998)	Aero-thermal performance of partial or full coverage film cooling from airfoil PS and SS	▪ Primary loss coefficient ▪ Thermodynamic loss coefficient ▪ Flow exit angle	Stagnation line, leading edge laminar separation bubble and endwall secondary flows
(Urban, et al., 1998)	Aerodynamic performance of single-row and full-coverage film cooling from PS and SS, with steam as working fluid	▪ Thermodynamic loss coefficient ▪ Profile pressure distribution ▪ Local total pressure loss coefficient	-
(Burd & Simon, 1999)	Influence of hole length-to-diameter on discharge coefficient in co-flow and counter-flow configurations	▪ Discharge coefficient ▪ Hole exit mean velocity ▪ Outlet additive losses	-
(Drost & Bölcs, 1999)	Aerodynamic performance of NGV with single-row and full-coverage film cooling from PS, SS and showerhead	▪ Primary loss coefficient ▪ Thermodynamic loss coefficient ▪ Discharge coefficient ▪ Flow angles	-
(Jackson, et al., 2000)	Aerodynamic performance in symmetric airfoil with film cooling from SS	▪ Discharge coefficient ▪ Local total pressure losses ▪ Integrated total pressure losses ▪ Integrated aerodynamic losses	Shock waves at the trailing edge

		▪ Downstream kinetic energy distribution	
(Day, et al., 2000)	Aerodynamic performance of single and multi-row film cooled NGV; methodology for losses in film-cooled annular cascade with compressible flow and foreign gas coolant	▪ Exit total pressure ▪ Exit isentropic Mach number ▪ Exit flow angles	Shock wave interaction with coolant jets (for a linear cascade)
(Kim, et al., 2000)	Instantaneous and averaged velocity fields in the vertical centerplane of a jet in cross-flow (JICF); effect of mainstream Reynolds number on flow structure	-	Mean flow field, streamwise and vertical velocity fluctuations, Reynolds shear stress
(Barthet & Bario, 2001)	Aerodynamic performance and flow structures in a large-scale film-cooled turbine blade with single-row injection from SS	▪ Stagnation pressure coefficient	Counter-rotating vortex pair (CRVP), jet lift-off, anti-kidney vortices, mean cross-sectional vorticity field, horseshoe vortex, 3D jet separation inside the hole
(Keogh, 2001)	Aerodynamic performance of film-cooled turbine stage and detailed breakdown of film cooling losses	▪ Profile entropy loss coefficient (Hartel's method) ▪ Endwall loss energy loss coefficient ▪ Shapiro's influence coefficient (rotor seal leakage)	-
(Kost & Nicklas, 2001)	Aero-thermal performance and secondary flow structures in a film-cooled endwall	▪ Contour Mach number, flow angle, total pressure turbulence level and coolant concentration ▪ Primary or enthalpy loss coefficient ▪ Thermodynamic loss coefficient	Horseshoe vortex, passage vortex, shock waves

(Peterson & Plesniak, 2002)	Velocity field of multiple JICF from a single row of (short) holes and implications on gas turbine performance; effect of plenum feed direction	-	CRVP, anti-kidney vortices, in-hole flowfield, jet flowfield, downstream spiral separation node vortices (DSSN)
(Peterson & Plesniak, 2004)	Evolution of JICF from a single row of (short) holes; effect of plenum feed direction and variable blowing ratio	-	Quantitative analysis of mean flow structures and qualitative analysis of instantaneous flowfield; in-hole and jet flowfield
(Bernsdorf, et al., 2006)	Flow structures in single-row film cooling with PS (steady) flow conditions NB: Variable density ratio and stereo-PIV	-	Streamwise (1 location) and midspan axial velocity, streamwise and normal vorticity; CRVP and jet lift-off
(Jovanovic, 2006)	Film cooling in holes with production imperfections	-	Streamwise (8 locations) and midspan instantaneous and average velocity fields, vorticity fields, vortical structures (CRVP) near the hole, windward, lee and spiral vortices; turbulence characteristics
(Jessen, et al., 2007)	Turbulent flow and vortex dynamics of JICF NB: Variable density ratio and stereo- PIV	-	Measurements in XY, YZ and XZ (11 streamwise horizontal and vertical planes and midspan plane) velocity field, observing jet penetration, spanwise spreading, recirculation regions
(Peterson & Plesniak, 2007)	Flow structures and skin friction in a single row of (short) holes	-	Velocity field (in- hole and jet flowfield) and skin friction distribution (surface features, but not high resolution near the hole)
(Aga, et al., 2008)	Flow structures in a single row of (compound angled) holes NB: Variable density ratio and stereo- PIV	-	Axial velocity, streamwise and normal vorticity, special attention to vortical structures
(Bernsdorf, et al., 2008)	Flow structures in single-row film cooling with PS (unsteady) flow conditions	-	Streamwise (1 location) axial velocity and general 3D velocity field, center line trajectory

	NB: Variable density ratio and stereo- PIV		and streamwise circulation, observing periodic lift-off and reattachment
(Narzary, 2009)	Thermal study of film cooled turbine blade including pressure measurements	▪ Total pressure loss ▪ Tip pressure distribution	-
(Aga, 2009)	Flow structures in a single row of (compound angle) holes and aero-thermal performance; influence of flow structures in thermal performance NB: Variable DR and stereo- PIV	▪ Pressure and temperature signals with FENT entropy probe	CRVP replaced by only one large streamwise oriented vortex; streamwise (1 location) axial velocity, streamwise vorticity and circulation, wall-normal vorticity, steady and unsteady measurements
(Chappell, et al., 2010)	Aerodynamic performance of single and multi-row film cooling from SS	▪ Local total pressure coefficient ▪ Local exit Mach number ▪ Local exit kinetic energy ▪ Integrated aerodynamic losses	-
(Stephan, et al., 2010)	Aero-thermal performance of single or multi-row film cooling from SS in a NGV	▪ Primary loss coefficient ▪ Thermodynamic loss coefficient ▪ Mixing loss coefficient ▪ Outlet flow angle	-
(Aga & Abhari, 2011)	Influence of flow structure of (compound angle) holes in thermal performance NB: Variable density ratio and stereo- PIV	-	CRVP replaced by only one large streamwise oriented vortex; streamwise (1 location) axial velocity, streamwise vorticity and circulation, wall-normal vorticity, steady and unsteady measurements
(auf dem Kampe, et al., 2011)	Flowfield and downstream thermal performance of single-row film cooling; effect of hole geometry NB: Variable density ratio and stereo- PIV	-	Flow physics and structures of the film cooling jets and cross-flow interaction, 3D-velocity fields

(Wright, et al., 2011)	Jet structure and surface effectiveness of single-row film cooling; effect of freestream turbulence	-	Mean and instantaneous streamwise velocity field (3 locations) and jet structure, flow and surface measurements
(Fawcett, et al., 2012)	Forms of unsteadiness and effect of unsteady film cooling on jet and mainstream mixing	▪ Discharge coefficient	Time-averaged and unsteady flow structures like CRVP, anti-kidney vortices, Kelvin-Helmholtz instabilities; 2D- velocity field (2 measurement planes), vorticity measurements
(Issakhanian, et al., 2012)	In-hole and mainflow velocity of low momentum JICF; water as working fluid	-	Mean flowfield measurements; secondary flows within the hole, CRVP; special attention to vortical structures
(Jessen, et al., 2012)	Turbulent flow field from full-coverage film cooling with adverse pressure gradient; influence on thermal performance NB: Variable density ratio and planar & stereo- PIV	-	Measurements in XY, YZ and XZ (midspan, 1 spanwise plane and 3 streamwise vertical planes) of mean velocity field and fluctuations, streamwise vorticity, observing vortical structures and jet penetration
(Nguyen, et al., 2012)	Effect of number of rows and injection patterns for full-coverage film cooling on thermal performance and film formation and development	-	-
(Schulz, et al., 2012)	Effect of anti-vortex hole design on secondary flow structures and thermal performance	-	Secondary flow structures and anti-kidney vortex pairs at each side of the CRVP and interacting with it, streamwise vorticity, jet lift-off and reattachment
(Zhang, et al., 2012)	Flow structures in multi-row film cooling blade with different setting angles	-	Jet Lee wakes, high and low velocity regions, differences in film adherent performance between pressure and suction side
(Abdullah & Funazaki, 2013)	Aero-thermal interaction of jet and mainstream flow in multi-row film cooling; effect of freestream turbulence	-	Vortical structures (4 streamwise vertical measurement planes)

(Hassan, 2013)	Flow characteristics and thermal performance of film cooling with a micro-tangential-jet scheme	-	3D velocity distribution, vorticity field, presence of CRVP
(Wright, et al., 2013)	Flow characteristics and thermal performance of a double hole design	-	3D velocity distributions (5 streamwise measurement planes), jet structure and CRVP development, combined flow and surface measurements
(Johnson, et al., 2014)	Effect of density ratio on mixing between coolant and mainstream in single-row film cooling NB: Variable DR and planar PIV	-	Instantaneous and time-averaged 2D velocity distribution, presence of reverse flow upstream of the hole, combined flow and surface measurements
(Eberly & Thole, 2014)	Effect of density ratio on time-resolved flow field in single-row film cooling NB: Variable DR and planar PIV	-	Time-averaged and time-resolved 2D velocity field (2 spanwise measurement planes) and vorticity contours, presence of Kelvin-Helmholtz breakdown in the jet-to-freestream shear layer
(Lin, et al., 2014)	Aerodynamic performance of multi-row film cooling and effect of film cooling parameters with an unconventional mixing losses quantification method	▪ Averaged total pressure with the Ideal Isentropic Mixing (IIM) method	-
(Pu, et al., 2014)	Influence of film cooling injection and freestream turbulence on secondary flows characteristics	-	Time-resolved measurements of leading edge horseshoe vortex, corner vortices, passage vortex
(Zheng & Hassan, 2014)	Flowfield downstream of an unconventional geometry consisting of a hole with an orifice (nozzle hole jet)	-	Presence of double-decker vortices structure, reduced CRVP strength
(Anderson, et al., 2015)	Correct coolant flow scaling parameter for shaped holes in film cooling experiments, based on thermal performance	-	-
(Mamaev, et al., 2015)	Aerodynamic performance of a turbine cooled vane block with film	▪ Loss factor for cooled cascade under isothermal blowing	-

	cooling and convective cooling system	▪ Profile loss factor ▪ Secondary loss factor (for peripheral area and for root area)	
(Wang, et al., 2015)	Effect of inlet velocity in flow characteristics of jet and mainstream mixing in the tip gap	-	Mean velocity and vorticity showing flow distribution both in the tip clearance and in the passage
(Zhou & Hui, 2015)	Flow characteristics and thermal performance of a novel hole configuration with a Barchan dune-shaped ramp	-	Dynamic mixing between coolant jet stream and mainstream flows, observing downwash and jet diffusion
(Nikparto & Schobeiri, 2016)	Aero-thermal investigation of multi-row film cooling from PS and SS under steady and periodic unsteady conditions	-	Surface static pressure and velocity fluctuations, boundary layer measurements. Observations on laminar separation bubble in SS, size of the separation zone, transition
(Rouina, et al., 2016)	Unsteady flow behaviour of single-row film cooling	▪ Discharge coefficients	Time-mean and unsteady flow in coolant and mainstream mixing; presence of CRVP
(Natsui, et al., 2016)	Hydrodynamic measurements of multi-row film cooling	-	Mean values and fluctuations in streamwise velocity (2 measurement planes: centerline and spanwise)
(Watson, et al., 2016)	Flowfield and thermal performance in single-row film cooling at high density ratio NB: Variable DR and stereo-PIV	-	Mean velocity and vorticity distribution in 4 streamwise measurement planes
(Schroeder & Thole, 2016)	Effect of freestream turbulence on the flowfield and thermal performance of single-row film cooling from (shaped) holes	-	Mean flowfield data in centerline and crossplane; presence of CRVP structures, jet penetration into mainstream and lateral spreading, turbulence characteristics
(Berkache & Dizene, 2017)	Flowfield in multi-row film cooling and comparison with numerical results	-	Time-averaged velocity and turbulent kinetic energy
(Haydt, et al., 2017)	Flowfield in single-row film cooling; effect of area ratio changes by increase of hole length and	-	Differences in jet structure between low and high blowing ratio cases, with velocity deficit and

	constant expansion angle (shaped holes)		attached jet or high jet core speed and separated jet; presence of CRVP
(Wernet, et al., 2017)	Flowfield of single-row film cooling in multiple streamwise locations, as database for CFD models	-	3D-velocity and 3D-vorticity (dual-plane PIV) at 25 streamwise measurement planes; presence of horseshoe vortex
(Prenter, et al., 2017)	Aero-thermal performance of reverse-oriented film cooling holes	▪ Total pressure loss coefficient	Time-averaged centerline velocity field, highly unsteady coolant and freestream interaction, shedding of multiple vortical structures, jet penetration, recirculation zone
(Strausswald, et al., 2017)	Flow characteristics and thermal performance near the hole in single row film cooling	-	Centerline 2D- mean flowfield and fluctuations, coolant jet detachment; simultaneous thermal and aerodynamic performance assessment
(Vinton & Wright , 2017)	Effect of flow acceleration on flowfield from single row film cooling with (round and shaped) holes NB: Variable density ratio and stereo- PIV	-	3D-velocity field, effect of flow vorticity on thermal performance, reduction of jet separation due to favourable pressure gradient, increase of jet lateral spreading
(Voet, et al., 2017)	Effect of density ratio on jet structure from multi-row film cooling NB: Variable density ratio and planar- PIV	-	Flow interactions and jet structure in the mixing; 2D streamwise velocity, jet penetration and coalescence, turbulence characteristics
(Voet, 2017)	Effect of density ratio on flow structure hydrodynamics from multi-row film cooling NB: Variable density ratio and planar- PIV	-	Streamwise velocity contours, jet penetration and detachment, jet trajectory tracking
(Yao, et al., 2017)	Interaction of flowfield and thermal performance in double-jet holes design; effect of spanwise distance	-	Time-averaged velocity and vorticity (in 3 streamwise locations); presence of anti-kidney vortex pair

Section 2.3. Experimental conditions and flow scaling parameters

Table I.2. Literature study table for Section 2.3.

Reference (authors, date)	Model	Operating conditions		Scaling parameters					Foreign gas/other technique
		$Re_{c,\ inlet}$	M_{exit}	MFR	VR	I	BR	DR	
(Brown & Helon, 1973)	Stator vane with 4 rows (0.2c, 0.4c, 0.6c, 0.8c) of holes in SS, 2D cascade	-	0.48, 0.62, 0.78	0-0.03	0-1	-	0-1	1	-
(Stabe & Kline, 1975)	1 or 3 cooled vanes in a 10 vanes 2D cascade	-	0.6-0.95	-	-	-	-	1	-
(Prust, 1975)	Stator vane with 12 rows of holes (6 in PS and 6 in SS), 2D cascade	$4\cdot10^3$ - $14\cdot10^3_{diameter}$	0.5, 0.65, 0.8	0-0.04	-	-	-	1	-
(Ito, et al., 1980)	6 blades with 1 row of holes, 2D cascade	$2.2\cdot10^5_{outlet}$	-	0-0.03	-	-	-	1, 1.52	CO_2
(Haller & Camus, 1984)	Airfoil with 5 rows of holes in SS, 2D cascade	$8.5\cdot10^5_{outlet}$	Transonic 0.8-1.4	-	-	-	0-1.5	1-2	CO_2
(Pietrzyk, et al., 1990)	Flat adiabatic test plate with 1 row of holes	-	-	-	-	-	0.5	2	-
(Schwarz, et al., 1990)	Convex and concave injection surfaces	-	-	-	-	-	0.3-2.7	0.95, 2	Helium tracer, Freon-12
(Day, et al., 1996)	First stage vane with 5 rows of staggered holes in leading edge	-	-	-	0.35, 0.45, 0.79	-	0.35, 0.45, 0.79	1	-
(Thole, et al., 1996)	Flat plates with three different hole geometries	$5.2\cdot10^4_{diameter}$	-	-	-	-	1	1	-

(Osnaghi, et al., 1997)	High pressure NGV with 12 injection rows (3 in showerhead, 3 in PS, 5 in SS, 1 in trailing edge) 2D cascade	-	0.7, 0.85, 0.96	-	-	-	0.56, 0.72, 0.83, 1.11, 1.28	1, 1.52	CO_2
(Haven, et al., 1997)	Flat plate with 1 row of 5 holes	10^5 X-distance	-	-	1	-	1	1	-
(Drost, 1998)	Flat plate with 1 row of holes and 5 airfoils in a 2D cascade with various holes configurations	-	0.17-0.82	-	-	0.06-1.36	0.3, 0.5, 0.7, 1,1.5	1,1.6	CO_2 and cooling
(Urban, et al., 1998)	High pressure untwisted NGV with 17 rows of holes (4 in SS, 6 in PS and 6 in showerhead) in 2D cascade with 7 blades	$4 \cdot 10^5$ outlet	0.6-0.75	-	-	0.5-2.8	0.63-2.6	1.47; 1.65	Superheated steam cooling
(Burd & Simon, 1999)	Flat plate with 1 row of holes	$0\text{-}3 \cdot 10^4$ diameter	-	-	-	< 2.3	-	1	-
(Drost & Bölcs, 1999)	NGV with 8 rows of holes in 2D cascade	$1.45 \cdot 10^6$ outlet	0.3, 0.65, 0.8	-	-	0.5-5.5	0-4.5	1.05, 1.38, 1.39, 1.52, 1.65	CO_2 and cooling
(Jackson, et al., 2000)	Symmetric airfoil with 1 row of holes in linear 2D cascade	-	Transonic	-	-	0-0.319	0-0.605	0.839-1.23	Heating and cooling
(Day, et al., 2000)	NGV with 14 rows of holes in annular 2D cascade	$2 \cdot 10^6$	Transonic 0.96	0.05	-	-	-	1.77	SF_6/Ar mixture
(Kim, et al., 2000)	No model (free jet coming from straight pipe)	$1.05 \cdot 10^3$-$2.1 \cdot 10^3$ diameter	-	-	3.3	-	3.3	1	-

(Barthet & Bario, 2001)	Large scale (1.4 m chord) turbine inlet guide vane with single-row film cooling from SS	$1.31 \cdot 10^6$ outlet	-	-	-	-	1	-	Heating (jet flow 55ºC > crossflow temperature)
(Keogh, 2001)	Highly loaded turbine stage: NGV with 12 rows of holes and rotor blade with 5 rows of holes, from PS, SS, showerhead and trailing edge	$5.6 \cdot 10^6$	-	-	-	0-2	0-1.4	-	Ar and CO_2, temperature ratio (TR) of 0.91 and 0.63
(Kost & Nicklas, 2001)	High pressure turbine (HPT) NGV in linear cascade with 3 rows of holes in the forward part	$2.4 \cdot 10^5$ $8.5 \cdot 10^5$ outlet	Transonic 1	-	1.4 (SS) - 3.7 (PS)	-	1.4 (SS) - 3.7 (PS)	1	-
(Peterson & Plesniak, 2002)	Plate with a single row of 5 holes	$1.55 \cdot 10^3$ theta $1.2 \cdot 10^4$ diameter	-	-	1	-	1	1	-
(Peterson & Plesniak, 2004)	Plate with a single row of 5 holes	$6 \cdot 10^3$ diameter 10^3 theta	-	-	0.5-1	-	0.5, 1	1	-
(Bernsdorf, et al., 2006)	Flat plate with a single row of 7 holes	-	0.5 mainstream	-	-	0.654-7.245	0.994-2.692	1-1.53	Cooling
(Jovanovic, 2006)	Flat plate with 1 hole	$1.7 \cdot 10^3$ -$1.7 \cdot 10^4$ diameter $3.23 \cdot 10^5$ x-distance	0.11, 0.27, 0.47 mainstream	-	0.25, 0.50, 0.90, 1, 1.50	-	0.25, 0.50, 0.90, 1, 1.50	1	-
(Jessen, et al., 2007)	Flat plate with a symmetrical leading edge nose and 1 row of 3 holes	$4 \cdot 10^5$	-	-	0.18-0.48	0.05-0.35	0.28- 0.73	1, 1.53	CO_2
(Peterson & Plesniak, 2007)	Plate with a single row of 5 holes	$1.55 \cdot 10^3$ theta	-	-	0.5, 1	-	0.5, 1	1	-

(Aga, et al., 2008)	Flat plate with a single row of 7 holes	-	0.3 mainstream	-	-	0.64-9	1,2,3	1, 1.55	Cooling
(Bernsdorf, et al., 2008)	Flat plate with a single row of 7 holes	-	0.3 mainstream	-	-	0.65-6.50	0.99-2.69	1.01-1.73	Cooling
(Narzary, 2009)	High pressure turbine blade with 2 or 4 rows of holes (inline design) in a 5-blade linear cascade	$7.5\cdot10^5$ outlet	0.44 0.27 inlet	0.006-0.052	-	0.478-2.1	1,1.5,2	1.1, 1.8, 2.1	Cooling and foreign gas (CO_2 and SF_6/Ar)
(Aga, 2009)	Flat plate with a single row of 7 holes	$4.3\cdot10^4$ diameter	0.3 mainstream	-	-	0.67-4	1,2	1,1.5	Cooling
(Chappell, et al., 2010)	Vane with 1 or 2 rows of holes (staggered design) in 2D cascade	$5\cdot10^5$	0.35	-	-	-	0.6, 1.2	1.77-1.99	CO_2
(Stephan, et al., 2010)	NGV with two film cooling configurations: 1 row of holes at 0.09c or 2 rows (0.2 or 0.77) in 5-blade 2D cascade	$1.056\cdot10^6$ outlet	0.8	0.001-0.006	-	-	-	1	-
(Aga & Abhari, 2011)	Flat plate with (compound angled) holes	$4.6\cdot10^4$ diameter	0.3 mainstream	-	-	1-4	1-2	1-1.5	Cooling
(auf dem Kampe, et al., 2011)	Flat plate with 1 hole, of stainless steel for aerodynamic performance and Tecapeek for thermal performance	$2\cdot10^4$-$3\cdot10^4$ diameter	0.185 mainstream	-	-	-	0.5-2	1.1, 1.4	Cooling
(Wright, et al., 2011)	Flat plate with a single row of 7 holes	$1.03\cdot10^5$	-	-	0.5,1,1.5	-	0.5,1,1.5	1	-
(Fawcett, et al., 2012)	Blade with a single row of holes (0.5c) in the PS in a large scale linear cascade	$6\cdot10^5$ outlet	0.01	-	0.5-2	0.25-4	0.5-2	1	-

(Issakhanian, et al., 2012)	Single hole in the bottom wall of a recirculating water channel	$3.75 \cdot 10^4$ diameter	-	-	0.25, 0.5, 1	0.0625, 0.25, 1	0.25, 0.5, 1	1	-
(Jessen, et al., 2012)	Flat plate with symmetric leading-edge nose with 3 rows of holes (staggered)	$4 \cdot 10^5$	0.2	-	-	0.05-0.23	0.28, 0.48	1,1.53	CO_2
(Nguyen, et al., 2012)	Flat plate with 4 rows of holes (staggered) and additional rows for different configurations	750 diameter, mainstr. 6650 diameter, coolant	-	-	-	-	4	-	-
(Schulz, et al., 2012)	Flat plate with 3 holes with secondary offshoots	$1.1 \cdot 10^4$ diameter $3.8 \cdot 10^5$ x-distance	-	-	-	-	1,2	1.1	-
(Zhang, et al., 2012)	Turbine stator blade with 6 rows of holes (2 in PS, 1 in SS and 3 in leading edge)	-	-	-	0.5,1,1.5	-	0.5,1,1.5	1	-
(Abdullah & Funazaki, 2013)	Flat plate with 5 rows of holes (in-line)	$6.2 \cdot 10^3$ diameter	-	-	-	-	1,2	-	-
(Hassan, 2013)	Flat plate and vane with 1 row of micro-holes in the PS and 1 row in the SS in 2D cascade	$1.16 \cdot 10^5$ diameter	-	-	0.5, 1, 1.5, 2	-	0.5, 1, 1.5, 2	1	-
(Wright, et al., 2013)	Flat plate with a single row of holes	$1.126 \cdot 10^5$	-	-	0.5, 1, 1.5	-	0.5, 1, 1.5	1	-
(Johnson, et al., 2014)	Flat plate with a single row of holes	$2.2 \cdot 10^5$ x-distance	-	-	0.31-0.90	0.16-0.94	0,0.4, 0.85, 1, 1.70, 2	0.97, 1, 1.53	N_2 and CO_2
(Eberly & Thole, 2014)	Flat plate with a single row of 5 holes	2500-7000 diameter	-	-	0.32-1.7	0.16-3.3	0.25-2	1.2, 1.6	Cooling
(Lin, et al., 2014)	Turbine guide vane with 3 rows of holes in	-	-	-	-	-	0.5-2	1.05	-

	SS (0.17c, 0.53c, 0.63c) and 3 rows in PS (0.13c, 0.34c, 0.52c), 4 vanes -linear cascade								
(Pu, et al., 2014)	High pressure blades with 1 row of holes in linear cascade	$4 \cdot 10^4$ $1.2 \cdot 10^5$ outlet	-	-	0, 0.5, 1, 1.5	-	0, 0.5, 1, 1.5	1	-
(Zheng & Hassan, 2014)	Flat plate with one hole with an orifice	$1.15 \cdot 10^5$ diameter	-	-	0.5-2	-	0.5-2	1	-
(Anderson, et al., 2015)	Flat plate with one row of 8 holes; shown scaling parameters for round holes (not shaped ones)	$5.5 \cdot 10^3$ diameter	-	-	0.25, 0.4, 0.70	0.15, 0.25, 0.75	0.3, 0.5, 0.7, 1	1.2, 1.4, 1.6	Cooling
(Mamaev, et al., 2015)	Vane block with 9 rows of film cooling holes (6 in showerhead, 1 in PS, 2 in SS) and trailing edge slot ejection	$3 \cdot 10^6$	-	0.053	-	-	-	1	-
(Wang, et al., 2015)	Blade tip with five film cooling holes in a 5-blades cascade	$9 \cdot 10^4$	-	-	-	-	0,0.5, 1, 1.3, 2.5	-	-
(Zhou & Hui, 2015)	Flat plate with a single row of Barchan dune-shaped ramps upstream and downstream of coolant holes	-	-	-	-	-	0.4, 0.85, 1, 1.25	1.53	CO_2
(Nikparto & Schobeiri, 2016)	Highly loaded blade with 13 rows of holes (6 in SS; 6 in PS and 1 in leading edge) in a linear cascade	$1.5 \cdot 10^5$ x-distance, outlet	-	-	1	-	1	1	-
(Rouina, et al., 2016)	Flat plate with a single row of 3 holes	-	-	-	-	-	0.5-1.5	-	-

(Natsui, et al., 2016)	Flat plate with 8 rows of holes	-	-	-	-	-	0.45, 0.75, 1.05	1.52	CO_2
(Watson, et al., 2016)	Flat plate with a single row of 5 holes	$1.126 \cdot 10^5$ outlet	-	-	-	0.0625-2.25	0.5, 1, 1.5	1,2,3,4	Ar/SF_6 mixture
(Schroeder & Thole, 2016)	Flat plate with a single row of 5 holes	-	-	-	-	-	1.5, 3	1.5	Cooling
(Berkache & Dizene, 2017)	Flat plate with 4 rows of (staggered) holes	$1.2 \cdot 10^5$	-	-	2	-	2	1	-
(Haydt, et al., 2017)	Flat plate with a single row with 5 holes	$5 \cdot 10^3$-$3 \cdot 10^4$ 670 theta $4.3 \cdot 10^3$ diameter	-	-	-	-	1, 3, 6	1.2	Cooling
(Wernet, et al., 2017)	Flat plate with single row of 3 holes or 1 hole	$1.1 \cdot 10^4$ diameter	-	-	-	-	1, 2 (or 1.15 and 2.3 with heating)	1, 0.89	Heating of coolant
(Prenter, et al., 2017)	Flat plate with a single row of 6 holes	$1.05 \cdot 10^4$ diameter	-	-	-	-	0.25, 0.5, 1	1.06-1.08	Heating of freestream
(Strausswald, et al., 2017)	Flat plate with a single row of 3 holes	$2.6 \cdot 10^3$ diameter	-	-	-	8	3.6	1.6	Cooling
(Vinton & Wright , 2017)	Flat plate with a single row of 5 holes	-	-	-	-	-	0.5-1.5	1, 3	Ar/SF_6
(Voet, et al., 2017)	Flat plate with 8 rows of holes	-	-	-	0.2-0.53	0.06-0.29	0.31-0.54	1, 1.5	CO_2
(Voet, 2017)	Flat plate with 8 rows of holes	-	-	-	0.21-1.39	0.07-2.02	0.32-1.45	1, 1.5	CO_2
(Yao, et al., 2017)	Flat plate with one double-jet hole	-	-	-	0.5, 1, 1.5, 2	-	0.5, 1, 1.5, 2	1	-

Section 2.4. Flow measurement techniques and use of PIV

Table I.3. Literature study table for Section 2.4.

Reference (authors, date)	Measurement technique	PIV setup	Qualitative flow visualisation
(Brown & Helon, 1973)	Exit survey probe (static pressure, total pressure and flow angle)	-	-
(Stabe & Kline, 1975)	Exit survey probe (static pressure, total pressure and flow angle)	-	-
(Prust, 1975)	Exit survey probe (static pressure, total pressure and flow angle)	-	-
(Ito, et al., 1980)	Yaw meter, impact tube and pitot tube	-	-
(Haller & Camus, 1984)	Wake pressure probe and surface pressure tabs	-	Schlieren photography
(Pietrzyk, et al., 1990)	Laser doppler velocimetry (LDV)	-	-
(Schwarz, et al., 1990)	Heat transfer measurement techniques	-	CO_2 vapor jets photography
(Day, et al., 1996)	PIV	planar	-
(Thole, et al., 1996)	LDV	-	-
(Osnaghi, et al., 1997)	Five-hole pressure probe	-	-
(Haven, et al., 1997)	PIV	planar	Laser induced fluorescence (LIF) in water
(Drost, 1998)	Five-hole pressure probe and constant temperature hot-wire anemometry (HWA) for turbulence measurements	-	▪ Oil flow visualisation (mixture of silicon oil and phenolphthalein powder) ▪ Shear stress sensitive liquid crystals
(Urban, et al., 1998)	Five-hole pressure probe widened with a thermocouple	-	-
(Burd & Simon, 1999)	HWA	-	-
(Drost & Bölcs, 1999)	Five-hole pressure probe	-	-
(Jackson, et al., 2000)	Pitot-static probe and four-hole conical-tripped pressure probe with attached thermocouples	-	Schlieren images
(Day, et al., 2000)	Four-hole pyramid pressure probe	-	Schlieren photography and holography
(Kim, et al., 2000)	PIV	planar	Instantaneous tomographic images, with a laser sheet beam at the jet centerplane and olive oil aerosols supplied into the jet flow

(Barthet & Bario, 2001)	PIV, LDV for near the wall regions (to avoid laser reflections) and stagnation pressure probes	planar	-
(Keogh, 2001)	Rake type pressure probe with 8 impact heads	-	-
(Kost & Nicklas, 2001)	Laser-2-focus (L2F) laser velocimetry technique from DLR, combined with Pitot-tube (for a plane shortly behind the cascade) and with pyramid-like pressure probes (for further downstream measurements at the wake)	-	▪ Oil flow visualisation ▪ Laser velocimetry ▪ Schlieren pictures
(Peterson & Plesniak, 2002)	PIV	planar	-
(Peterson & Plesniak, 2004)	PIV and HWA for turbulence measurements	planar	-
(Bernsdorf, et al., 2006)	PIV	stereoscopic	-
(Jovanovic, 2006)	PIV	planar	Laser induced fluorescence
(Jessen, et al., 2007)	PIV	planar and stereoscopic	-
(Peterson & Plesniak, 2007)	PIV (velocity field) and Fringe-imaging skin friction oil-film interferometry (skin friction)	planar	-
(Aga, et al., 2008)	PIV	stereoscopic	-
(Bernsdorf, et al., 2008)	PIV	stereoscopic	-
(Narzary, 2009)	Pressure sensitive paint (PSP) and surface pressure taps for local static pressure and an array of 8 pitot tubes for exit total pressure	-	-
(Aga, 2009)	PIV and Fast Response Entropy Probe (FREP) for mixing losses	stereoscopic	-
(Chappell, et al., 2010)	Four-hole conical-tipped pressure probe with a thermocouple for total and static pressure and recovery temperature	-	-
(Stephan, et al., 2010)	Straight five-hole pressure probe	-	-
(Aga & Abhari, 2011)	PIV	stereoscopic	-

(auf dem Kampe, et al., 2011)	PIV and 3D-LDV	stereoscopic	-
(Wright, et al., 2011)	PIV and PSP	planar	-
(Fawcett, et al., 2012)	PIV and high-speed imaging (for higher frequency and smaller structures of the shear layer)	planar	-
(Issakhanian, et al., 2012)	Magnetic resonance velocimetry (MRV)	-	-
(Jessen, et al., 2012)	PIV	planar and stereoscopic	-
(Nguyen, et al., 2012)	Thermal measurements (IR Thermography)	-	-
(Schulz, et al., 2012)	PIV	planar	-
(Zhang, et al., 2012)	PIV	planar	-
(Abdullah & Funazaki, 2013)	LDV	-	-
(Hassan, 2013)	PIV	stereoscopic	-
(Wright, et al., 2013)	PIV and PSP	stereoscopic	-
(Johnson, et al., 2014)	PIV and PSP	planar	-
(Eberly & Thole, 2014)	PIV and LDV	planar	-
(Lin, et al., 2014)	Five-hole probe fixed on a shifting axis	-	-
(Pu, et al., 2014)	PIV	planar	-
(Zheng & Hassan, 2014)	PIV	stereoscopic	-
(Anderson, et al., 2015)	Thermal measurements (IR Thermography)	-	-
(Mamaev, et al., 2015)	Five-point L-shaped orientated probe for total pressure and nine sensors for static pressure	-	-
(Wang, et al., 2015)	PIV and pressure tabs	planar	High speed photography
(Zhou & Hui, 2015)	PIV and PSP	planar	-
(Nikparto & Schobeiri, 2016)	Static pressure tabs connected to pneumatic pressure transducers and 3-axis traversing system	-	-
(Rouina, et al., 2016)	PIV (whole flow field visualisation) and LDV (boundary layer measurements upstream and downstream of the holes)	planar	PIV with vegetable oil seeded in the coolant flow

(Natsui, et al., 2016)	PIV	planar	Particle scattering
(Watson, et al., 2016)	PIV	stereoscopic	-
(Schroeder & Thole, 2016)	PIV	planar and stereoscopic	-
(Berkache & Dizene, 2017)	PIV	planar	-
(Haydt, et al., 2017)	PIV	stereoscopic	-
(Wernet, et al., 2017)	PIV	dual-plane PIV (2 stereo-PIV systems)	-
(Prenter, et al., 2017)	PIV and pitot-probe for exit total pressure measurements	planar	PIV with high seed density in coolant flow and particulate-free freestream
(Strausswald, et al., 2017)	Thermographic PIV	-	-
(Vinton & Wright , 2017)	PIV	stereoscopic	-
(Voet, et al., 2017)	PIV	planar	-
(Voet, 2017)	PIV	planar	-
(Yao, et al., 2017)	Seven-hole probe in traversing system and HWA for turbulence measurements	-	-

Appendix II: Bronkhorst flow controller

In this Appendix, the calibration certificate for the Bronkhorst flowcontroller used in the experiments is included. It shows the calibration curve, calibration conditions and accuracy level of the measurements. Information about the gas conversion factor (calculation method and values) extracted from Bronkhorst *Instruction manual of mass flow/pressure meters and controllers* is also presented.

Calibration certificate

Bronkhorst®

CALIBRATION CERTIFICATE

FLUID NO. 1 OF 1

CERTIFICATE NO. BHTG19/2352563

Calibration by comparison
Calibration date: 21 Jun 2017

We hereby certify that the instrument mentioned below has been calibrated in accordance with the stated values and conditions. The calibration standards used are traceable to national standards of the Dutch Metrology Institute VSL.

Calibrated instrument

Type	Flow controller (D)
Serial number	M12200234A
Model number	F-202AV-M20-DGD-55-V
Rated accuracy*	±(0.5%Rd + 0.1%FS)

Calibration standard

Type	Rotor meter
Serial number	80186
Certificate no.	NMi/G16S3938
Uncertainty	±0.3% Rd

Customer conditions

Fluid	**AiR**
Flow	**260.0 ln/min**
Pressure	**7.0 bar (a)**
Temperature	**20.0 °C**

Calibration conditions

Fluid	AiR
Flow	260.4 ln/min (equivalent flow)
Pressure	5.0 bar (a)
Temperature	21.3 °C
Atm. pressure	1017.1 hPa (a)

Calibration and conversion results

Output signal	Customer flow** AiR	Equivalent flow** AiR	Reference flow AiR	Measured deviation*	Measurement uncertainty*
100.82%	262.1 ln/min	262.6 ln/min	261.4 ln/min	0.46 % Rd	0.4 % Rd
50.20%	130.5 ln/min	130.8 ln/min	130.7 ln/min	0.08 % Rd	0.4 % Rd
0.00%	0.000 ln/min	0.000 ln/min	0.000 ln/min	-	-

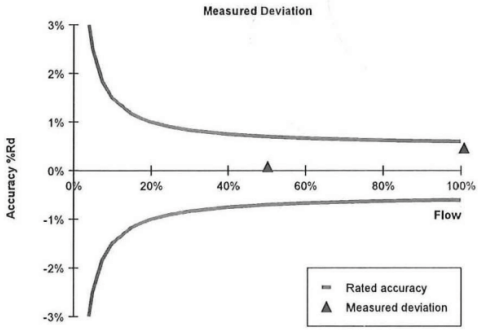

Notes

Flow unit ln/min is defined at conditions 0.00 °C, 1013.25 hPa (a).
* Rated accuracy, measured deviation and measurement uncertainty are specified under calibration conditions in digital mode.
** The customer flow at customer conditions is converted to equivalent flow at calibration conditions using Bronkhorst High-Tech FLUIDAT® software.

Measurement uncertainties are based upon 95% (k=2) confidence limits. Although the item calibrated meets the specifications and performance at the time of calibration, due to any number of factors, this does not imply continuing conformance to the specifications.

Calibrator M.Se.

QC H.Wi.

Date 21 Jun 2017

Signed .....

MultiCal V2.06 FLUIDAT® V5.73 (Database: 05-05-1999) Report V1.13

Figure II.1 Calibration certificate for the Bronkhorst flowcontroller used in the experiments

Bronkhorst gas conversion factor

BRONKHORST®

1.8 Conversion factors

1.8.1 Gas conversion factors

The general formula for determining the relationship between signal and mass flow is:

$$V_{signal} = K \cdot c_p \cdot \Phi_m = K \cdot c_p \cdot \rho \cdot \Phi_v$$

in which:

V_{signal}	= output signal
K	= constant
ρ	= density
c_p	= specific heat
Φ_m	= mass flow
Φ_v	= volume flow

As soon as the c_p value and density of the gas to be metered change, the signal must be corrected. The conversion factor C is:

$$C = \frac{c_{p_1} \cdot \rho_1}{c_{p_2} \cdot \rho_2}$$

in which:

c_p	= specific heat
ρ_n	= density at normal conditions

(1) gas calibrated
(2) gas to be measured

BRONKHORST®

The approximate accuracy of the conversion factors listed is:

typical for conversion factors;	> 1	**2% x factor**
	< 1	**2% / factor**

However, as the accuracy of the factor also depends on viscosity, pressure and temperature, special attention should be taken for gases in the gas/liquid state where specific heat, density and viscosity can vary tremendously. Apply to factory for more detailed information.

Figure II.2 Bronkhorst gas conversion factor calculation method provided in the Instruction manual

GAS CONVERSION FACTOR

Nr.:	Name:	Symbol	Density ρ_n [g / l] 0°C, 1 atm.	Heat capacity* c_p – cal[cal / g.K] 20°C, 1 atm.	Conversion factor 20°C, 1 atm.
1	Acetylene (Ethyne)	C_2H_2	1.172	0.438	0.61
2	Air	Air	1.293	0.241	1.00
3	Allene (Propadiene)	C_3H_4	1.832	0.392	0.43
4	Ammonia	NH_3	0.7693	0.524	0.77
5	Argon	Ar	1.784	0.125	1.40
6	Arsine	AsH_3	3.524	0.133	0.66
7	Boron trichloride	BCl_3	5.227	0.136	0.44
8	Boron trifluoride	BF_3	3.044	0.188	0.54
9	Bromine pentafluoride	BrF_5	7.803	0.156	0.26
10	Butadiene (1,3-)	C_4H_6	2.504	0.405	0.31
11	Butane	C_4H_{10}	2.705	0.457	0.25
12	Butene (1-)	C_4H_8	2.581	0.415	0.29
13	Butene (2-) (Cis)	C_4H_8	2.503	0.387	0.32
14	Butene (2-) (Trans)	C_4H_8	2.503	0.421	0.30
15	Carbonylfluoride	COF_2	2.983	0.194	0.54
16	Carbonylsulfide	COS	2.724	0.175	0.65
17	Carbon dioxide	CO_2	1.977	0.213	0.74
18	Carbon disulfide	CS_2	3.397	0.152	0.60
19	Carbon monoxide	CO	1.25	0.249	1.00
20	Chlorine	Cl_2	3.218	0.118	0.82
21	Chlorine trifluoride	ClF_3	4.125	0.188	0.40
22	Cyanogen	C_2N_2	2.376	0.275	0.48
23	Cyanogen chloride	ClCN	2.743	0.185	0.61
24	Cyclopropane	C_3H_6	1.919	0.374	0.43
25	Deuterium	D_2	0.1798	1.73	1.00
26	Diborane	B_2H_6	1.248	0.577	0.43
27	Dibromo difluoromethane	Br_2CF_2	9.361	0.17	0.20
28	Dichlorosilane	SiH_2Cl_2	4.506	0.17	0.41
29	Dimethylamine	C_2H_6NH	2.011	0.417	0.37
30	Dimethylpropane (2,2-)	C_5H_{12}	3.219	0.462	0.21
31	Dimethylether	C_2H_6O	2.105	0.378	0.39
32	Disilane	Si_2H_6	2.857	0.352	0.31
33	Ethane	C_2H_6	1.355	0.468	0.49
34	Ethylene (Ethene)	C_2H_4	1.261	0.414	0.60
35	Ethylene oxide	C_2H_4O	1.965	0.303	0.52
36	Ethylacetylene (1-Butyne)	C_4H_6	2.413	0.401	0.32
37	Ethylchloride	C_2H_5Cl	2.878	0.263	0.41
38	Fluorine	F_2	1.696	0.201	0.91
39	Freon-11	CCl_3F	6.129	0.145	0.35
40	Freon-113	$C_2Cl_3F_3$	8.36	0.174	0.21
41	Freon-1132A	$C_2H_2F_2$	2.889	0.244	0.44
42	Freon-114	$C_2Cl_2F_4$	7.626	0.177	0.23
43	Freon-115	C_2ClF_5	7.092	0.182	0.24
44	Freon-116	C_2F_6	6.251	0.2	0.25
45	Freon-12	CCl_2F_2	5.547	0.153	0.37
46	Freon-13	$CClF_3$	4.72	0.165	0.40
47	Freon-13B1	$CBrF_3$	6.768	0.12	0.38
48	Freon-14	CF_4	3.946	0.18	0.44
49	Freon-21	$CHCl_2F$	4.592	0.154	0.44
50	Freon-22	$CHClF_2$	3.936	0.168	0.47
51	Freon-23	CHF_3	3.156	0.191	0.52
52	Freon-C318	C_4F_8	9.372	0.222	0.15
53	Germane	GeH4	3.45	0.16	0.56

* c_p - cal (T,p) = c_p (T + 50°C, p)

Figure II.3. Bronkhorst gas conversion factors table provided in the Instruction manual

Appendix III: Pressure measurements results

In this section the pressure measurements results presented in Chapter 4 are extended, including the wake profile and aerodynamic losses for all the film cooling configurations, and both air and CO_2.

Air as secondary flow

Wake gauge total pressure, P_t $[Pa]$

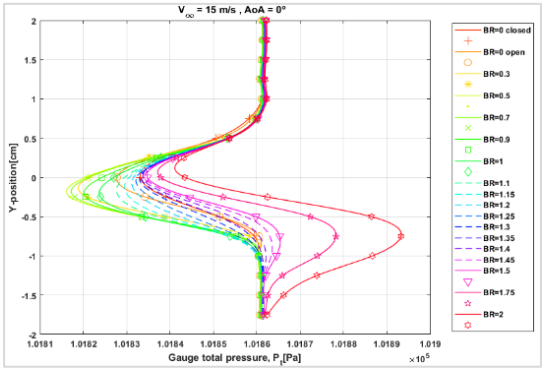

Baseline configuration

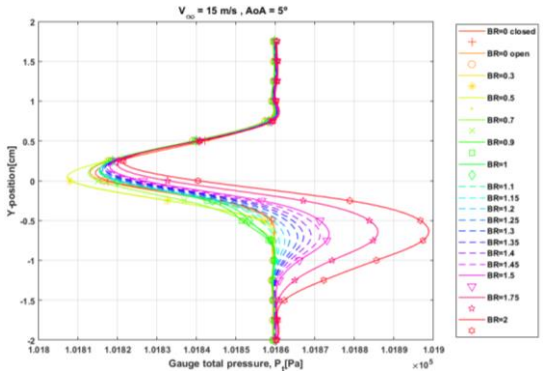

AoA=5°

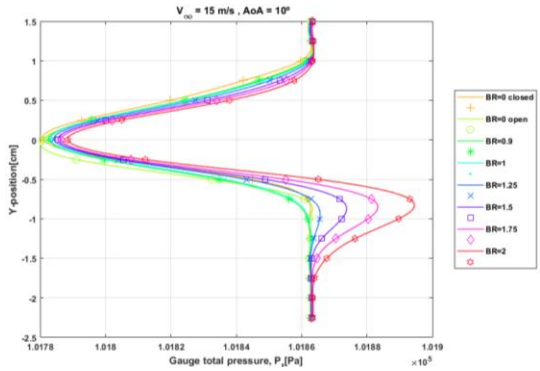

AoA=10°

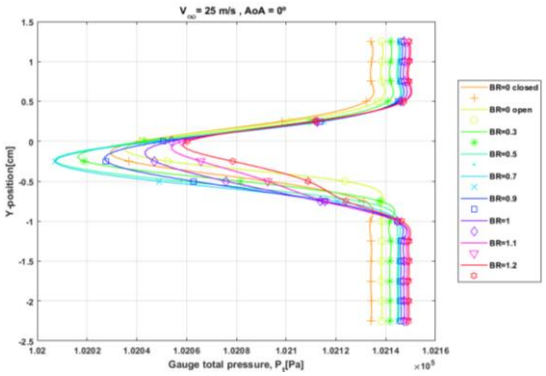

$V_\infty = 25\ m/s$

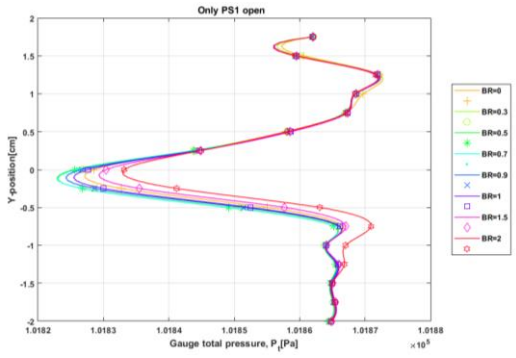

Partial injection: only PS1 open

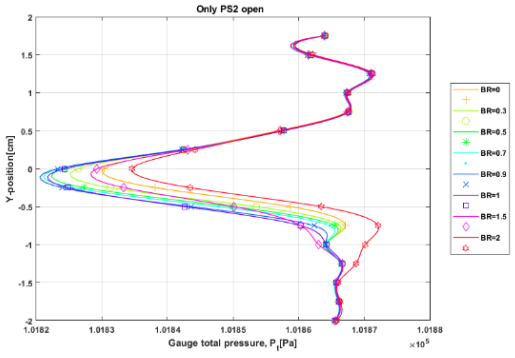

Partial injection: only PS2 open

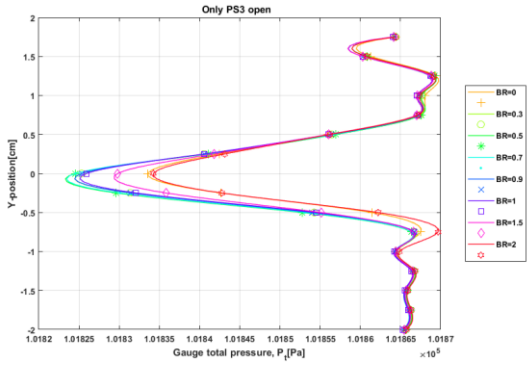

Partial injection: only PS3 open

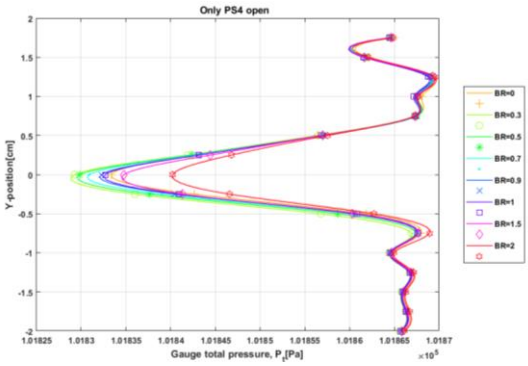

Partial injection: only PS4 open

Figure III.1. Wake gauge total pressure profile for all tested configurations. Air as secondary flow.

Wake velocity, V_2 $[m/s]$

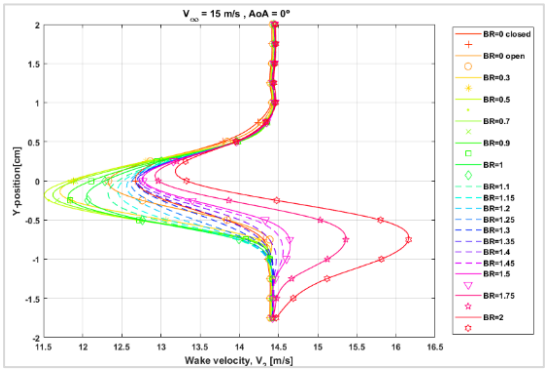

Baseline configuration

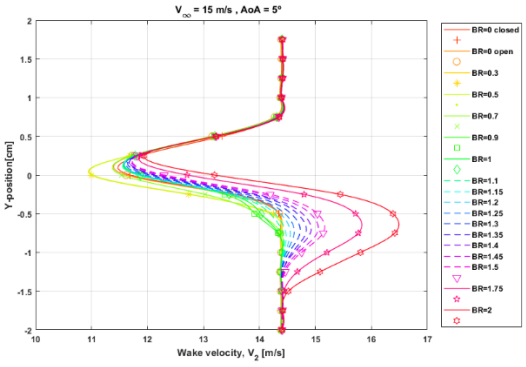

AoA=5°

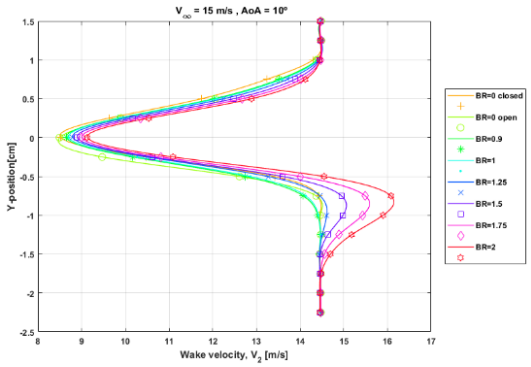

AoA=10°

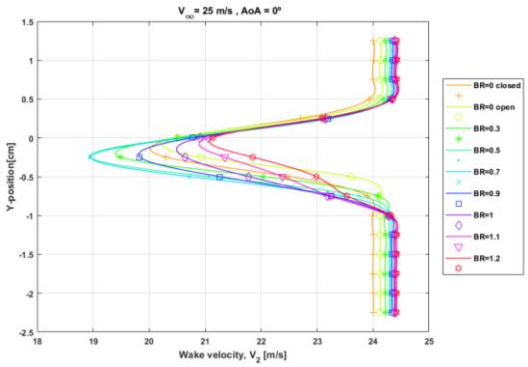

$V_\infty = 25\ m/s$

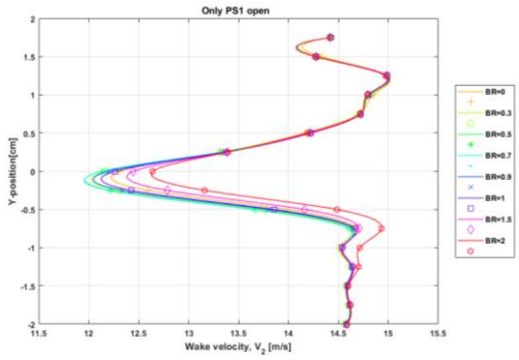

Partial injection: only PS1 open

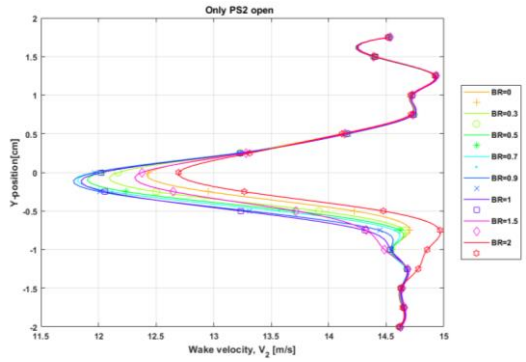

Partial injection: only PS2 open

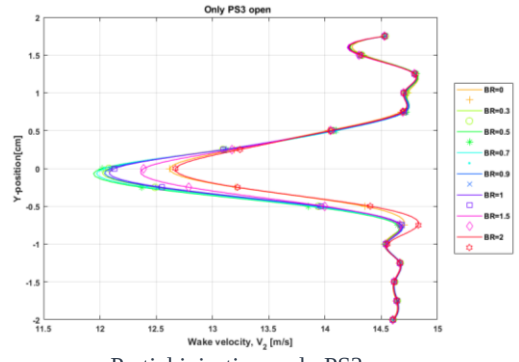

Partial injection: only PS3 open

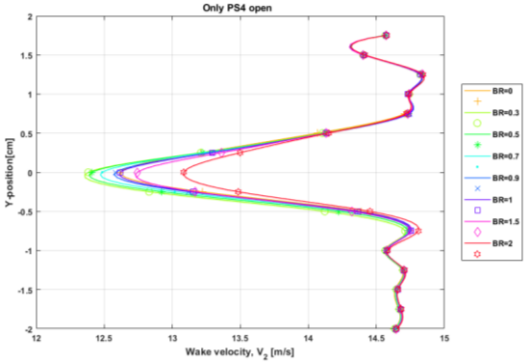

Partial injection: only PS4 open

Figure III.2. Wake velocity profile for all tested configurations. Air as secondary flow.

Primary loss coefficient, ξ_p [-]

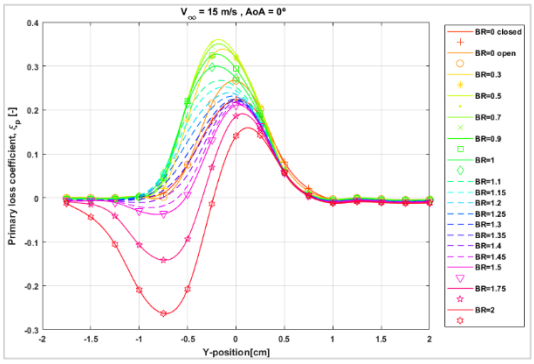

Baseline configuration

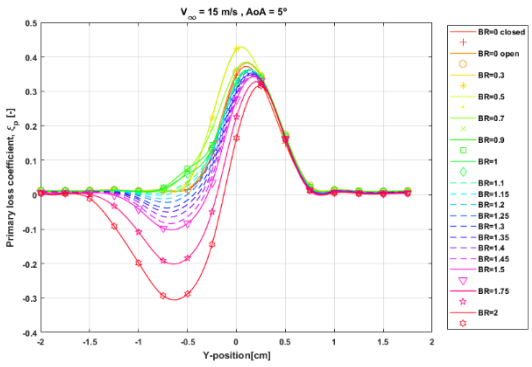

AoA=5°

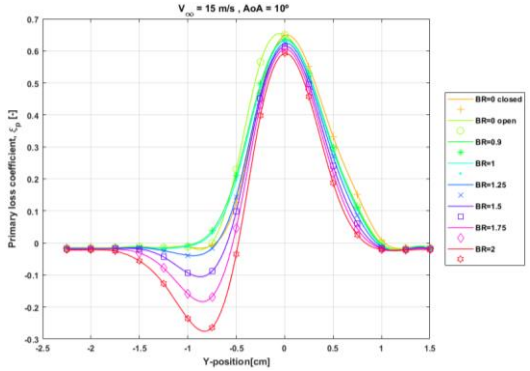

AoA=10°

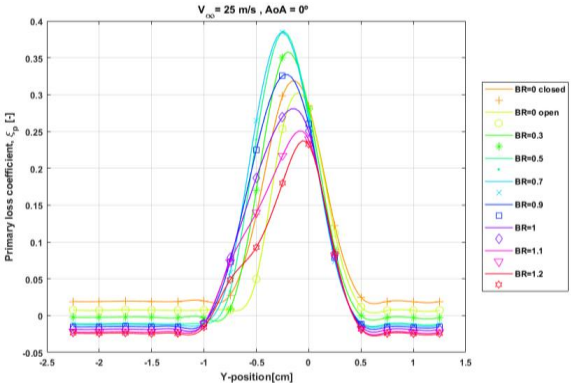

$V_\infty = 25\ m/s$

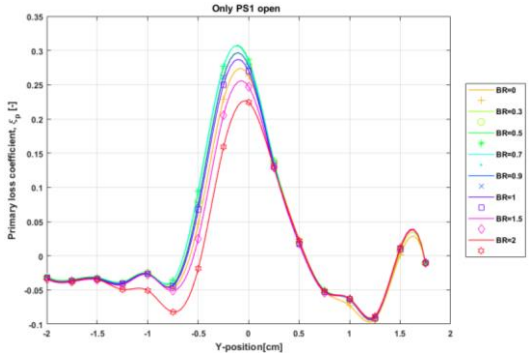

Partial injection: only PS1 open

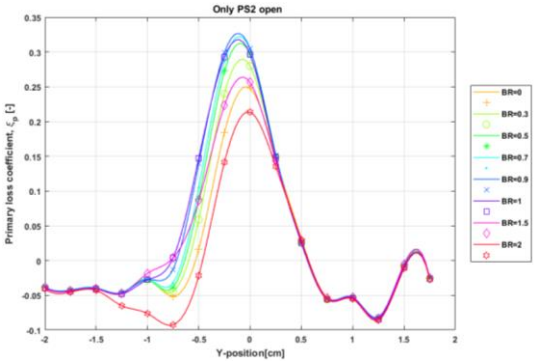

Partial injection: only PS2 open

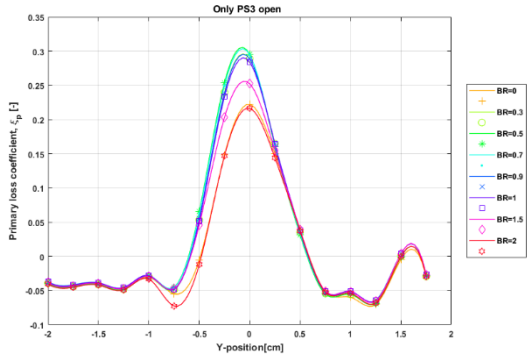

Partial injection: only PS3 open

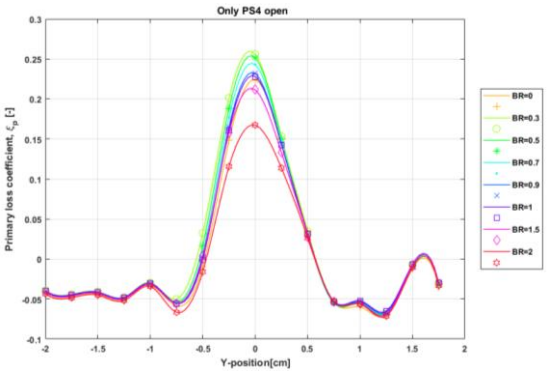

Partial injection: only PS4 open

Figure III.3. Wake primary loss coefficient for all tested configurations. Air as secondary flow.

Local total pressure loss coefficient, C_p [-]

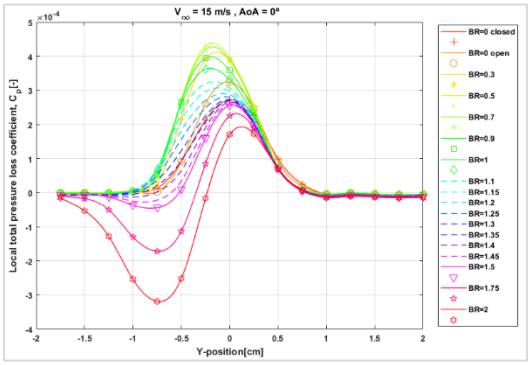

Baseline configuration

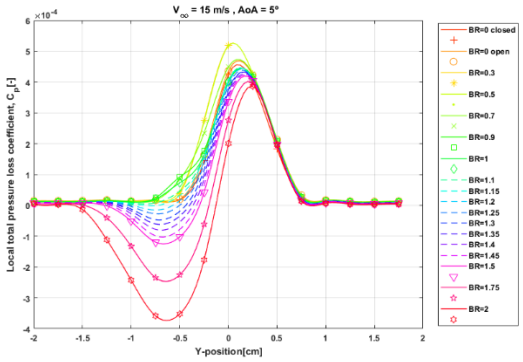

AoA=5°

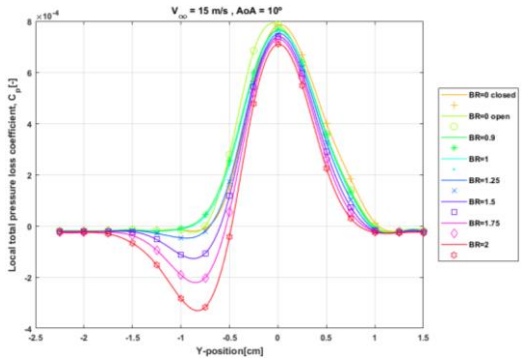

AoA=10°

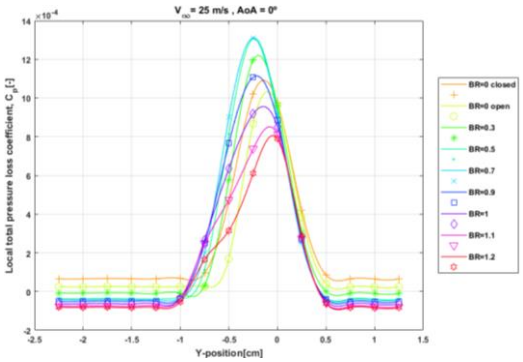

$V_\infty = 25\ m/s$

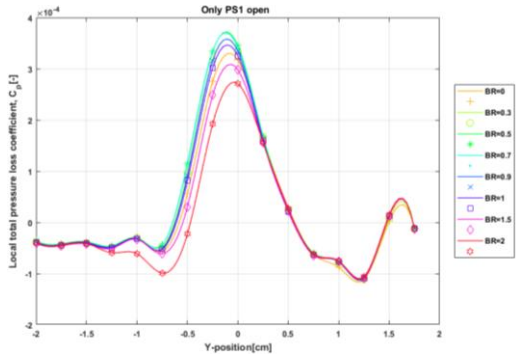

Partial injection: only PS1 open

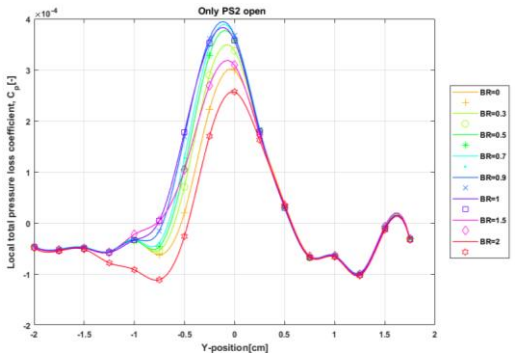

Partial injection: only PS2 open

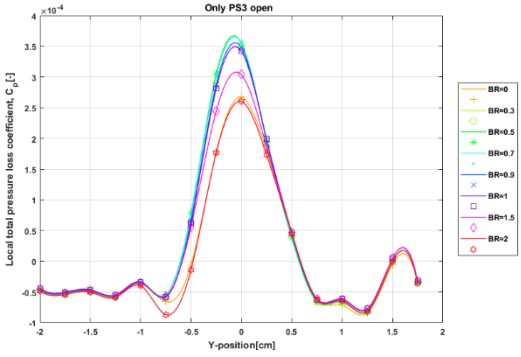

Partial injection: only PS3 open

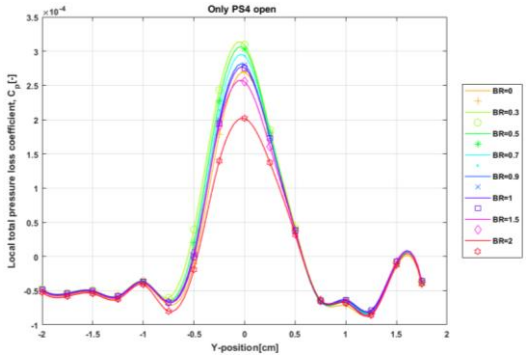

Partial injection: only PS4 open

Figure III.4. Wake local total pressure loss coefficient for all tested configurations. Air as secondary flow.

Total pressure loss coefficient, C_{pt} [-]

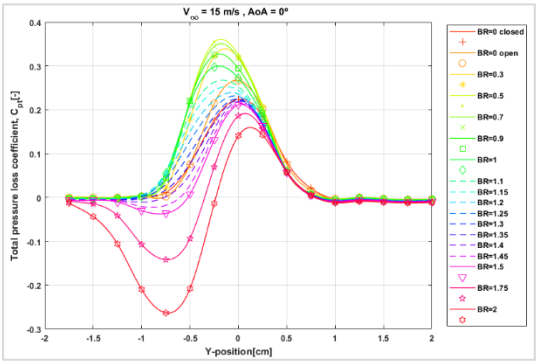

Baseline configuration

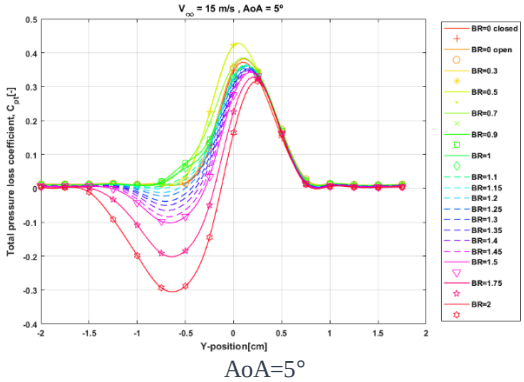

AoA=5°

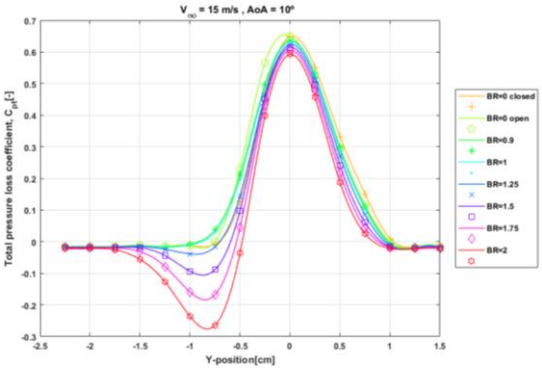

AoA=10°

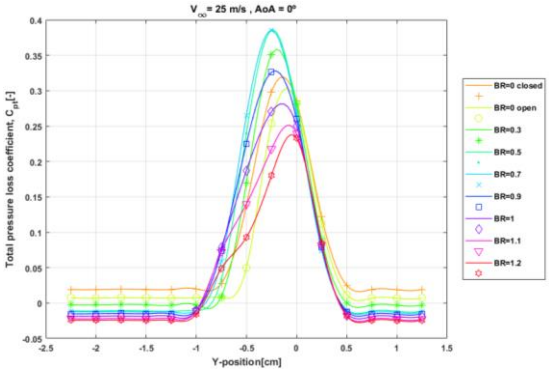

$V_\infty = 25\ m/s$

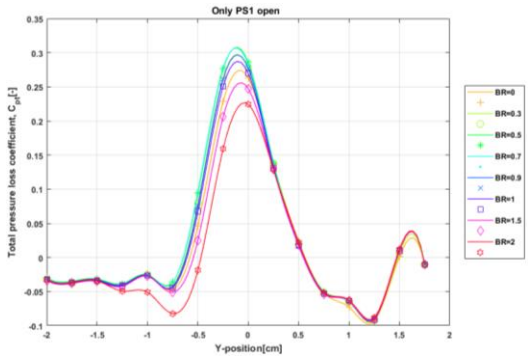

Partial injection: only PS1 open

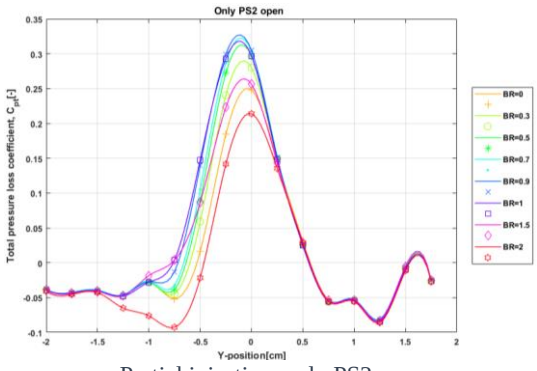

Partial injection: only PS2 open

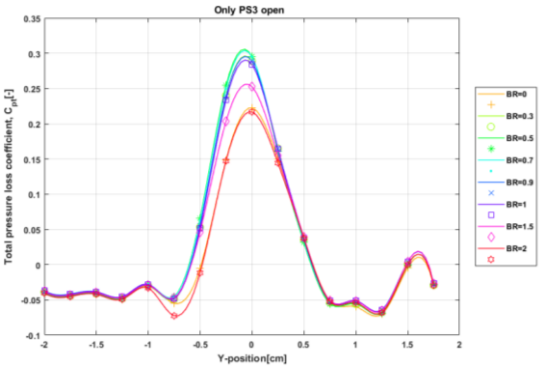

Partial injection: only PS3 open

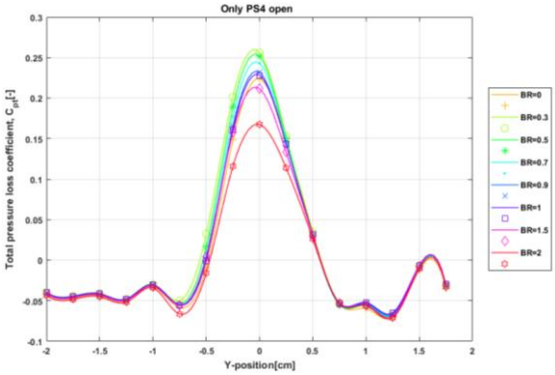

Partial injection: only PS4 open

Figure III.5. Wake total pressure loss coefficient for all tested configurations. Air as secondary flow.

Integrated aerodynamic losses, *IAL* [-]

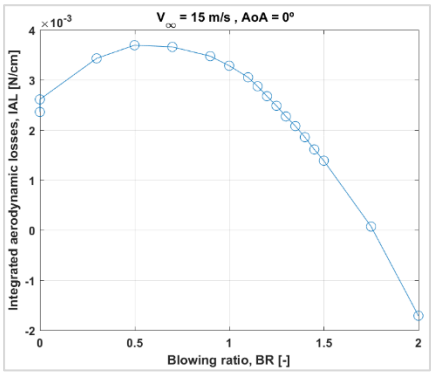

Baseline configuration

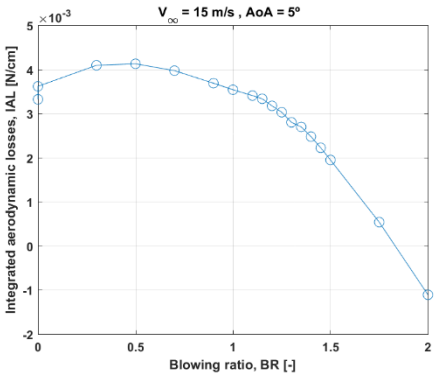

AoA=5°

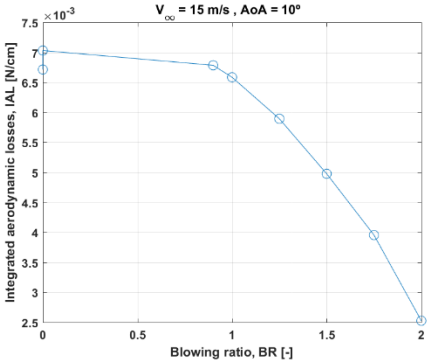

AoA=10°

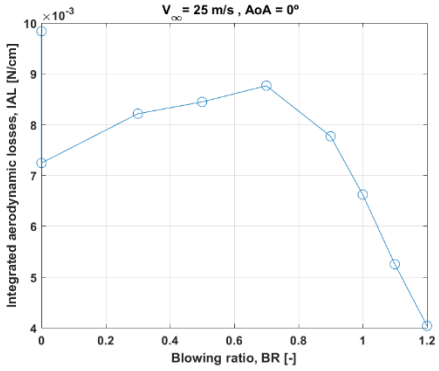

$V_\infty = 25\ m/s$

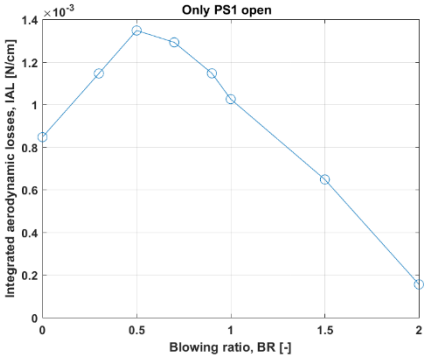

Partial injection: only PS1 open

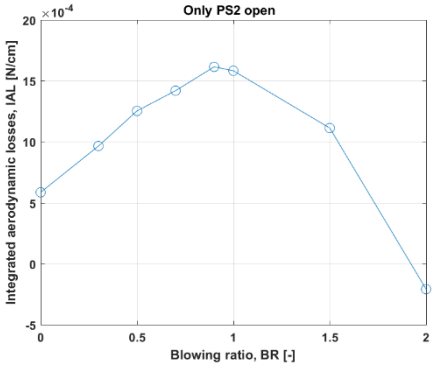

Partial injection: only PS2 open

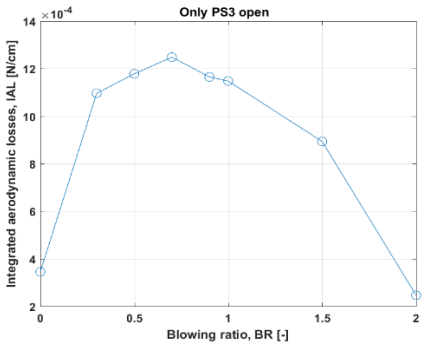

Partial injection: only PS3 open

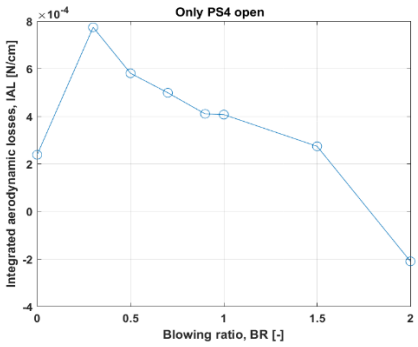

Partial injection: only PS4 open

Figure III.6. Wake integrated aerodynamic losses for all tested configurations. Air as secondary flow.

Area-averaged loss coefficient, λ [-]

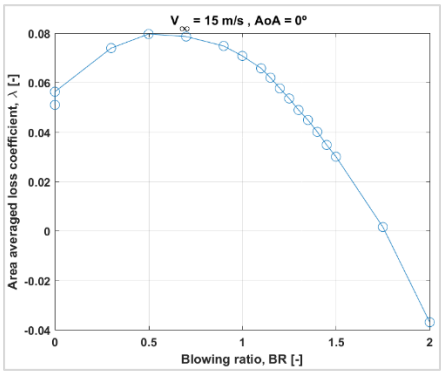

Baseline configuration

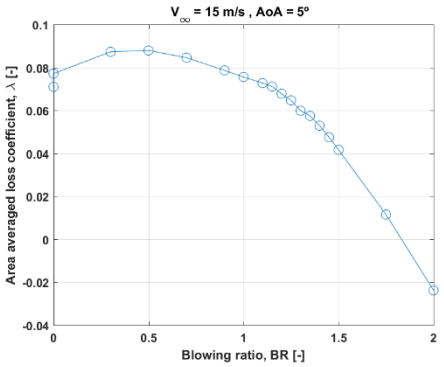

AoA=5°

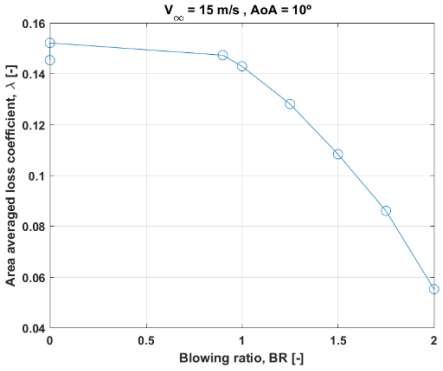

AoA=10°

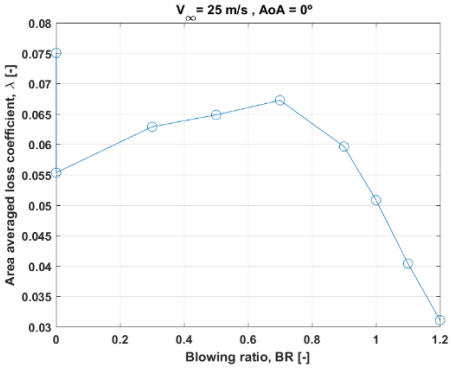

$V_\infty = 25\ m/s$

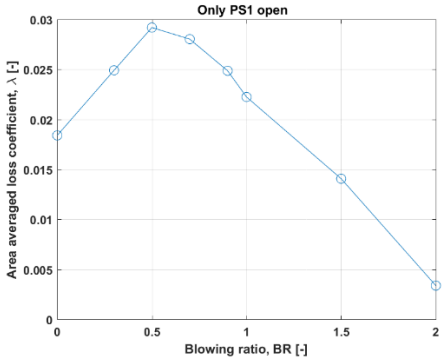

Partial injection: only PS1 open

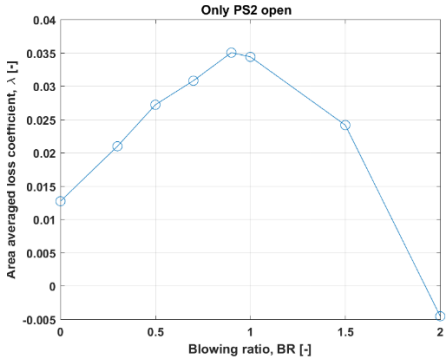

Partial injection: only PS2 open

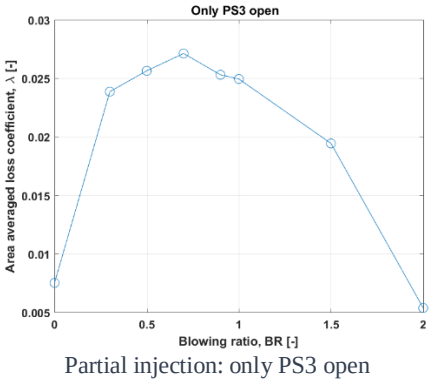

Partial injection: only PS3 open

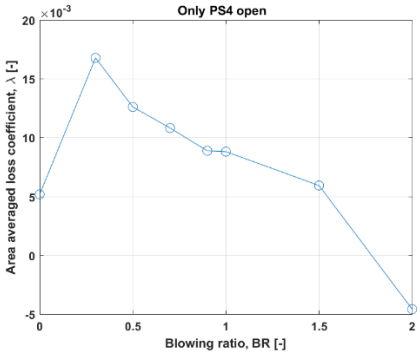

Partial injection: only PS4 open

Figure III.7 Wake area-averaged loss coefficient for all tested configurations. Air as secondary flow.

Area-averaged loss coefficient minus profile losses, $\Delta\lambda$ [-]

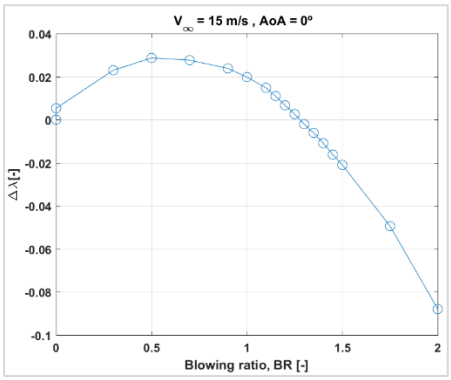

Baseline configuration

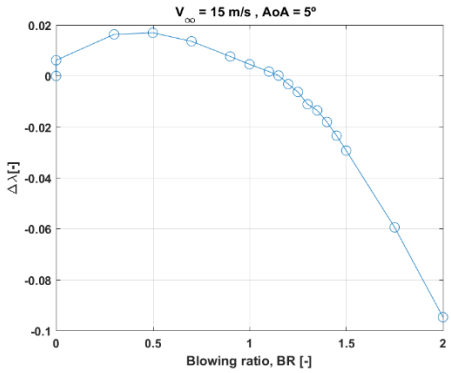

AoA=5°

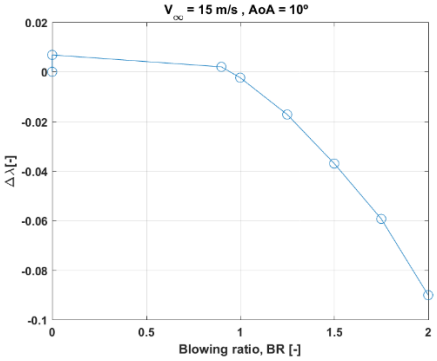

AoA=10°

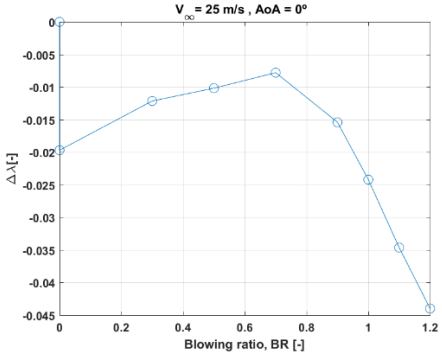

$V_\infty = 25\ m/s$

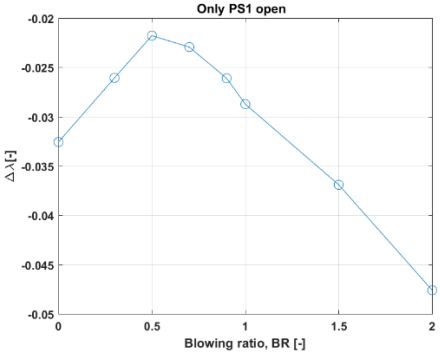

Partial injection: only PS1 open

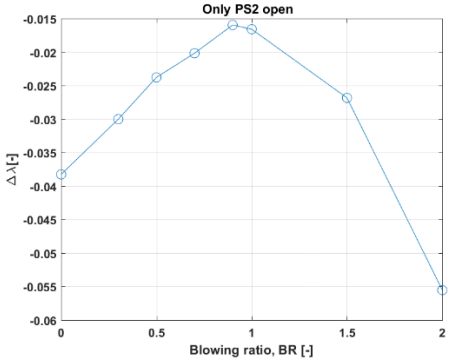

Partial injection: only PS2 open

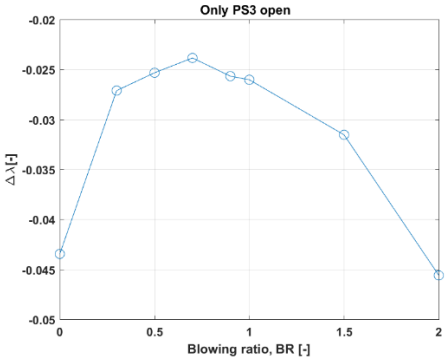

Partial injection: only PS3 open

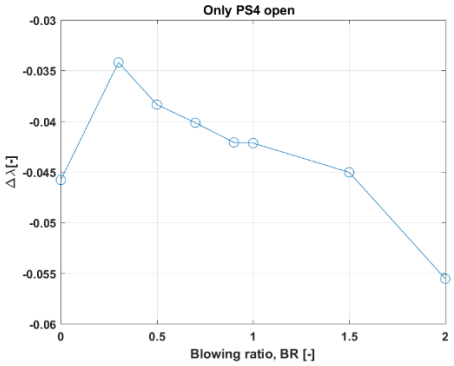

Partial injection: only PS4 open

Figure III.8 Wake area-averaged loss coefficient minus profile losses for all tested configurations. Air as secondary flow.

CO_2 as secondary flow

Wake gauge total pressure, P_t $[Pa]$

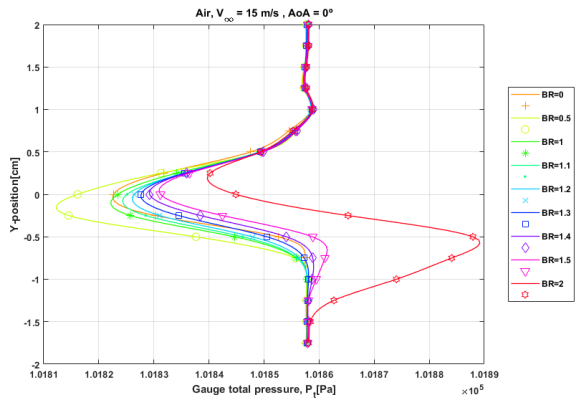

Baseline configuration, air

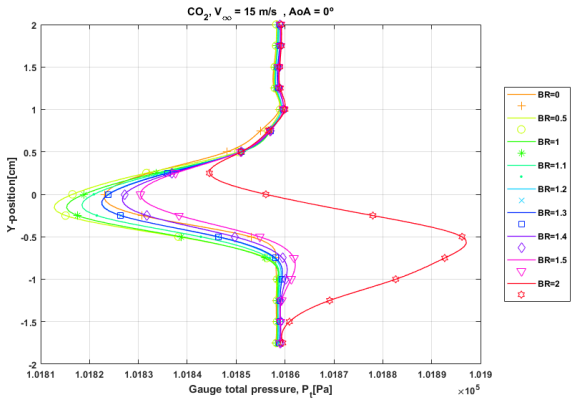

Baseline configuration, CO_2

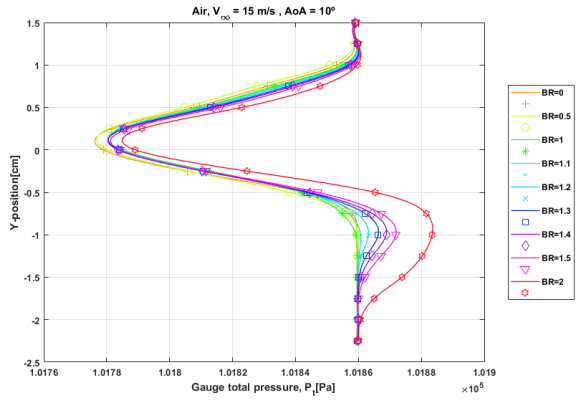

AoA=10°, air

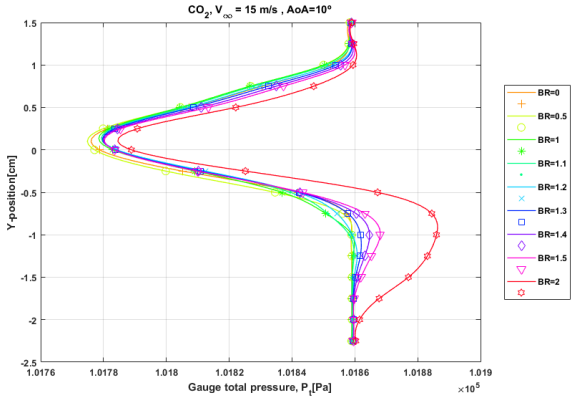

AoA=10°, CO_2

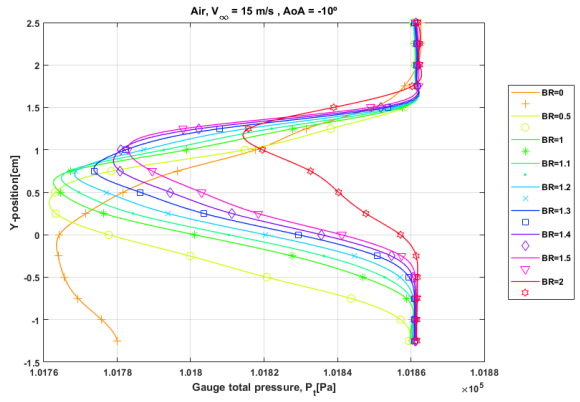

AoA= -10°, air

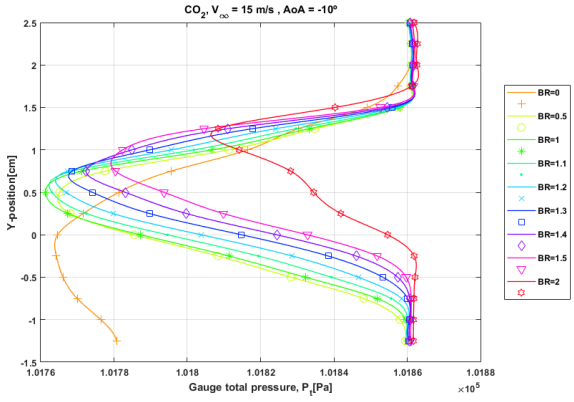

AoA= -10°, CO_2

Figure III.9 Wake gauge total pressure profile for all tested configurations. CO_2 as secondary flow.

Wake velocity, V_2 $[m/s]$

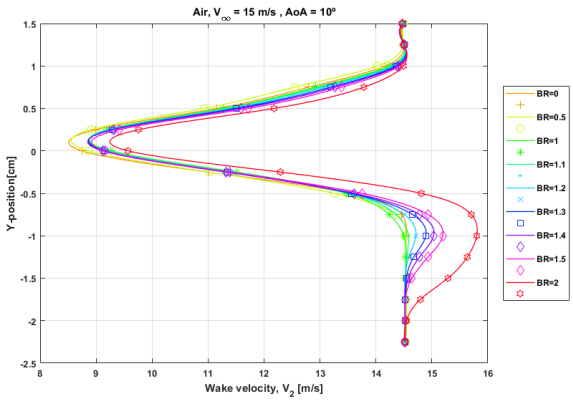

Baseline configuration, air

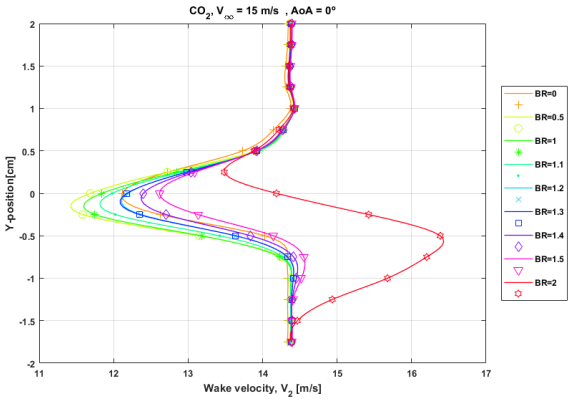

Baseline configuration, CO_2

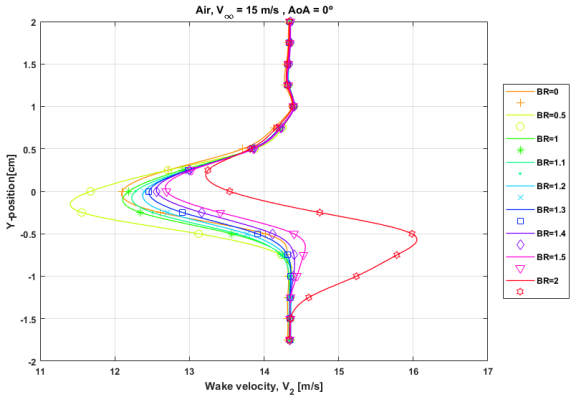

AoA=10°, air

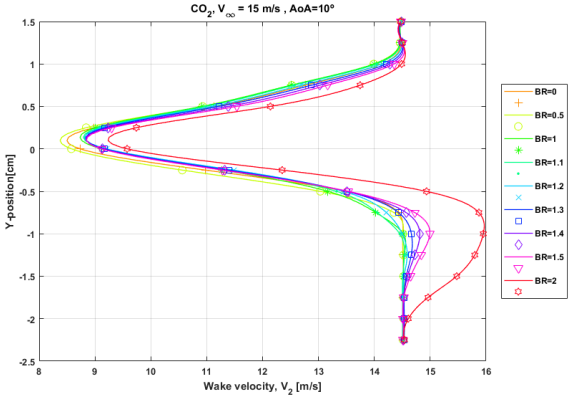

AoA=10°, CO_2

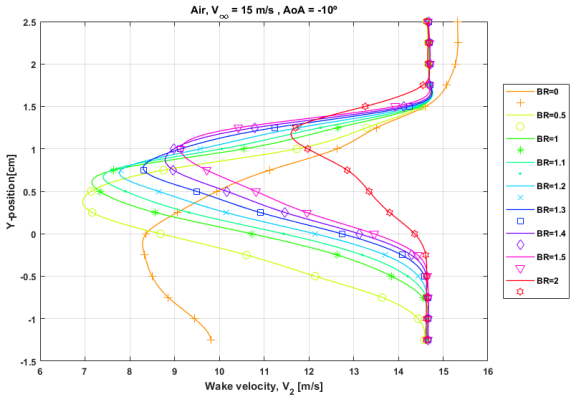

AoA= -10°, air

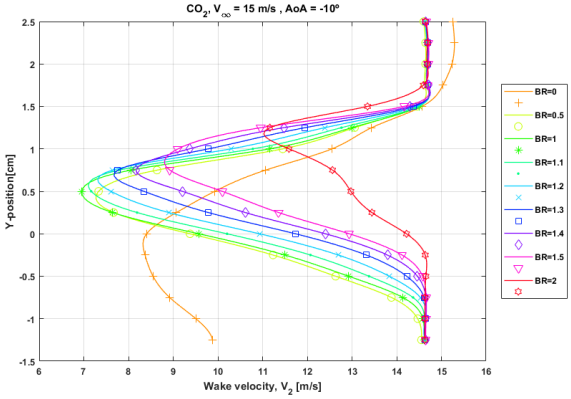

AoA= -10°, CO_2

Figure III.10 Wake velocity profile for all tested configurations. CO_2 as secondary flow.

Primary loss coefficient, ξ_p [-]

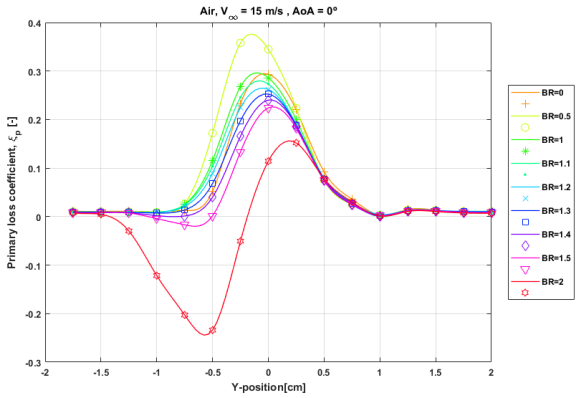

Baseline configuration, air

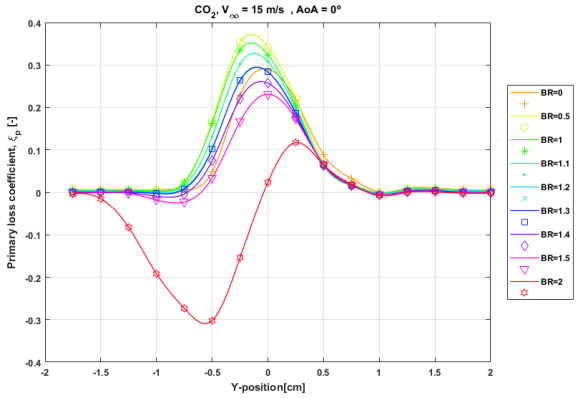

Baseline configuration, CO_2

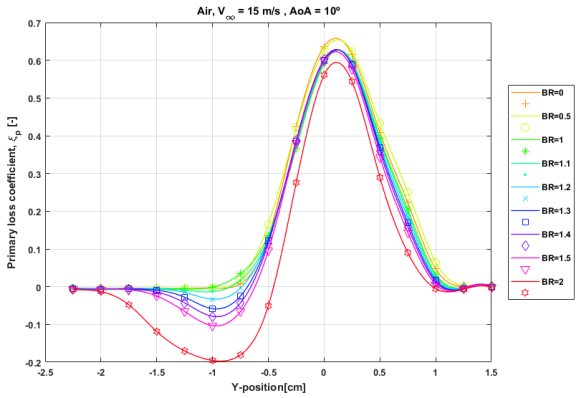

AoA=10°, air

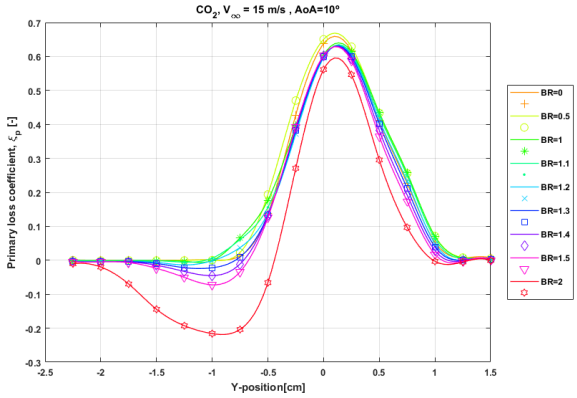

AoA=10°, CO_2

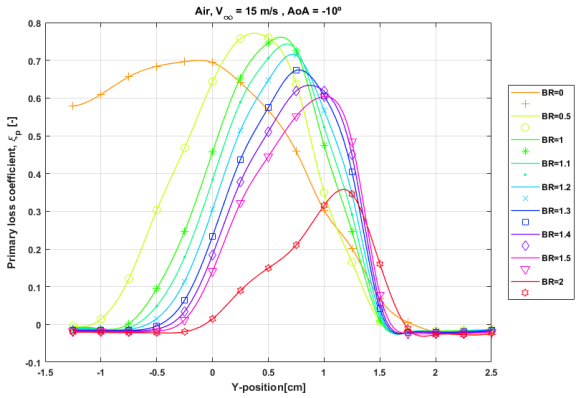

AoA= -10°, air

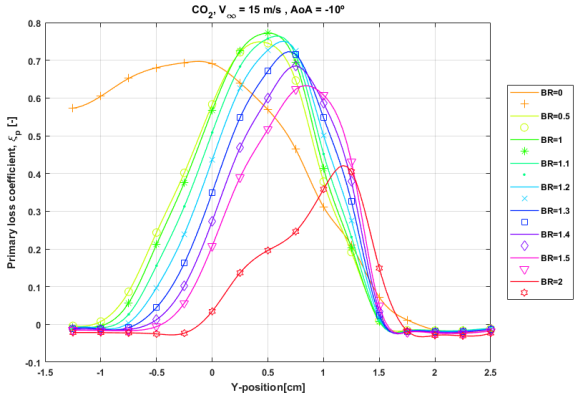

AoA= -10°, CO_2

Figure III.11 Wake primary loss coefficient for all tested configurations. CO_2 as secondary flow.

Local total pressure loss coefficient, C_p [-]

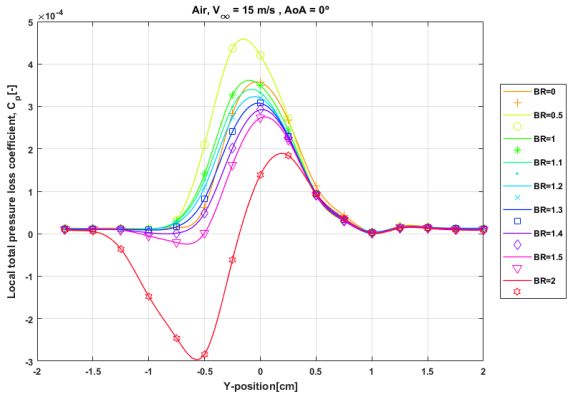

Baseline configuration, air

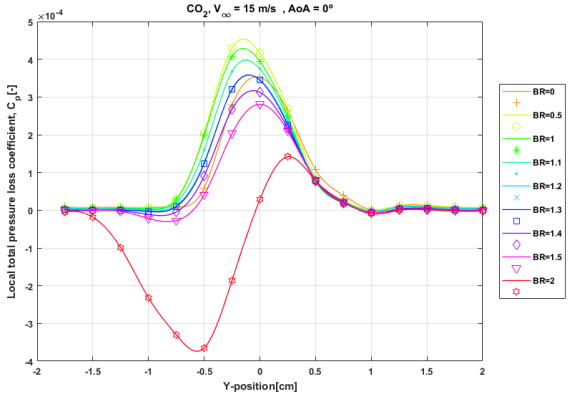

Baseline configuration, CO_2

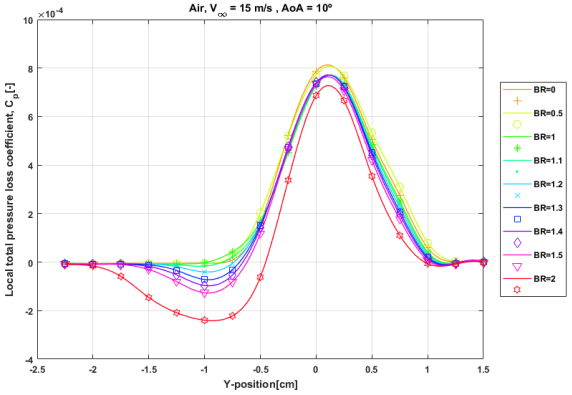

AoA=10°, air

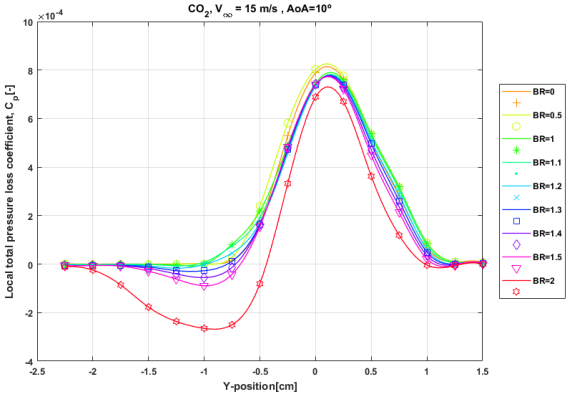

AoA=10°, CO_2

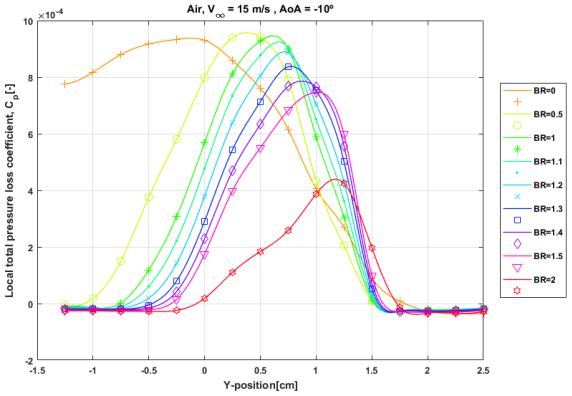

AoA= -10°, air

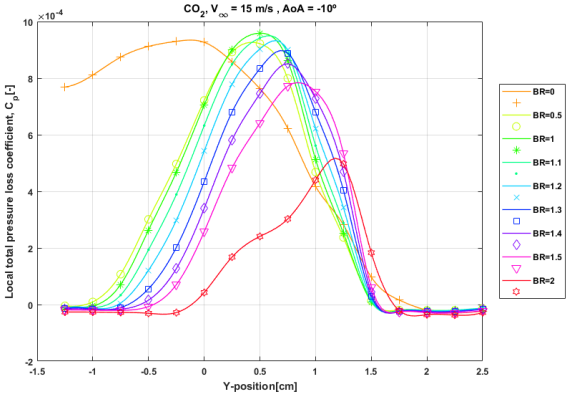

AoA= -10°, CO_2

Figure III.12 Wake local total pressure loss coefficient for all tested configurations. CO_2 as secondary flow.

Total pressure loss coefficient, C_{pt} [-]

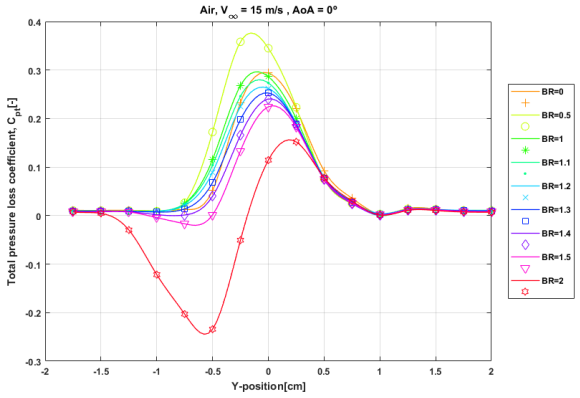

Baseline configuration, air

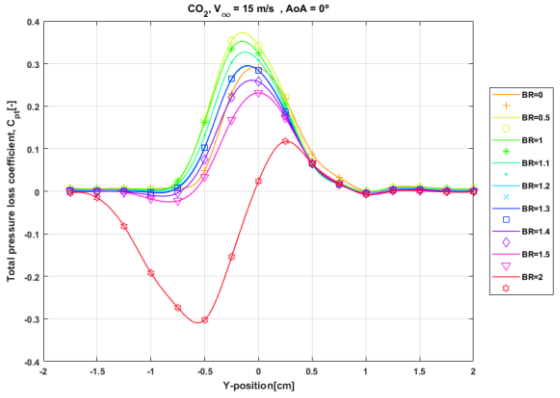

Baseline configuration, CO_2

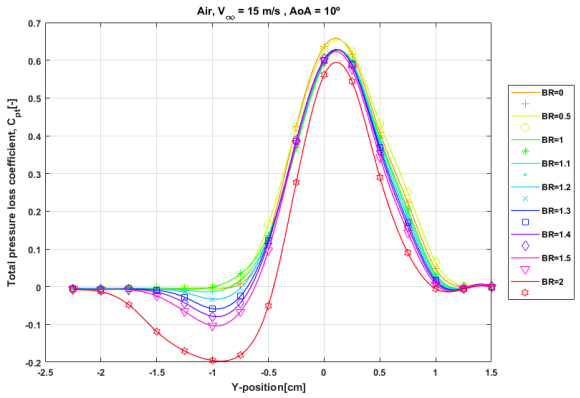

AoA=10°, air

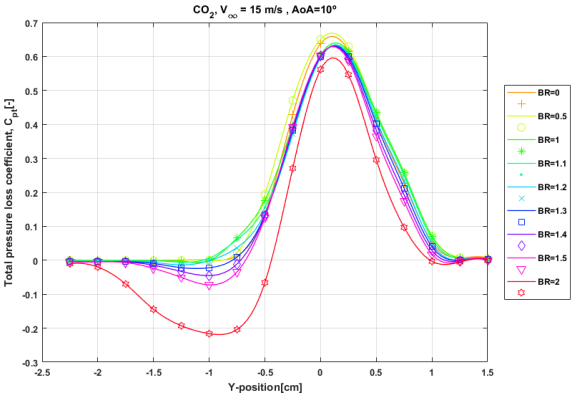

AoA=10°, CO_2

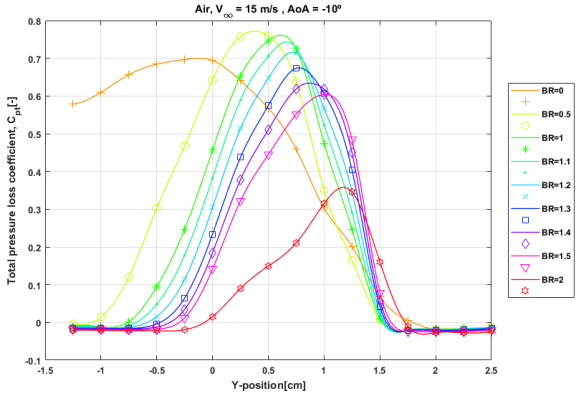

AoA= -10°, air

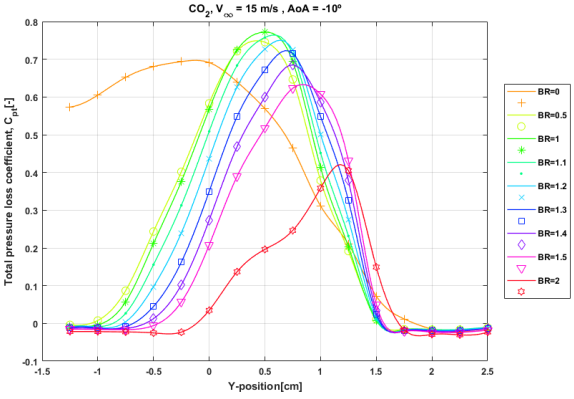

AoA= -10°, CO_2

Figure III.13 Wake total pressure loss coefficient for all tested configurations. CO_2 as secondary flow.

Integrated aerodynamic losses, *IAL* [-]

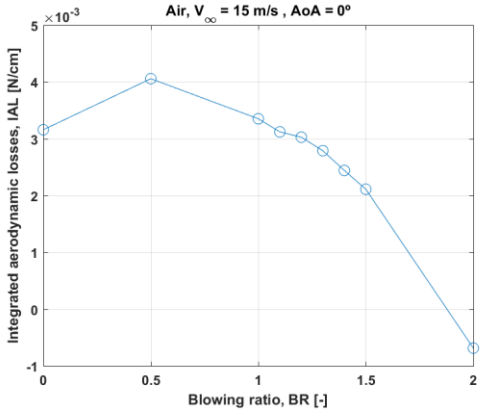

Baseline configuration, air

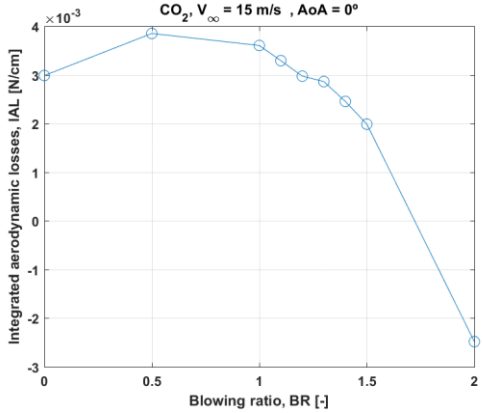

Baseline configuration, CO_2

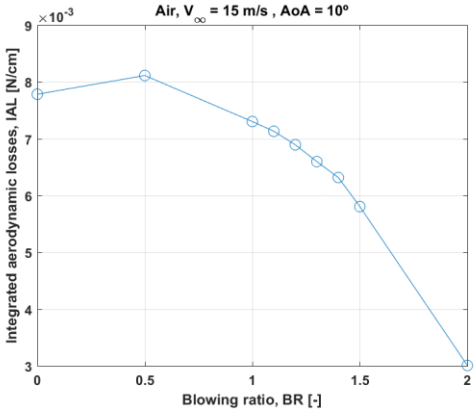

AoA=10°, air

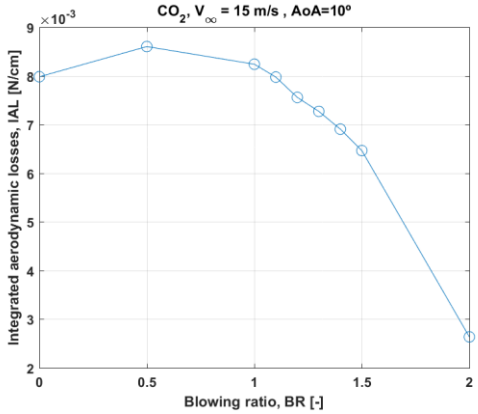

AoA=10°, CO_2

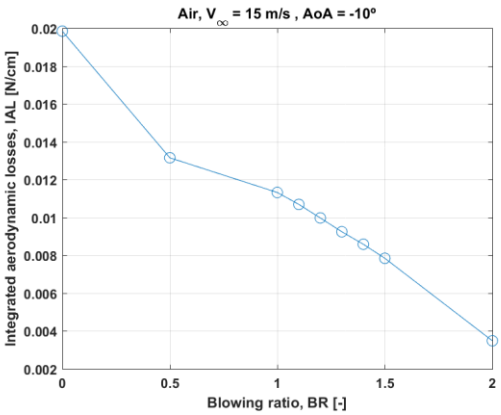

AoA= -10°, air

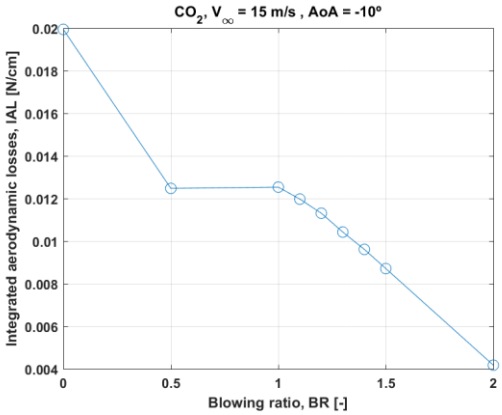

AoA= -10°, CO_2

Figure III.14 Wake integrated aerodynamic losses for all tested configurations. CO_2 as secondary flow.

Area-averaged loss coefficient, λ [-]

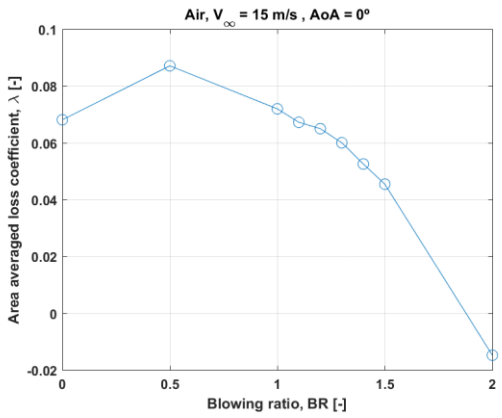

Baseline configuration, air

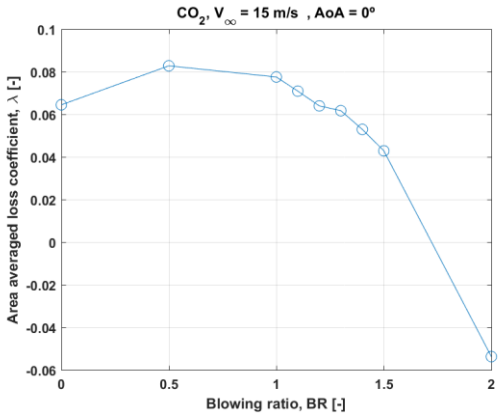

Baseline configuration, CO_2

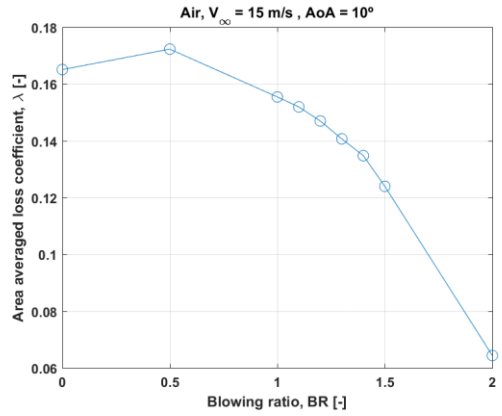

AoA=10°, air

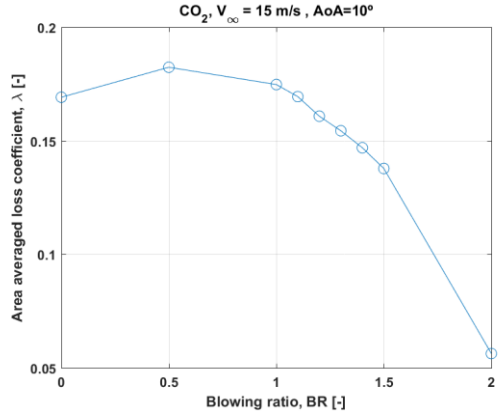

AoA=10°, CO_2

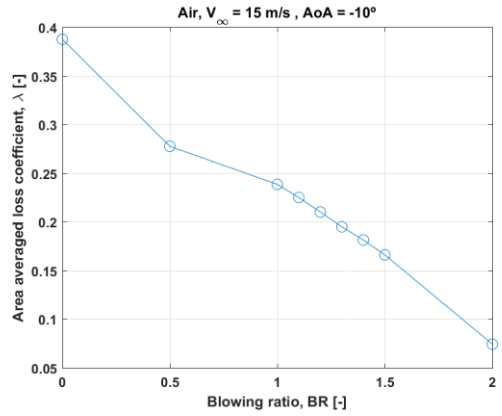

AoA= -10°, air

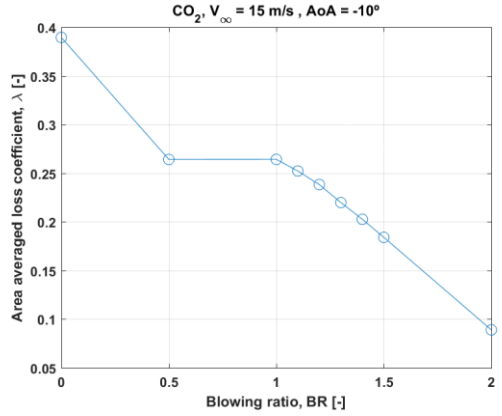

AoA= -10°, CO_2

Figure III.15 Wake area-averaged loss coefficient for all tested configurations. CO_2 as secondary flow.

Comparison of losses vs. coolant scaling parameter, AoA=5º and AoA=10º

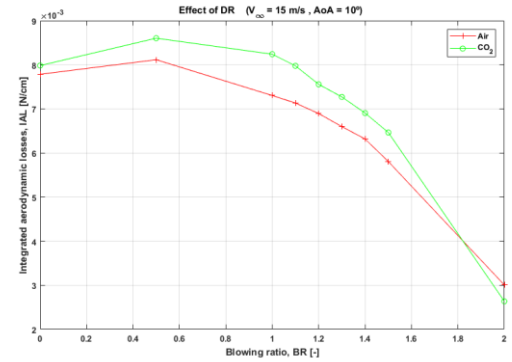

IAL vs. BR, AoA= +10º

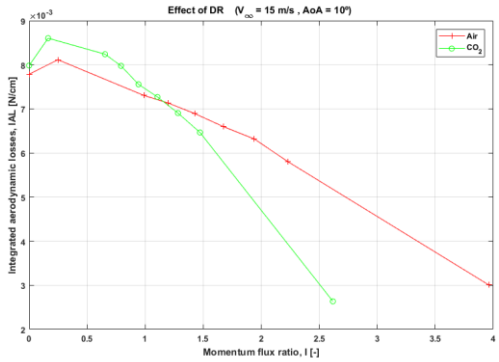

IAL vs. I, AoA= +10º

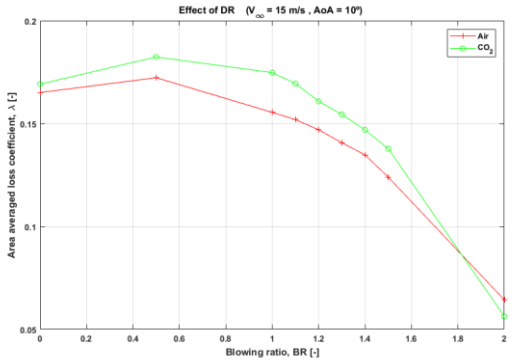

λ vs. BR, AoA= +10º

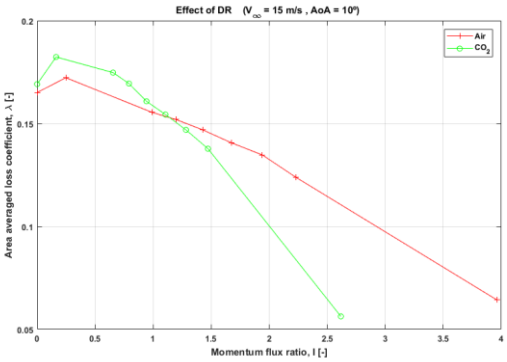

λ vs. I, AoA= +10º

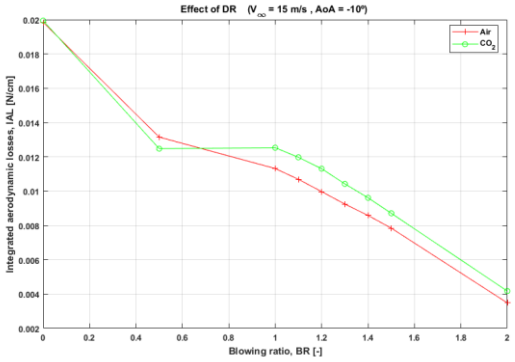

IAL vs. BR, AoA= -10º

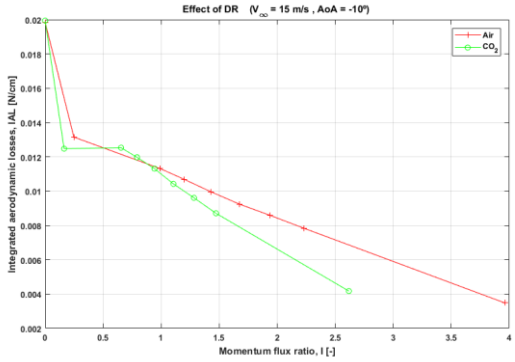

IAL vs. I, AoA= -10º

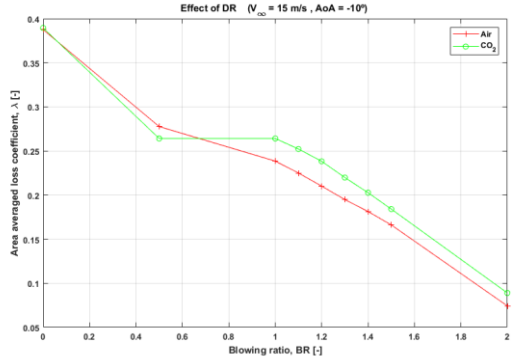

λ vs. BR, AoA= -10º

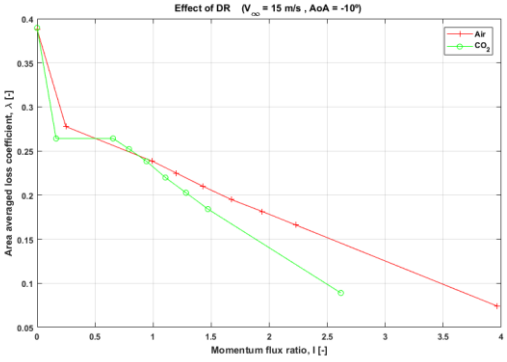

λ vs.I, AoA= -10º

Figure III.16 Comparison of IAL and λ vs. BR and I for test cases $AoA = +10°$ and $AoA = -10°$

Appendix IV: Planar PIV results

In this section the global flowfield planar PIV results presented in Chapter 5 are extended, including all the BR test cases for the baseline configuration and for higher angle of attack, higher freestream velocity and partial injection.

Baseline configuration, V_x $[m/s]$

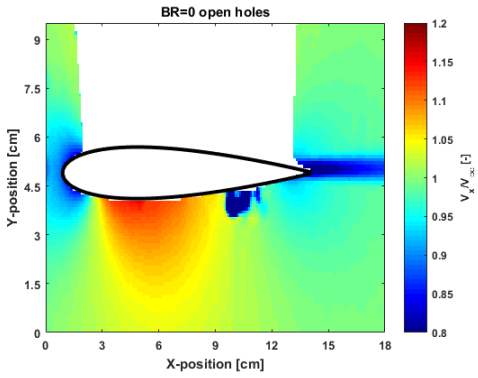

BR=0, open holes

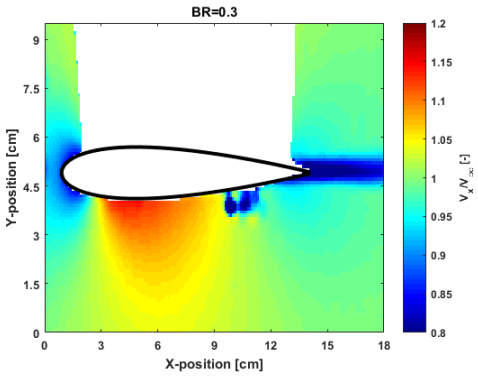

BR=0.3

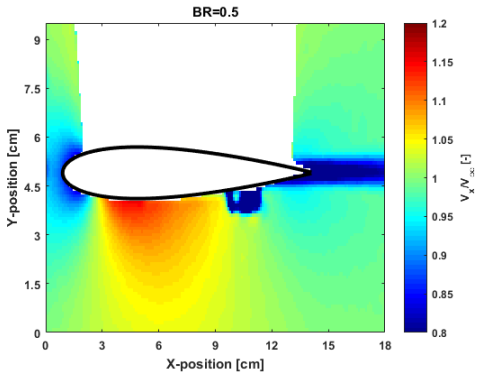

BR=0.5

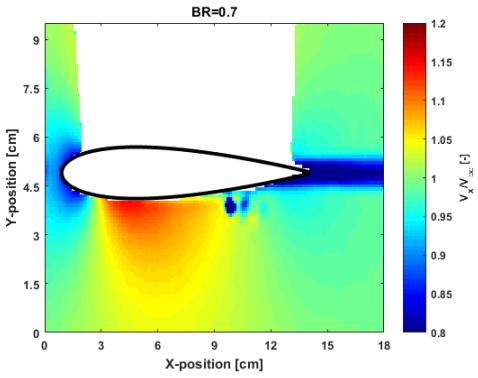

BR=0.7

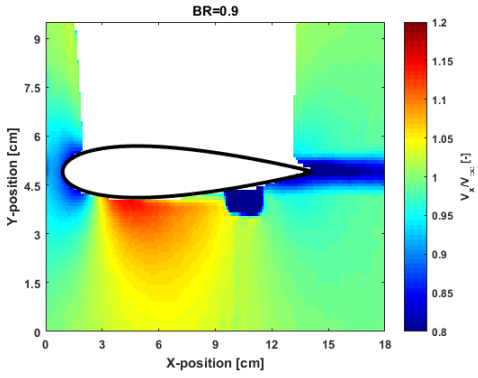

BR=0.9

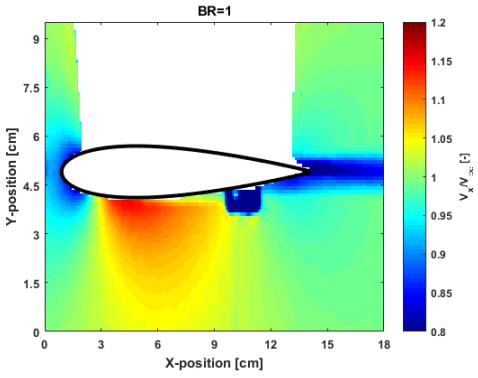

BR=1

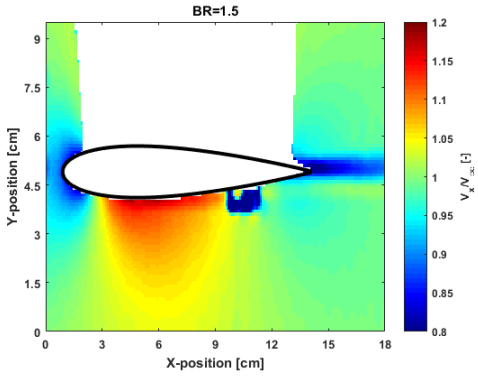

BR=1.5

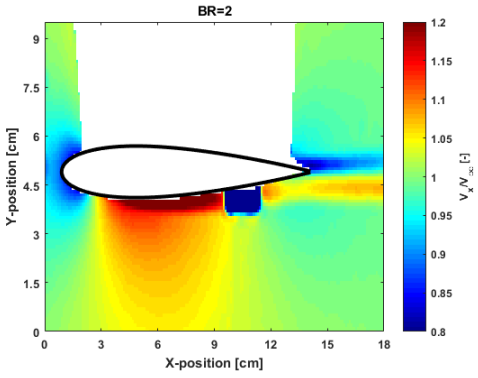

BR=2

Figure IV.1. Planar PIV results for the baseline configuration

AoA=5º, V_x $[m/s]$

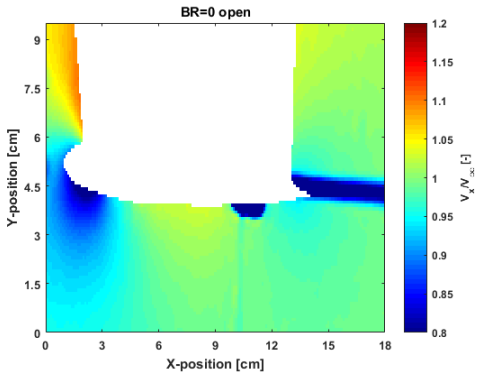

BR=0, open holes

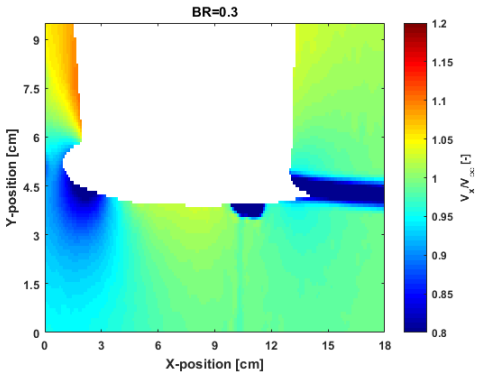

BR=0.3

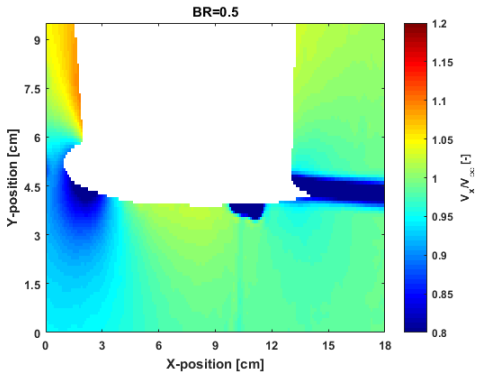

BR=0.5

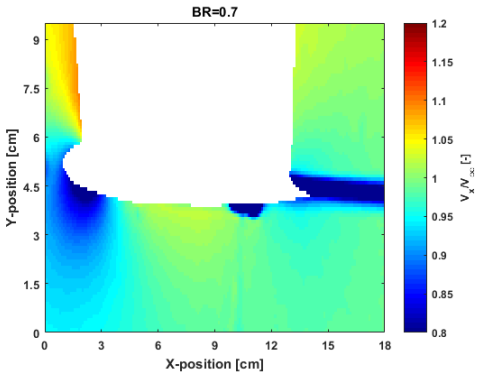

BR=0.7

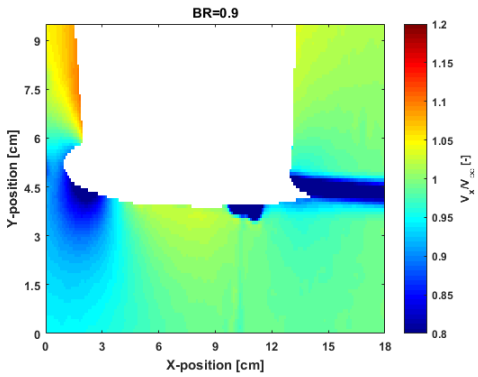

BR=0.9

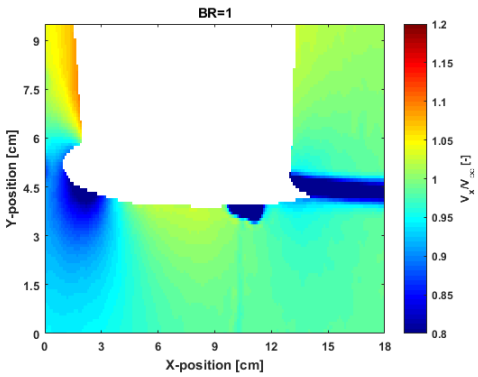

BR=1

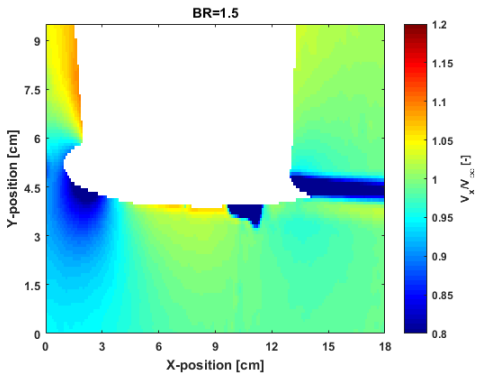

BR=1.5

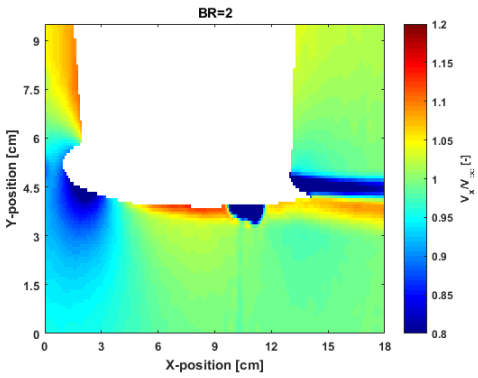

BR=2

Figure IV.2. Planar PIV results for AoA=5º

AoA=10º, V_x $[m/s]$

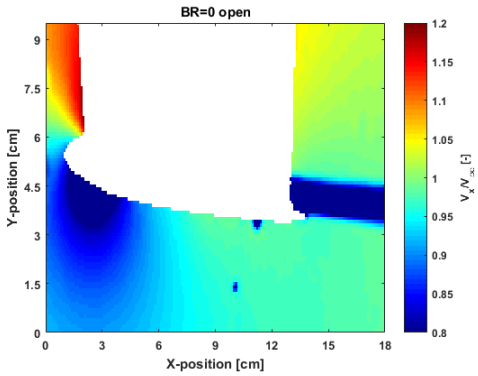

BR=0, open holes

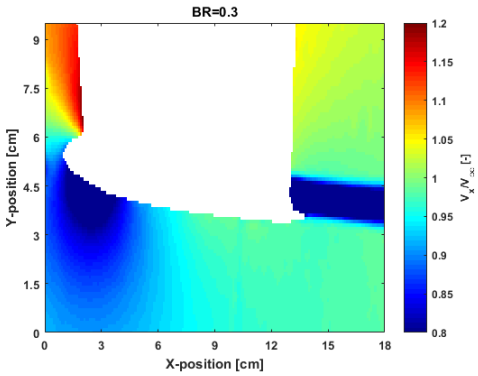

BR=0.3

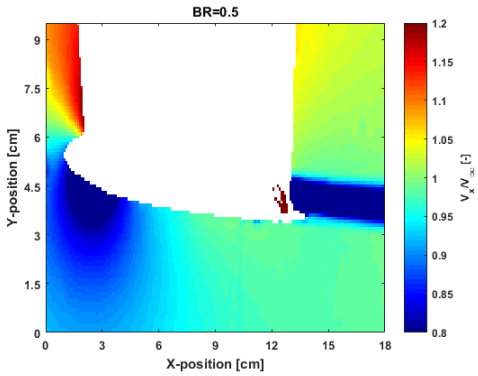

BR=0.5

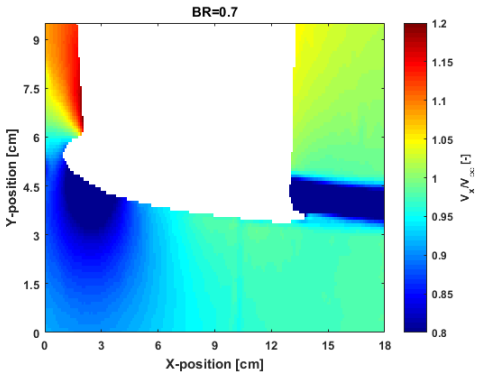

BR=0.7

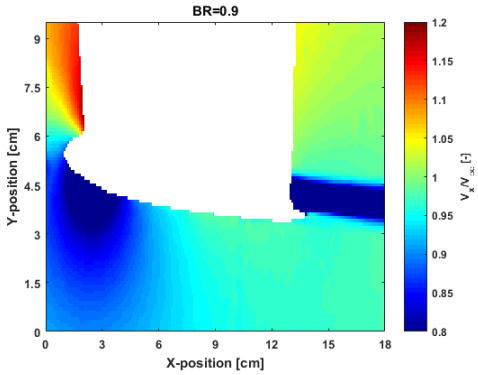

BR=0.9

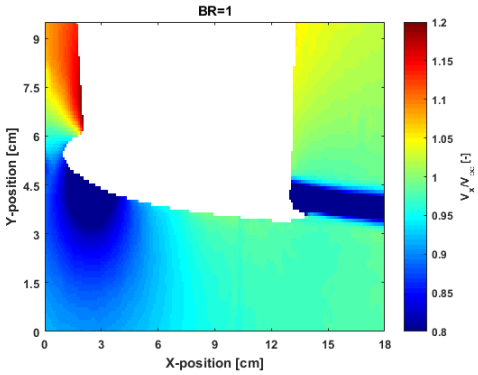

BR=1

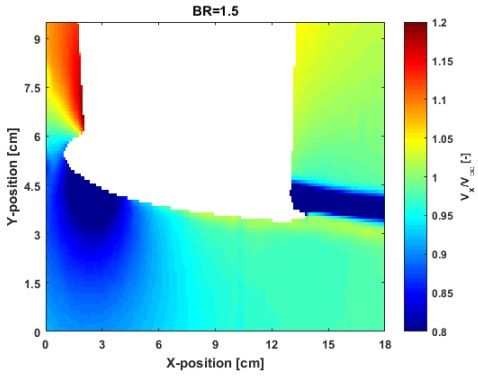

BR=1.5

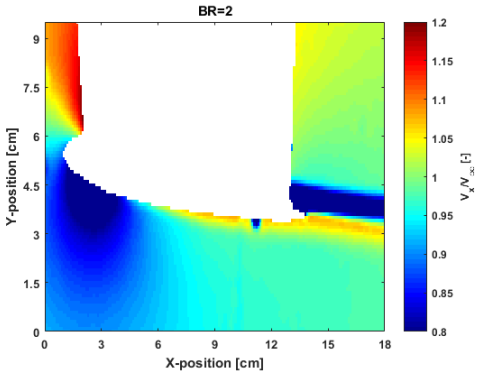

BR=2

Figure IV.3. Planar PIV results for AoA=10º

$V_\infty = 25\ m/s, V_x\ [m/s]$

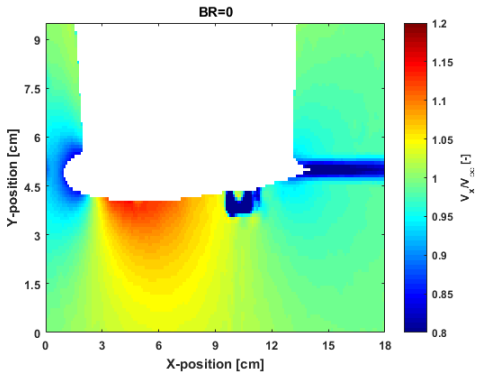

BR=0, open holes

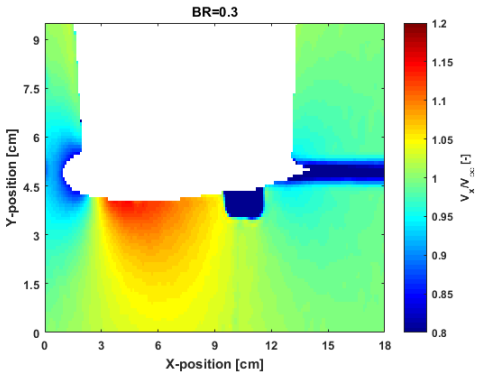

BR=0.3

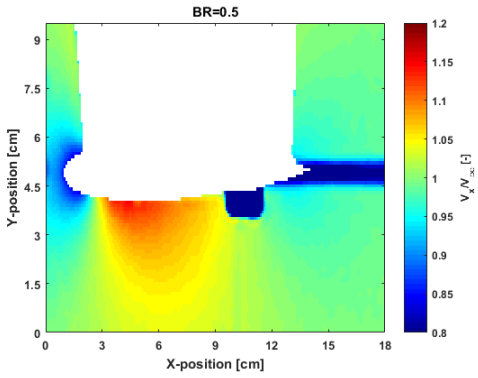

BR=0.5

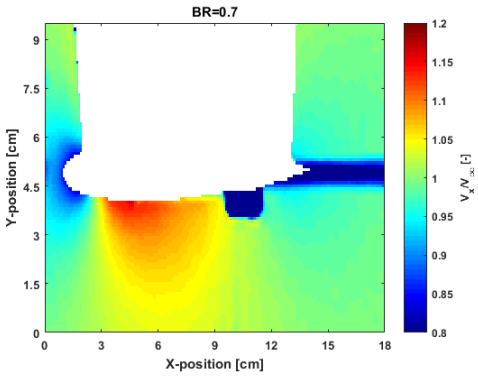

BR=0.7

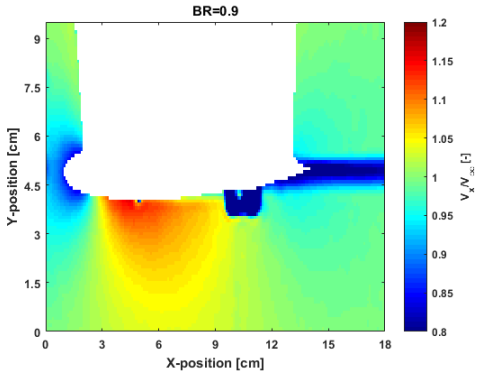

BR=0.9

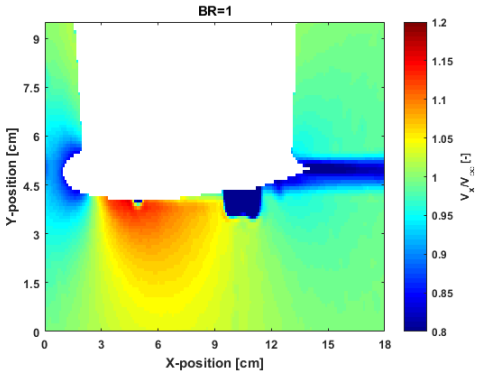

BR=1

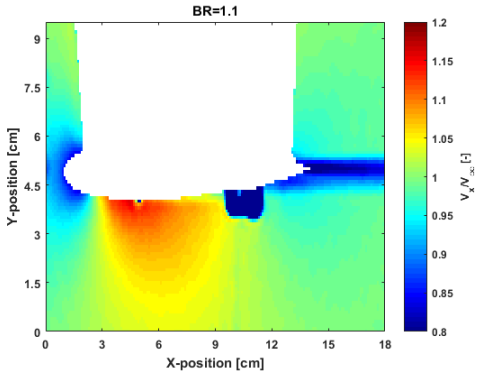

BR=1.1

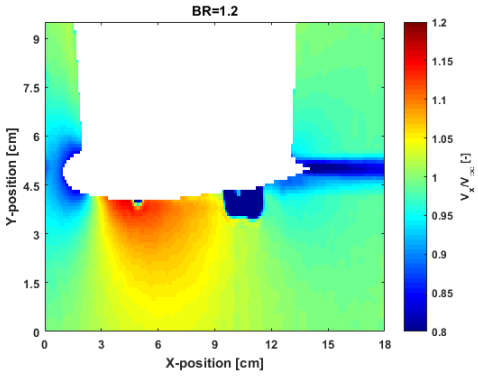

BR=1.2

Figure IV.4. Planar PIV results for $V_\infty = 25\ m/s$

PS1 injection, V_x $[m/s]$

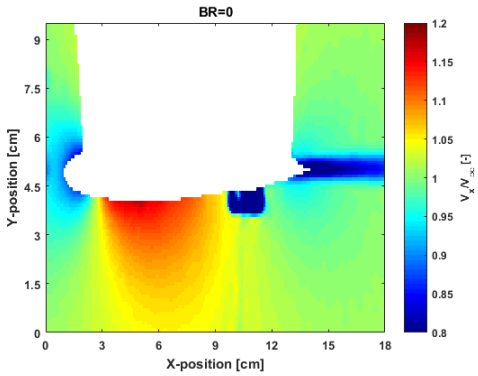

BR=0, open holes

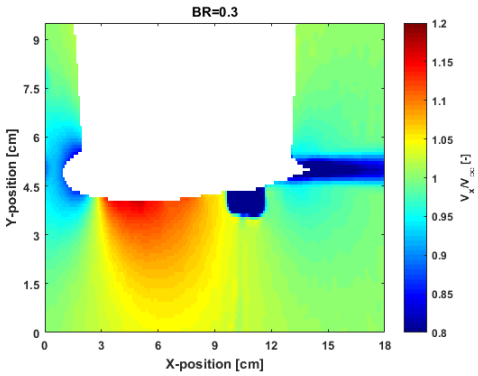

BR=0.3

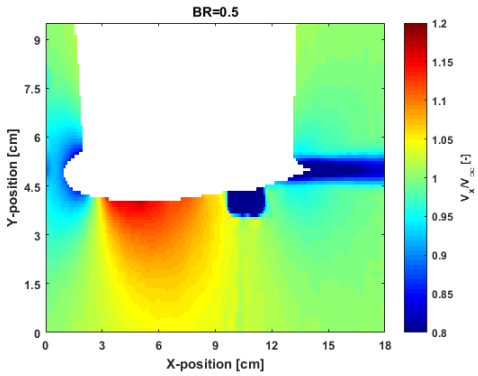

BR=0.5

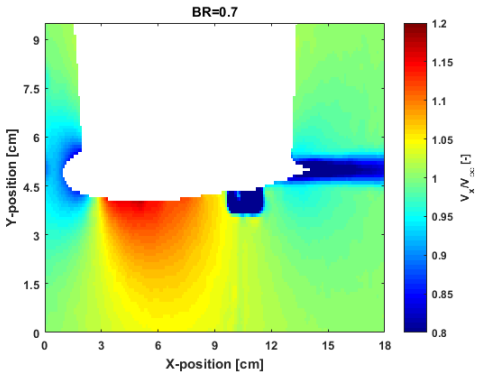

BR=0.7

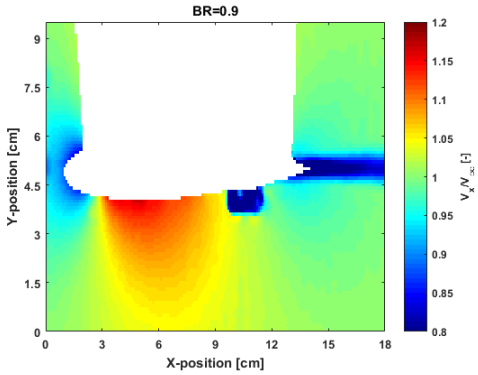

BR=0.9

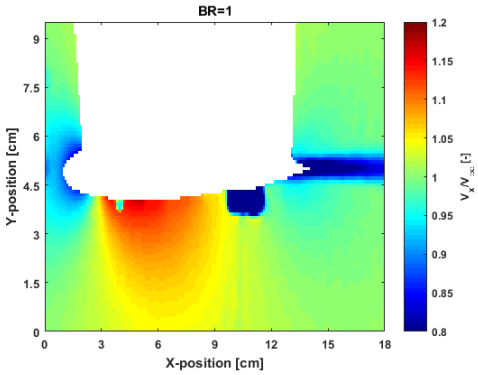

BR=1

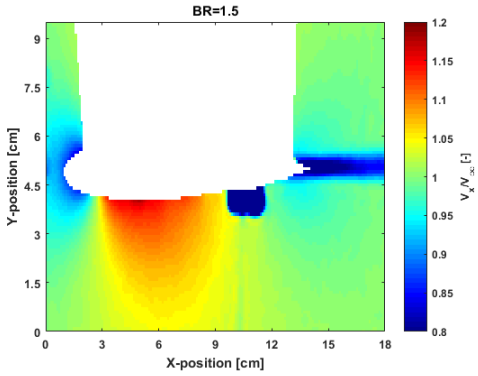

BR=1.5

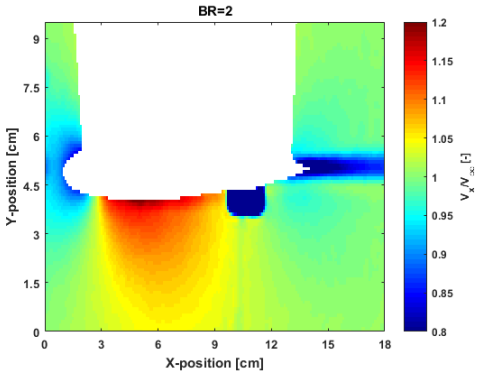

BR=2

Figure IV.5. Planar PIV results for partial injection from PS1

PS2 injection, V_x $[m/s]$

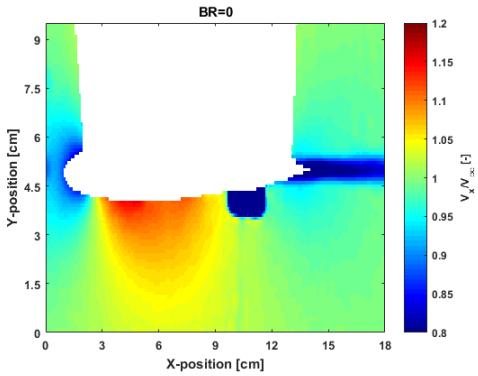

BR=0, open holes

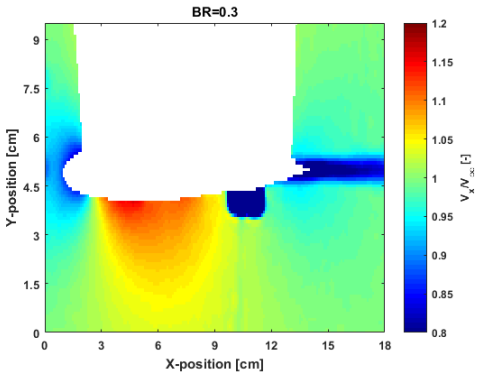

BR=0.3

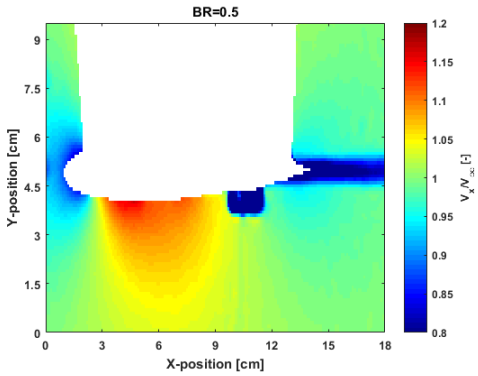

BR=0.5

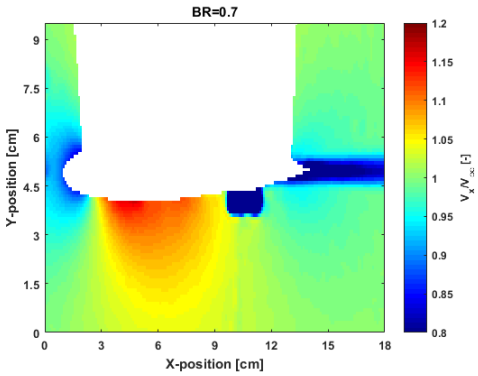

BR=0.7

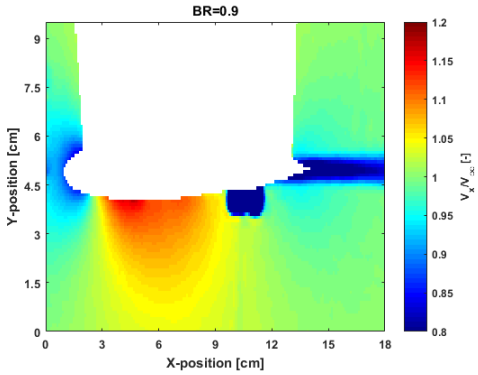

BR=0.9

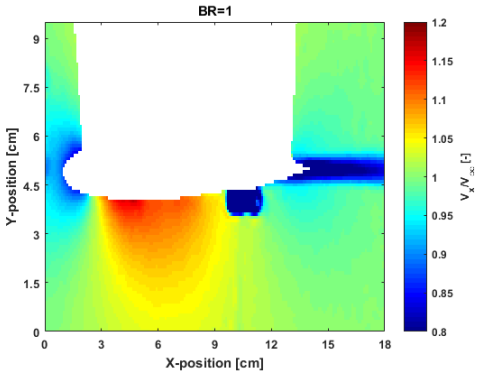

BR=1

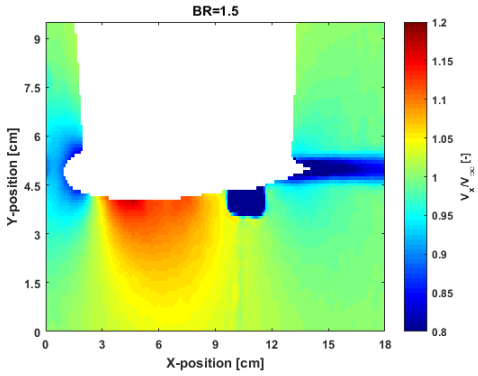

BR=1.5

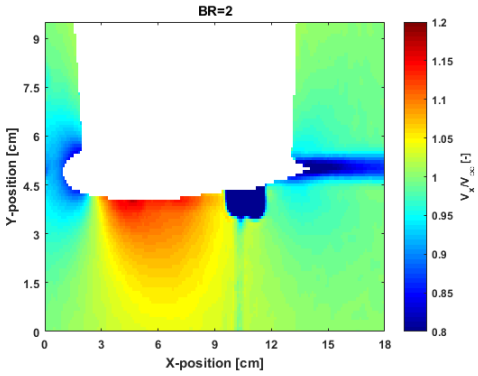

BR=2

Figure IV.6. Planar PIV results for partial injection from PS2

Acknowledgements

B.G. (Before Graduation) days have not been easy sometimes… I´ve often lacked motivation, focus and self-discipline. For this reason, nothing is more precious for me in this whole report than saying a big thank you to all of you who have offered me your help. In the form of ideas, small daily gestures, relentless support or the exact piece of advice or word I needed on a day when I was feeling low to have a fresher and more positive approach, stop complaining and keep going. Once I have my diploma and then ´the hard B.G. days´ might turn into ´the good old B.G. days in Delft that I miss and want to come back to´ when reading this report, it is your faces connected to a big gratitude feeling what I will mainly see through it.

In the first place, thank you, Arvind, for many things. Thank you for your continuous encouragement during all these months and for believing in me multiple times, even when I was not being very responsive. For caring about me enjoying my work, feeling curious about doing research and happy about all the achievements along the process. I am very grateful for all the opportunities you gave me to explore what I like, such as the teacher assistant job, the hackathon or all the possible thesis topics that I could change to after that long discussion we had on a Friday afternoon-evening. Thank you very much for all your time and availability, during your calls or visits when I was in the windtunnel (even on the weekend) and during the weekly meetings which gave me the structure, broader perspective, peace of mind, advices and positive feedback that I needed to continue with the next steps. I always felt that I could come to you for guidance or help but at the same time you kept motivating me to work independently and at my own rhythm.

Thank you, Andrea, for all your help and support before, during and after the test campaigns. Thank you for helping me booking and finding the equipment, thinking of the setup and planning the realistic time that all the runs I had in mind would take. For your time building the PIV setups and your trips to the M-tunnel to explain me how to use it, suggest or make changes to it, check how I was doing and solve the problems. After the test campaigns, thank you for your guidance on how to process the results, suggestions on the report and your prompt feedback on the draft (a very happy day). Above all, I am very thankful to you for the useful, practical and simplifying advices you gave me along the way and your fast answers to my questions or (sometimes irregular) updates, even late in the evening or on Christmas day.

Thank you, Lanzi, for all your previous work during your MSc thesis which was a great starting point for me. I used it as a reference and guideline many times and it saved me lots of time and effort.

Thank you, Stefan, Leo and Nico. Your kind help during the test campaigns was crucial to make things work. Thank you, Stefan and Leo, for providing me with some of the equipment, for ordering the CO_2 tanks and for helping me transporting, fixing, testing and building connections or something from scratch when I needed it. Thank you, Nico, for your remote help or trips to the M-tunnel to solve the problems with DaVis. Also, thank you, Dani and Marios, for helping me with PIV whenever I intercepted you in the LSL.

Thank you, Sumit, for your enthusiasm and drive to do things well. The days at the M-tunnel were easier and more fun when you started coming every day to check how everything was going and help me optimising the PIV setup or acquiring the oil flow visualisation and CO_2 runs.

Thank you to the kitepower room: to start with, for sheltering me, although ‘Clara is not here’. For the unique atmosphere in the room, even with some random Spanish sentences while working, and for (unsuccessfully) trying to show me how to fly a kite or how 12.15h can be an enjoyable time for lunch. Thank you to the lunch group, for making me excited about my lunch every day and for the home/windtunnel food deliveries. Thank you for becoming good friends and in particular, thank you Pranav, Maarten, Jo, Matteo, Greeshma, Bas, Luca. Especially, thank you, Pranav. for being there for me so many times, making sure that I am fed, energetic and motivated, for always offering your support straight away, for all your help with Matlab, and for your company biking back home in the evenings or in your visits to the windtunnel.

Thank you, Reynard, for bringing me to this kitepower room when I was a nomad looking for a good place to work on the thesis and for driving the van from HSL to LSL, with lots of flow(meter). You have always been ready to help me with whatever I needed.

Thank you to my families in Menno: Machín, Dani, Mario, Nicco, Vicky, Lu, Johans, Cam, Michele and Iñigo. Thank you for creating a home, for taking care of me so many times, for cheering me up, feeding me and listening to me. Thank you also to all the rest, who did not live in Menno but have been my family in Delft too. Thank you for all the great moments and things we’ve done together, for sharing yourselves with me, for all the laughs, jokes, surprises, advices, fruitful and less fruitful debates, nice gestures, good energy and fun.

Thank you to my friends, cousins and rest of the family in Madrid and in Burgos: you are always on my mind. Thank you for finding ways to be present, keep connected and send me energy despite the distance. Thank you even more to those who managed to come to Delft to get to know and share a bit of my life here. You have been essential.

Thank you, Matteo. For your unwavering support until almost the end of this project. For encouraging me to start this thesis in the first place and believing in me doing experiments in a windtunnel more than I did myself. Thank you for trying to make me understand and enjoy Matlab, and for all the nested structures. Thank you for keeping me positive and strong so many times and for all your care, joy and love.

Thank you, Doug and Dave. I have only known you for four months, but by no means would this thesis be finished without you (and without the sneaky access to the hospital library). You are truly amazing. Thank you for making my moving to the UK so smooth. For your mood-lifting funny and inspiring stories and the cheerful breakfasts and dinners, for listening to me and helping me relax when I needed it, for preparing tons of food for me and for your dedication in keeping me healthy and joyful.

Finally, mum, dad and Adri. But first than thank you, sorry. Sorry for all the stress that this thesis has caused to you. Then, the biggest thank you of all. Thank you for always ending up supporting me and being there for me, loving me and taking care of me. Especially when you disagree and think that I should do things differently or when you are fed up with me or disappointed and you need some time and patience to understand my reasons. Thank you mum and dad for continuously adapting and devoting yourselves to me and for giving me endless opportunities to grow throughout my whole life. Thank you for all the funny moments that we keep having together and thank you Adri, for your unique way of making me happy and for often being a role model to me. I am so proud of you and you are my favourite of all.